

# Oil & Natural Gas Technology

DOE Award No.: DE-FC26-04NT15506

## Final Report

### Imaging Reservoir Quality: Seismic Signatures of Geologic Processes

Submitted by:  
Department of Geophysics  
Stanford University, Office of Sponsored Research  
340 Panama Street  
Stanford, CA 94305-6203

Prepared for:  
United States Department of Energy  
National Energy Technology Laboratory

August 7, 2008



Office of Fossil Energy



## **DISCLAIMER**

This report was prepared as an account of work sponsored by an agency of the United States Government. Neither the United States Government nor any agency thereof, nor any of their employees, makes any warrantee, express or implied, or assumes any legal liability or responsibility for the accuracy, completeness, or usefulness of any information, apparatus, product, or process disclosed, or represents that its use would not infringe privately owned rights. Reference herein to any specific commercial product, process, or service by trade name, trademark, manufacturer, or otherwise does not necessarily constitute or imply its endorsement, recommendation, or favoring by the United States Government or any agency thereof. The views and opinions of authors expressed herein do not necessarily state or reflect those of the United States Government or any agency thereof.

## ABSTRACT

Lithofacies successions from diverse depositional environments show distinctive patterns in various rock-physics planes (velocity-porosity, velocity-density and porosity-clay). Four clear examples of decameter-scale lithofacies sequences are documented in this study: (1) Miocene fluvial deposits show an inverted-V pattern indicative of dispersed fabric, (2) a fining-upward sequence of mud-rich deep deposits shows a linear trend associated with laminated sand-clay mixtures, (3) sand-rich deposits show a pattern resulting from the scarcity of mixed lithofacies, and (4) a coarsening-upward sequence shows evidence of both dispersed and horizontally laminated mixed lithofacies, with predominating dispersed mixtures generated by bioturbation..

It was observed that carbonate-cemented sandstones are extremely heterogeneous in the project deep-water study area. Those from the base of incisions are usually associated with lower shaliness, lower porosity and higher P-impedance, while from the top of flooding surfaces exhibit higher shaliness, higher porosity and lower P-impedance. One rock physics model that captures the observed impedance-porosity trend is the “stiff-sand model.” For this model, the high-porosity end-member is unconsolidated sand whose initial porosity is a function of sorting and shaliness, while the low-porosity end-member is solid mineral. These two end points are joined with a Hashin-Shtrikman equation.

A systematic variation of quartz:clay ratio from proximal to distal locations was observed in the study area even within a single facies. The quartz:clay ratio changes from [0.5:0.5] to [1:0] along the direction of flow, based on the trends of P-impedance vs. porosity as predicted by the rock model for uncemented sands. The results are in agreement with spill-and-fill sequence stratigraphic model in mini-basin setting. In addition, porosity at the distal location (~25 % to 35%) is higher than the porosity at the proximal location (~20 % to 23%). This trend is explained by a sequence stratigraphic model which predicts progressive increase in sorting by turbidity current along the flow, as well as, quantified by a rock model that heuristically accounts for sorting. The results can be applied to improve quantitative prediction of sediment parameters from seismic impedance, away from well locations.

## TABLE OF CONTENTS

TITLE PAGE	1
Title: Imaging Reservoir Quality: Seismic Signatures of Geologic Processes	1
DISCLAIMER	2
ABSTRACT	3
TABLE OF CONTENTS	4
LIST OF GRAPHICAL MATERIALS	5
EXECUTIVE SUMMARY	7
REPORT DETAILS	10
OBJECTIVE	10
APPROACH	10
RESULTS DURING THE PROJECT	12
REFERENCES	43
ABREVIATIONS AND ACRONYMS	47
PROJECT STATUS REPORT	48
MILESTONE LOG	50
ATTACHMENT A	51
ATTACHMENT B	88
ATTACHMENT C	97
ATTACHMENT D	131
ATTACHMENT E	159

## LIST OF GRAPHICAL MATERIALS

- Figure 1. Conceptual model illustrating the concomitant changes in porosity and elastic properties of clastic sediments. These textural effects have been documented by previous studies: e.g. Murphy (1982), Han (1986), Marion *et al.* (1992), Dvorkin *et al.* (1994), Dvorkin and Nur (1996), Bachrach *et al.* (1998), Avseth *et al.* (2000), Dvorkin and Gutierrez (2001), and Zimmer (2003).
- Figure 2. Rock-physics template to evaluate the patterns of concomitant variations of porosity and elastic properties within clastic sequences.
- Figure 3. Well-log data from two different lithofacies sequences: (a) fining-upward lithofacies sequence from fluvial deposits of the Miocene Guayabo Formation (Llanos Basin Colombia); (b) fining-upward lithofacies sequence from Miocene deep-water deposits offshore West Africa. Fluid substitution has been applied to the velocity and density logs in (b).
- Figure 5 Well-log Porosity-Clay Fraction cross plots from the clastic depositional sequences shown in Figure A-8 (a and b), and Figure A-9 (c and d). Porosity determined from density and neutron (in sands) logs, clay fraction determined from gamma ray and the difference between neutron and density porosities.
- Figure 6. Bivariate histograms of well-log P-wave velocity and porosity (PHID) from the four different clastic depositional sequences shown in Figure A-10. Q indicates the sand points (quartzose sand) and C indicates the clay-rich shale point. Black lines outline the diagenetic trend for quartzose sands; magenta lines outline the depositional trend for sands at 25 MPa, with different proportions of clay (0, 50% and 100%).
- Figure 7. Cross plots of well-log P-wave velocity and density color-coded by fraction of clay for the same four different clastic depositional sequences shown in Figure 6. The plots also show contours of impedance. Notice that for the cases of (a) and (d) the highest impedances correspond to the mixed lithofacies.
- Figure 8: Three parasequences (PS) interpreted within progradational depositional lobes. Changes in sorting is abrupt across the para-sequence boundaries and gradual along the boundaries.
- Figure 9: In well log blocky motif corresponds to aggradational / channel deposits and coarsening-up motif corresponds to progradational depositional lobes.
- Figure 10. Well-log data from two different lithofacies sequences: (a) fining-upward lithofacies sequence from fluvial deposits of the Miocene Guayabo Formation (Llanos Basin Colombia); (b) Figure 3: The scatter points show measurements of porosities and velocities from well log in prograding lobes. The magenta line is obtained using rock physics modeling for unconsolidated sand.
- Figure 11: AVO modeling results: Intercept and Gradient crossplot color-coded by porosity. They indicate distinct trend of variation in reservoir properties from landward to basin-ward
- Figure 12: The depositional trend of sands in the velocity-porosity plane. The data corresponds to uncemented sands from fluvial deposits (well Apiay-1). Data color-coded by clay fraction (V<sub>clay</sub>).
- Figure 13: Well-log data of sandstones from one single stratigraphic sequence within an oil field. The graph shows the three main trends for sandstones: the flat trend associated with the sorting effect, the compaction trend, and the steep diagenetic trend. As predicted from the theoretical model, the MHSLB constitutes an upper bound for the sorting trend.
- Figure 14: There are two major categories of cement based on their spatial relationship to framework grains: rim cements (left) and occluding cements (right). The morphology of carbonate cement is distinctive than siliciclastic cement. Carbonate cements occlude in the pore network, and siliciclastic cements form coatings or rims around framework grains.
- Figure 15: Post-stack, time-migrated seismic section showing sediments deposited in the mini-basin developed on continental slope at Equatorial Guinea. The orange curve represents an erosional surface. The well-logs (yellow: gamma-ray and green: resistivity) can be used to identify the vertical stacking of sands. The synthetics (pink curve) displayed at the well is of reverse polarity. Cemented sands are acoustically harder (blue event) than uncemented sands (red event)
- Figure 16: Comparisons of the V<sub>p</sub>/V<sub>s</sub> of carbonate-cemented sandstone from well logs with the V<sub>p</sub>/V<sub>s</sub> given by Greenberg and Castagna (1992). The blue circles are from

the calcite-interval and yellow-triangles from the ankerite interval. The data show wide range of scatters.

- Figure 17: P-impedance ( $I_p$ ) vs total porosity ( $\phi_{it}$ ) from well logs color-coded by cement mineralogy. The blue circles are from the calcite cemented interval and the yellow-triangles from the ankerite cemented interval. The data from different cement mineralogy indicate different intercepts.
- Figure 18: P-impedance ( $I_p$ ) vs total porosity ( $\phi_{it}$ ) from well logs color-coded by gamma ray index. We think that the sandstones with lower shale content are more prone to cementation, hence, exhibit reduced porosities.
- Figure 19: Comparisons of  $I_p$  and porosity of carbonate-cemented sandstone with those predicted by existing rock physics models. The clusters A and B represent data from the incision-surfaces and top of the flooding-surfaces respectively. The contact cement model (magenta line) does not fit the data from cluster B. The stiff-sand model (green line) overpredicts  $I_p$ . The constant cement model with 1% constant cement (red line) fits both clusters A and B.
- Figure 20: Comparisons of  $I_p$  and porosity of carbonate-cemented sandstone with those predicted by the stiff-sand model (green) and the modified stiff-sand model (red). The modified stiff-sand model is obtained by changing critical porosity from 40 % to 15%. The modified stiff-sand model provides a better fit to the data than original stiff-sand model.
- Figure 21: Comparisons of  $I_p$  and porosity of carbonate-cemented sandstone with those predicted by the conventional DEM (blue) and the modified DEM (red). The parameters in modified DEM model are: 40 % percolation porosity, background matrix consisting quartz, calcite and clay, and inclusions with aspect ratio 0.5. The modified DEM provides a better fit to the data than the conventional model.
- Figure 22: Seismic stratigraphic interpretation. Right: Present-day sea-floor map interpreted from 3D post-stack, time-migrated seismic data. We observe incisions created by submarine canyons on the continental slope. Right: Geometry of mini-basin on vertical seismic section. The mini-basins are formed by incision of submarine canyons. The incised-fill sandstones may be potential reservoir.
- Figure 23: P-impedance ( $I_p$ ) vs. total porosity at well-1 situated at proximal location. [Q,C] represent quartz and clay content input to uncemented rock model. The black lines represent P-impedance predicted by uncemented rock model for different quartz:clay ratio at different porosities. Magenta line shows  $I_p$ -porosity trend predicted by cemented-sand rock model.
- Figure 24: P-impedance ( $I_p$ ) vs. total porosity at well-2 along with predictions from rock models.
- Figure 25: P-impedance ( $I_p$ ) vs. total porosity at well-3 along with predictions from rock models.
- Figure 26: Seismic amplitude map showing channelized turbidite sequence. Well-1, 2 and 3 are located from proximal to distal locations. The black arrow indicates flow direction within channel. Spatial patterns of P-impedance vs. porosity can be observed from the trends predicted by rock model at the well locations.

## EXECUTIVE SUMMARY

We report methodologies for using rock physics models to link stratigraphic, log, and seismic data for better reservoir characterization.

Lithofacies successions from diverse depositional environments show distinctive patterns in various rock-physics planes (seismic velocity-porosity, velocity-density and porosity-clay volume). These patterns are the consequence of textural and compositional variations in the mm- to cm-scale fabric associated with the mechanics of deposition, and coeval post-depositional processes like bioturbation. Four clear examples of decameter-scale lithofacies sequences are documented in this study: (1) fluvial deposits from the Miocene of Colombia show an inverted-V pattern indicative of mm- to cm-scale dispersed fabric in the mixed lithofacies, (2) a fining-upward lithofacies sequence of mud-rich deep water deposits from offshore West Africa shows a linear trend associated with mm- to cm-scale horizontally laminated sand-clay mixtures, (3) sand-rich deep water deposits from offshore Gulf of Mexico present a pattern resulting from the scarcity of mixed lithofacies, and (4) a coarsening-upward lithofacies sequence of shallow marine deposits from Colombia presents evidence of both dispersed and horizontally laminated mixed lithofacies, with predominating dispersed mixtures generated by bioturbation.

The applicability of the patterns observed to predict the seismic properties of larger sequences and away from well control depends on vertical and lateral persistence of the lithofacies assemblage. Syntectonic fluvial deposits from one area present good vertical persistence, resulting in remarkable similarity between the rock-physics patterns of decameter-scale and the larger-scale sequences. Shallow marine deposits from the same area constitute a good example of lateral continuity of lithofacies assemblages. In contrast, mud-rich deep water deposits show a high vertical variability of lithofacies. Three different types of clay-rich lithofacies occur, their vertical distribution apparently controlled by changes in relative sea level. Extrapolation of the patterns observed to similar depositional settings in other basins depends on the repeatability of the lithofacies assemblage and diagenesis.

Rock-physics models can predict the changes that diagenetic processes and confining pressure induce on the velocity-porosity patterns of lithofacies successions. The shape variation with depth of the inverted “V” pattern, predicted by the Marion-Yin model, coincides with the patterns observed in fluvial deposits at different depths, although rather than confining pressure, the actual mechanism might be either pressure solution or incipient cementation

Sequence stratigraphy is the geologic interpretation of process/response events that can predict the likely occurrence of reservoir facies, source rocks and seals. Traditional stratigraphic interpretation from post-stack seismic data has been predominantly qualitative based on visual inspection of geometric patterns in the seismic reflections. However, quantitative interpretation of seismic amplitude is possible if we can extract information about compositional maturity (mineralogy, clay content) and textural maturity (sorting, grain angularity, sphericity and roundedness) using principles of sedimentology. Quantitative seismic interpretation uses rock physics to link seismic amplitude with reservoir properties, like, porosity, clay-content, sorting, diagenetic cements etc. that are estimated from the stratigraphic analysis.

We have applied this concept in a deep-water turbidite system from Campos Basin, offshore Brazil. Our interpretation was based on (a) basin history (b) geometry and truncation patterns of reflectors and (c) stacking patterns of well logs. We considered three para-sequences within the prograding depositional lobes and used sequence stratigraphic principles to predict relative trends of sorting, an important control on porosity. Corresponding elastic properties were estimated using the soft-sediment model, which combines Hertz-Mindlin contact mechanics with the Hashin-Shtrikman lower bound. AVO signatures at the sequence boundaries were predicted, showing, for example, distinct landward-basinward trends of intercept and gradient.

The soft sediment model trend is considered to be solely the effect of sorting. However, our mathematical models demonstrate that packing also has an influence. The velocity-porosity trend observed in subsurface data agrees with the flat trend predicted from our theoretical analysis. A least-squares regression between sorting and porosity from the core data indicates a small negative correlation between porosity and the grain size, which indicates a minor influence of packing, probably associated with grain angularity (fine grains tend to be more angular than coarser sands). However, the effect of sorting on porosity, in these sands, is stronger than the effect of packing. The high-porosity have better sorting than the low-porosity clean sands. These two different types of sands create the flat trend observed in the velocity-porosity plane.

We have explored how carbonate-cemented sandstones associated with parasequence boundaries increase the acoustic impedance of those sediments. It was observed that carbonate-cemented sandstones are extremely heterogeneous in nature in the project study area, offshore Equatorial Guinea, West Africa. Their grain-size, sorting, mineralogy, clay-content, amount of cement and degree of leaching vary considerably. Two distinct behaviors were identified. Carbonate-cemented sandstones from the base of incisions are usually associated with lower shaliness, lower porosity and higher P-

impedance, while data from the top of flooding surfaces exhibit higher shaliness, higher porosity and lower P-impedance.

Traditional stratigraphic interpretation from post-stack seismic data has been predominantly qualitative based on visual inspection of geometric patterns in the seismic reflections. However, quantitative interpretation of seismic amplitude is possible if we can extract information about compositional maturity (mineralogy, clay content) and textural maturity (sorting, grain angularity, sphericity and roundedness) using principles of sedimentology. Quantitative seismic interpretation uses rock physics to link seismic amplitude with reservoir properties, like, porosity, clay-content, sorting, diagenetic cements etc. that are estimated from the stratigraphic analysis. We have applied this concept to a field site offshore Equatorial Guinea, West Africa. We observe a systematic variation of quartz:clay ratio from proximal to distal locations even within a single facies. Furthermore, we quantify that the quartz:clay ratio changes from [0.5:0.5] to [1:0] along the direction of flow, based on the trends of P-impedance vs. porosity as predicted by the rock model for uncemented sands. The down-dip trend of quartz:clay ratio as revealed from the data, contradicts the grain-size predictions from common sequence-stratigraphic models. However, the results are in agreement with spill-and-fill sequence stratigraphic model in mini-basin setting. In addition, porosity at the distal location (~25 % to 35%) is higher than the porosity at the proximal location (~20 % to 23%). This trend is explained by a sequence stratigraphic model which predicts progressive increase in sorting by turbidity current along the flow, as well as, quantified by a rock model that heuristically accounts for sorting. Our results can be applied to improve quantitative prediction of sediment parameters from seismic impedance, away from well locations.

## REPORT DETAILS

### OBJECTIVE

The overall objective of this project is to improve the accuracy and resolution of interpreting lithofacies, pore fluids, and reservoir quality from seismic. A related goal is to establish quantitative rock physics links between highly successful, but often disconnected technologies, such as attributes analysis, AVO, seismic inversion (including acoustic and elastic impedance), 3D-seismic geomorphology, sequence and seismic stratigraphy, and basin modeling. Too often, quantitative seismic analysis, processing, and inversion are done without the benefit of geologic expertise, while geologic modeling and interpretation might be done without being able to quantify the seismic attributes that might distinguish multiple geologic hypotheses. A key to managing complexity and risk in exploration and production has always been effective integration of the diverse petroleum technologies. Workstations, visualization software, and geostatistics have contributed to integrating the vast amounts of *data* that we sometimes drown in. Perhaps more important are the asset teams that exploit diverse data by *integrating expertise*. Our objective includes helping to make the links between geology, seismic, and reservoir properties more *quantitative*.

### APPROACH

Our approach is to introduce fundamental rock physics relations, which help to quantify the geophysical signatures of rock and fluid properties. Since rock properties are a consequence of geological processes, we begin to quantify the seismic signatures of various geologic trends. We also fully embrace probabilistic and geostatistical tools, as quantitative means for managing the inevitable uncertainty that accompanies all quantitative methods. Quantifying, managing, and understanding the uncertainties is critical for survival in a risky environment.

The results of this work will help to define an interpretation strategy for relating high-resolution seismic images of natural heterogeneities to the geologic systems and rock parameters that control the storage and mobility of natural hydrocarbons. Our approach is to combine, within the geologic framework of the basin and/or reservoir, carefully processed seismic, core-calibrated down-hole measurements, and engineering data to reliably characterize reservoir heterogeneities.

We are using a multidisciplinary approach to examine and quantify grain-scale processes in rocks and to explore how to quantitatively recognize those properties seismically. We will develop improved models for the elastic signatures of compaction and diagenesis not only for sands but also for shales and mixed lithologies. Geologic compaction trends are often described separately for sands and for shales. However, mixed lithologies pose interesting problems. Understanding these mixing laws can be critical to relating seismic signatures to sedimentary processes. The study consists of three main parts:

- (1) **Geologic controls on rock microstructure.** We will work to better understand the variation of composition, fabric and physical properties of different types of shale according to their depositional environments, in order to distinguish them from sand reservoirs. From these, we will be using models and data to explore the impact of these fabrics on elastic properties.
- (2) **Quantify the elastic (seismic) signatures** of lithology, textural maturity, pore pressure, and diagenetic processes of compaction, pressure solution, and cementation. We will evaluate the effect that stratigraphic sequences of different scales and their lithology trends have on seismic response.
- (3) **Validate by integrating and interpreting reservoir field data.** We will combine the geologically calibrated rock physics relations with statistical analysis of the reservoir variability and measurement-related uncertainties. This will allow us to identify the most likely estimates of reservoir rock and fluid properties and their variation in space and time. Finally, we will quantify the uncertainties of these interpretations, and identify ways of reducing this uncertainty.

## **RESULTS DURING THE PROJECT**

Project researchers completed and validated workflows aimed at using rock physics methods to integrate stratigraphic, log, and seismic data for improved reservoir characterization. Results of the project are summarized here, with more extensive discussions included in five Attachments. The work is presented in five sections:

- Rock Physics Patterns of Clastic Depositional Sequences
- Reservoir Quality Prediction by Integrating Sequence Stratigraphy and Rock Physics
- Sorting and Packing Effects on the Elastic Properties of Sands
- Seismic Response of Carbonate-Cemented Sandstones
- Quantifying Spatial Trends of Sedimentological Parameters

Methods presented in each section were developed and validated using data from real field sites.

### **ROCK PHYSICS PATTERNS OF CLASTIC DEPOSITIONAL SEQUENCES**

#### **Introduction**

Besides fluids and pressure, rock texture and lithofacies strongly influence seismic rock properties (e. g. Yin, 1992; Wang, 2001). The lateral variations in elastic properties of an intact, water-saturated, sedimentary rock, under uniform effective pressure and temperature, are determined by the lateral variations in clay content, sorting, packing, mineral composition, and cementation. These textural variations are the result of depositional and diagenetic processes (Figure 1). The impact of textural variations in seismic properties constitutes an important source of uncertainty in the prediction of reservoir properties from seismic data. Understanding the relationships between rock texture, fabric, and seismic response can reduce, or at least assess, the uncertainty associated with these predictions.

During this project, significant progress was made in documenting and understanding how rock microtexture, and hence rock elastic properties, vary from location to location, while being controlled in a somewhat predictable way by sedimentologic processes. We concisely summarize key results in this section. A more complete presentation of the technical details is given in the Attachment A.

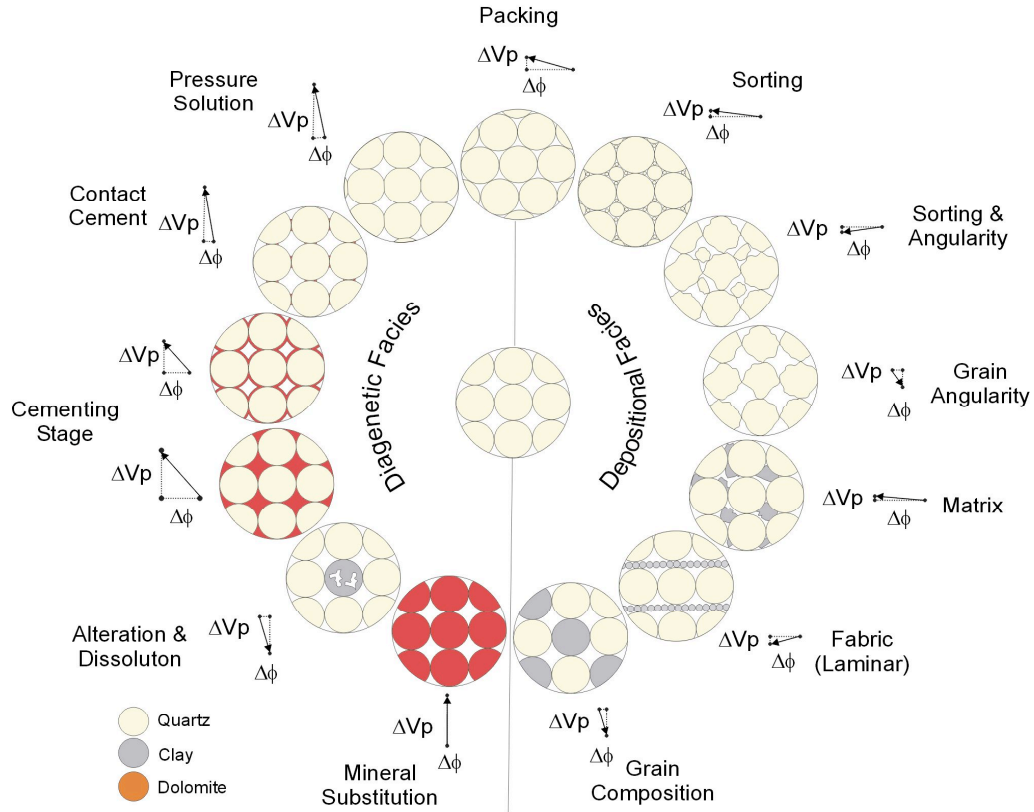


Figure 1. Conceptual model illustrating the concomitant changes in porosity and elastic properties of clastic sediments. These textural effects have been documented by previous studies: e.g. Murphy (1982), Han (1986), Marion *et al.* (1992), Dvorkin *et al.* (1994), Dvorkin and Nur (1996), Bachrach *et al.* (1998), Avseth *et al.* (2000), Dvorkin and Gutierrez (2001), and Zimmer (2003).

## Methodology

This work involved the evaluation of well-log data from different basins and depositional environments.

We use three main cross plots to perform the analysis and comparison of the variation of elastic and bulk properties (porosity) within clastic depositional sequences: (1) bivariate histograms and color-coded cross plots of seismic P-wave velocity ( $V_p$ ) and porosity ( $\phi$ ); (2) cross plots of porosity as a function of clay fraction ( $V_{clay}$ ); and (3) color-coded cross plots of P-wave velocity and density. In general, we refer to these cross plots as the rock-physics planes.

The rationale behind this approach is the application of rock-physics diagnostics (Dvorkin and Nur, 1996) constrained to stratigraphic sequences (Gutierrez *et al.*, 2001). We analyze the patterns of lithofacies sequences with a clear trend in clay content, inferred from both the gamma ray readings and the difference between neutron (NPHI)

and density (PHID) porosities. In the cross plots the porosity corresponds to density porosity (PHID). The analyzed sequences correspond to genetically related lithofacies assemblages that form part of larger stratigraphic sequences.

Fluid substitution has been applied to velocity and density data in the case of hydrocarbon-bearing sands, in order to remove the fluid effect on the rock's elastic properties. Since the rocks analyzed are at similar pressure and temperature conditions, share a similar burial history, and have similar fluid saturations after fluid substitution, texture and composition are the dominant factors controlling the observed variations in elastic properties and porosity within any analyzed lithofacies sequence.

The rock-physics template shown in Figure 2 illustrates one of the frameworks used for rock physics diagnostics. The template was built as follows: the black lines correspond to the diagenetic trend. The magenta lines correspond to the unconsolidated sandstone model (Mavko *et al.*, 1998) for different quartz-clay compositions. The anchor point for the unconsolidated model is given by the Hertz-Mindlin model at 25 MPa, with a correction factor of 0.7 for the shear stiffness. It is important to bear in mind that the purpose of these lines is not to fit the data, although in some cases they do it very well. The lines provide a framework that allows us to identify variations between different data sets, and to infer the textural changes that can explain these differences. The inferred textures can be compared with the description of mudlog cuttings, core analysis, or other logging tools.

### **Rock-Physics Patterns of Selected Depositional Sequences**

This section presents the patterns observed in four selected lithofacies sequences from different depositional environments, illustrated in Figure 3 and Figure 4. The first example (Figure 3a) corresponds to fluvial deposits of the Miocene Guayabo Formation from the Llanos Basin (Colombia). The following case (Figure 3b) corresponds to Miocene, mud-rich, deep-water deposits from offshore West Africa. The third case (Figure 4a) shows sand-rich deep-water deposits from offshore Gulf of Mexico. The last case (Figure 4b) illustrates a coarsening-upward trend of shallow marine deposits from the Miocene Leon Formation, in the Llanos Basin (Colombia).

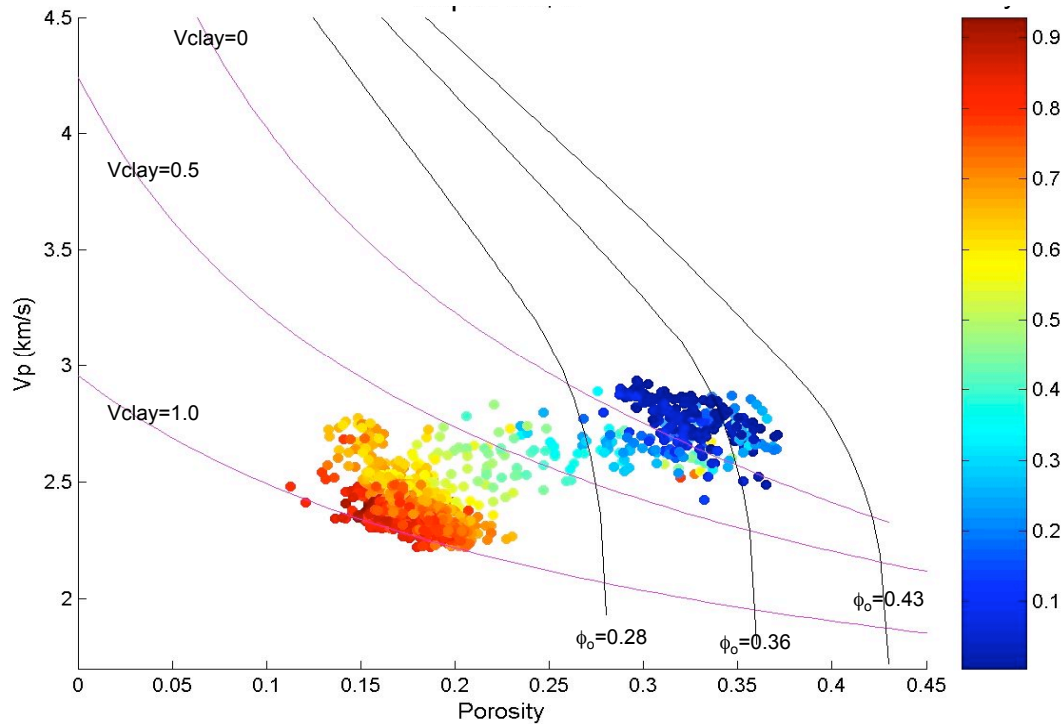
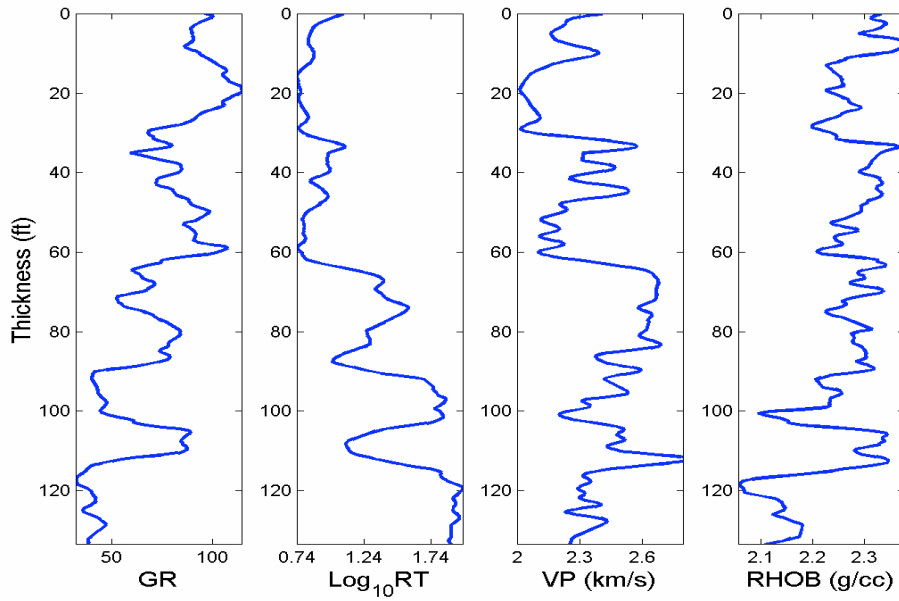
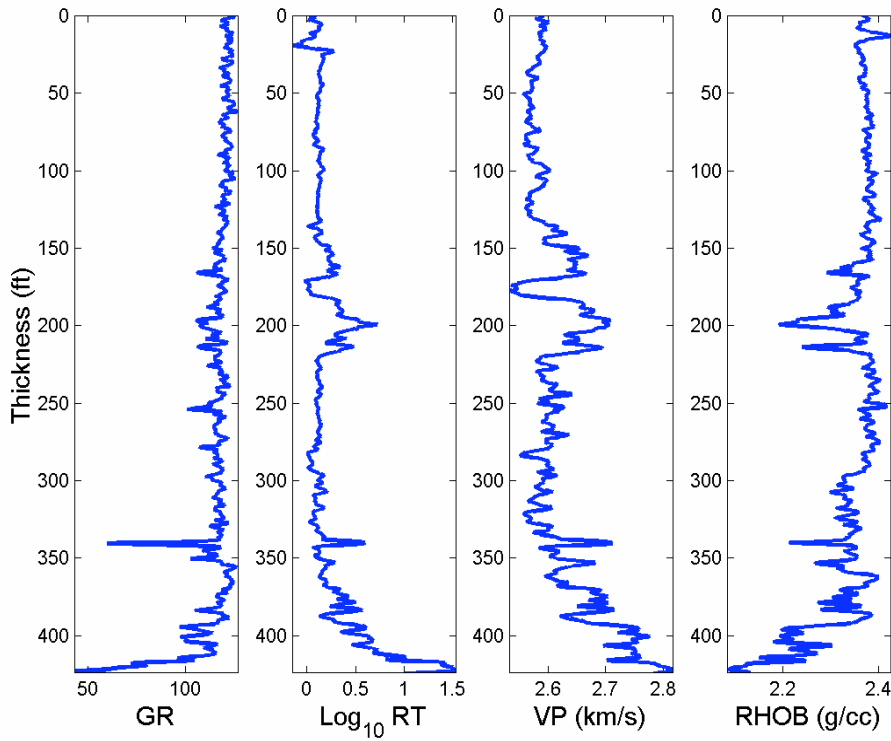


Figure 2. Rock-physics template to evaluate the patterns of concomitant variations of porosity and elastic properties within clastic sequences. Color-coding is clay volume fraction.

The differences between these four lithofacies sequences start to become conspicuous by looking at the cross plot of porosity and clay fraction (Figure 5). The fluvial deposits show an approximate “V” pattern (Figure 5a) contrasting with the linear trend observed in the mud-rich deep-water deposits from offshore West Africa (Figure 5b). The pattern observed in the fluvial deposits indicates the predominance of mm- to cm-scale dispersed fabric in the mixed lithofacies, whereas the linear trend observed in the deep-water deposits (Figure 5b) suggests the predominance of mm- to cm-scale horizontally laminated fabric. These two patterns are also different from the patterns observed in Figure 5c and Figure 5d. The sand-rich deep water deposits (Figure 5c) show two clouds of data points, corresponding to the sand and shale intervals, without a gradual transition between the two. The coarsening-upward lithofacies sequence (Figure 5d) shows another approximate V pattern with higher clay content, and significant scatter for clay fractions larger than 0.4. In the cases of the fluvial and shallow marine deposits, the lowest porosity occurs at the midpoint between the clean sand and the highest clay content, indicating the presence of dispersed sand-clay mixtures. The mud-rich deepwater deposits show a pattern consistent with the predominance of laminar sand-clay mixtures. In contrast, the pattern outlined by the sand-rich deepwater deposits suggests the absence of sand-clay mixtures.



**(a)**



**(b)**

Figure 3. Well-log data from two different lithofacies sequences: (a) fining-upward lithofacies sequence from fluvial deposits of the Miocene Guayabo Formation (Llanos Basin Colombia); (b) fining-upward lithofacies sequence from Miocene deep-water deposits offshore West Africa. Fluid substitution has been applied to the velocity and density logs in (b).

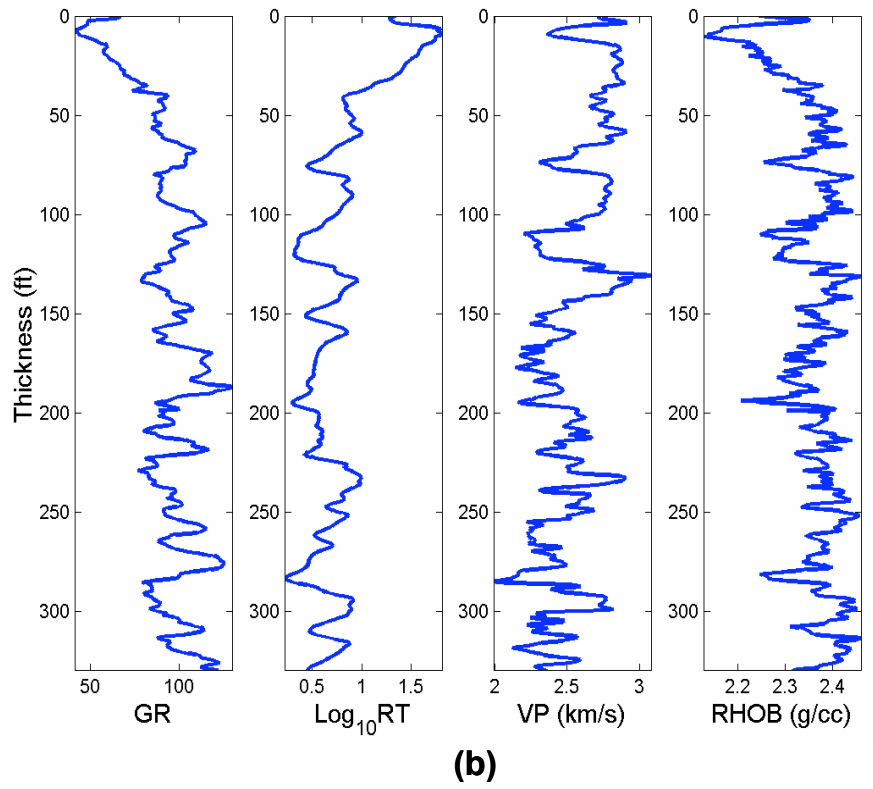
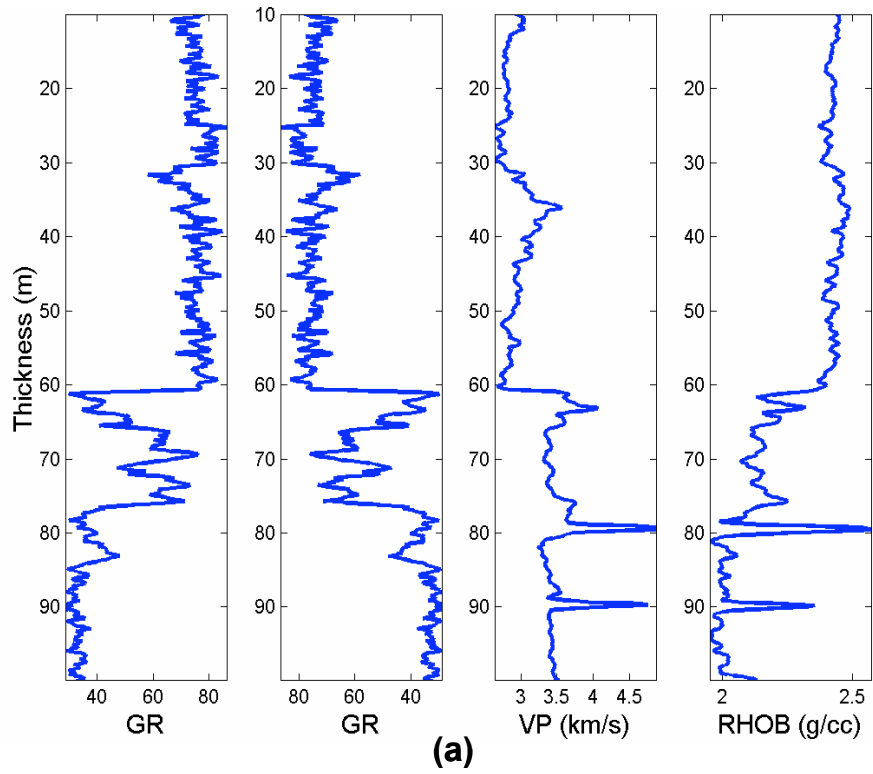


Figure 4. Well-log data from two different depositional sequences: (a) deep-water blocky sandstone from offshore Gulf of Mexico; (b) coarsening-upward lithofacies sequence of shallow-marine Miocene deposits from Colombia (Upper Leon, well Apiay-1, Llanos Basin). Fluid substitution has been applied to the velocity and density logs in (a).

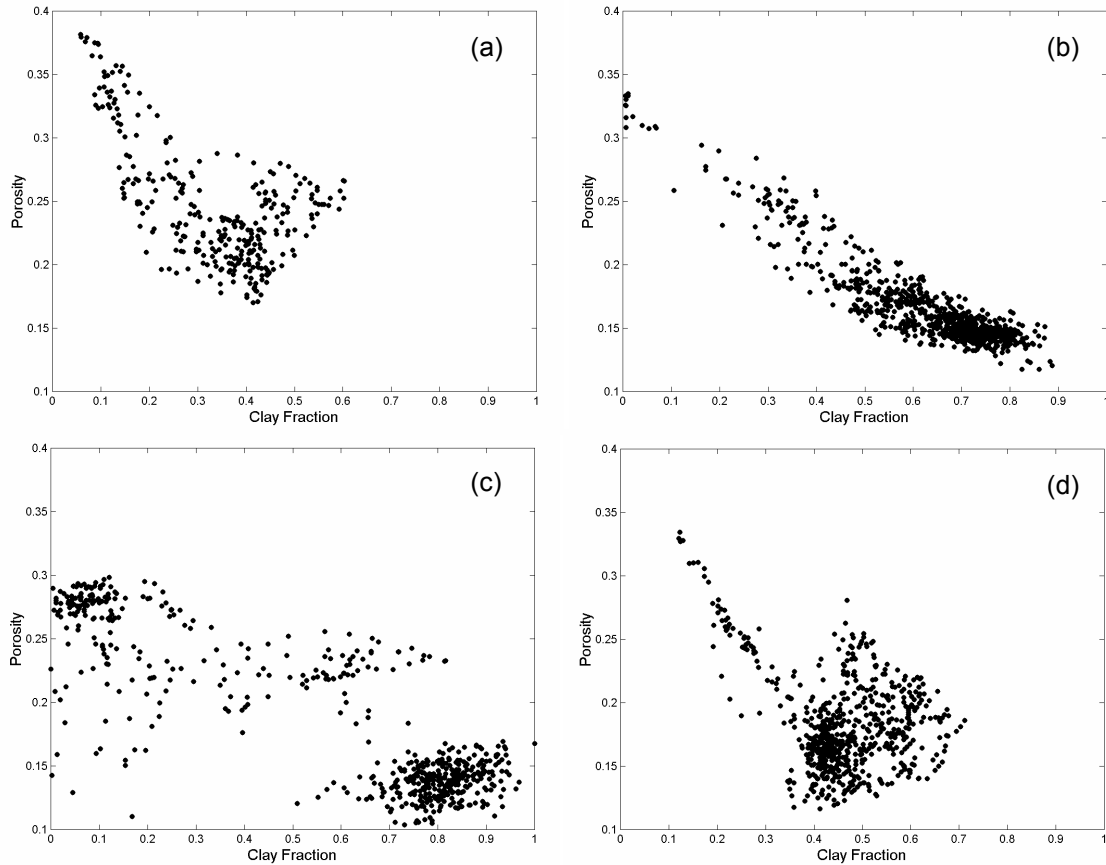


Figure 5 Well-log Porosity-Clay Fraction cross plots from the clastic depositional sequences shown in Figure 3 (a and b), and Figure 4 (c and d). Porosity determined from density and neutron (in sands) logs, clay fraction determined from gamma ray and the difference between neutron and density porosities.

The velocity-density bivariate histograms (Figure 6) corroborate the sedimentary fabric inferred from the porosity-V<sub>clay</sub> cross plots. In Figure 6 the pure end members of the lithofacies sequences are indicated as Q for sand and C for clay-rich shale. As shown in Figure 6a, the fluvial deposits present a clear inverted-V pattern, similar to the one predicted by the Marion-Yin model (Marion *et al.*, 1992). In the case of the mud-rich deep water deposits, Figure 6b shows a clear linear trend as predicted for horizontally laminated sand-clay mixtures from the Backus average (e.g. Mavko et al, 1998), and the linear variation in porosity as a function of clay content. In contrast, Figure 6c illustrates the absence of mixed lithofacies in the sand-rich deepwater deposits. Finally, Figure 6d demonstrates the predominance of dispersed sand-clay mixtures in the shallow marine deposits, and suggests the occurrence of some subordinate laminated lithofacies.

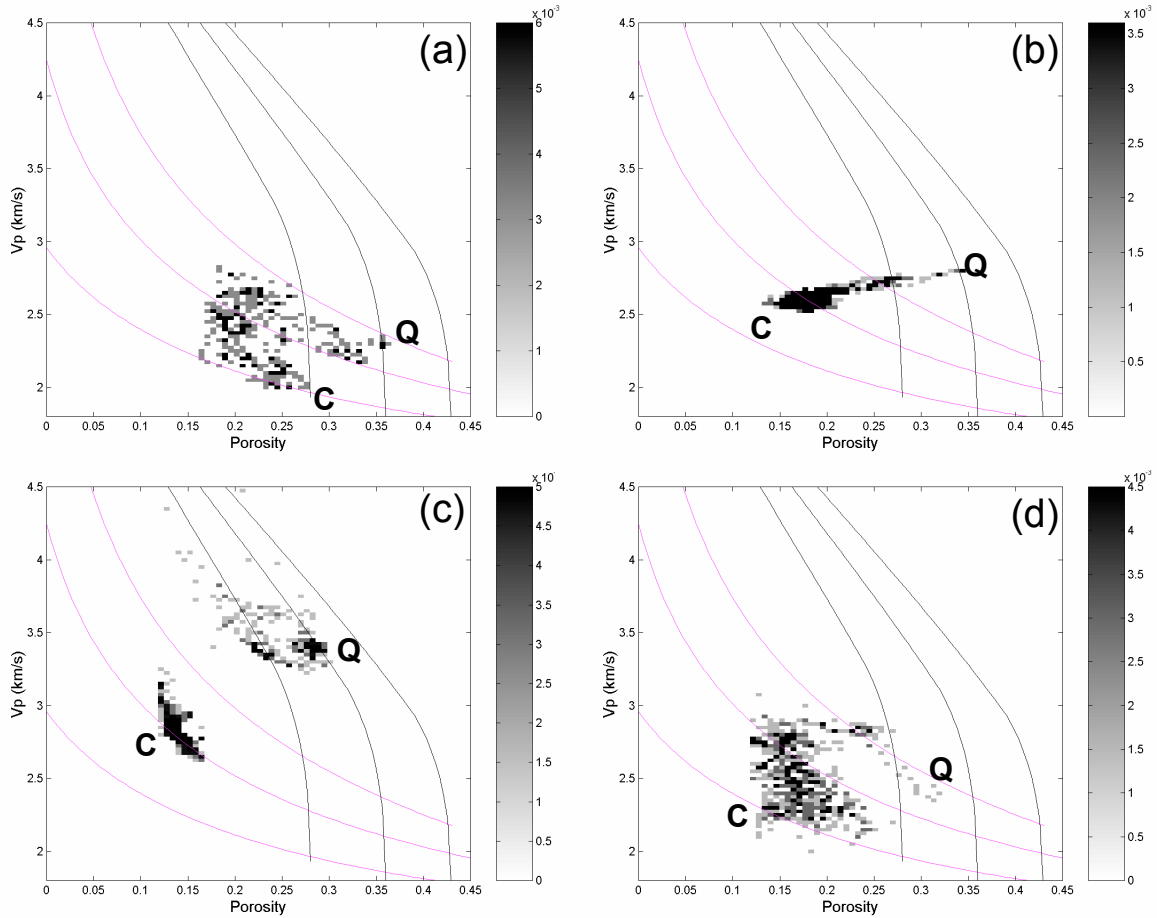


Figure 6. Bivariate histograms of well-log P-wave velocity and porosity (PHID) from the four different clastic depositional sequences shown in Figure 5. Q indicates the sand points (quartzose sand) and C indicates the clay-rich shale point. Black lines outline the diagenetic trend for quartzose sands; magenta lines outline the depositional trend for sands at 25 MPa, with different proportions of clay (0, 50% and 100%).

The differences between these four lithofacies sequences can be summarized in the velocity-density cross plot color-coded by clay content (Figure 7). In this plane, contours of iso-impedance can be superimposed, since acoustic impedance is the product of velocity and density. The cross plots illustrate that the patterns observed are the result of the concomitant variations in density (porosity) and elastic properties (velocity) associated with clay content.

The most striking difference occurs between the pattern outlined by the lithofacies sequence from fluvial deposits, Figure 7a, and the pattern depicted by the lithofacies sequence from mud-rich deep water deposits, shown in Figure 7b. The variations in clay content, density, porosity, and elastic properties observed in the fluvial deposits clearly indicate the predominance of a dispersed fabric in the mixed lithofacies. In contrast, the

variations in clay content, density, porosity and elastic properties observed in the mud-rich deep-water deposits clearly indicate the presence of horizontally laminated sand-clay mixtures. Another significant difference is the contrast between the scarcity of mixed sand-clay lithofacies in the sand-rich deep water deposits, Figure 7c, and the abundance of both dispersed and laminar mixed lithofacies in the shallow marine deposits shown in Figure 7d.

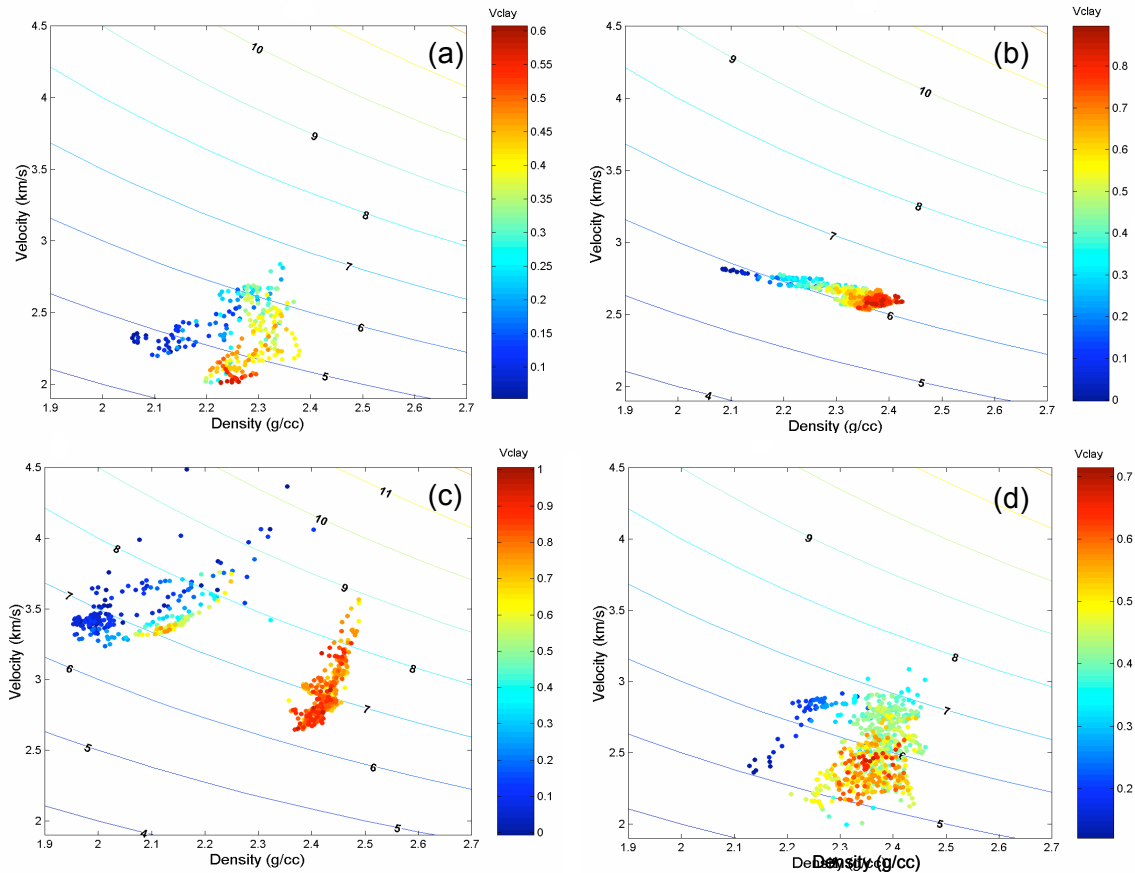


Figure 7. Cross plots of well-log P-wave velocity and density color-coded by fraction of clay for the same four different clastic depositional sequences shown in Figure 6. The plots also show contours of impedance. Notice that for the cases of (a) and (d) the highest impedances correspond to the mixed lithofacies.

### Depositional Settings and the Fabric of Sand-Clay Mixtures

Although dispersed and horizontally laminated sand-clay mixtures cannot be considered exclusive of a particular depositional setting, their occurrence within a given environment is associated with specific depositional and post-depositional processes, like bioturbation.

The ideal conditions for millimetric to centrimetric interposition of clean sand and clay-rich mud occur in flat settings affected by oscillating or seasonal currents. Asymmetrical tides provide an excellent example of these conditions, as discussed by Allen (2001, p. 256). Reineck and Singh (1980) summarize the occurrence of these lithofacies from different depositional settings. They classify these deposits as coarsely interlayered bedding and thinly interlayered bedding (rhythmites), which different authors have found in deposits associated with lakes and transitional environments like tidal flats and estuaries (Reineck and Singh, 1980, p. 123). Howard and Reineck (1972) report the presence of these lithofacies in shallow marine shoreface deposits. Smith (1987) discusses the presence of laminated sand-clay mixtures fluvial deposits, which are commonly associated with areas with high water tables.

Bioturbation (e.g. Reading, 1980, p. 223; Reineck and Singh, p. 387) seems to be the dominant mechanism generating dispersed sand-clay mixtures in water-laid deposits. Fast accumulation rates associated with fluidized flows with high sediment concentration could be an alternative mechanism. Metric to decimetric intervals of silty mudstone and muddy sandstone, associated with fluvial deposits like the Guayabo Formation of Colombia, seem to be the result of burrowing, plant growth, and pedogenetic processes that destroy the primary sedimentary structures (Galloway and Hobday, 1996, p.75).

## **Discussion**

The results presented for this section of the project show that the existing rock-physics models predict the variations in elastic and hydraulic properties associated with the textural trends in clastic depositional sequences. The models, based on laboratory and theoretical analysis, can reproduce the patterns of clastic depositional sequences in the rock-physics planes, based on well-log measurements. Mineral composition, sorting and the type of mixture are the main depositional lithofacies influencing the observed patterns. Cementation, compaction, pressure solution, and confining pressure are the dominant factors influencing the variations associated with diagenesis.

The variations observed among depositional sequences from diverse environments result from the intrinsic relationship that exists between textural trends, or lithofacies successions, and the flow regimes and conditions of sedimentation for each particular setting. These variations are produced by the presence, or absence, of mixed lithofacies and their specific fabrics. In general, ignoring the effect of mixed lithofacies and assuming that seismic reflections come from simple sand and shale interfaces can lead to erroneous interpretations.

## **RESERVOIR QUALITY PREDICTION BY INTEGRATING SEQUENCE STRATIGRAPHY AND ROCK PHYSICS**

Sequence stratigraphy is the geologic interpretation of process/response events (Mulholland, 1998). This can predict the likely occurrence of reservoir facies, source rocks and seals. Traditional stratigraphic interpretation from post-stack seismic data has been predominantly qualitative based on visual inspection of geometric patterns in the seismic reflections. However, quantitative interpretation of seismic amplitude is possible if we can extract information about compositional maturity (mineralogy, clay content) and textural maturity (sorting, grain angularity, sphericity and roundedness) using principles of sedimentology.

Quantitative seismic interpretation (Avseth et al., 2005) uses rock physics to link seismic amplitude with reservoir properties, like, porosity, clay-content, sorting, diagenetic cements etc. that are estimated from the stratigraphic analysis.

Our workflow consists of the following steps:

### **Step-1A: Understanding the systematic change of sedimentological properties with depositional cycles in a predictable fashion**

VanWagoner et al. (1990) showed that the following sedimentological properties change predictably during transgression and regression:

- Sand-shale ratio
- Bed Thickness
- Grain-size
- Sorting
- Bio-turbation

Interestingly the changes in these sediment properties have opposite trends for transgression (shore line is approaching towards land) vs. regression (shore line is retreating towards basin). However there is uncertainty in these trends. During regression depositional energy tend to increase upward resulting in increase in bed-thickness, higher net-to-gross, better sorting and decrease in bio-turbation. On the other hand, marine transgression signifies decrease in depositional energy and exhibits an opposite trend of the above sediment parameters. These sediment parameters can be grouped as,

compositional maturity and textural maturity parameters. They constitute important sediment properties that affect the elastic properties of the rocks and in turn affect seismic amplitudes.

### **Step-1B: Understanding spatial gradients of sedimentological properties**

Gradients of sediment parameters are not same across the seismic reflector vs. along the reflector. Most seismic reflectors and their amplitude correspond to chronostratigraphic surfaces with a few exceptions. Chronostratigraphic surfaces represent depositional hiatus. Changes in sedimentological properties are abrupt across the hiatus and gradual along the hiatus (Emery and Myers, 1996).

The spatial gradients can be calibrated from well data. Estimating the lateral trends require multiple wells or horizontal wells. In the absence of such data one might assume that sediment parameters change linearly along the seismic reflector and in discrete steps across the reflector. Thus, using sequence stratigraphy, we obtain relative trends of variation in sediment properties within a depositional sequence. These trends then constrain the input parameters in rock physics modeling.

### **Step-2: Rock physics analysis**

Rock physics establishes the relation between sedimentological properties and elastic moduli. After we determine the spatial trends of sediment parameters in a stratigraphic package, appropriate rock physics models are selected. The input parameters are guided by our results from step 1. The rock models are calibrated to well log data. As output we obtain effective bulk modulus, shear modulus and density, as well as  $V_p$  and  $V_s$  as a function of porosity.

### **Step-3: AVO modeling and interpreting seismic amplitude**

AVO forward modeling (Shuey's approximation) is used to obtain intercept and gradient at key stratigraphic interfaces using effective moduli predicted from rock physics analysis in step 2. Trends in compositional and textural maturity are carried through from sequence stratigraphy, to the AVO plane, via rock physics. Finally, the modeling results can be used to interpret observed amplitudes in terms of sedimentological properties and reservoir quality.

We have preliminarily applied this concept in a deep-water turbidite system from Campos Basin, offshore Brazil. Our interpretation was based on (a) basin history (Peres, 1990) (b) geometry and truncation patterns of reflectors (Figure 8) and (c) stacking patterns of well logs (Figure 9).

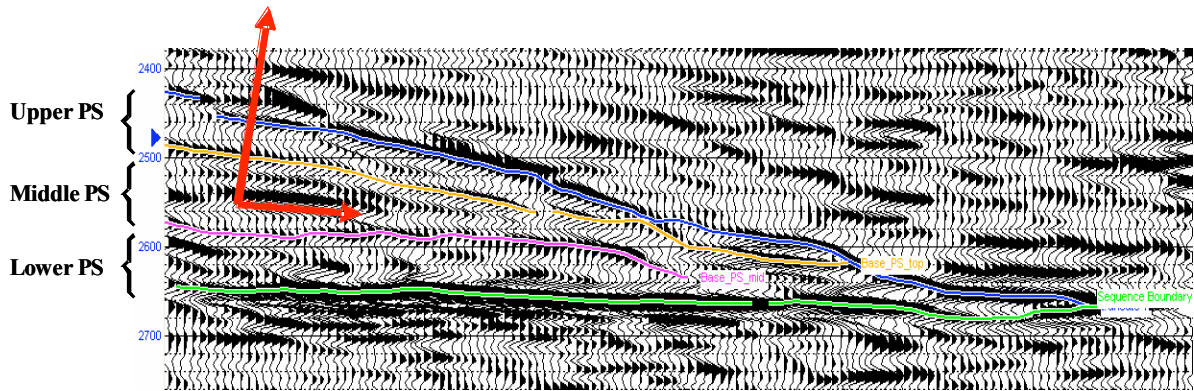


Figure 8: Three parasequences (PS) interpreted within progradational depositional lobes. Changes in sorting is abrupt across the para-sequence boundaries and gradual along the boundaries.

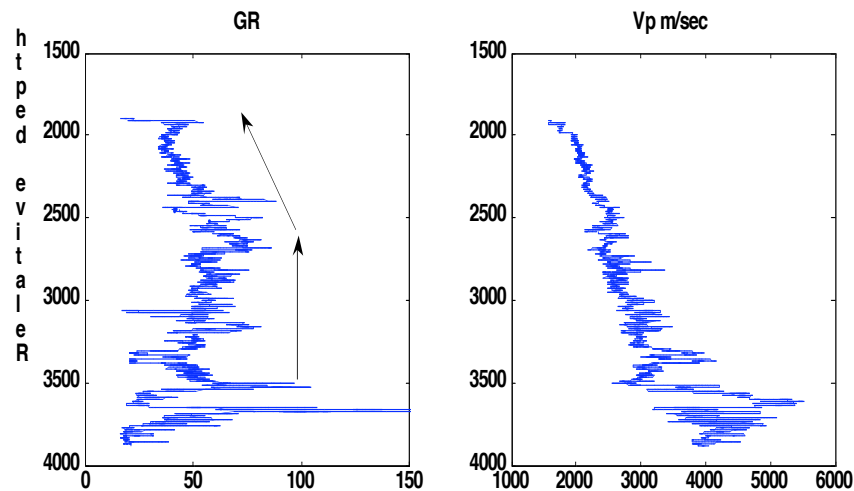


Figure 9: In well log blocky motif corresponds to aggradational / channel deposits and coarsening-up motif corresponds to progradational depositional lobes.

We considered three para-sequences (PS) within the prograding depositional lobes (Figure 8) and used sequence stratigraphic principles to predict relative trends of sorting, an important parameter that controls porosity, elastic moduli, and hence seismic velocities. We combined these trends with experimental sorting-porosity relationships for artificially mixed sand (Beard and Weyl, 1973; Jorden and Campbell, 1984).

To estimate elastic properties of the sediments, we used the soft sediment model (Dvorkin and Nur, 1996; Mavko et al., 1998) with a composition appropriate for compositionally mature sediments. Sediment elastic properties at zero porosity are simply the properties of the solid minerals; the sediment elastic moduli at critical porosity (~40%) are estimated using the Hertz-Mindlin theory for a packing of clean, well-sorted

spherical grains. Moduli of poorly sorted sand with porosities between 0 to critical porosity are interpolated between mineral point and well-sorted end member using the lower Hashin-Shtrikman bound. Figure 10 shows porosities and velocities obtained from a neighboring well log and the predicted velocities using the soft sediment model. Calibration of the model with well data is important for understanding the effects of mineralogy, effective stress, pore fluids, and porosity.

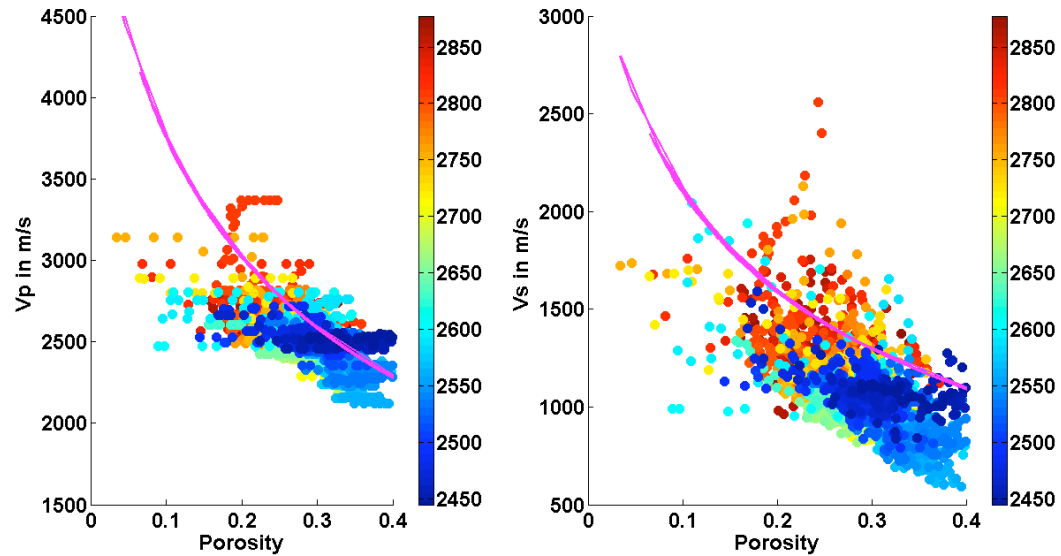


Figure 10: The scatter points show measurements of porosities and velocities from well log in prograding lobes. The magenta line is obtained using rock physics modeling for unconsolidated sand.

The corresponding effective  $V_p$ ,  $V_s$ , and density are used to compute intercept ( $R_0$ ) and gradient ( $G$ ) at the interfaces of the three para-sequences. They indicate distinct trends in  $R_0$ - $G$  plane (Figure 11). These trends can be used as a template to guide the interpretation of observed intercept and gradient from real seismic data

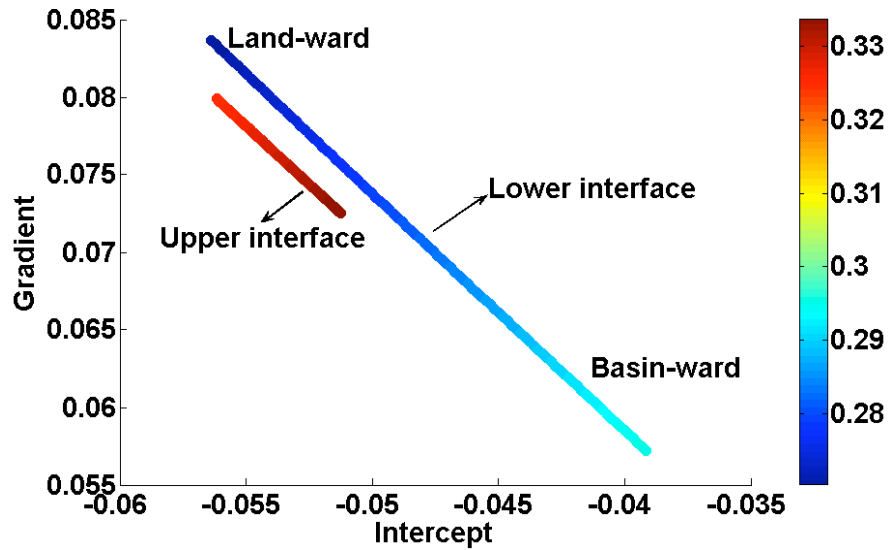


Figure 11: AVO modeling results: Intercept and Gradient crossplot color-coded by porosity. They indicate distinct trend of variation in reservoir properties from landward to basin-ward.

## **SORTING AND PACKING EFFECTS ON THE ELASTIC PROPERTIES OF SANDS**

Sandstones at similar depths or confining pressures present a relatively flat trend in the velocity-porosity plane (Figure 12). This flat trend results from significant changes in porosity associated with very small changes in elastic stiffness. The main porosity-reduction mechanisms related to this flat-trend are matrix (clay) content, sorting, and mechanical compaction, as shown by Marion *et al.* (1992), Avseth *et al.* (2000), Dvorkin and Gutierrez (2001), Zimmer *et al.* (2002), and Zimmer (2003). For uncemented sandstones at the same pressure conditions, sorting and clay are considered to be the dominant mechanisms affecting this velocity-porosity trend. The trend can be reproduced using the modified Hashin-Shtrikman lower bound (MHSLB), and has been called the uncemented sandstone model (Mavko *et al.*, 1998), or the rock physics depositional trend (Avseth, 2000).

In the case of clean sand aggregates at similar pressure conditions, the uncemented trend is considered to be solely the effect of sorting (Avseth, 2000; Gutierrez, 2001). However, our mathematical models of identical spheres demonstrate that a similar effect can be obtained by changing the packing of the aggregate, without increasing the

confining pressure. Therefore, packing and sorting seem to have a similar effect on the velocity-porosity trend.

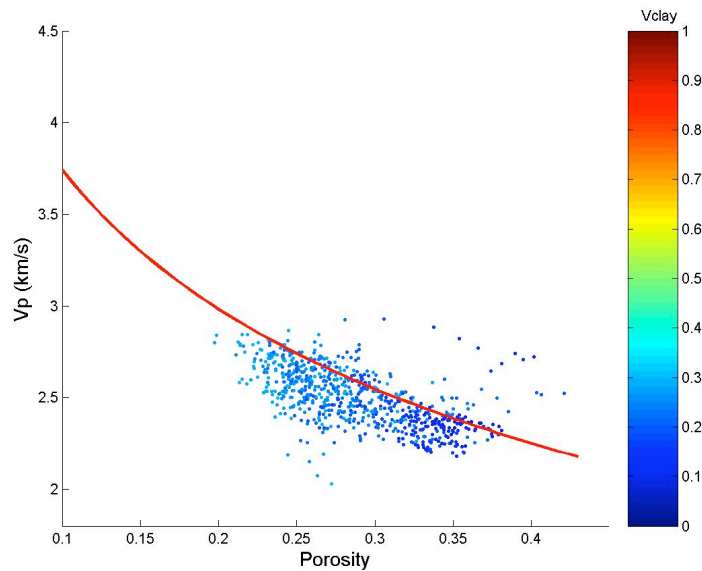


Figure 12: The depositional trend of sands in the velocity-porosity plane. The data corresponds to uncemented sands from fluvial deposits (well Apiay-1). Data color-coded by clay fractio ( $V_{clay}$ ).

Given a similar stage of packing, porosity of granular materials decreases as the standard deviation of the grain-size distribution increases. In other words, porosity decreases as sorting deteriorates. This relationship has been demonstrated by various authors (Walton and White, 1937; Sohn and Moreland, 1968; Beard and Weyl 1973; and Zimmer, 2003).

Among several measures of packing the most common are the grain concentration, the coordination number (Allen, 2001), and the intergranular contact (Fuchtbauer, 1974). The grain concentration, or fractional volume concentration of particles ( $X$ ), is directly related to porosity ( $\phi$ ):

$$\phi = 1 - X$$

The coordination number ( $C$ ), the average number of grains in contact with each individual grain, affects the stiffness of the aggregate. The intergranular contact describes the type of grain contact –punctual, tangential, concave-convex, or sutured, and is usually a measure of the degree of mechanical compaction and pressure-solution, two processes related to diagenesis rather than to the depositional environment.

Like sorting, packing has a strong effect on porosity and therefore on permeability. The relationship between packing, coordination number and porosity has been analyzed

by several authors (Graton and Fraser, 1935; Bourbie *et al.*, 1987; Murphy, 1982; Cumberland and Crawford, 1987). The effect of packing on both porosity and permeability was extensively analyzed by Graton and Fraser (1935).

In order to take into account the effect of grain-size distributions on the effective elastic properties of granular material, our approach is to take the existing effective-medium models for uniform sphere packs, and modify them to incorporate the appropriate grain-size average. In other words, by finding the relevant averages of the variables involved in the computation, we can find approximate solutions to the effective elastic modulus.

In the case of idealized spheres, the main effects of grain rearrangement are reducing porosity and incrementing coordination number. Other possible additional effects involve grain stabilization and change in the grain-contact area.

There is good agreement between the sorting effect in both velocity and porosity observed in laboratory experiments (Zimmer, 2003), and the one predicted from our model presented in Attachment C.

The velocity-porosity trend observed in uncemented sandstones in the subsurface agrees with the flat trend predicted from our theoretical analysis (Figure 13). The flat trend is depicted by the shallower sands (blue dots in Figure 13), and follows a gentler slope than the one predicted from the unconsolidated sediment model (magenta lines in Figure 13). The velocity and porosity data shown correspond to well-log measurements obtained along an interval where core porosity and sorting data were also available. A least-squares regression was obtained for the correspondence between sorting and porosity from the core data. The least-squares regression also indicates a small negative correlation between porosity and the grain size, which indicates a minor influence of packing, probably associated with grain angularity (fine grains tend to be more angular than coarser sands). However, the effect of sorting on porosity, in these sands, is stronger than the effect of packing. The high-porosity have better sorting than the low-porosity clean sands. These two different types of sands create the flat trend observed in the velocity-porosity plane.

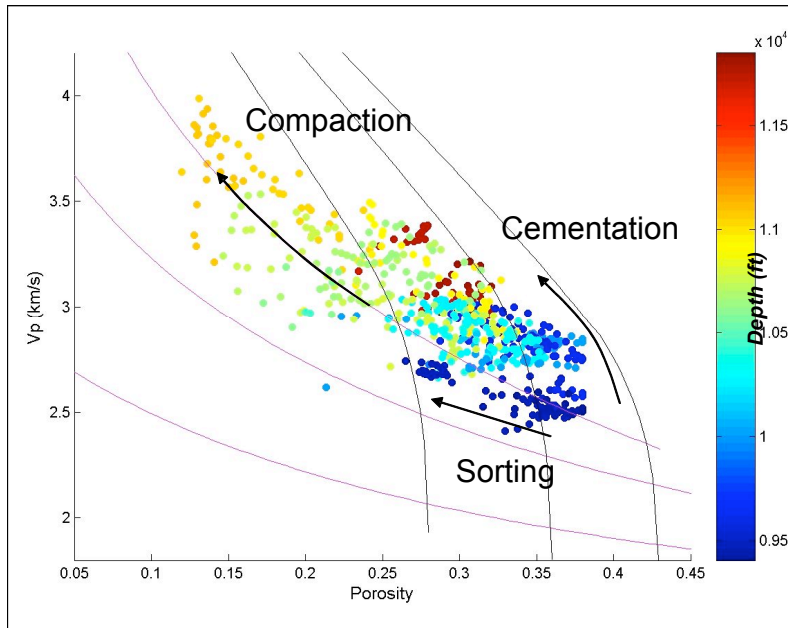


Figure 13: Well-log data of sandstones from one single stratigraphic sequence within an oil field. The graph shows the three main trends for sandstones: the flat trend associated with the sorting effect, the compaction trend, and the steep diagenetic trend. As predicted from the theoretical model, the MHSLB constitutes an upper bound for the sorting trend.

The theoretical analysis presented in this work indicates that the effect of sorting on both porosity and the elastic properties of granular materials differs from the effect of packing. This conclusion is also corroborated by the laboratory measurements and subsurface data. According to these results, variations in sorting generate a flatter trend in the velocity-porosity plane, with a slope gentler than the modified Hashin-Shtrikman lower bound (MHSLB). In contrast, variations in packing tend to generate a steeper slope than that predicted using the MHSLB. In general, whereas the MHSLB is a reasonable upper bound for the sorting effect, it constitutes a lower bound for the packing effect.

### Discussion

The refined rock models, though never perfect, have shown excellent predictive power when compared with laboratory and field data. The workflow for applying these models involves a number of detailed steps, beginning with a careful stratigraphic interpretation of the seismic and log data. The workflow will be applied during the coming year on one or more high quality data sets that should provide for validation and refinement.

## SEISMIC RESPONSE OF CARBONATE-CEMENTED SANDSTONES

Carbonate diagenetic processes, cementation and dissolution, can destroy or enhance the reservoir quality of rock. Precipitation of extensive calcite cement during burial diagenesis can strongly modify the depositional porosity and permeability of a sandstone reservoir. Carbonate cement may make flow paths more tortuous and decrease permeability (Kantorowicz et al., 1987; Saigal and Bjørlykke, 1987; Bjørkum and Walderhaug, 1990; McBride et al., 1995; Morad, 1998) because it is commonly concentrated in layers or concretions rather than being uniformly distributed. As noted by Kantorowicz et al. (1987), these cemented zones may segment a reservoir into relatively isolated compartments, as well as create barriers to lateral or vertical flow of hydrocarbons and formation waters.

This paper focuses on how such carbonate cementation can impact seismic impedance.

### Morphology of Carbonate Cements

Cements can be placed in two major categories based on their spatial relationship to framework grains: rim cements and occluding cements (Figure 14). Rim cements, such as quartz overgrowths, exhibit a regular relationship to framework grain boundaries. Occluding cements, such as carbonate cements, fill pores with no preferred relationship to grain surfaces.

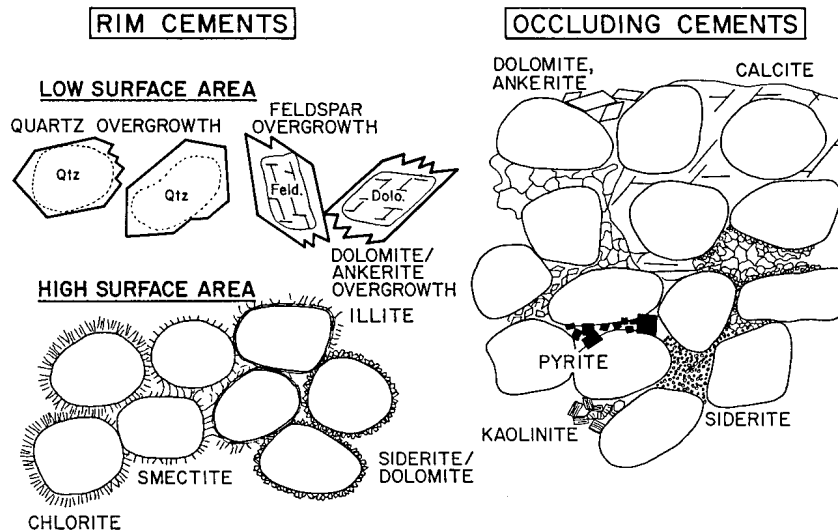


Figure 14: There are two major categories of cement based on their spatial relationship to framework grains: rim cements (left) and occluding cements (right). The morphology

of carbonate cement is distinctive than siliciclastic cement. Carbonate cements occlude in the pore network, and siliciclastic cements form coatings or rims around framework grains.

## High Resolution Sequence Stratigraphic Interpretation

We perform high-resolution sequence stratigraphic interpretation followed by rock physics analysis of carbonate-cemented sandstones. Our study integrates data from different scales, such as, 3D post-stack seismic, well logs, cores, thin-section, XRD and grain-size data. The data used in present paper are from turbidite slope channels offshore Equatorial Guinea, West Africa.

The reflection seismic data shows the geometry of a mini-basin formed by erosion of channels during fall in relative sea level (Figure 15). The seismic reflections, calibrated with well logs and core observations, demonstrate that cemented sandstones below uncemented sandstones generate significant impedance contrast. Reflections from overlying mudstones to underlying uncemented sandstones are characterized by a decrease in acoustic impedance, while reflections from overlying uncemented sandstones to underlying cemented sandstones are characterized by an increase in acoustic impedance. We find that the cemented sandstones are a seismically mappable unit over a lateral distance of about 100s of meter

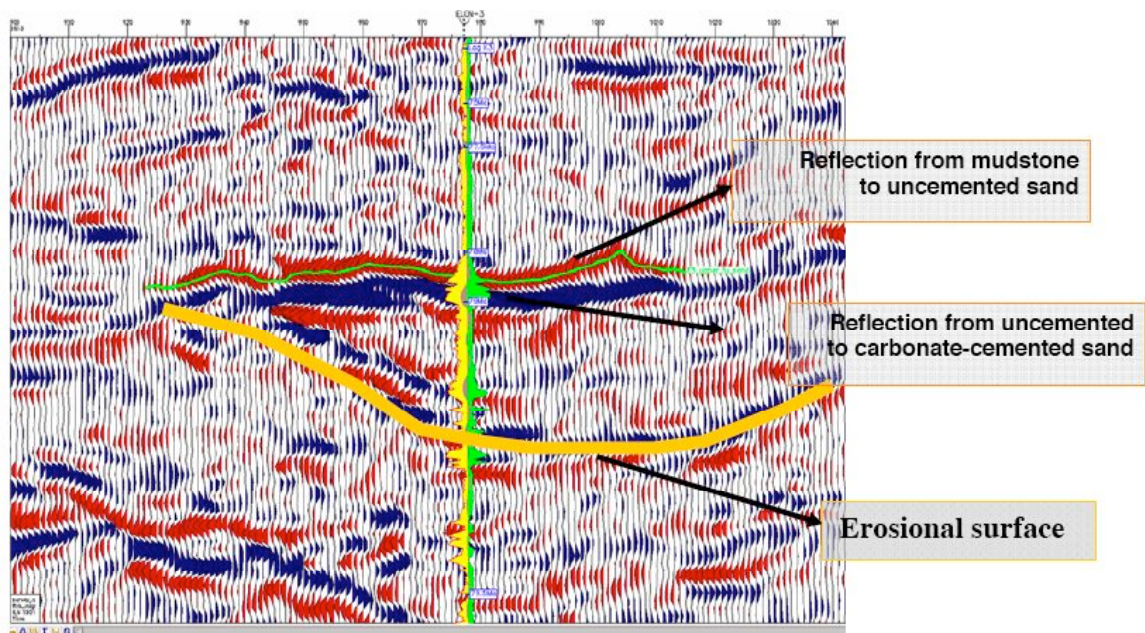


Figure 15: Post-stack, time-migrated seismic section showing sediments deposited in the mini-basin developed on continental slope at Equatorial Guinea. The orange curve represents an erosional surface. The well-logs (yellow: gamma-ray and green: resistivity) can be used to identify the vertical stacking of sands. The synthetics (pink curve) displayed at the well is of reverse polarity. Cemented sands are acoustically harder (blue event) than uncemented sands (red event)

## **Key Sedimentological Parameters Within Carbonate-cemented Sandstones and their Impact on P-Impedance**

### *1. Mineralogy of Cement*

The XRD analysis of 11 samples from the carbonate-cemented sandstone interval show that carbonate cement mineralogy varies from Calcite (Ca-rich) to Ankerite (Mg-rich). Ankerite is an intermediate product between calcite (the calcium-rich end member) and dolomite (the magnesium-rich end member). The samples below 1190 meter depth are mostly rich in ankerite. The other dominant phases in cemented-sand include quartz, K-feldspar and plagioclase. There are trace amount of pyrite, illite, smectite, kaolinite and chlorite.

Figure 16 shows the  $V_p/V_s$  of carbonate-cemented sandstones from well logs. The  $V_p/V_s$  predicted by Greenberg and Castagna (1992) for different lithologies, such as, sandstone, shale, limestone and dolomite are also plotted in the same figure. The  $V_p/V_s$  of calcite-cemented sandstones have slightly higher  $V_p/V_s$  trend predicted by the model for limestone. The  $V_p/V_s$  of ankerite-cemented sandstones show a large scatter. The scatter in  $V_p/V_s$  for same mineralogy could be due to variation in other sediment parameters.

Figure 17 shows P-impedance ( $I_p$ ) vs. total porosity ( $\phi_{it}$ ) from the same well logs, color-coded by cement mineralogy. The samples below 1192 meter depth in the well are mostly rich in ankerite cement. We observe that calcite-cemented sands and ankerite-cemented sands have different trends in P-impedance vs. porosity plane. The sandstones rich in ankerite cement display higher intercept than the sandstones rich in calcite cement.

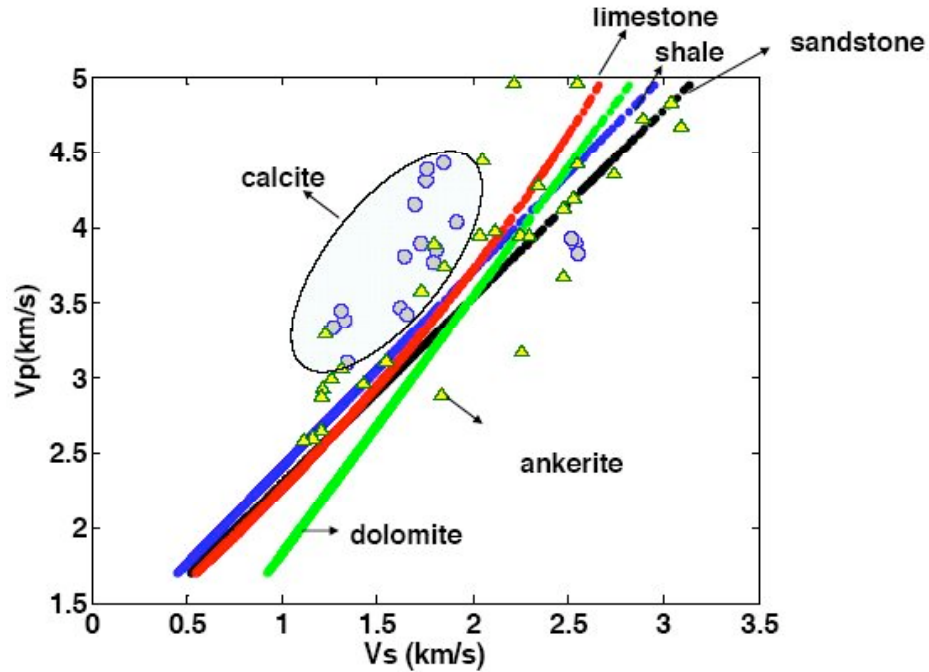


Figure 16: Comparisons of the  $V_p/V_s$  of carbonate-cemented sandstone from well logs with the  $V_p/V_s$  given by Greenberg and Castagna (1992). The blue circles are from the calcite-interval and yellow-triangles from the ankerite interval. The data show wide range of scatters.

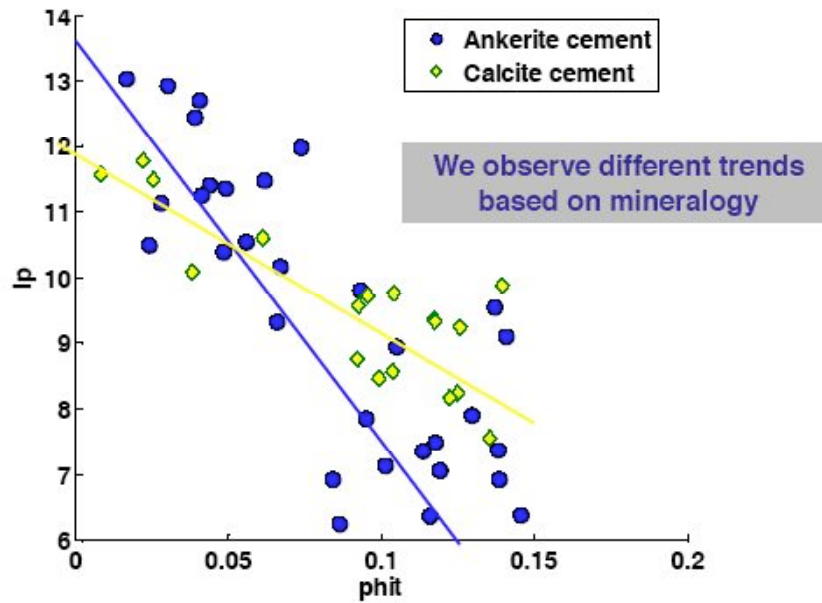


Figure 17: P-impedance ( $I_p$ ) vs total porosity ( $phit$ ) from well logs color-coded by cement mineralogy. The blue circles are from the calcite cemented interval and the yellow-triangles from the ankerite cemented interval. The data from different cement mineralogy indicate different intercepts.

## 2. Amount of cement

The XRD analysis indicates that amount of cement is highly variable. It can occupy 2% to 40% of solid volume of rock. Carbonate cements, when present in higher amounts (~40 % of rock volume), can occlude all the interparticle porosity. Thin-sections show that ankerite is more prone to leaching (dissolution) than calcite. Leaching reduces cement volume and can create secondary porosity.

## 3. Clay content

In order to understand the effect of clay-content on P-impedance, we crossplot P-impedance vs. porosity measured from well logs color-coded by gamma-ray index. We assume that gamma-ray index is an indicator of clay-content in the present data. We observe that cemented sands with higher clay content are associated with higher porosity, which contradicts the usual relationship between clay content and porosity (Figure 18). Usually increasing shaliness adds clay in the pore-network and decreases porosity (Avseth et al., 2005). In this case, we think that sandstones with lower shale content are more prone to cementation; hence, exhibit reduced porosities with cements occluding the pore space. The samples with higher total porosity show lower P-impedance (Figure 18).

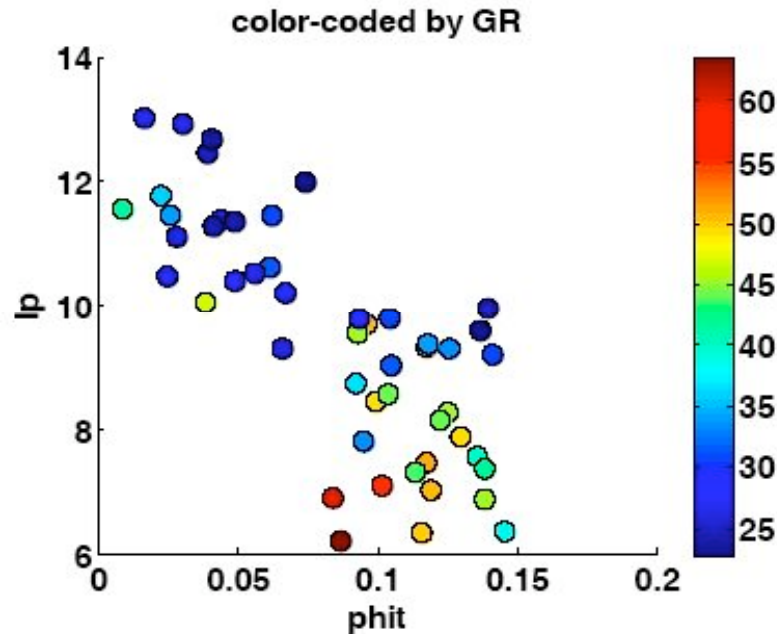


Figure 18: P-impedance ( $I_p$ ) vs total porosity (phit) from well logs color-coded by gamma ray index. We think that the sandstones with lower shale content are more prone to cementation, hence, exhibit reduced porosities.

#### *4. Position of cements with respect to stratigraphic surfaces*

We find that reservoir quality depends on position of cements with respect to flooding surfaces. A flooding surface is defined as a surface created in response to an increase in water depth and typically bounds parasequences (Posamentier & Allen, 1999). A flooding surface is also termed as parasequence boundary. We identify the flooding surfaces based on the patterns in gamma-ray logs. Usually, each parasequence is characterized by a fining-upward pattern on gamma-ray log and a flooding surface is identified when gamma-ray index reaches its maximum value. On the contrary, an incision surface is characterized by minimum value of gamma-ray index.

#### **Rock Physics Modeling of Carbonate-Cemented Sandstones**

We test three different granular media models: the contact cement model (Dvorkin et al., 1996), the stiff-sand model (Gal et al., 1998), and the constant-cement model (Avseth et al., 2000) in order to evaluate how the  $I_p$ -porosity trends predicted by these models correspond to the data from carbonate-cemented sandstones. These models have been shown useful for quartz cemented sandstones (Avseth et al., 2005).

Figure 19 shows  $I_p$  and porosity measured at the well in carbonate-cemented sandstones, along with the modified upper and lower Hashin-Shtrikman bounds computed for a mixture of calcite and water. The  $I_p$  vs. porosity trends predicted by the contact cement, constant cement, and stiff-sand models are also shown in Figure 19. We observe that the contact cement model (Dvorkin et al., 1996) does not fit the data at all porosity range. The identification of incision-surface and flooding surface reveal that the Dvorkin's cemented sand model explains the  $I_p$ -porosity trend of carbonate-cemented sands deposited at the incision-surface. However, this model fails to explain the  $I_p$ -porosity trend of data deposited at the top of flooding surfaces.

The stiff-sand model (Gal et al., 1998) also fails to explain the  $I_p$ -porosity trend of the carbonate-cemented sand (Figure 19). This model over-predicts P-impedance. Although the stiff-sand model does not fit the  $I_p$ -porosity trend in our data, we can obtain a reasonable fit by changing critical porosity from 40 % to 15 % in this model (Figure 20). We call this modified stiff-sand model in this paper. The heuristic argument for changing critical porosity is that the onset of carbonate cementation starts at much lower porosity (about 15 %). The modified stiff-sand model provides a better fit to the data than original stiff-sand model (Figure 20).

The constant-cement model (Avseth et al., 2000) with 1% constant cement explains the  $I_p$ -porosity trend in these data reasonably well (Figure 19). The advantage of constant cement model is that it considers sorting variation, and, from our previous section on data mining we know that sorting coefficient is variable from 0.75 to 2.75 within the carbonate-cemented sandstones.

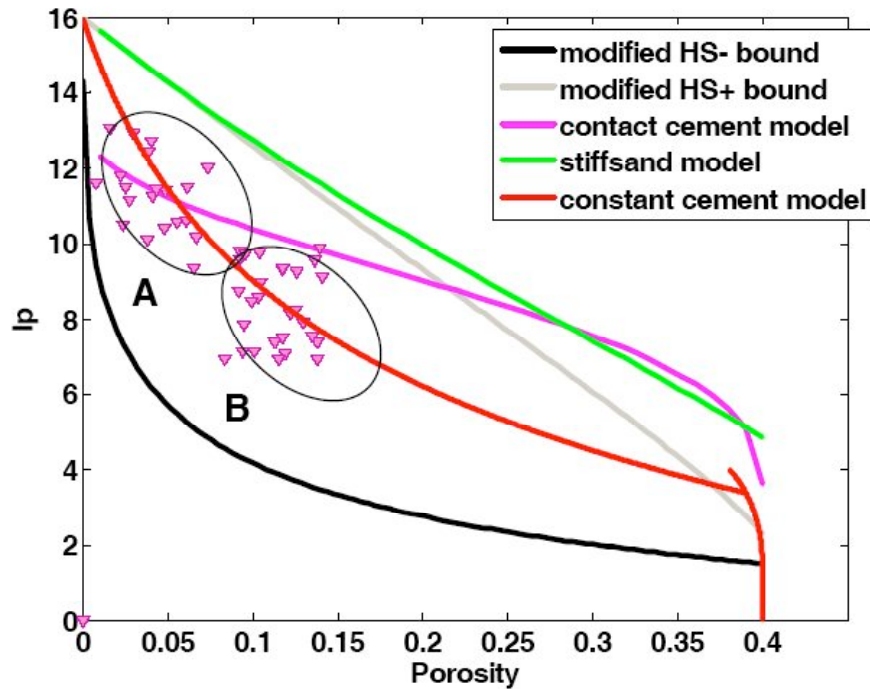


Figure 19: Comparisons of  $I_p$  and porosity of carbonate-cemented sandstone with those predicted by existing rock physics models. The clusters A and B represent data from the incision-surfaces and top of the flooding-surfaces respectively. The contact cement model (magenta line) does not fit the data from cluster B. The stiff-sand model (green line) overpredicts  $I_p$ . The constant cement model with 1% constant cement (red line) fits both clusters A and B.

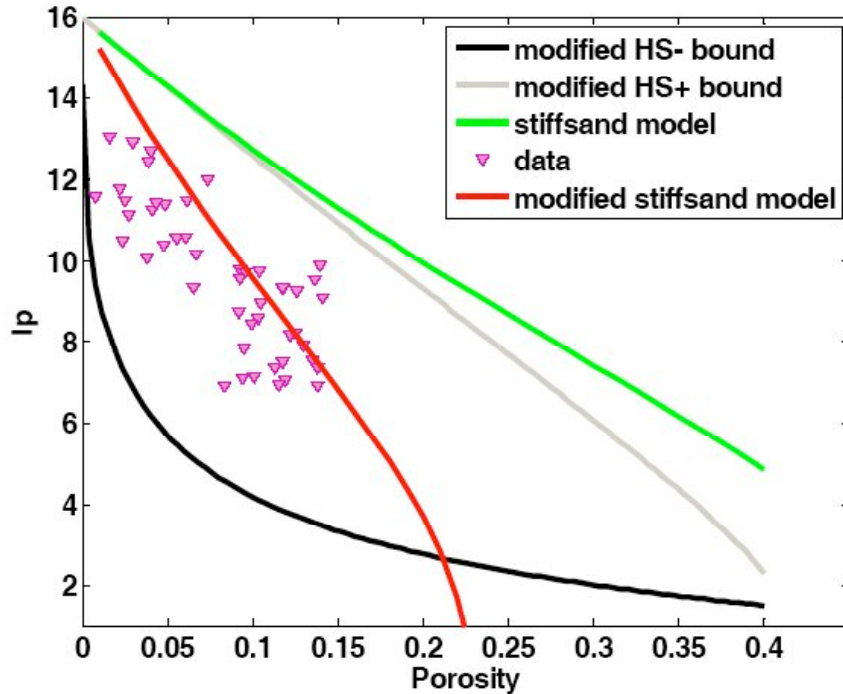


Figure 20: Comparisons of  $I_p$  and porosity of carbonate-cemented sandstone with those predicted by the stiff-sand model (green) and the modified stiff-sand model (red). The modified stiff-sand model is obtained by changing critical porosity from 40 % to 15%. The modified stiff-sand model provides a better fit to the data than original stiff-sand model.

Figure 21 shows the data along with predictions of  $I_p$  at different porosities using conventional DEM and modified DEM (Mukerji et al., 1995). The conventional DEM overpredicts  $I_p$  significantly. The modified DEM with 40 % percolation porosity, background matrix consisting quartz and calcite, and inclusions with aspect ratio 0.5 provides a reasonable fit to these data.

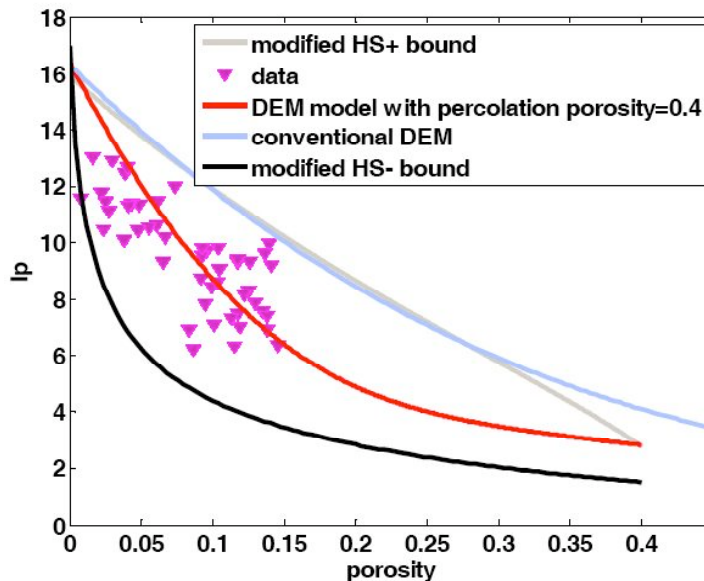


Figure 21: Comparisons of Ip and porosity of carbonate-cemented sandstone with those predicted by the conventional DEM (blue) and the modified DEM (red). The parameters in modified DEM model are: 40 % percolation porosity, background matrix consisting quartz, calcite and clay, and inclusions with aspect ratio 0.5. The modified DEM provides a better fit to the data than the conventional model.

## **Discussion**

We conclude that the carbonate cements are different than siliciclastic cements in terms of sedimentological parameters, and the common rock physics model for quartz cemented sandstones are not always suitable to predict P-impedance vs. porosity trends for the carbonate-cemented sandstones. The carbonate-cemented sandstones are found to be extremely heterogeneous in nature, even within a depth interval of ~60 meter in our study area offshore Equatorial Guinea, West Africa. Their grain-size, sorting, mineralogy, clay-content, amount of cement and degree of leaching vary considerably. There are two distinct clusters of data in the P-impedance vs. porosity plane. The carbonate-cemented sandstones from the base of incision surfaces exhibit lower shaliness, lower porosity and higher P-impedance. On the contrary, data from the top of flooding surfaces exhibit higher shaliness, higher porosity and lower P-impedance. The contact cement model fails to predict the trend shown by the later cluster of data. The predictions of constant cement model and the modified stiff-sand model agree with both clusters of data reasonably well. Furthermore, the modified differential effective media model and the modified self-consistent model provide reasonable fits to these carbonate-cemented sandstones. We recommend testing the predictions of rock physics models against data, classified by key stratigraphic surfaces.

## **QUANTIFYING SPATIAL TRENDS OF SEDIMENTOLOGICAL PARAMETERS**

This part of the work focuses on quantifying variation of sediment properties from proximal to distal location based on geophysical measurements.

### **Sequence Stratigraphic Setting of the Study Area**

We select channelized turbidite sandstones deposited offshore Equatorial Guinea, West Africa. We select these data to test the predictions of sand:shale ratio and sorting

from sequence stratigraphic model of similar environment, and link these sediment parameters with seismic impedance at the well.

We find that much of the sandstones in the study are likely to be deposited within the confines of submarine canyons. Figure 22 shows our interpretation of present-day seabed mapped from 3D post-stack, time-migrated seismic data. The map shows incisions or erosions by the submarine channels. This incision can create ~200 m of depression. These depressions created by the submarine canyon give rise to mini-basin settings. The geometry of the mini-basin and successive fills can be observed from the vertical seismic section. The sandstones deposited within mini-basin constitute the primary exploration target in deep water (Dailly et al., 2002).

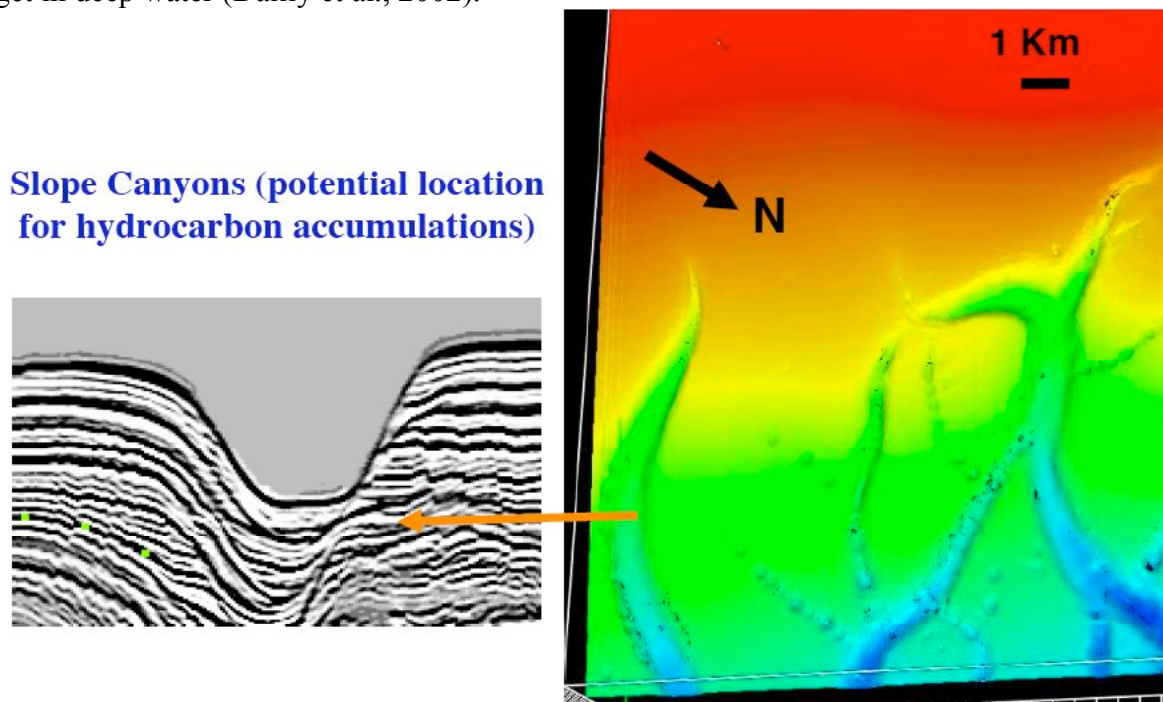


Figure 22: Seismic stratigraphic interpretation. Right: Present-day sea-floor map interpreted from 3D post-stack, time-migrated seismic data. We observe incisions created by submarine canyons on the continental slope. Right: Geometry of mini-basin on vertical seismic section. The mini-basins are formed by incision of submarine canyons. The incised-fill sandstones may be potential reservoir.

We select three wells from proximal to distal locations of the channelized turbidite sequence. Well-1 is the proximal well, well-2 is the middle well, and well-3 is the distal well. The well logs show fining-up motif, which is typical for channelized sequences and indicate decrease in depositional energy vertically upward. We observe a blocky motif on the well logs just beneath the fining-up sequence. The core descriptions report that the fining-up sequence is usually uncemented, and the blocky sequence is usually associated with carbonate-cemented sandstones.

We expect that quartz:clay should decrease from well-1 to well-3 for a channelized sequence. The depositional energy decreases along the flow direction, thereby, resulting in higher fractions of finer particles at the distal location. In addition, we expect that sorting should improve at the distal location with deflocculation process.

Figures 23, 24 and 25 compare data from wells ranging from proximal to distal location along with predictions of P-impedance vs. porosity trends from rock physics models. The data are color-coded by vshale. The solid black lines indicate predictions from the uncemented rock model for different quartz:clay ratios, and, the magenta lines are predictions from the cemented sand model for quartz:clay ratio equal to 1:0. We observe that the uncemented rock model predicts an increase in P-impedance with increase in quartz:clay ratio for a constant porosity. This suggests that as the composition maturity (quartz:clay ratio) improves and the other parameters remain unchanged, the P-impedance will increase. We obtain different contours of clay content by varying quartz:clay ratio in the uncemented or friable-sand rock model. This model predicts an increase in P-impedance with decrease in porosity along a particular clay contour (Figure 23, 24 and 25). We attribute the increase in P-impedance along a particular clay contour due to different degree of sorting, according to the argument by the friable-sand model.

Finally, we summarize the spatial patterns of P-impedance vs. porosity as observed from three well locations in Figure 26. The black arrow indicates flow direction within the channel. There are two different patterns of P-impedance vs. porosity at the proximal well locations and the distal well location. In the proximal well locations, the sand-rich and shale-rich facies separate into two different clouds. On the contrary, there is a gradual transition from sandy to shaly facies at the distal location. This probably suggests that two distinct depositional energy prevailed at the proximal locations, whereas, depositional energy changed gradually at the distal location. The rock physics models calibrated at the wells can be used to predict sediment parameters from P-impedance.

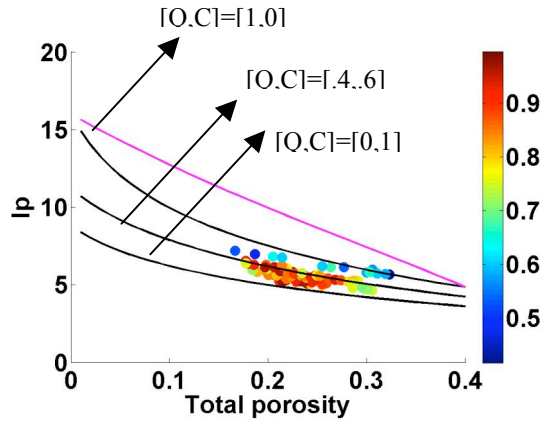


Figure 23: P-impedance ( $I_p$ ) vs. total porosity at well-1 situated at proximal location. [Q,C] represent quartz and clay content input to uncemented rock model. The black lines represent P-impedance predicted by uncemented rock model for different quartz:clay ratio at different porosities. Magenta line shows  $I_p$ -porosity trend predicted by cemented-sand rock model.

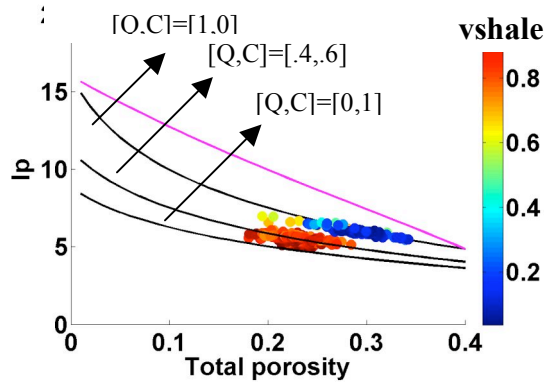


Figure 24: P-impedance ( $I_p$ ) vs. total porosity at well-2 along with predictions from rock models.

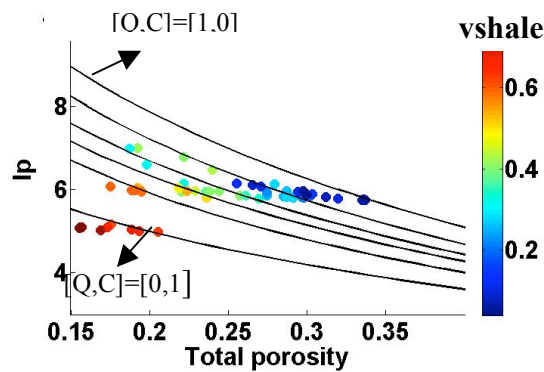


Figure 25: P-impedance ( $I_p$ ) vs. total porosity at well-3 along with predictions from rock models.

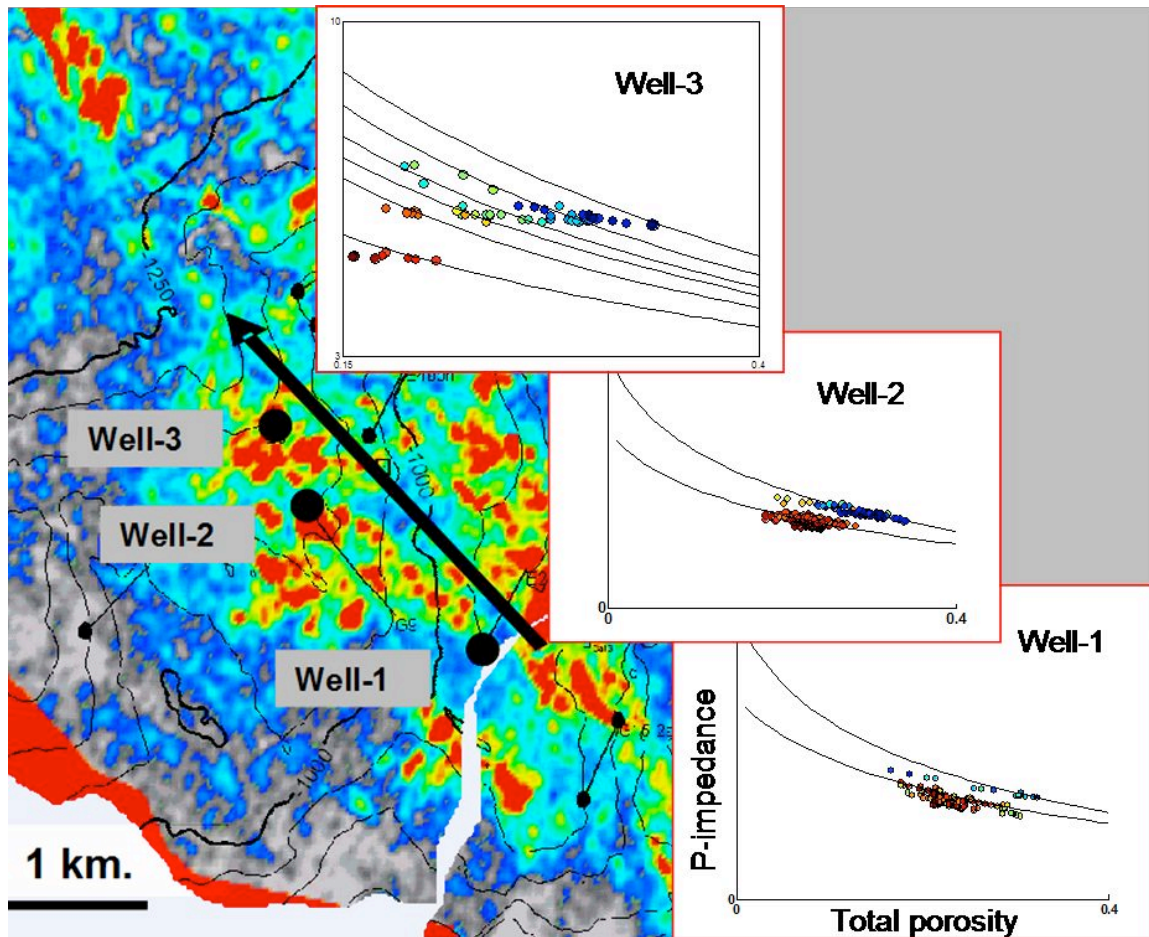


Figure 26: Seismic amplitude map showing channelized turbidite sequence. Well-1, 2 and 3 are located from proximal to distal locations. The black arrow indicates flow direction within channel. Spatial patterns of P-impedance vs. porosity can be observed from the trends predicted by rock model at the well locations.

## Discussions

We have quantified the trends of spatial variations of sedimentological parameters in a rock-physics plane (P-impedance vs. porosity plane). The spatial trends of quartz:clay ratio and sorting are obtained for channelized turbidite facies deposited in mini-basin settings at Equatorial Guinea, West Africa. The sand-rich and clay-rich facies separate in two distinct clusters in P-impedance vs. porosity plane at the proximal and the middle well. The sand-rich facies (low vshale content) exhibit higher P-impedance than shaly facies (low vshale content). Two distinct clay contours of 0 % and 60 % clay as obtained from uncemented rock model pass through the mean of these clusters. However in the

distal well, P-impedance from sand to shale increases gradually and transects different clay contours ranging from 0 to 100 % clay content. This probably suggests distinct depositional energy prevailed at the proximal locations, whereas, depositional energy changed gradually at the distal location.

We have selected thick-bedded to massive sandstone facies deposited at the base of fining-up sequences (potential reservoir facies) to identify spatial patterns of reservoir qualities and link them with seismic impedances. Rock physics modeling shows that the same facies is characterized by higher P-impedance at the distal well location, which corresponds to a higher quartz:clay ratio. The quartz:clay ratio changes from [0.5:0.5] to [1:0] along the direction of flow. In addition, porosities at the distal location (~25% to 35%) are higher than porosities at the proximal location (~20% to 23%).

In general, we expect a downdip decrease of coarser fractions (quartz) with depositional energy diminishing along the flow direction. However, in present study, we observe an increase in quartz:clay ratio from proximal to distal locations (Figure 26). This can be explained by spill-and-fill model in mini-basin settings. Brunt et al. (2004) show that progressively greater proportions of coarser grained material are transported downstream as the degree of confinement is reduced in mini-basins. Therefore, downdip increase in quartz:clay ratio can be interpreted in terms of downdip decrease in confinement of flow. The higher porosity at the distal well location observed in P-impedance vs. porosity plane are in agreement with sequence stratigraphy, which predicts progressive increase in sorting by turbidity currents along flow direction.

We have developed a methodology to quantify spatial trends of sediment parameters using stratigraphic interpretations and rock models calibrated at the wells. The method is applied on a turbidite, channelized sequence to quantify spatial trends of quartz:clay ratio and sorting. Our method can be applied to interpret sediment parameters from P-impedance prediction of sediment parameters from seismic impedance, away from well locations.

## **REFERENCES**

- Allen, J. R. L., 2001, Principles of Physical Sedimentology, George Allen & Unwin (Publishers), London, 272 p.
- Avseth, P., 2000, Combining rock physics and sedimentology for seismic reservoir characterization in North Sea turbidite systems: Ph.D. thesis, Stanford University.

- Avseth, P., Mukerji, T., and Mavko, G., 2005, *Quantitative Seismic Interpretation: Applying Rock Physics Tools to Reduce Interpretation Risk*: Cambridge University Press.
- Avseth, P., J. Dvorkin, G. Mavko, and J. Rykkje, 2000, Rock physics diagnostic of North Sea sands: Link between microstructure and seismic properties. *Geophysical Research Letters*, vol. 27, no. 17 p. 2671-2764.
- Bachrach, R., 1998, *High-resolution Shallow Seismic Subsurface Characterization*, Ph. D. thesis, Stanford University.
- Beard, D. C., and P. K. Weyl, 1973, Influence of texture on porosity and permeability of unconsolidated sand. *American Association of Petroleum Geologists Bulletin*, 15, 2, 349-369.
- Bjørkum, P. A., and O. Walderhaug, 1990, Geometrical arrangement of calcite cementation within shallow marine sandstones: *Earth-Science Reviews*, **29**, 145–161.
- Bourbie, T., O. Coussy, and B. Zinsner, 1987, *Acoustics of Porous Media*, Gulf Publishing Co., Houston, 334 pp.
- Cumberland, D. J. and R. J. Crawford, 1987, *The Packing of Particles*, Elsevier Science Publishers, Amsterdam.
- Dailly, P., Lowry, P., Goh, K., and Monson, G., 2002, Exploration and development of Ceiba Field, Rio Muni Basin, Southern Equatorial Guinea: *The Leading Edge*, **21**, 1140-1146.
- Dvorkin, J. and Nur, A., 1996, Elasticity of high-porosity sandstones: Theory for two North Sea datasets: *Geophysics*, **61**, 1363-1370.
- Dvorkin, J., A. Nur, and H. Yin, 1994, Effective properties of cemented granular materials, *Mechanics of Materials*, 18, 351-366.
- Dvorkin, J., and A. Nur, 1996, Elasticity of high-porosity sandstones: Theory for two North Sea datasets, *Geophysics*, 61, 1363-1370.
- Dvorkin, J., and M. A. Gutierrez, 2001, Textural sorting effect on elastic velocities, part II: elasticity of a bimodal grain mixture, *Society of Exploration Geophysicist Annual Meeting*, Expanded Abstracts.
- Emery, D., and Myers, K., 1996, *Sequence stratigraphy*: Blackwell scientific publications, Inc.
- Fuchtbauer, H., 1974, *Sediments and Sedimentary Rocks 1*, in *Sedimentary Petrology* by W. v. Engelhardt, H. Fuchtbauer and G. Muller, Part II. John Wiley and Sons, New York, 464 pp.
- Gal, D., Dvorkin, J., and Nur, A., 1998, A Physical Model for Porosity Reduction in Sandstones: *Geophysics*, **63**, 454-459.
- Galloway, W., and D. Hobday, 1996, *Terrigenous Clastic Depositional Systems*, Springer Verlag, New York, 489 pp.
- Graton, L. C., and H. J. Fraser, 1935, Systematic packing of spheres –with particular relation to porosity and permeability: *Journal of Geology*, 43, 785-909.

- Greenberg, M.L., and Castagna, J.P., 1992, Shear-wave velocity estimation in porous rocks: Theoretical formulation, preliminary verification and application: *Geophysical Prospecting*, **40**, 195-209.
- Gutierrez, M., J. Dvorkin and A. Nur, 2001, Stratigraphy-guided rock-physics reservoir characterization, AAPG Meeting 2001, Expanded Abstracts.
- Gutierrez, M., 2001, Rock physics and 3D Seismic Characterization of Reservoir Heterogeneities to Improve Recovery Efficiency, Ph. D. dissertation, Stanford University.
- Han, D., 1986, Effects of Porosity and Clay Content on Acoustic Properties of Sandstones and Unconsolidated Sediments, Ph. D. thesis, Stanford University.
- Howard, J. D., and H. E., Reineck, 1972, Georgia coastal region, Sapelo Island, USA, sedimentology and biology IV, physical and biogenic sedimentary structures of the nearshore shelf, *Senckenbergiana Maritime*, 4, 81-123.
- Jorden, J. R., and Campbell, F. L., 1984, Well Logging I - rock properties, borehole environment, mud and temperature logging: Society of Petroleum Engineers (SPE) of American Institute of Mining, Metallurgical and Petroleum Engineers (AIME).
- Kantorowicz, J. D., Bryant, I. D., and Dawans, J. M., 1987, Controls on the permeability and distribution of carbonate cements in Jurassic sandstones: Bridport Sands, southern England, and Viking Group, Troll field, Norway, in J. D. Marshall, ed., *Diagenesis of sedimentary sequences*: Oxford, Blackwell, 103–118.
- Marion, D., Nur, A., Yin, H., and Han, D., 1992, Compressional velocity and porosity in sand-clay mixtures, *Geophysics*, **57**, 554-563.
- Mavko, G., T. Mukerji and J. Dvorkin, 1998, *The Rock Physics Handbook, tools for seismic analysis in porous media*: Cambridge University press, New York, 329.
- McBride, E. F., Milliken, K. L., Cavazza, W., Cibin, U., Fontana, D., Picard, M.D., and Zuffa, G.G., 1995, Heterogeneous distribution of calcite cement at the outcrop scale in Tertiary sandstones, northern Apennines, Italy: *AAPG Bulletin*, **79**, 1044–1063.
- Mukerji T., Berryman J.G., Mavko G. and Berge P.A, 1995, Differential effective medium modeling of rock elastic moduli with critical porosity constraints: *Geophysical Research Letters*, **22**, 555–558.
- Mulholland, J.W., 1998, Sequence stratigraphy: basic elements, concepts and terminology: *The Leading Edge*, **17**, 37-40.
- Murphy, W. F., III, 1982, Effects of Microstructure and Pore Fluids on the Acoustic Properties of Granular Sedimentary Materials, Ph.D. dissertation, Stanford University.
- Peres, W.E., 1990, Seismic-stratigraphic study of the Oligocene-Miocene shelf-fed turbidite systems of the Campos Basin, Brazil: Ph.D. thesis, The University of Texas at Austin.

- Posamentier, H.W., and Allen, G.P., 1999, Siliciclastic sequence stratigraphy: concepts and applications: *SEPM Concepts in Sedimentology and Paleontology*, 7, 210 p.
- Reading, H. G., 1980, *Sedimentary Environments and Facies*, Elsevier, New York, 557 pp.
- Reineck, H. E., and I. B. Singh, 1980, *Depositional Sedimentary Environments*, 2<sup>nd</sup> edition, Springer-Verlag, New York, 549 pp.
- Saigal, G. C., and K. Bjørlykke, 1987, Carbonate cements in clastic reservoir rocks from offshore Norway—relationships between isotopic composition, textural development and burial depth, in J. D. Marshall, ed., *Diagenesis of sedimentary sequences*: Oxford, Blackwell, 313–324.
- Smith, D., 1987, Point bar lithofacies models, In: Ethridge, F., R. M. Flores, and M., Harvey: *Recent Developments in Fluvial Sedimentology*, Society of Economic Paleontologists and Mineralogists, 39, 83-91.
- Sohn, H. Y. and C. Moreland, 1968, The effect of particle size distribution on packing density, *Canadian Journal of Chemical Engineering*, 46, 162-167.
- Van Wagoner, J.C. ., Mitchum, R.M., Campion, K.M., and Rahmanian, V.D., 1990, Siliciclastic sequence stratigraphy in well logs, cores and outcrops: *The American Association of Petroleum Geologists, Methods in Exploration Series*, no. 7.
- Wang, Z., 2001, Fundamentals of seismic rock physics, *Geophysics*, 66, 398-412.
- White, H. E., and S. F. Walton, 1937, Particle packing and particle shape, *Journal of the American Ceramists Society*, 20, 155-166.
- Yin, H., 1992, *Acoustic Velocity and Attenuation of Rocks: Isotropy, Intrinsic Anisotropy, and Stress-Induced Anisotropy*, Ph. D. thesis, Stanford University.
- Zimmer, M., M. Prasad, and G. Mavko, 2002, Empirical velocity-pressure and porosity-pressure trends in unconsolidated sands, *SEG Annual Meeting, Expanded Technical Program Abstracts*, 72, 1866-1869.
- Zimmer, M., 2003, *Controls on the Seismic Velocities of Unconsolidated Sands: Measurements of Pressure, Porosity and Compaction Effects*, Ph. D. dissertation, Stanford University.

## ABBREVIATIONS AND ACRONYMS

$I_p$	Seismic P-wave impedance
$V_p$	Seismic P-wave velocity
$V_s$	Seismic S-wave velocity
$V_{clay}$	volume fracture of clay
$\phi$	porosity
$N_{phi}$	neutron porosity

DOE F 4600.6

U.S. DEPARTMENT OF ENERGY

OMB Control No.

(10-94)

FEDERAL ASSISTANCE PROGRAM/PROJECT

1910-0400

Replaces EIA-459F

STATUS REPORT

All Other Editions Are

Obsolete

### OMB Burden Disclosure Statement

Public reporting burden for this collection of information is estimated to average 47.5 hours per response, including the time for reviewing instructions, searching existing data sources, gathering and maintaining the data needed, and completing and reviewing the collection of information. Send comments regarding this burden estimate or any other aspect of this collection of information, including suggestions for reducing this burden, to Office of Information Resources Management Policy, Plans, and Oversight, Records Management Division, HR-422 - GTN, Paperwork Reduction Project (1910-0400), U.S. Department of Energy, 1000 Independence Avenue, S.W., Washington, DC 20585; and to the Office of Management and Budget (OMB), Paperwork Reduction Project (1910-0400), Washington, DC 20503.

1. Program/Project Identification No. <b>DE-FC26-04NT15506</b>	2. Program/Project Title <b>Imaging Reservoir Quality : Seismic Signatures of Geologic Processes</b>	3. Reporting Period <b>01/01/05</b> through <b>6/30/08</b>
4. Name and Address <b>Professor Gary Mavko (Research) Geophysics Department, Stanford University, 397 Panama Mall, Stanford, CA 94305-2215</b>		5. Program/Project Start Date <b>01/01/05</b>  6. Completion Date <b>06/30/08</b>
7. Approach Changes  <input checked="" type="checkbox"/> None		
8. Performance Variances, Accomplishments, or Problems  <input checked="" type="checkbox"/> None		

9. Open Items	
<input checked="" type="checkbox"/> None	
10. Status Assessment and Forecast	
<input checked="" type="checkbox"/> No Deviation from Plan is Expected	
11. Description of Attachments	
<input checked="" type="checkbox"/> None	
12. Signature of Recipient and Date	13. Signature of U.S. Department of Energy (DOE) Reviewing Representative and Date



## ATTACHMENT A

### Rock Physics Patterns of Clastic Depositional Sequences

#### Introduction

Besides fluids and pressure, rock texture and lithofacies strongly influence seismic rock properties (e. g. Yin, 1992; Wang, 2001). The lateral variations in elastic properties of an intact, water-saturated, sedimentary rock, under uniform effective pressure and temperature, are determined by the lateral variations in clay content, sorting, packing, mineral composition, or cementation. These textural variations are the result of depositional and diagenetic processes (Figure A-1). The impact of textural variations in seismic properties constitutes an important source of uncertainty in the prediction of reservoir properties from seismic data. Understanding the relationships between rock texture, fabric, and seismic response can reduce, or at least assess, the uncertainty associated with these predictions.

Lithofacies distribution in sedimentary rocks is not random. Lithofacies, a descriptive term to characterize both texture and fabric of sedimentary rocks (Teichert, 1958), reflects both the mechanical processes that operated during deposition (e. g. Walker, 1984; Allen, 2001), and the diagenetic processes that affected the rock after burial (e. g. Fuchtbauer, 1974). The terms *depositional* and *diagenetic* lithofacies can be used to distinguish between these processes, although for some parameters, like packing, the distinction between the two is not always evident. The vertical and lateral distribution of depositional lithofacies within a stratigraphic package follows Walter's law of lithofacies superposition (Teichert, 1958). It reflects the variation in the mechanics of deposition and sediment supply as sediments accumulated. The final architectural configuration controls the fluid distribution, the mechanical deformation, and the chemical interactions during diagenesis. The lithofacies distribution reflects, in essence, the depositional and diagenetic history of a sedimentary package.

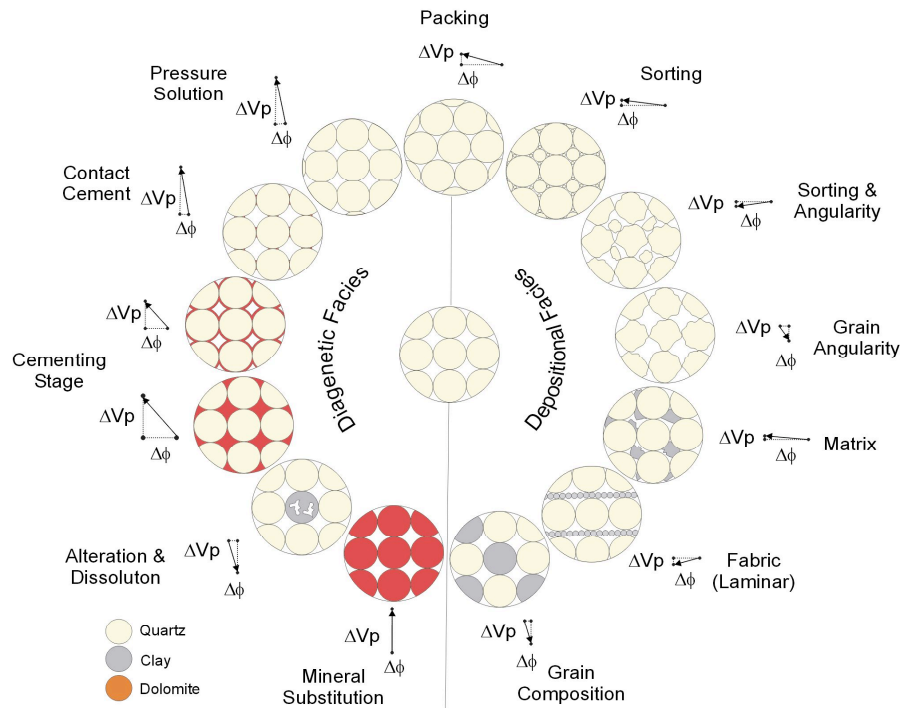


Figure A-1. Conceptual model illustrating the concomitant changes in porosity and elastic properties of elastic sediments. These textural effects have been documented by previous studies: e.g. Murphy (1982), Han (1986), Marion *et al.* (1992), Dvorkin *et al.* (1994), Dvorkin and Nur (1996), Bachrach *et al.* (1998), Avseth *et al.* (2000), Dvorkin and Gutierrez (2001), and Zimmer (2003).

Rock-physics models, based on theoretical analysis, empirical relationships and laboratory data, provide the basis to understand the variations in seismic properties associated with changes in rock texture and fabric. Mavko *et al.* (1998) document the main effective-medium models for granular materials, based on contact mechanics (e. g. Mindlin, 1949; Timoshenko and Goodier, 1970) and variational principles (Hashin and Shtrikman, 1963). Tosaya and Nur (1982), and Han (1986) studied the effect of clay, porosity, and confining pressure. Murphy (1982) analyzed the effect of packing and porosity. Yin (1992) analyzed the changes in both petrophysical and elastic properties of dispersed mixtures of sand and clay. Yin's study provided the basis for the Marion-Yin model for sand-clay mixtures (Marion, 1990; Marion *et al.*, 1992). Estes *et al.* (1994), and more recently Avseth *et al.* (2000), Dvorkin and Gutierrez (2001), Gutierrez (2001), and Zimmer (2003) have analyzed the effect of sorting. Dvorkin *et al.* (1994) formulated a mathematical theory to model the effect of cement on granular aggregates. Dvorkin and Nur (1996) presented rocks-physics diagnostics as a technique to determine textural

variations from seismic data. The links between rock physics, sedimentology and stratigraphy have been outlined by Avseth (2000), Avseth *et al.* (2000), and Gutierrez *et al.* (2001).

This report demonstrates that the vertical succession of lithofacies within a specific depositional setting translates into a characteristic pattern in the rock-physics planes, including cross plots of velocity-porosity ( $V_p$ - $\phi$ ), velocity-density, and porosity-clay fraction ( $\phi$ - $V_{clay}$ ). This report illustrates the variations that these characteristic patterns can have as a result of compaction and/or cementation. These results constitute a contribution toward understanding the link between geologic processes and the final seismic properties of sedimentary rocks. This link is the key for seismic forward modeling and for uncertainty assessment of the predictions of reservoir properties from seismic data, away from well control.

### Porosity of Sand-Clay Mixtures

Thomas and Stieber (1975) and Marion *et al.* (1992) describe the gradual changes in porosity for dispersed sand-clay mixtures. According to them, the porosity of unconsolidated, clayey sand decreases compared to porosity of clean sands, as clay replaces pore space. The lowest porosity is reached when all the pores in the sand framework are replaced by clay (Figure A-2). The mixture porosity ( $\phi_m$ ) depends on the clean-sand porosity ( $\phi_{cs}$ ), the volume fraction of clay ( $V_{clay}$ ), and the clay porosity ( $\phi_{clay}$ ), according to the following expression:

$$\phi_m = \phi_{cs} - V_{clay}(1 - \phi_{clay}). \quad (A-1).$$

Similarly, compared to pure-clay sediments, the porosity of sandy (or silty) clay decreases as well, as non-porous sand grains replace porous clay. The porosity along this branch is given by

$$\phi_m = V_{clay}\phi_{clay} \quad (A-2)$$

This is equivalent to Equation A-1, when we make the volume of shale equal to the clean-sand porosity.

In contrast, porosity of laminar mixtures corresponds to the arithmetic average of the clean-sand and pure-clay porosities (Thomas and Stieber, 1975); that is,

$$\phi_m = \phi_{cs}V_{ss} + V_{clay}\phi_{clay} \quad (A-3)$$

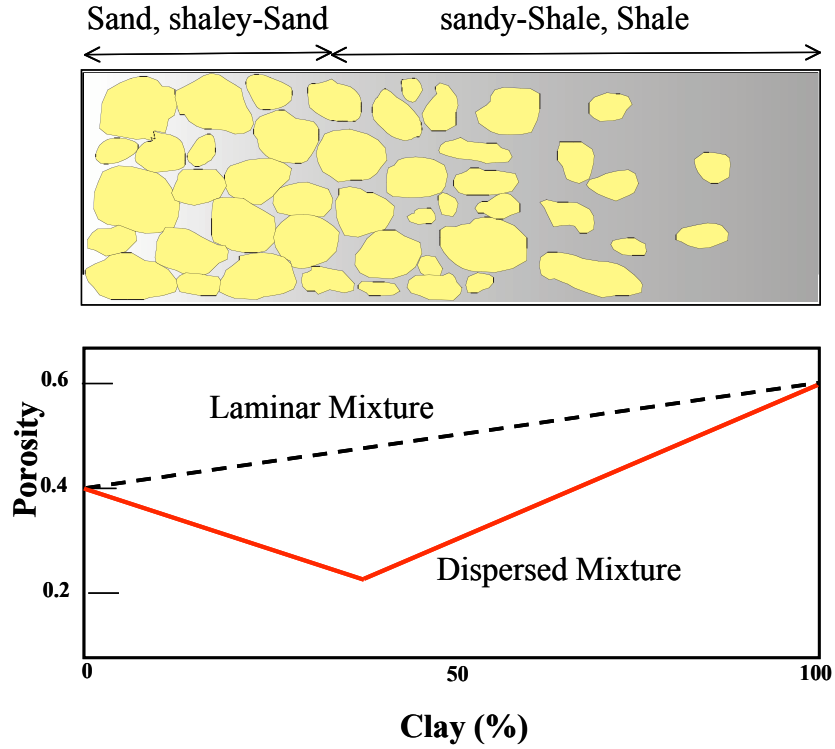


Figure A-3. Porosity variation for different mixtures of sand and shale, defining different lithofacies. Based on Thomas and Stieber (1975) and Marion *et al.* (1992).

Structural clay refers to clay particles that occur as part of the load-bearing material in sand-supported frameworks (Thomas and Stieber, 1975). Structural clay can occur as intraclasts derived from erosion of adjacent clay layers, or as grain replacement of stiff grains (e.g. kaolinite replacing feldspars). In the case of structural clay, porosity of the mixture is given by

$$\phi_m = \phi_{cs} + V_{clay}\phi_{clay} \quad (A-4)$$

### Elasticity of Laminar Mixtures

The effective elastic stiffness of horizontal laminar mixtures for vertically propagating P-waves is given by the harmonic average of the stiffnesses, or Reuss average:

$$M_{eff} = \left( \sum_i f_i M_i^{-1} \right)^{-1}, \quad (A-5)$$

with

$$M_i = K_i + \frac{4}{3}\mu_i, \quad (\text{A-6})$$

where  $M$  denotes the compressional (P-wave) modulus,  $K$  the bulk modulus,  $\mu$  the shear modulus, and  $f_i$  the volume fraction of the  $i$ th component. A laminar mixture is a transversely isotropic medium with its elastic stiffness tensor characterized by five independent constants (Mavko *et al.*, 1998). Using abbreviated notation, the stiffness tensor can be written as a 6x6 matrix. This simplifies the notation, even though the matrix is no longer a tensor:

$$C = \begin{bmatrix} c_{11} & c_{12} & c_{13} & 0 & 0 & 0 \\ c_{12} & c_{11} & c_{13} & 0 & 0 & 0 \\ c_{13} & c_{13} & c_{33} & 0 & 0 & 0 \\ 0 & 0 & 0 & c_{44} & 0 & 0 \\ 0 & 0 & 0 & 0 & c_{44} & 0 \\ 0 & 0 & 0 & 0 & 0 & \frac{1}{2}(c_{11} - c_{12}) \end{bmatrix}. \quad (\text{A-7})$$

Backus (1962) derived the expressions for each one of these constants. In terms of the lame constant ( $\lambda$ ), shear modulus ( $\mu$ ) and P-wave modulus ( $M$ ) of the component layers, these constants are as follows:

$$c_{11} = 4 \sum_i f_i (\lambda_i \mu_i + \mu_i^2) M_i^{-1} + \left( \sum_i f_i M_i^{-1} \right)^{-1} \left( \sum_i f_i \lambda_i M_i^{-1} \right)^2, \quad (\text{A-8})$$

$$c_{12} = 2 \sum_i f_i \lambda_i \mu_i M_i^{-1} + \left( \sum_i f_i M_i^{-1} \right)^{-1} \left( \sum_i f_i \lambda_i M_i^{-1} \right)^2, \quad (\text{A-9})$$

$$c_{23} = \left( \sum_i f_i M_i^{-1} \right)^{-1} \left( \sum_i f_i \lambda_i M_i^{-1} \right), \quad (\text{A-10})$$

$$c_{33} = \left( \sum_i f_i M_i^{-1} \right)^{-1}, \quad (\text{A-11})$$

$$c_{44} = \left( \sum_i f_i \mu_i^{-1} \right)^{-1}. \quad (\text{A-12})$$

One of the evident differences between laminar and dispersed mixtures is anisotropy. Lamellar mixtures are significantly anisotropic, whereas we expect dispersed mixtures to be more isotropic. Although this is one additional aspect that should be considered for seismic modeling, it is not discussed in this study. Throughout this analysis I assume the logs are reading the response to a P-wave propagating along a direction perpendicular to

the bedding surfaces. Unless the well is deviated or the layers are significantly tilted, this is a reasonable assumption.

### Elasticity of Dispersed Mixtures

Marion *et al.* (1992) analyzed the elasticity of dispersed sand-clay mixtures based on laboratory data. The data show that the point with the lowest porosity in the mixture also corresponds to the point of the highest velocity. The velocities of the end members, clean sand and pure-clay, are the lowest and, at low confining-pressures, about the same (Figure A-3). As sediments are buried, those with clay as the load-bearing material present a high porosity-reduction gradient, whereas those with sand as the load-bearing material have a lower porosity-reduction gradient. As a result, the pattern depicted by gradual mixtures of sand and clay in the velocity-porosity plane varies from a collapsed-V shape, at low confining pressures, to an inverted-V shape at high confining pressures (A-4).

Marion *et al.* (1992) applied fluid substitution to calculate the velocities of a dispersed mixture of clay and sand, along the sand load-bearing framework. This method assumes that pore-filling clay acts like a soft mixture of clay and water (like a mush) rather than a solid. The clay stiffens the pore-filling material, without affecting the frame properties of the sand. Following Gassman's equations (Mavko *et al.*, 1998) the elastic properties of the mixture ( $K_{mix}$ ) depend on the properties of the clay-water mush ( $K_{mush}$ ), the dry-sand modulus ( $K_{dry}$ ), the sand-grain mineral modulus ( $K_{qz}$ ), and the porosity of the clean sand ( $\phi_{cs}$ ), as follows:

$$\frac{K_{mix}}{K_{qz} - K_{mix}} = \frac{K_{dry}}{K_{qz} - K_{dry}} + \frac{K_{mush}}{\phi_{cs} (K_{qz} - K_{mush})} \quad (\text{A-13})$$

$$\mu_{mix} = \mu_{dry} \quad (\text{A-14})$$

A consequence of this assumption is that the pore-filling clay would not affect the shear modulus of the rock.

The elastic properties of the clay load-bearing branch are exactly given by the Reuss average (Equation A-11), since the mixture acts as a suspension of sand particles in clay. The density of the sand-shale mixture where porosity reduces due to pore filling clay can be calculated using the following formula:

$$\rho_{mix} = (1 - \phi_{cs})\rho_{qz} + V_{clay}(1 - \phi_{clay})\rho_{clay} + (\phi_{cs} - V_{clay}(1 - \phi_{clay}))\rho_w, \quad (\text{A-15})$$

where  $\rho_{qz}$ ,  $\rho_{clay}$ , and  $\rho_{fl}$  are the densities of sand grains (quartz), clay mineral and saturating fluid, respectively.

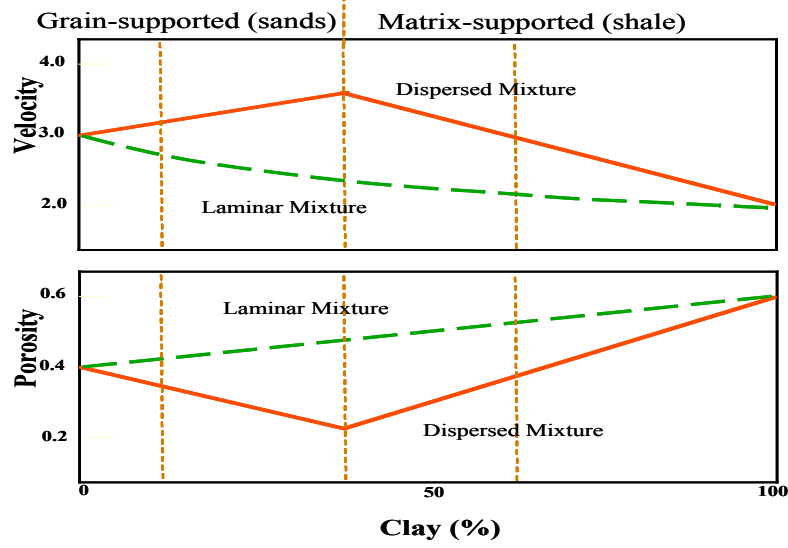


Figure A-3. Velocity and porosity variation in both laminar and dispersed mixtures of sand and shale, as inferred from the Marion-Yin model.

Instead of using Gassmann theory, we can use the modified lower Hashin-Shtrikman bound to calculate velocity-porosity trends for dispersed mixtures of quartz sand and clay. The method, similar to the one developed by Dvorkin and Gutierrez (2001), uses the unconsolidated sediment model to calculate the elastic properties of the sand and clay end points of the inverted-V, then uses equations A-1, A-2, and A-3 to determine the porosities of the mixtures. Finally, it uses modified Hashin-Shtrikman lower bounds to determine the elastic properties connecting the three end points (clean sand, minimum porosity, and pure clay).

For a mixture of two constituents, the Hashin-Shtrikman bounds (Hashin and Shtrikman, 1963; Mavko *et al.*, 1998) for the effective bulk ( $K_{eff}$ ) and shear ( $\mu_{eff}$ ) moduli are given by:

$$K_{eff}^{HS} = K_1 + \frac{f_2}{(K_2 - K_1)^{-1} + f_1(K_1 + \frac{4}{3}\mu_1)^{-1}} \quad (A-16)$$

$$\mu_{eff}^{HS} = \mu_1 + \frac{f_2}{(\mu_2 - \mu_1)^{-1} + \frac{2f_1(K_1 + 2\mu_1)}{5\mu_1(K_1 + 2\mu_1)}}, \quad (A-17)$$

where  $K_1$ ,  $K_2$ ,  $\mu_1$ ,  $\mu_2$ ,  $f_1$ , and  $f_2$ , are the moduli and the volume fractions of individual phases. The lower bound is computed when the softest material is subscripted 1. The unconsolidated model uses Hertz-Mindlin theory and the modified lower Hashin-Shtrikman bound to calculate the elastic properties of sediments with similar composition but different porosity, at specified pressures (Mavko *et al.*, 1998).

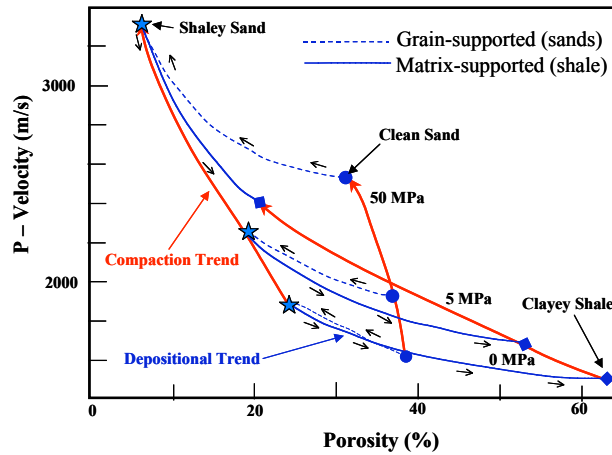


Figure A-4. Variation of velocity-porosity trends for sand-clay mixtures as a function of confining stress. After Marion (1990).

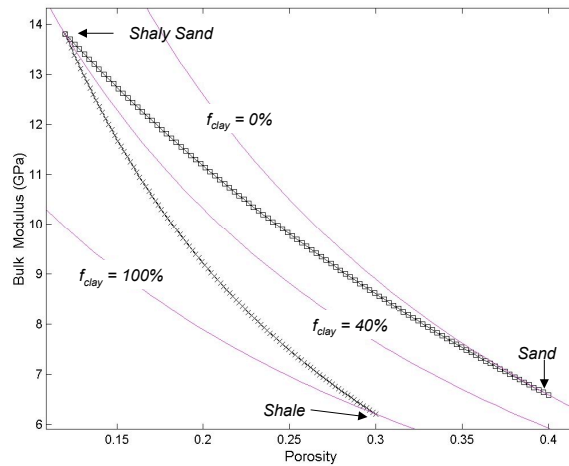


Figure A-5. Inverted-V pattern calculated from the combination of modified Hashin-Shtrikman lower bounds. The upper branch represents the shaly sands, the lower branch the silty or sandy shale. The three end members are obtained using the unconsolidated sediment model (magenta lines) for specified porosity, composition and pressure.

## Rock-Physics Models and Lithofacies Successions

Large stratigraphic sequences are composed of repetitive lithofacies successions derived from either gradual depositional processes or episodic catastrophic events (Ager, 1993). The best example of these repetitive lithofacies successions is the parasequence, a term introduced by Van Wagoner *et al.* (1990) to exclusively refer to the shallow-marine facies successions derived from oscillations in relative sea level, like the deltaic bar

shown in Figure A-6. Another well-known example is the fining-upward lithofacies succession characteristic of meandering fluvial deposits (Walker, 1984; Allen, 2001). The sand-clay mixtures analyzed in the Thomas-Stieber and Marion-Yin models resemble the vertical lithofacies successions observed in parasequences and single depositional events (Figure A-6).

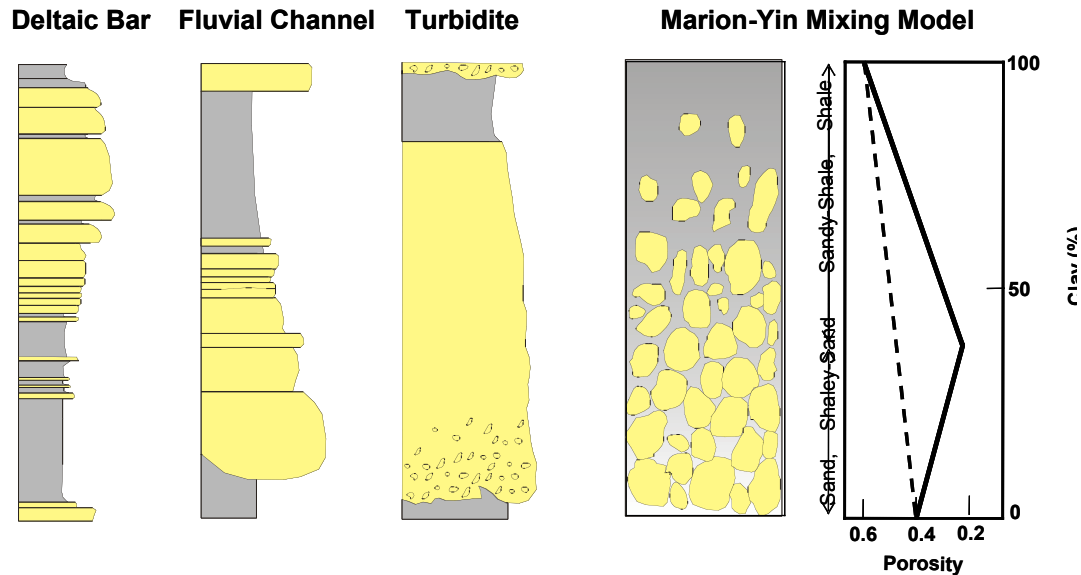


Figure A-6. Comparison of the Marion-Yin mixing model with the facies succession found in parasequences, and individual depositional cycles and events.

Rock physics models predict the changes in P-wave velocity and porosity of clastic lithofacies successions. These repetitive lithofacies successions are the building blocks of larger stratigraphic sequences. They present relatively simple lithofacies trends: fining upward, coarsening upward, blocky, or serrated. Both fining-upward and coarsening-upward trends show gradual transitions from clay-rich shale to clean-sand lithofacies. Although the textural trends in sedimentary rocks are in general more complex than the lithofacies transitions assumed in the rock-physics models, they capture the essence of these variations: type of mixture, compositional changes associated with clay content, changes in cementation, and changes in sorting. In principle, we should be able to identify the rock fabric from the velocity-porosity trend observed within a stratigraphic sequence.

In uncemented sands, the differences in the mechanics of deposition should be reflected in the patterns of concomitant velocity and porosity variations of mixed lithofacies. The depositional texture of a sedimentary rock is determined by the mechanics of deposition. The main variables associated with the depositional texture are

the load-bearing framework (grains or mud), grain size distribution, grain size, matrix (clay) content, and fabric. Differences in the mechanics of deposition and their transitions might be reflected in the patterns of the simultaneous change in velocity and porosity associated with the textural change. This is the general idea that we will explore throughout this paper.

Rock-physics models can also be used to predict the changes in both elastic and hydraulic properties of sedimentary rocks caused by diagenetic processes. Based on experimental results, Marion (1990) and Yin (1992) postulate that the patterns of sand-clay mixtures will change with confining pressure (Figure A-4). In general, their model predicts that as confining pressure increases, the pattern will change from a flat collapsed shape to an inverted-V shape. Based on numerical modeling, Jizba (1991) postulated an increase in elastic stiffness of sands compared to the surrounding shale and mixed lithofacies, as cementation takes place.

## **Methodology**

This work involved the evaluation of well-log data from different basins and depositional environments. Well logs from several basins and depositional settings were evaluated and some of them had to be disregarded because of the lack of geologic information or lack of quality control in the data.

We use three main cross plots to perform the analysis and comparison of the variation of elastic and bulk properties (porosity) within clastic depositional sequences: (1) bivariate histograms and color-coded cross plots of P-wave velocity ( $V_p$ ) and porosity ( $\phi$ ); (2) cross plots of porosity as a function of clay fraction ( $V_{clay}$ ); and (3) color-coded cross plots of P-wave velocity and density. In general, we refer to these cross plots as the rock-physics planes.

The rationale behind this approach is the application of rock-physics diagnostics (Dvorkin and Nur, 1996) constrained to stratigraphic sequences (Gutierrez *et al.*, 2001). We analyze the patterns of lithofacies sequences with a clear trend in clay content, inferred from both the gamma ray readings and the difference between neutron (NPHI) and density (PHID) porosities. In the cross plots the porosity corresponds to density porosity (PHID). The analyzed sequences correspond to genetically related lithofacies assemblages that form part of larger stratigraphic sequences.

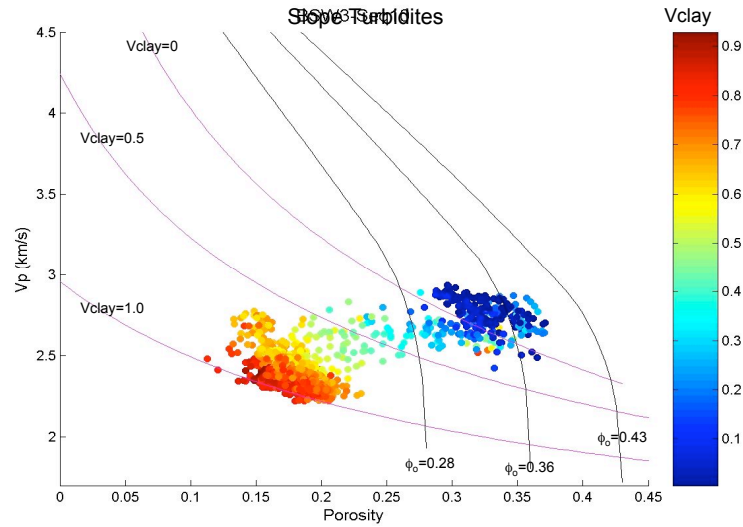


Figure A-7. Rock-physics template to evaluate the patterns of concomitant variations of porosity and elastic properties within clastic sequences.

Fluid substitution has been applied to velocity and density data in the case of hydrocarbon-bearing sands, in order to remove the fluid effect on the rock's elastic properties. Since the rocks analyzed are at similar pressure and temperature conditions, share a similar burial history, and have similar fluid saturations after fluid substitution, texture and composition are the dominant factors controlling the observed variations in elastic properties and porosity within any analyzed lithofacies sequence.

The rock-physics template shown in Figure A-7 illustrates one of the frameworks used for rock physics diagnostics. The template was built as follows: the black lines correspond to the diagenetic trend. The magenta lines correspond to the unconsolidated sandstone model (Mavko *et al.*, 1998) for different quartz-clay compositions. The anchor point for the unconsolidated model is given by the Hertz-Mindlin model at 25 MPa, with a correction factor of 0.7 for the shear stiffness. It is important to bear in mind that the purpose of these lines is not to fit the data, although in some cases they do it very well. The lines provide a framework that allows us to identify variations between different data sets, and infer the textural changes that can explain these differences. The inferred textures can be compared with the description of mudlog cuttings, core analysis, or other logging tools.

Rock physics diagnostics encompasses four basic steps: (1) petrophysic analysis and quality control of well-log data, (2) fluid substitution and cross plotting, (3) rock physics analysis, and (4) comparison with cores and other sources of information. The last step is

often difficult to perform because cored intervals are not always available and commonly correspond to a limited segment of the sedimentary section.

### **Rock-Physics Patterns of Selected Depositional Sequences**

This section presents the patterns observed in four selected lithofacies sequences from different depositional environments, illustrated in Figure A-8 and Figure A-9. The first example (Figure A-8a) corresponds to fluvial deposits of the Miocene Guayabo Formation from the Llanos Basin (Colombia). The following case (Figure A-8b) corresponds to Miocene, mud-rich, deep-water deposits from offshore West Africa. The third case (Figure A-9a) shows sand-rich deep-water deposits from offshore Gulf of Mexico. The last case (Figure A-9b) illustrates a coarsening-upward trend of shallow marine deposits from the Miocene Leon Formation, in the Llanos Basin (Colombia).

The differences between these four lithofacies sequences start to become conspicuous by looking at the cross plot of porosity and clay fraction (Figure A-1-). The fluvial deposits show an approximate V pattern (Figure A-10a) contrasting with the linear trend observed in the mud-rich deep-water deposits from offshore West Africa (Figure A-10b). The pattern observed in the fluvial deposits indicates the predominance of mm- to cm-scale dispersed fabric in the mixed lithofacies, whereas the linear trend observed in the deep-water deposits (Figure A-1-b) suggests the predominance of mm- to cm-scale horizontally laminated fabric. These two patterns are also different from the patterns observed in Figure A-1-(c) and Figure A-10(d). The sand-rich deep water deposits (Figure A-10c) shows two clouds of data points, corresponding to the sand and shale intervals, without a gradual transition between the two. The coarsening-upward lithofacies sequence (Figure A-1-d) shows another approximate V pattern with higher clay content, and significant scatter for clay fractions larger than 0.4. In the cases of the fluvial and shallow marine deposits, the lowest porosity occurs at the midpoint between the clean sand and the highest clay content, indicating the presence of dispersed sand-clay mixtures. The mud-rich deep water deposits show a pattern consistent with the predominance of laminar sand-clay mixtures. In contrast, the pattern outlined by the sand-rich deep water deposits suggests the absence of sand-clay mixtures.

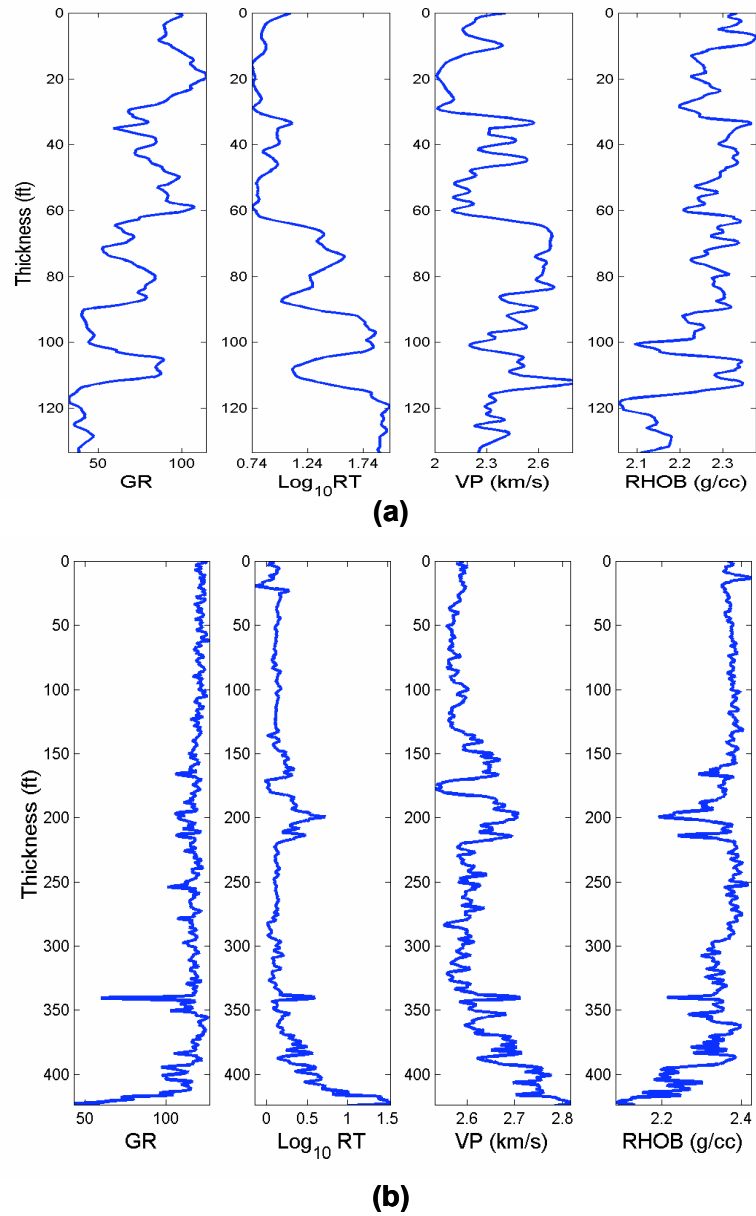


Figure A-8. Well-log data from two different lithofacies sequences: (a) fining-upward lithofacies sequence from fluvial deposits of the Miocene Guayabo Formation (Llanos Basin Colombia); (b) fining-upward lithofacies sequence from Miocene deep-water deposits offshore West Africa. Fluid substitution has been applied to the velocity and density logs in (b).

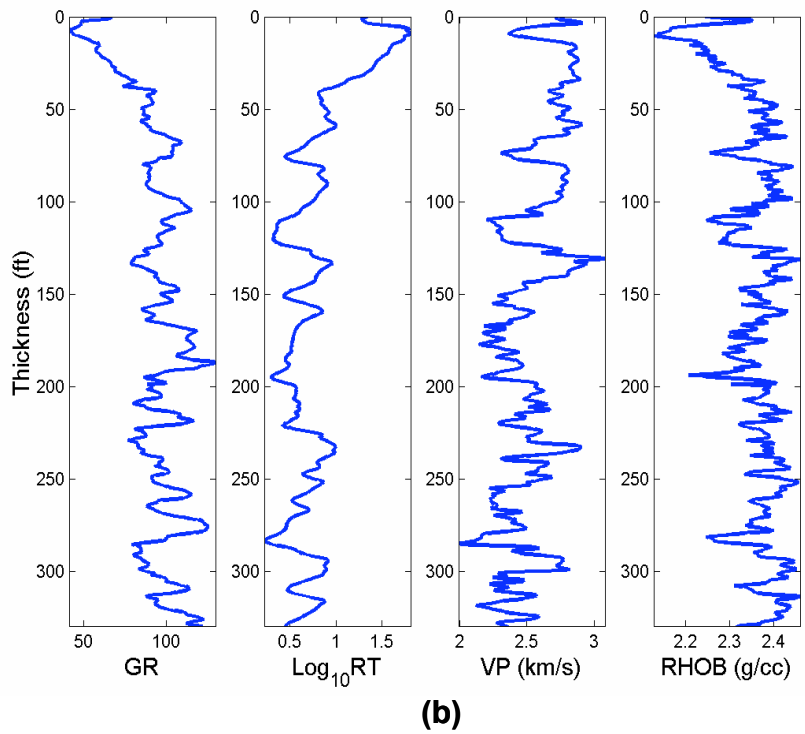
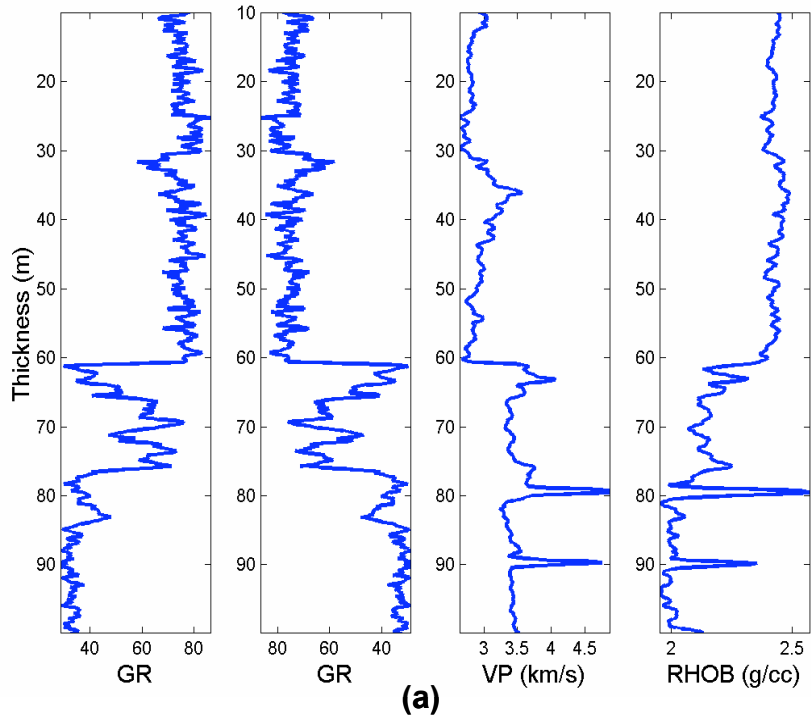


Figure A-9. Well-log data from two different depositional sequences: (a) deep-water blocky sandstone from offshore Gulf of Mexico; (b) coarsening-upward lithofacies sequence of shallow-marine Miocene deposits from Colombia (Upper Leon, well

Apiay-1, Llanos Basin). Fluid substitution has been applied to the velocity and density logs in (a).

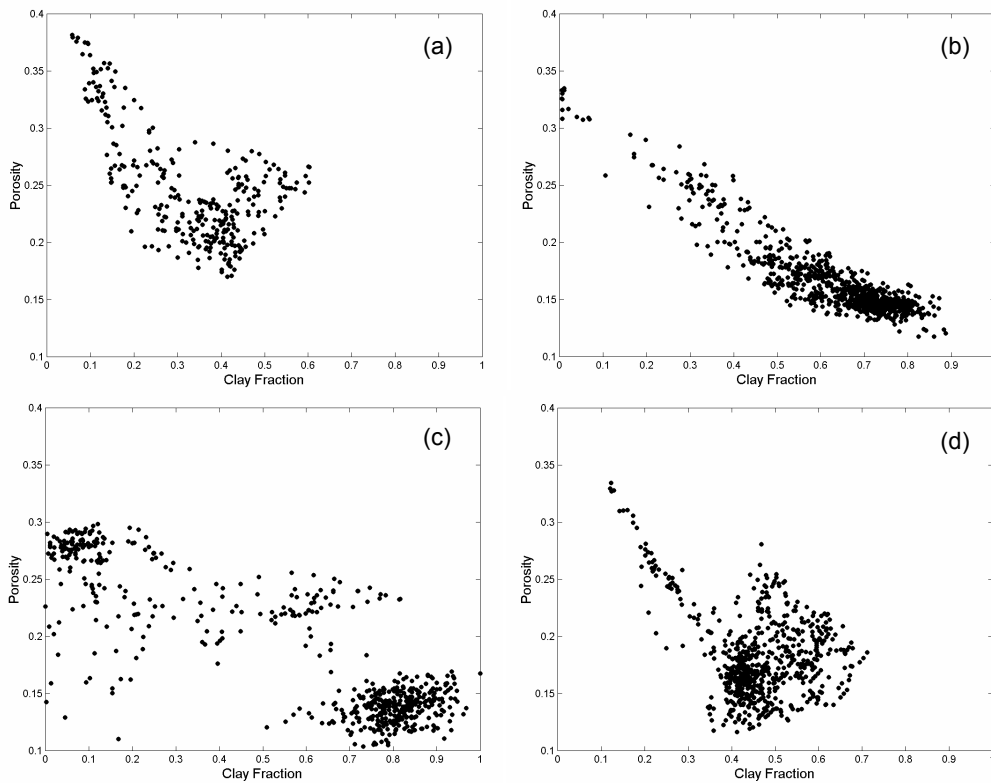


Figure A-10 Well-log Porosity-Clay Fraction cross plots from the clastic depositional sequences shown in Figure A-8 (a and b), and Figure A-9 (c and d). Porosity determined from density and neutron (in sands) logs, clay fraction determined from gamma ray and the difference between neutron and density porosities.

The velocity-density bivariate histograms (Figure A-11) corroborate the sedimentary fabric inferred from the porosity-V<sub>clay</sub> cross plots. In Figure A-11 the pure end members of the lithofacies sequences are indicated as Q for sand and C for clay-rich shale. As shown in Figure A-11(a), the fluvial deposits present a clear inverted-V pattern, similar to the one predicted by the Marion-Yin model (Marion *et al.*, 1992). In the case of the mud-rich deep water deposits, Figure A-11(b) shows a clear linear trend as predicted for horizontally laminated sand-clay mixtures from the Backus average (e.g. Mavko et al, 1998), and the linear variation in porosity as a function of clay content. In contrast, Figure A-11(c) illustrates the absence of mixed lithofacies in the sand-rich deep water deposits. Finally, Figure A-11(d) demonstrates the predominance of dispersed sand-clay mixtures in the shallow marine deposits, and suggests the occurrence of some subordinate laminated lithofacies.

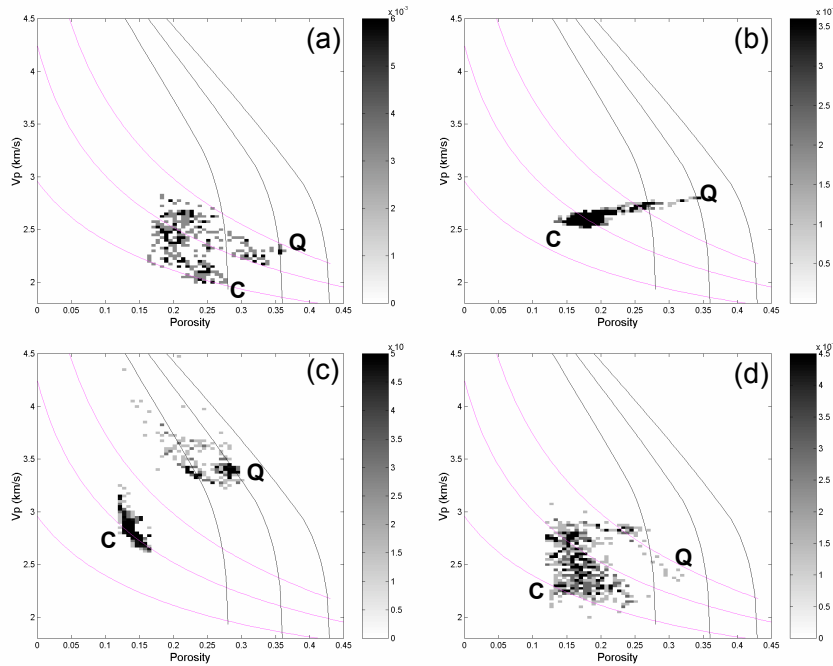


Figure A-11. Bivariate histograms of well-log P-wave velocity and porosity (PHID) from the four different clastic depositional sequences shown in Figure A-10. Q indicates the sand points (quartzose sand) and C indicates the clay-rich shale point. Black lines outline the diagenetic trend for quartzose sands; magenta lines outline the depositional trend for sands at 25 MPa, with different proportions of clay (0, 50% and 100%).

The differences between these four lithofacies sequences can be summarized in the velocity-density cross plot color-coded by clay content (Figure A-12). In this plane, contours of iso-impedance can be superimposed, since acoustic impedance is the product of velocity and density. The cross plots illustrate that the patterns observed are the result of the concomitant variations in density (porosity) and elastic properties (velocity) associated with clay content.

The most striking difference occurs between the pattern outlined by the lithofacies sequence from fluvial deposits, Figure A-12(a), and the pattern depicted by the lithofacies sequence from mud-rich deep water deposits, shown in Figure A-12(b). The variations in clay content, density, porosity, and elastic properties observed in the fluvial deposits clearly indicate the predominance of a dispersed fabric in the mixed lithofacies. In contrast, the variations in clay content, density, porosity and elastic properties observed in the mud-rich deep-water deposits clearly indicate the presence of horizontally laminated sand-clay mixtures. Another significant difference is the contrast between the

scarcity of mixed sand-clay lithofacies in the sand-rich deep water deposits, Figure A-12(c), and the abundance of both dispersed and laminar mixed lithofacies in the shallow marine deposits shown in Figure A-12(d).

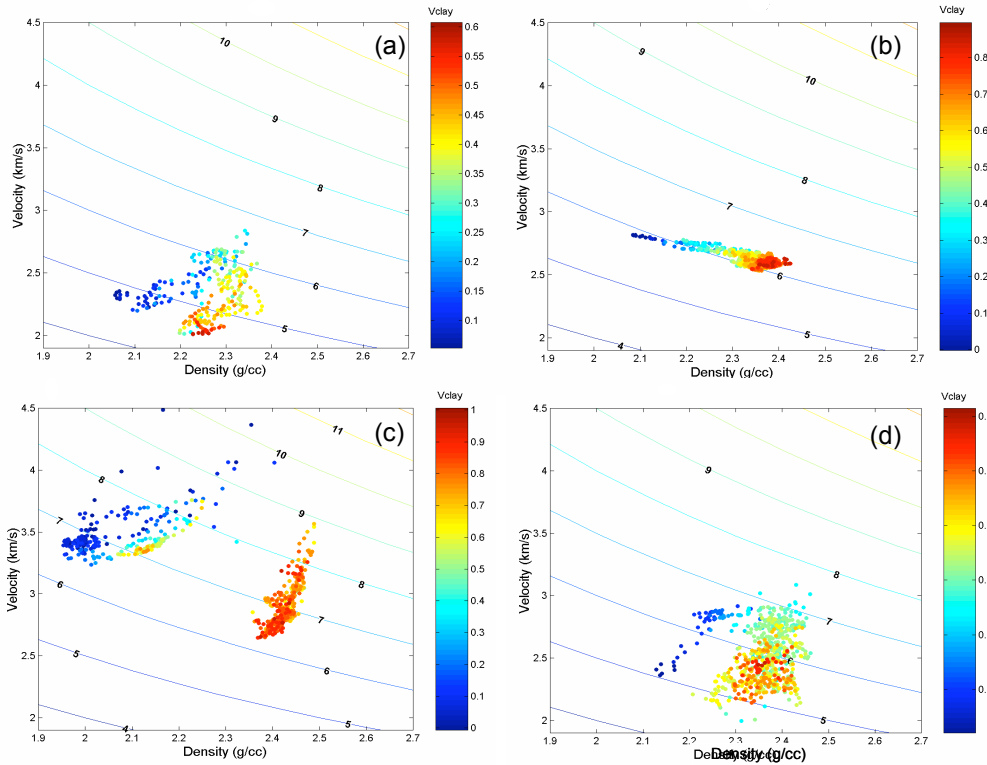


Figure A-12. Cross plots of well-log P-wave velocity and density color-coded by fraction of clay for the same four different clastic depositional sequences shown in Figure A-11. The plots also show contours of impedance. Notice that for the cases of (a) and (d) the highest impedances correspond to the mixed lithofacies.

The millimetric and centimetric fabrics of these lithofacies sequences, inferred from the different cross plots, agree with the observed and reported fabrics from outcrops, cores, and image-log analysis. The shallow marine deposits of the Miocene Leon Formation commonly present fine-grained to very-fine grained argillaceous sandstones with horizontal, wavy, and lenticular lamination (Cardona and Gutiérrez, 1995). These rocks also present a massive or dispersed sand-clay fabric associated with intense bioturbation. As shown in Figure A-13, the mixed lithofacies of the fluvial deposits from the Miocene Guayabo Formation in Colombia are characterized by massive, structureless, variegated, reddish, sandy to silty mudstones and argillaceous fine-grained sandstones (e. g. Aguilera and López, 1994). In contrast, the dominant fabric in the mixed lithofacies from mud-rich deep water deposits is mm- to cm-scale horizontal lamination and

interbedding (Figure A-13). Similar thinly interbedded and laminated sand-clay lithofacies occur in outcrop analogues of mud-rich deep water deposits in Chile (Beaubouef, 2004).

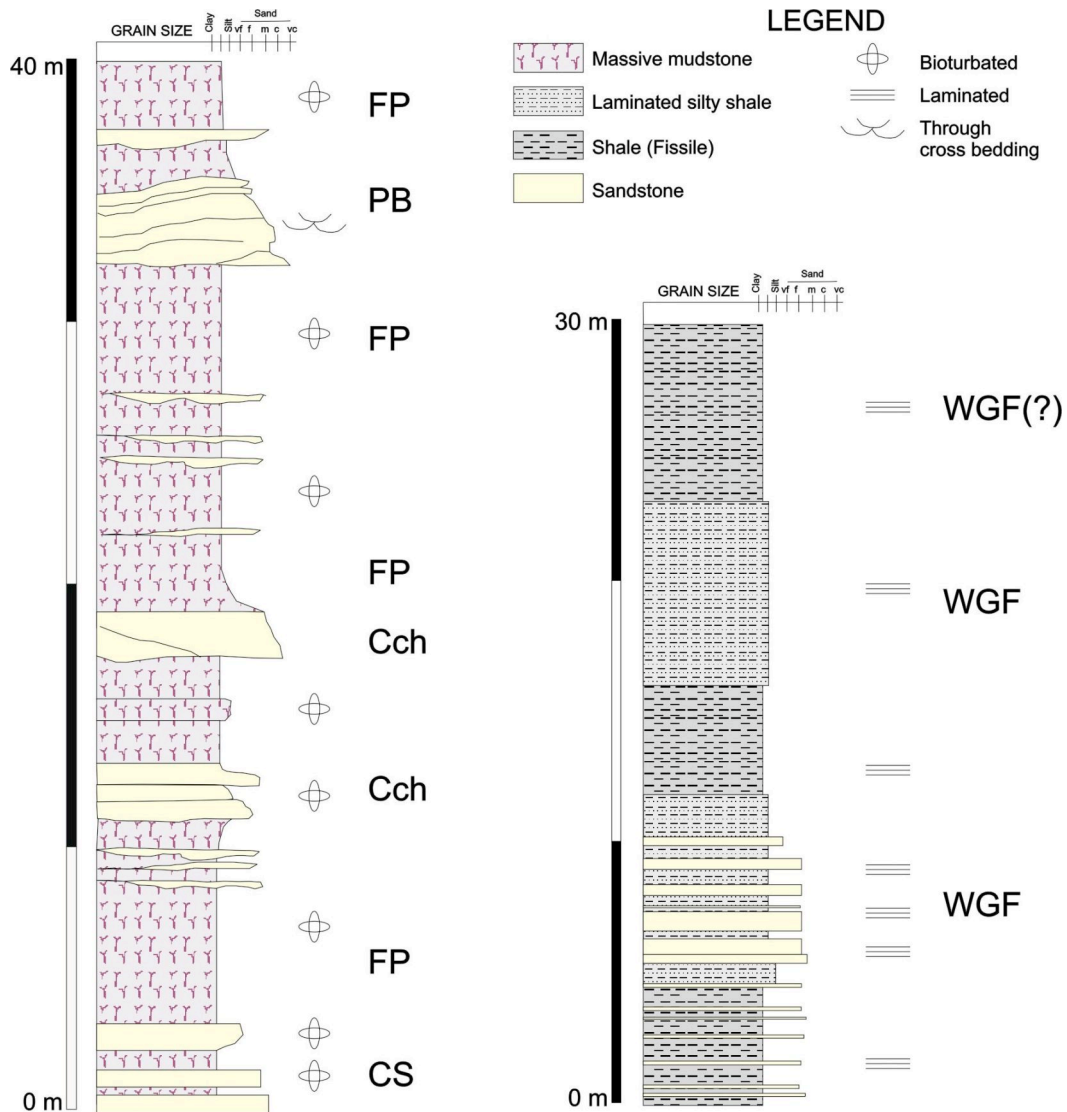


Figure A-13. On the left, clay-rich lithofacies from fluvial deposits (outcrop description of lower Guayabo Formation), on the right shaly lithofacies from mud-rich deep water deposits (high-resolution, core-calibrated, image-log interpretation, courtesy of ChevronTexaco). The mm- to cm-scale internal fabric is indicated by the symbols: bioturbated or horizontally laminated. The upper case letters refer to the inferred depositional environment or mechanism: floodplain (FP), point bar (PB), crevasse channel (Cch), crevasse splay (CS), and waning gravity flows (WGF).

## **Continuity and Repeatability of Rock-Physics Patterns**

The similarity or dissimilarity between the rock-physics patterns outlined by decameter-scale lithofacies sequences and those depicted by larger-scale sequences depend on the vertical persistence of lithofacies. This similarity determines the ability to predict, for modeling purposes, the seismic properties of large-scale sequences from the patterns observed at decameter-scale lithofacies successions. The vertical persistence or variation of lithofacies sequences is the result of the interaction between the rate of space accommodation, of the depositional setting, and the rate of sediment supply (e.g. Emery and Myers, 1996; Miall, 1998). Lithofacies assemblages can be very similar throughout thick stratigraphic intervals, like the case of the lower Guayabo Formation (Figure A-14); or can have a significant variability, as is the case of mud-rich deep water deposits from offshore West Africa (Figure A-15).

The applicability of the observed patterns to frontier areas, and regions with scarce well-log data, depends on the repeatability and lateral persistence of lithofacies sequences. Repeatability refers to the similarity between lithofacies sequences accumulated in the same depositional environment at different basins. The lateral persistence relates to the aerial continuity of the lithofacies assemblage within a basin, which again is the result of the interplay between sediment supply and accommodation (Emery and Myers, 1996). As an example of repeatability, I compare the sand-rich deep water deposits from the Gulf of Mexico (Figure A-9a) with the same type of deposits from the North Sea (Figure A-16). The Miocene Leon Formation (Figure A-17), from the Colombian Llanos Basin, is presented as an example of the lateral persistence of lithofacies sequences.

## **The Patterns of Larger-scale Depositional Sequences**

The lower Guayabo Formation presents patterns in the rock-physics planes (porosity-Vclay, velocity-porosity, and velocity-density) very similar to those depicted by the single, dispersed-fabric, fluvial lithofacies sequence analyzed in the section 4.3. The patterns observed in figures 4.10(a), 4.11(a), and 4.12(a) are almost identical to those presented in figures 4.18(a), 4.19(a), and 4.20(a), respectively. The fining-upward cycle analyzed in section 4.3 is part of the lower Guayabo Formation (is located between 100-220 ft in Figure A-14). The Guayabo Formation is a fluvial syntectonic deposit (Aguilera and López, 1995), accumulated during the uplift of the Eastern Cordillera in Colombia (Cooper et al., 1995). The vertical persistence of this lithofacies assemblage resulted from

the dynamic equilibrium between subsidence (accommodation) and sediment supply. This vertical persistence of the lithofacies assemblage produces the resemblance between the single decameter-scale lithofacies sequence and the larger-scale lower-Guayabo Formation.

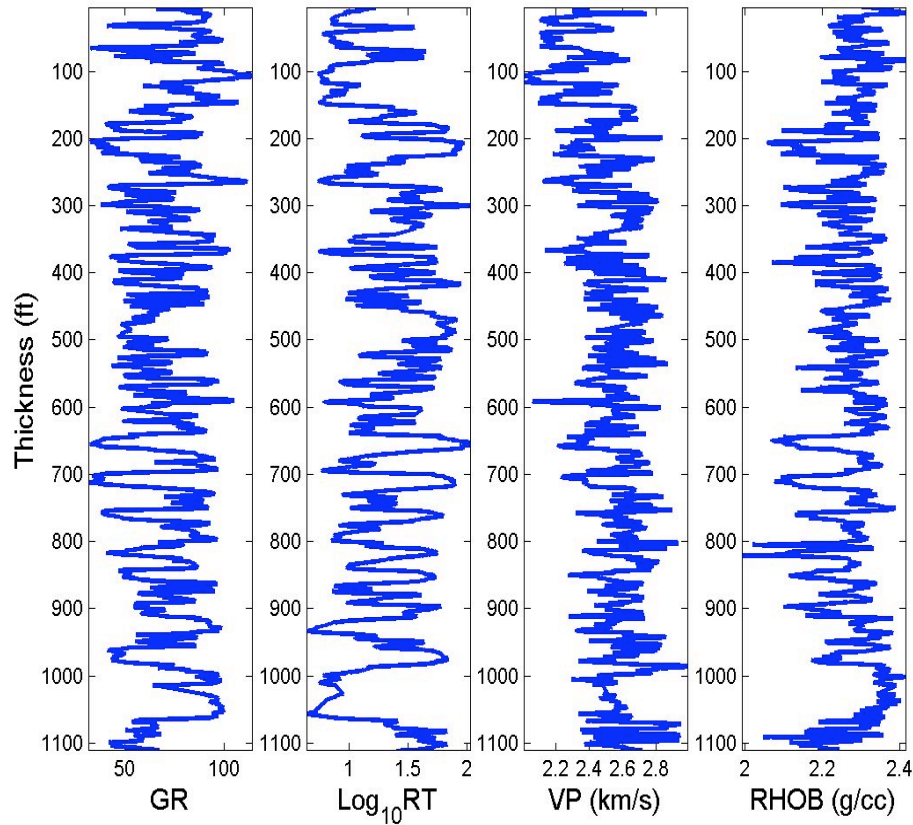


Figure A-14. Lower-Guayabo Sequence formed by fining upward lithofacies cycles associated with fluvial environments (e. g. Aguilera and López, 1995). Well Apiay-1, Llanos Basin (Colombia).

In contrast, the mud-rich deep water sequence (Figure A-15), which contains the laminar mixture analyzed in section 4.3, presents patterns significantly different from those associated with a laminar mixture. Exception made of the porosity-Vclay cross plot (Figure A-18b), the complete sequence shows patterns that resemble those associated with mm- and cm-scale dispersed fabrics (Figure A-19b, and Figure A-10b). The main reason for this variation is the presence of shale with different composition and degree of compaction within the same stratigraphic sequence. Notice in Figure A-18b the high variability in porosity for high clay content. As illustrated in Figure A-15, the sequence contains at least three types of shale-rich facies. As determined from high-resolution image logs and core descriptions, the shale-rich lithofacies are from base to top: mud

flows (MF), overbank deposits (C1), and hemipelagic shale (C2). Mud flow deposits are the stiffest and densest shale-rich deposits. Overbank deposits have an intermediate stiffness and density, whereas hemipelagic shale is the softest and lightest shale-rich lithofacies. Besides, the sands have also slightly different elastic properties, as can be observed in Figure A-20b. The sands, however, are mixed only with one type of shale, the overbank deposits, which have an intermediate stiffness.

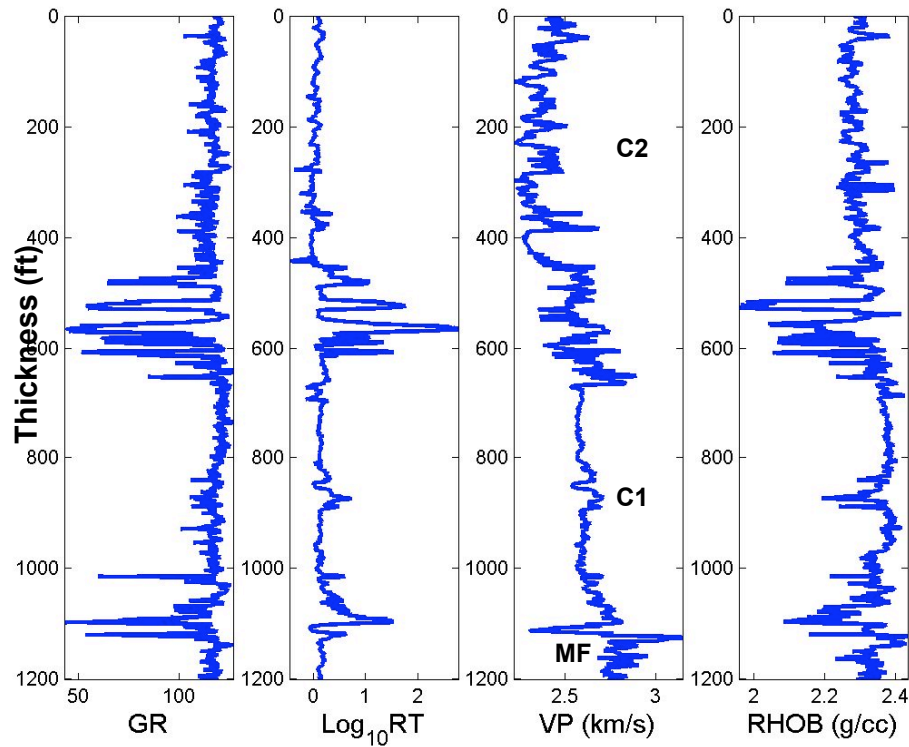


Figure A-15. Stratigraphic sequence of mud-rich deep water deposits from offshore West Africa. The velocity log identifies three types of clay-rich deposits: hemipelagic shale (C2), overbank shale (C1), and mud flows (MF) at the base. Velocity and density logs after fluid substitution.

The variability of shaly lithofacies within the mud-rich deep water sequence can be explained using sequence stratigraphy. The thicker mud-flow deposits are associated with low relative sea level (low-stand systems tract, LST), and consequently tend to occur towards the base of the stratigraphic sequence. Above them, confined turbidite complex are deposited, which include shale-rich overbank deposits. The thick intervals of hemipelagic shale, in contrast, are associated with periods of relative high sea level (high-stand systems tract, HST).

Both the hemipelagic shale and the mud flows introduce the higher variability in elastic properties in the mud-rich deep water deposits. In addition to a dispersed fabric,

mud flows probably have a higher degree of compaction and a higher proportion of silty material than the hemipelagic and overbank shale. Similarly, the overbank shale seems to have a higher proportion of silt and a higher degree of compaction than the hemipelagic shale. The dominant fabric of the mixed lithofacies within the overbank complex is the interposition of mm-scale to cm-scale layers of relatively clean sand and overbank shale. This fabric can be inferred from the monotonic variation in elastic properties as clay content increases (or decreases) and has been corroborated by core observations and high-resolution image logs (Figure A-13b).

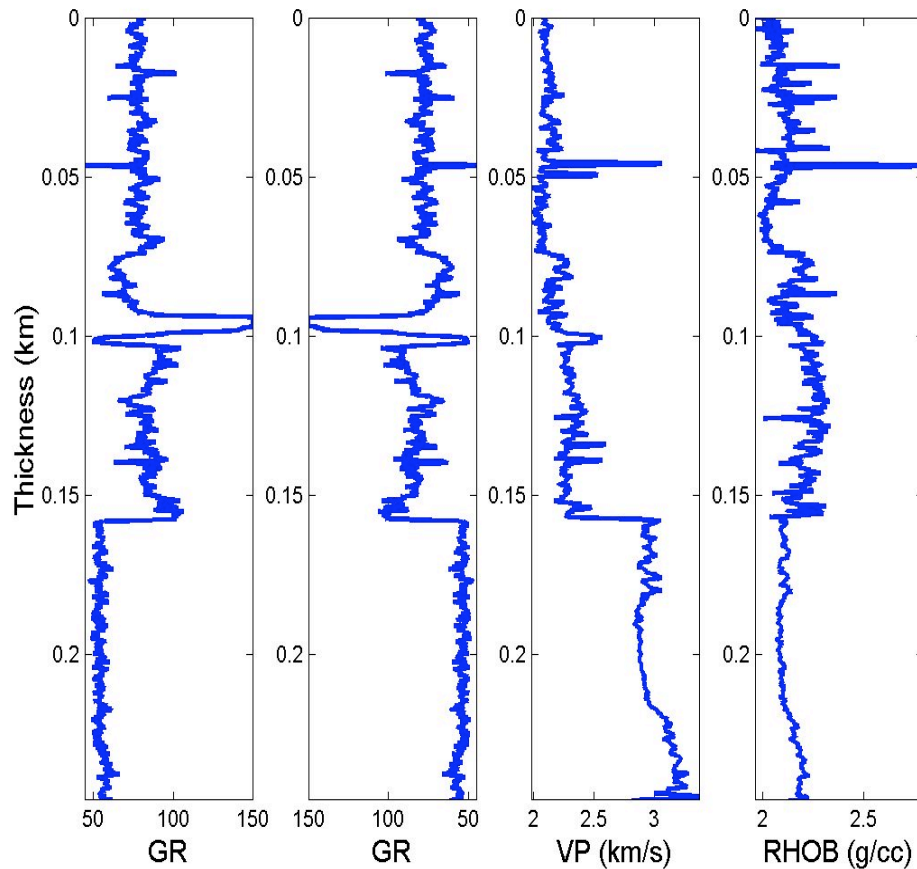


Figure A-16: Stratigraphic sequence of sand-rich deep water deposits from the North Sea. Velocity and density logs after fluid substitution.

Similar depositional environments generate repetitive lithofacies sequences with comparable elastic properties. The comparison between the rock physics patterns of two sand-rich deep water deposits from different basins, the Gulf of Mexico and the North Sea, provides an excellent example. The patterns of the sand-rich deposit from offshore Gulf of Mexico are illustrated in, Figure A-10c, Figure A-11c, and Figure A-12c. They are very similar to the patterns of the sand-rich deep water deposit from the North Sea,

shown in Figure A-18c, Figure A-19c, and Figure A-10c. The absolute velocities are different because of the difference in compaction between these two deposits. The deposit from the Gulf of Mexico is buried about 1 km deeper than the deposit from North Sea. However, the two deposits present a conspicuous contrast in elastic properties between the sandy lithofacies and the shale-rich lithofacies, derived from the scarcity of mixed lithofacies in this depositional setting. This contrast provides a method to differentiate sand-rich deep water deposits from mud-rich deep water deposits.

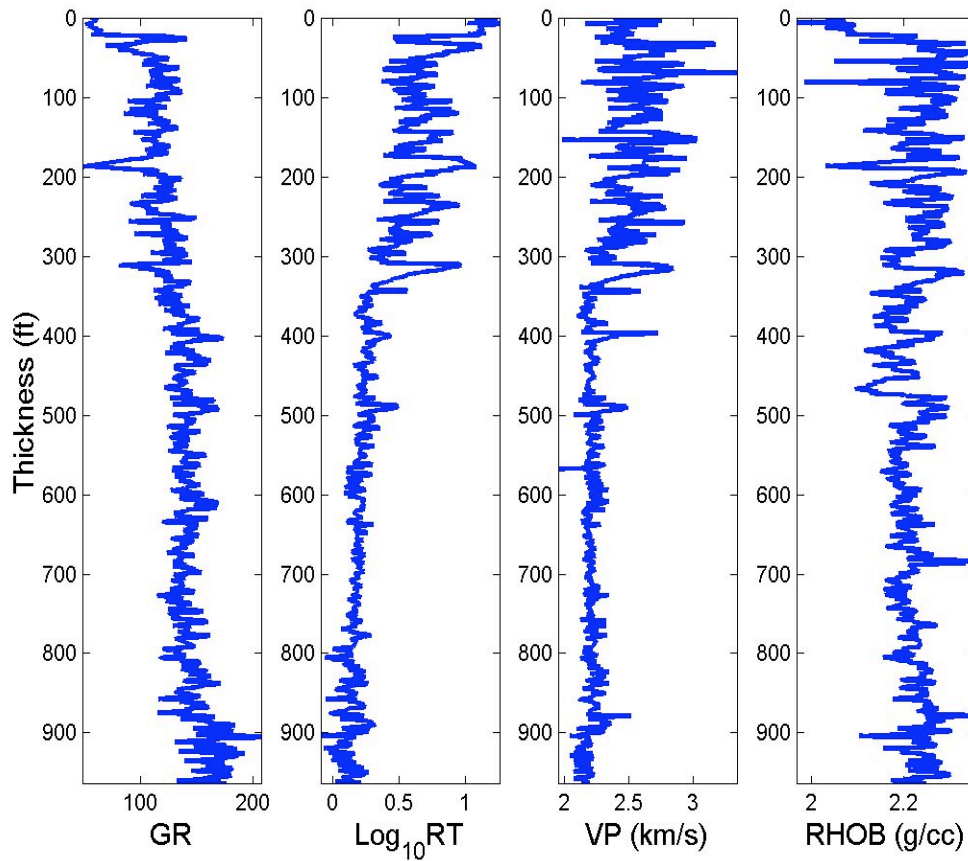


Figure A-17. Coarsening upward lithofacies sequence from shallow marine deposits, Leon Formation (Miocene), well Tambaquí-1, Llanos Basin (Colombia).

The Miocene Leon Formation (Llanos Basin, Colombia), provides an excellent example of lateral persistence of lithofacies, and therefore elastic properties. This formation consists of a coarsening upward lithofacies sequence (Figure A-17) accumulated as the result of a tectonically-driven regional flooding event and the posterior basin-filling process. In terms of sequence stratigraphy it can be considered a high-stand systems tract (e.g. Cooper *et al.*, 1995). The rock-physics patterns that this formation presents at the well Tambaquí-1 (Figure A-18d, Figure A-19d, and Figure A-

20d), are remarkably similar to the patterns outlined by upper segment of the same formation at the well Apiay-1, about 200 km to the south west, illustrated in Figure A-10d, Figure A-11d, and Figure A-12d.

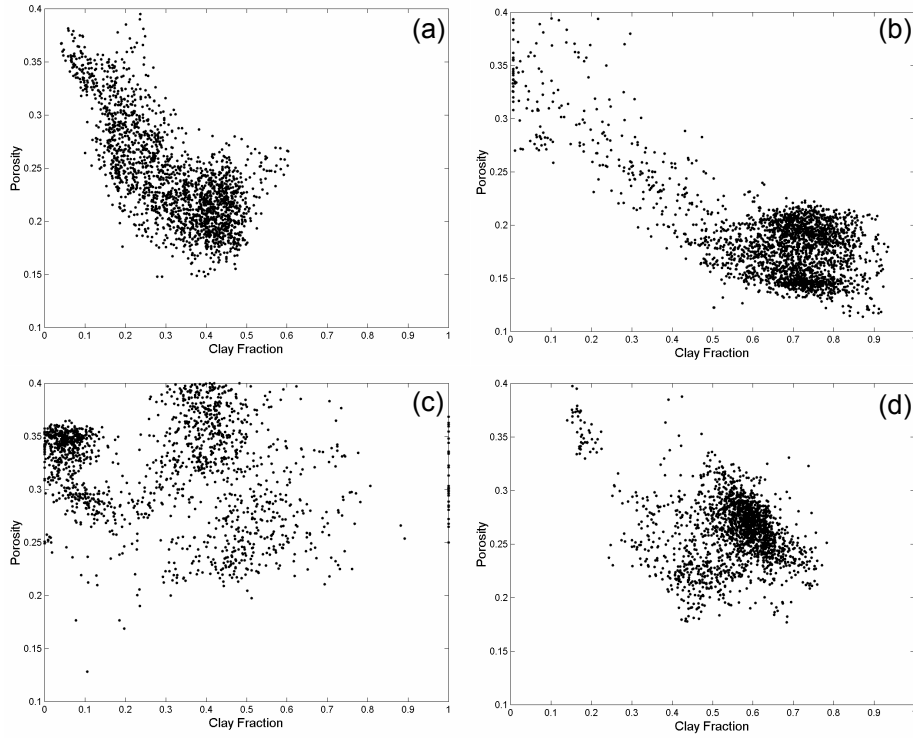


Figure A-18. Cross plots of Porosity ( $\phi$ ) and clay fraction ( $V_{clay}$ ). Figures A-17 (a), (b), (c) and (d) correspond to the lithofacies sequences presented in Figure A-14, Figure A-15, Figure A-16, and Figure A-17, respectively.

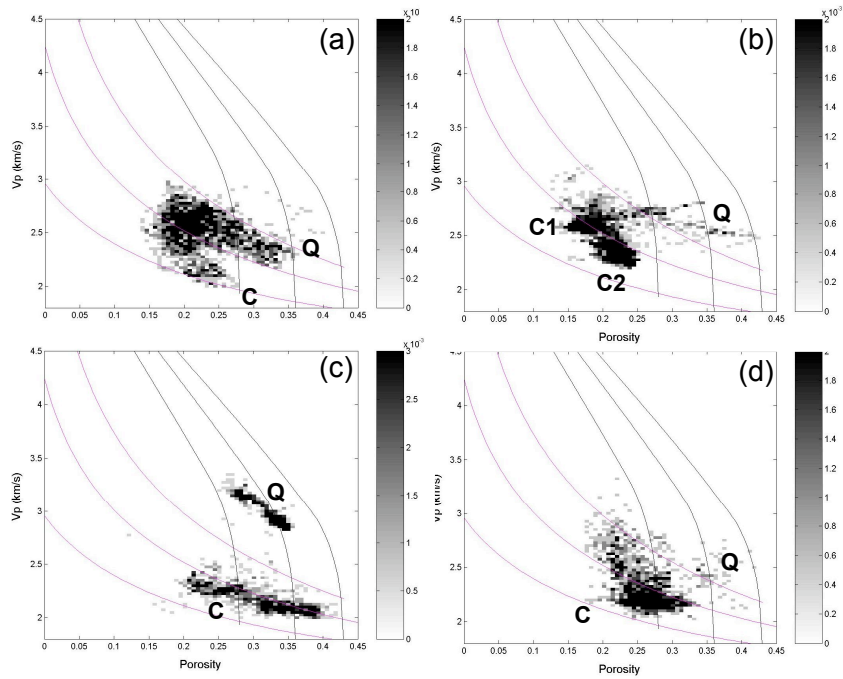


Figure A-19: Bivariate histograms of P-wave velocity ( $V_p$ ) and Porosity ( $\phi$ ). Q indicates the sand point, and C indicates the clay-rich points. Figures 4.18 (a), (b), (c), and (d) correspond to the lithofacies sequences shown in Figure A-14, Figure A-15, Figure A-16, and Figure A-17, respectively.

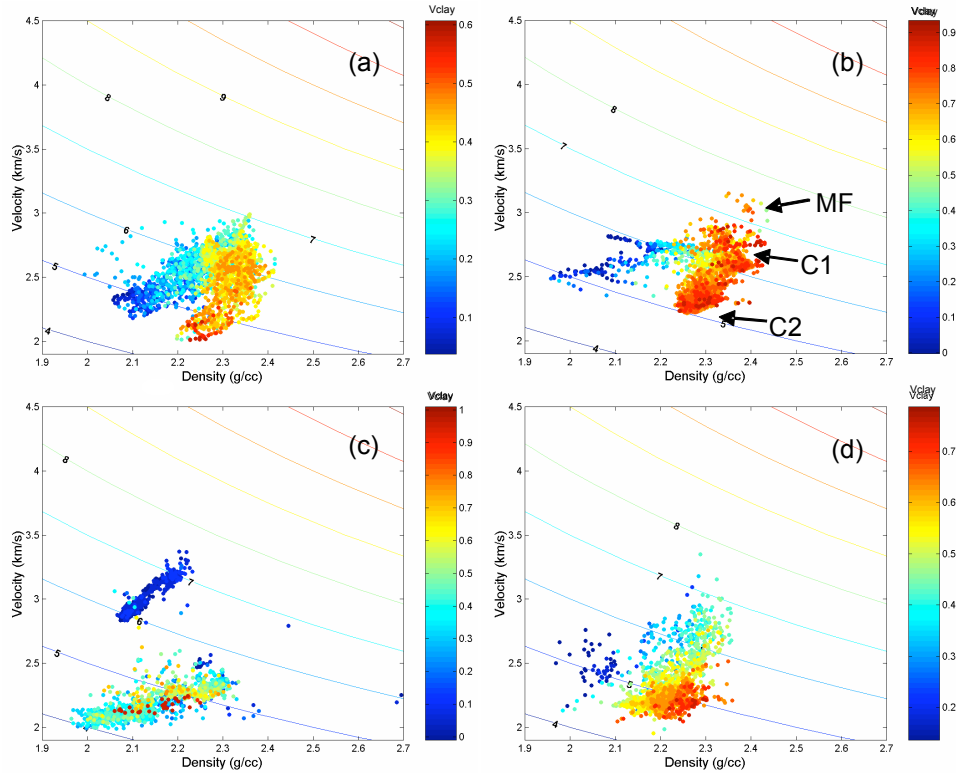


Figure A-20. P-wave velocity ( $V_p$ ) and density cross plots, color-coded by clay fraction ( $V_{clay}$ ). The data corresponds to different lithofacies sequences: (a) fluvial deposits, (b) mud-rich deep water deposits, (c) sand-rich deep water, and (d) shallow marine to low-energy intertidal deposits. In (c) the arrows indicate the different types of shale.

The rock-physics patterns of large-scale clastic stratigraphic sequences depend on the proportion and type of lithofacies assemblages. Figure A-18, Figure A-19, and Figure A-20 show that these patterns may vary significantly from one depositional setting to another. The most striking difference illustrated in these figures is the contrast between the patterns of sand-rich deep water deposits and those of mud-rich deep water deposits. This contrast is the result of the scarcity of mixed lithofacies in the sand-rich depositional setting. However, as explained earlier, another significant contrast can occur between sequences with predominant mm- to cm-scale dispersed mixed lithofacies and those with mm- to cm-scale horizontally laminated mixed lithofacies.

### Depositional Settings and the Fabric of Sand-Clay Mixtures

Although dispersed and horizontally laminated sand-clay mixtures cannot be considered exclusive of a particular depositional setting, their occurrence within a given environment is associated with specific depositional and post-depositional processes, like bioturbation. In his discussion of the mechanics of deposition of muddy sediments, Allen

(2001, p. 142) demonstrates that the net rate of bed deposition ( $D$ ) of muddy deposits is given by

$$D = \rho\chi V_b \left(1 - \frac{\tau}{\tau_{cr}}\right), \quad (\text{A-18})$$

where  $\rho$  is the clay (mud) density,  $\chi$  is the near-bed fractional volume concentration of clay,  $V_b$  corresponds to the terminal fall velocity of the near-bed particles (referenced to the ground),  $\tau$  is the boundary shear stress due to the fluid motion, and  $\tau_{cr}$  is the critical stress for mud deposition. Three cases become evident from Equation 4.18, the stage of deposition from a stagnant fluid ( $\tau = 0$ ), the stage of no deposition ( $\tau = \tau_{cr}$ ), and the stage of erosion ( $\tau > \tau_{cr}$ ). For any fluidized flow with clay and sand, fluctuations between these three stages will determine the occurrence and distribution of horizontally laminated sand-clay mixtures.

The ideal conditions for millimetric to centrimetric interposition of clean sand and clay-rich mud occur in flat settings affected by oscillating or seasonal currents. Asymmetrical tides provide an excellent example of these conditions, as discussed by Allen (2001, p. 256). Reineck and Singh (1980) summarize the occurrence of these lithofacies from different depositional settings. They classify these deposits as coarsely interlayered bedding and thinly interlayered bedding (rhythmites), which different authors have found in deposits associated with lakes and transitional environments like tidal flats and estuaries (Reineck and Singh, 1980, p. 123). Howard and Reineck (1972) report the presence of these lithofacies in shallow marine shoreface deposits. Smith (1987) discusses the presence of laminated sand-clay mixtures fluvial deposits, which are commonly associated with areas with high water tables.

Bioturbation (e.g. Reading, 1980, p. 223; Reineck and Singh, p. 387) seems to be the dominant mechanism generating dispersed sand-clay mixtures in water-laid deposits. Fast accumulation rates associated with fluidized flows with high sediment concentration could be an alternative mechanism. Metric to decimetric intervals of silty mudstone and muddy sandstone, associated with fluvial deposits like the Guayabo Formation of Colombia, seem to be the result of burrowing, plant growth, and pedogenetic processes that destroy the primary sedimentary structures (Galloway and Hobday, 1996, p.75).

The final depositional fabric is the result of the predominant depositional mechanism and sediment composition. The examples documented in this chapter show that the proportion of dispersed and laminar mixed lithofacies, and actually the proportion of mixed lithofacies, vary among the different depositional environments. As a general rule, dispersed mixtures result from either bioturbation or the inability of the medium to

separate fine and coarse fractions, whereas laminar mixtures indicate cyclic deposition (like tidal deposits and varves) or efficient separation between the traction and suspension fractions. A good example is the differentiation, made by Smith (1987), between fluvial point bars without laminated lithofacies, and fluvio-estuarine point bars with laminated lithofacies. However, the specificities of the mechanics of deposition are normally more complex. For example, in their analysis of textural trends in deep-water turbidite and mass-flow deposits, Sylvester and Lowe (2004) showed that the development of mud-rich sands and slurry beds, with a dispersed mixture of sand and clay, depends on how efficiently the settling sediment traps mud particles. Therefore, at least for the case of turbidite deposits, the difference between the depositional mechanism that generated the laminated turbidites shown in Figure A-13b, and the mechanism that would have generated a higher proportion of the dispersed-mixture slurry beds might be relatively small.

### **The Diagenetic Effects**

The rock physics patterns of clastic depositional sequences can change because of diagenetic effects. Marion (1990) and Yin (1992) analyzed the variations in these patterns associated with confining pressure. Jizba (1991) modeled the effect of differential cementation between clean sands and shaly sands. Dvorkin *et al.* (2002) showed a remarkable continuity in the shale and sand diagenetic trends of deep-water deposits from the Gulf of Mexico and the North Sea. Chapter 3 explains the role that pressure solution can play in the diagenetic trend of quartzose sands. In this section, I present two clear examples of the effect that diagenesis and confining pressure have on the rock physics patterns of clastic sequences.

#### **Confining Pressure, Pressure Solution, and Incipient Cementation**

Marion's and Yin's analyses (Marion, 1990; Yin, 1992) postulate that as confining pressure increases, the velocity-porosity pattern of dispersed mixtures of sand and clay change from a flat trend to an inverted-V pattern. Figure A-21 shows two fining-upward cycles of fluvial origin. They both come from well Apiay-1, the same well that presented the inverted-V pattern in the whole Pliocene Lower Guayabo stratigraphic sequence. The examples shown below correspond to stratigraphic intervals located above and below the Lower Guayabo. The shallow interval is part of the Upper Guayabo, whereas the deep interval is part of the lower Carbonera, C5 formation. In spite of the similar lithofacies that these intervals show, the rock physics patterns are very different and conform to the

predictions of Marion (1990) and Yin (1992). Figure A-22 shows the velocity-porosity patterns of these two fining-upward sequences. The shallow lithofacies sequence shows a flat pattern, whereas the deep lithofacies sequence presents what is becoming a classical inverted-V pattern.

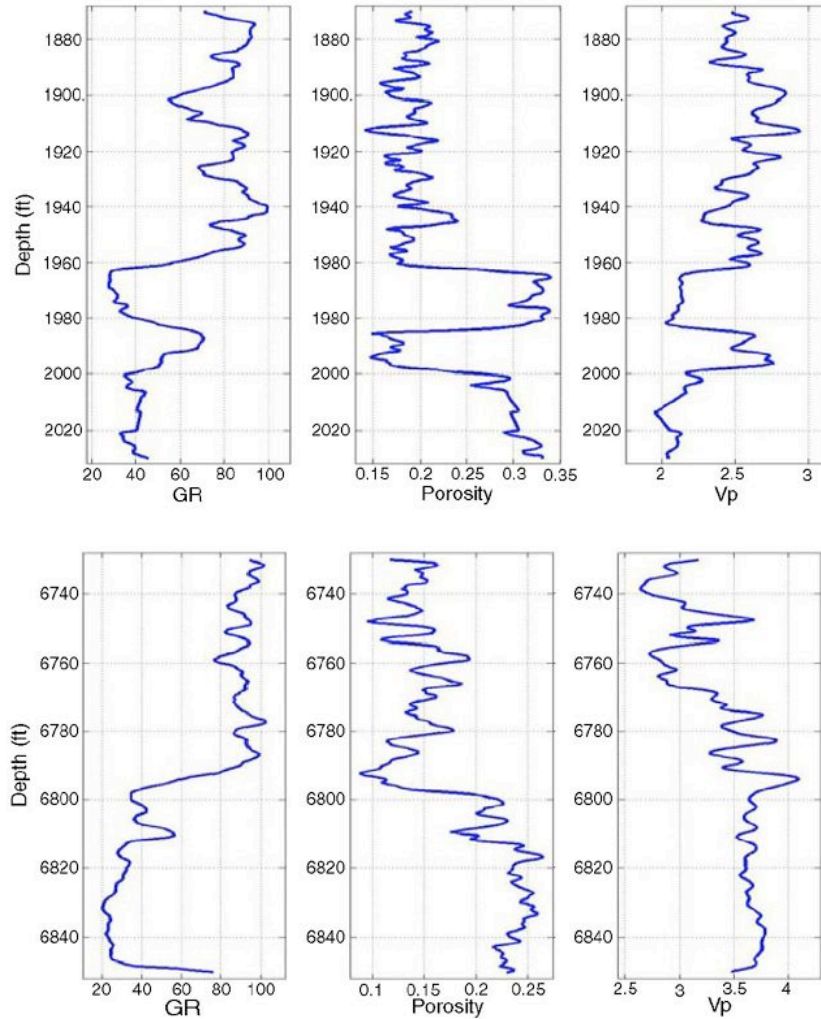


Figure A-21. Log signature of fining-upward sequences with dispersed sand-clay mixtures, at different burial depths. Well Apiay-1, Llanos Basin (Colombia).

Although the patterns observed follow exactly the predictions from the Marion-Yin model, the actual mechanisms reducing porosity and increasing elastic stiffness may not be the same. Yin's laboratory studies induced an elastic deformation in the samples, and the increase in elastic stiffness was mainly associated with the effect of confining pressure. Although confining pressure definitely plays a role in increasing stiffness, the porosity reduction mechanism operating in nature is not necessarily elastic deformation. Incipient cementation or pressure-solution processes can induce similar changes in

porosity and stiffness (see Chapter 3). Following the analysis presented in Chapter 3, the fact that these sandstones are about 2000 ft above the threshold temperature for quartz cementation suggests that pressure solution, an inelastic deformation mechanism, is probably the dominant process in this case.

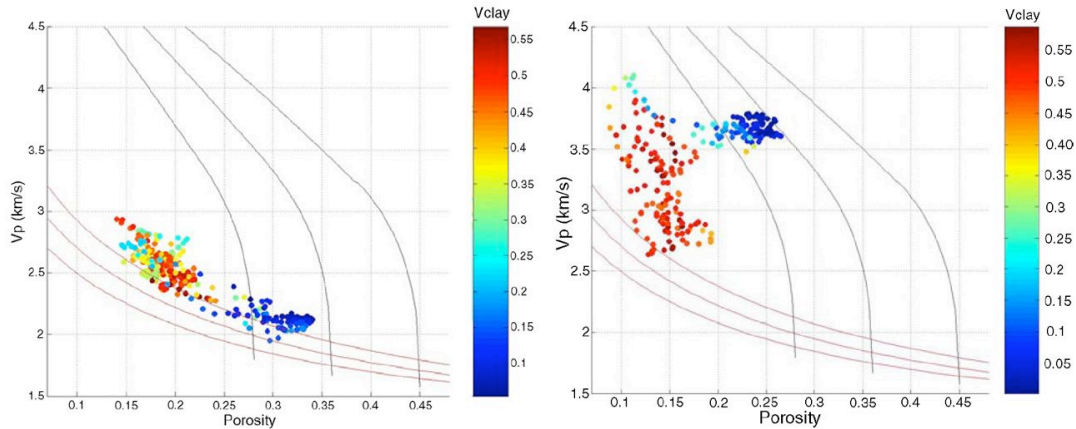


Figure A-22. Flat (left) and inverted-V (right) patterns of the shallow and deep, respectively, lithofacies sequences shown in Figure A-21.. Well Apiay-1, Llanos Basin, Colombia.

### Preferential Diagenesis

It is generally accepted that quartz cementation is the main porosity-reduction mechanism in intermediate to low-porosity quartzose sands (Paxton *et al.*, 2002). The alternative mechanism is compaction enhanced by pressure solution, which although likely, is less common in quartzarenites. Quartz cementation occurs preferentially in clean sands, rather than dirty sands, because clean sands have higher permeability (Jizba, 1991), and have larger surface area for quartz precipitation (e.g. Walderhaug, 1994). Jizba (1991) postulated that the inverted-V pattern of dispersed sand-clay mixtures would be modified by this differential cementation in low-porosity quartzose sands. According to her model, cementation will reduce porosity and increase stiffness in the clean lithofacies, without altering the properties of the shale and mixed lithofacies (Jizba, 1991).

Figure A-23 shows the gamma-ray signature and rock-physics patterns of deltaic deposits from the Upper Cretaceous of the Llanos Basin (well La Punta-1). These deltaic deposits contain two types of graded parasequences: 1) deltaic channels, with a fining upward trend similar to that of meandering fluvial channels; and 2) distributary mouth bars (DMB), characterized by a coarsening-upward trend. The depositional sequence shown corresponds to the basal transgressive systems tract that pre-dates the major

Turonian-Coniacian transgressions in this basin. From base to top, the depositional sequence consists of: (1) a basal transgressive sandstone (BTS) on top of the Paleozoic, (2) two coarsening-upward parasequences interpreted as prograding distributary mouth bars, (3) two fining-upward trends interpret as deltaic channels, and (4) a marine flooding event on top of the sequence.

The pattern that the complete sequence presents in the velocity-porosity plane is puzzling. Since the sequence is composed of fining-upward and coarsening-upward trends, we should expect an inverted V. However, the pattern looks more like an L, with two types of clean-sandstone end-members. To understand this pattern we have split the sequence into its smaller components, the channel and the DMB parasequences.

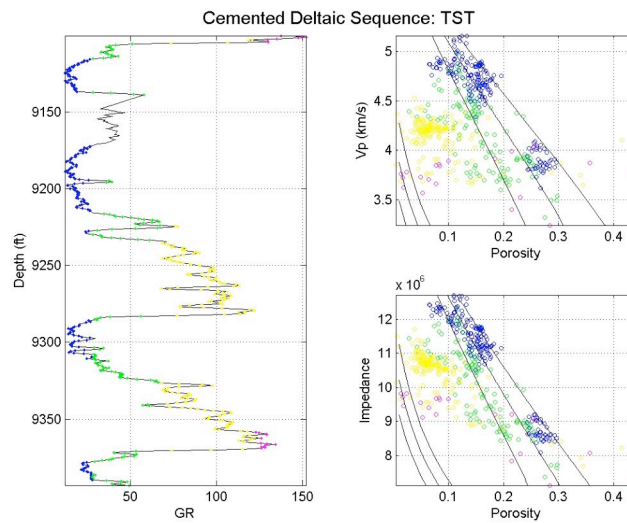


Figure A-23. A complete prograding deltaic sequence from the Cretaceous of the Llanos Basin. The color code indicates lithofacies: blue is sand, green is shaly sand, yellow corresponds to sandy or silty shale, and magenta to clay-rich shale.

There is a huge contrast in rock properties between the lower and upper sandstones (Figure A-24). The data from the shaly intervals have been discarded due to wellbore geometry; therefore we are left with the sandstone intervals. The difference in porosity between these two clean sands ranges from 10% to 15%. The fact that, in the  $V_p$ - $\phi$  and Impedance- $\phi$  planes, the data from the sandstones align along the predicted diagenetic trend for quartzarenites (Hashin-Strickman upper bound) suggests that the cause of this difference in porosity is the amount of cement, and actually that the cement is very likely quartz. An alternative explanation is compaction induced by pressure solution; however this mechanism is not likely to predominate in a low-strain domain like the Llanos basin. Core samples or other detailed data were not available, therefore the presence of calcite

cementation cannot be ruled out. However, quartz cementation appears to be the most reasonable explanation for the difference in elastic properties and porosity of these sands.

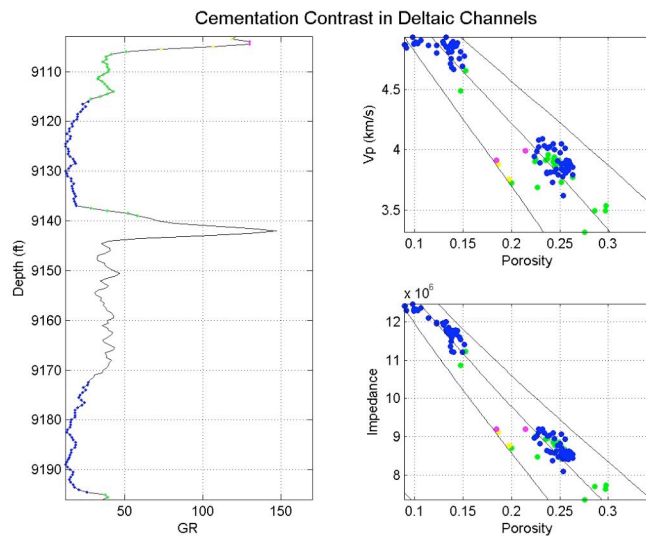


Figure A-24. Contrast in porosity and velocity between the clean quartzarenites of the deltaic channels. This contrast is considered to be the result of a significant difference in quartz cementation that occurs within less than 100' of burial-depth separation. The sandstones are part of the same stratigraphic sequence.

The pattern of the two DMB parasequences departs from the inverted-V expected for dispersed mixtures, or the linear trend observed in laminar mixtures (Figure A-25). The observed departure from the inverted-V pattern follows a trend previously modeled by Jizba (1991). Velocities and porosities in the DMB clean sandstones are similar to those of the sandstone in the lower deltaic-channel. On the other hand, although there is scatter in the data, the mixed lithofacies show gradual transitions from either the higher porosity or the lower porosity clean sandstones (Figure A.23) to the compacted clay-rich shale (magenta). This indicates that the mechanism driving diagenesis affects the clean sandstones and some of the shaly sandstones, leaving the low-permeability facies intact. Consequently, the pre-existing pattern, which probably was similar to an inverted V, has been modified. The velocity-porosity pattern that these parasequences of DMB deposits show follows exactly the one predicted by Jizba (1991), explained as the result of preferential cementation of the clean sands.

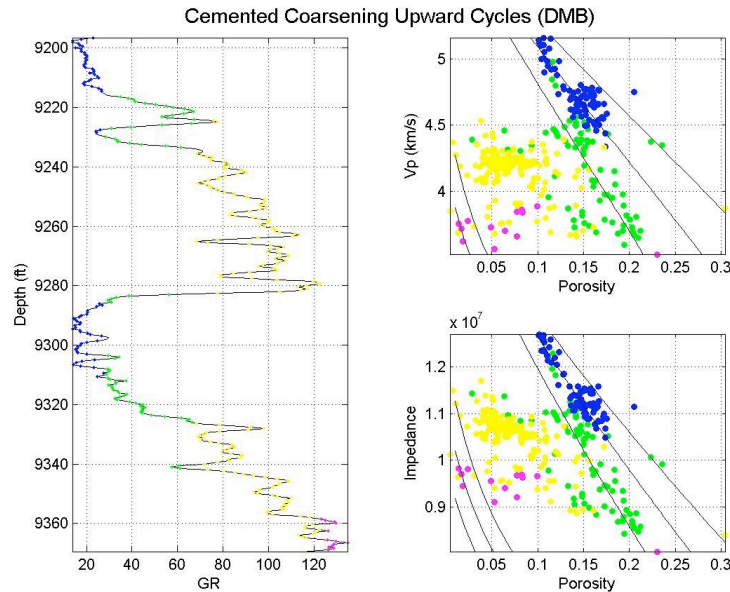


Figure A-25. Coarsening upward parasequences corresponding to distributary mouth bar deposits (DMB), and their pattern in the velocity-porosity and impedance-porosity plane. The upward shift of the clean sandstone (blue), and some of the shaly sandstones (green) is interpreted to be the result of quartz cementation.

## Discussion

The results presented in this study show that the existing rock-physics models predict the variations in elastic and hydraulic properties associated with the textural trends in clastic depositional sequences. The models, based on laboratory and theoretical analysis, can reproduce the patterns of clastic depositional sequences in the rock-physics planes, based on well-log measurements. Mineral composition, sorting and the type of mixture are the main depositional lithofacies influencing the observed patterns. Cementation, compaction, pressure solution, and confining pressure are the dominant factors influencing the variations associated with diagenesis.

The variations observed among depositional sequences from diverse environments result from the intrinsic relationship that exists between textural trends, or lithofacies successions, and the flow regimes and conditions of sedimentation for each particular setting. These variations are produced by the presence, or absence, of mixed lithofacies and their specific fabrics. In general, ignoring the effect of mixed lithofacies and assuming that seismic reflections come from simple sand and shale interfaces can lead to erroneous interpretations.

## References

- Ager, D., 1993, *The Nature of The Stratigraphic Record*, third edition, John Wiley & Sons, New York.
- Aguilera, R. C. and E. López, 1995, *Tectosedimentología de las Formaciones León y Guayabo, Región del Piedemonte Llanero*, B. Sc. Thesis, Departamento de Geociencias, Universidad Nacional de Colombia.
- Allen, J. R. L., 2001, *Principles of Physical Sedimentology*, George Allen & Unwin (Publishers), London, 272 p.
- Avseth, P., 2000, *Combining Rock Physics and Sedimentology for Seismic Reservoir Characterization in North Sea Turbidite Systems*, Ph. D. thesis, Stanford University.
- Avseth, P., J. Dvorkin, G. Mavko, and J. Rykkje, 2000, Rock physics diagnostic of North Sea sands: Link between microstructure and seismic properties. *Geophysical Research Letters*, vol. 27, no. 17 p. 2671-2764.
- Beaubouef, R. T., 2004, Deep-water leveed-channel complexes of the Cerro Toro Formation, Upper Cretaceous, Chile, *American Association of Petroleum Geologists Bulletin*, **88**, 1471-1500.
- Bachrach, R., 1998, *High-resolution Shallow Seismic Subsurface Characterization*, Ph. D. thesis, Stanford University.
- Backus, G. E., 1962, Long-wave elastic anisotropy produced by horizontal layering, *Journal of Geophysical Research*, **67**, 4427-4440.
- Brown, A., 2003, *Interpretation of Three-dimensional Seismic Data*, fourth edition, American Association of Petroleum Geologist Memoirs, **42**.
- Cardona, P., and G. Gutierrez, 1995, *Estratigrafía y Ambientes de Deposito de La Formacion Carbonera al Noroeste de Yopal-Casanare (Colombia)*, B. Sc. Thesis, Departamento de Geociencias, Universidad Nacional de Colombia.
- Cooper, M. A., F. T. Addison, R. Alvarez, M. Coral, R. H. Graham, A. B. Hayward, S. Howe, J. Martinez, J. Naar, R. Peñas, A. J. Pulham, and A. Taborda, 1995, Basin Development and Tectonic History of the Llanos Basin, Eastern Cordillera and Middle Magdalena Valley, Colombia. *American Association of Petroleum Geologists Bulletin*, v. 79 No. 10, pp 1421-1443.
- Dvorkin, J., A. Nur, and H. Yin, 1994, Effective properties of cemented granular materials, *Mechanics of Materials*, 18, 351-366.
- Dvorkin, J., and A. Nur, 1996, Elasticity of high-porosity sandstones: Theory for two North Sea datasets, *Geophysics*, 61, 1363-1370.

- Dvorkin, J., and M. A. Gutierrez, 2001, Textural sorting effect on elastic velocities, part II: elasticity of a bimodal grain mixture, Society of Exploration Geophysicist Annual Meeting, Expanded Abstracts.
- Dvorkin, J., M. Gutierrez and A. Nur, 2002, On the universality of diagenetic trends, *The Leading Edge*, **21**, 40-43.
- Emery, D. and K. Myers, 1996, *Sequence Stratigraphy*, Blackwell Science, Oxford, 279 pp.
- Estes, C.A., G. Mavko, H. H. Yin, and T. Cadoret, 1994, Measurements of velocity, porosity and permeability on unconsolidated granular materials Stanford Rock Physics and Borehole Geophysics Project, annual report, 55, p. G1-G9.
- Fuchtbauer, H., 1974, Sediments and Sedimentary Rocks 1, in *Sedimentary Petrology* by W. V. Engelhard, H. Fuchtbauer and G. Muller, Part II. John Wiley and Sons, New York, 464 pp.
- Galloway, W. E., 1989, Genetic stratigraphic sequences in basin analysis I: architecture and genesis of flooding-surface bounded depositional units. *American Association of Petroleum Geologists Bulletin*, **73**, 143-154.
- Galloway, W., and D. Hobday, 1996, *Terrigenous Clastic Depositional Systems*, Springer Verlag, New York, 489 pp.
- Gutierrez, M., 2001, *Rock Physics and 3D Seismic Characterization of Reservoir Heterogeneities to Improve Recovery Efficiency*, Ph. D. thesis, Stanford University.
- Gutierrez, M., J. Dvorkin and A. Nur, 2001, Stratigraphy-guided rock-physics reservoir characterization, AAPG Meeting 2001, Expanded Abstracts.
- Han, D., 1986, *Effects of Porosity and Clay Content on Acoustic Properties of Sandstones and Unconsolidated Sediments*, Ph. D. thesis, Stanford University.
- Hashin, A., and Shtrikman, S., 1963, A variational approach to the elastic behavior of multiphase materials, *Journal of the Mechanics and Physics of Solids*, **11**, 127-140.
- Howard, J. D., and H. E., Reineck, 1972, Georgia coastal region, Sapelo Island, USA, sedimentology and biology IV, physical and biogenic sedimentary structures of the nearshore shelf, *Senckenbergiana Maritime*, **4**, 81-123.
- Jizba, D., 1991, *Mechanical and Acoustical Properties of Sandstones and Shale*, Ph. D. Thesis, Stanford University.
- Marion, D., 1990, *Acoustical, Mechanical and Transport Properties of Sediments and Granular Materials*, Ph. D. Thesis, Stanford University.
- Marion, D., Nur, A., Yin, H., and Han, D., 1992, Compressional velocity and porosity in sand-clay mixtures, *Geophysics*, **57**, 554-563.
- Mavko, G., T. Mukerji and J. Dvorkin, 1998, *The Rock Physics Handbook, Tools for Seismic Analysis in Porous Media*, Cambridge University press, New York, 329 pp.
- Miall, A. D., 1997, *The Geology of Stratigraphic Sequences*, Springer Verlag, New York, 433 pp.

- Mindlin, R. D., 1949, Compliance of elastic bodies in contact, *Journal of Applied Mechanics*, **16**, 259-268.
- Mitchum R. M. Jr., P. Vail, and J. B. Sangree, 1977, Seismic stratigraphy and global changes of sea level, Part 6: Stratigraphic interpretation of seismic reflection patterns in depositional sequences. In: Payton, C. E., ed., *Seismic Stratigraphy –Applications to Exploration*, American Association of Petroleum Geologists Memoirs, **26**, 117-133.
- Murphy, W. F., III, 1982, Effects of Microstructure and Pore Fluids on the Acoustic Properties of Granular Sedimentary Materials, Ph.D. dissertation, Stanford University.
- Paxton, S. T., J. O. Szabo, J. M. Ajdukiewicz, and R. E. Klimentidis, 2002, Construction of an intergranular volume compaction curve for evaluating and prediction compaction and porosity loss in rigid-grain sandstone reservoirs, *American Association of Petroleum Geologists Bulletin*, **86**, 2047-2067.
- Reading, H. G., 1980, *Sedimentary Environments and Facies*, Elsevier, New York, 557 pp.
- Reineck, H. E., and I. B. Singh, 1980, *Depositional Sedimentary Environments*, 2<sup>nd</sup> edition, Springer-Verlag, New York, 549 pp.
- Smith, D., 1987, Point bar lithofacies models, In: Ethridge, F., R. M. Flores, and M., Harvey: *Recent Developments in Fluvial Sedimentology*, Society of Economic Paleontologists and Mineralogists, **39**, 83-91.
- Sylvester, Z., and D. Lowe, 2004, Textural trends in turbidites and slurry beds from the Oligocene flysch of the East Carpatians, Romania; *Sedimentology*, **51**, 1-26.
- Teichert, C., 1958, Concept of facies, *American Association of Petroleum Geologists Bulletin*, **42**, 2718-2744.
- Thomas, E. C., Stieber, S.J., 1975, The distribution of shale in sandstones and its effect on porosity, *Transactions of the SPWLA Annual Logging Symposium*, **16**, 1-14.
- Timoshenko, S. P., and J. N. Goodier, 1970, *Theory of Elasticity*, 3<sup>rd</sup> edition, McGraw-Hill, New York, 567 pp.
- Tosaya, C., and A. Nur, 1982, Effects of diagenesis and clays on compressional velocities in rocks, *Geophysics Research Letters*, v. 9, p. 5-8.
- Van Wagoner, J. C., R. M. Mitchum, K. M. Campion and V. D. Rahmanian, 1990, Siliciclastic sequence stratigraphy in well logs, cores and outcrops, *American Association of Petroleum Geologists, Methods in Exploration Series 7*, 55.
- Walderhaug, O., 1994, Temperatures of quartz cementation in Jurassic sandstones from the Norwegian continental shelf –evidence from fluid inclusions: *Journal of Sedimentary Research A*, **64**, 311-323.
- Walker, R. G., 1984, *Facies Models*, 2<sup>nd</sup>, ed., Geoscience Canada Reprint Series 1.
- Wang, Z., 2001, Fundamentals of seismic rock physics, *Geophysics*, **66**, 398-412.

- Yin, H., 1992, Acoustic Velocity and Attenuation of Rocks: Isotropy, Intrinsic Anisotropy, and Stress-Induced Anisotropy, Ph. D. thesis, Stanford University.
- Zimmer, M., 2003, Controls on the Seismic Velocities of Unconsolidated Sands: Measurements of Pressure, Porosity and Compaction Effects, Ph. D. dissertation, Stanford University.

## **ATTACHMENT B**

### **Reservoir Quality Prediction by Integrating Sequence Stratigraphy and Rock Physics**

#### **Summary**

We present a methodology to improve the prediction of reservoir quality by combining principles of sequence stratigraphy and rock physics. The purpose of this study is to demonstrate how we can obtain critical sedimentological parameters and relative trends of their spatial variation from sequence stratigraphic interpretation. In turn, these sedimentological parameters can serve as constraints in rock physics modeling thereby reducing uncertainty in predicting reservoir properties from seismic amplitude.

#### **Introduction**

Sequence stratigraphy is the correct geologic interpretation of process/response events (Mulholland, 1998). This can predict the likely occurrence of reservoir facies, source rocks and seals. Traditional stratigraphic interpretation from post-stack seismic data has been predominantly qualitative based on visual inspection of geometric patterns in the seismic reflections. However, quantitative interpretation of seismic amplitude is possible if we can extract information about compositional maturity (mineralogy, clay content) and textural maturity (sorting, grain angularity, sphericity and roundedness) using principles of sedimentology.

Quantitative seismic interpretation (Avseth et al., 2005) uses rock physics to link seismic amplitude with reservoir properties, like, porosity, clay-content, sorting, diagenetic cements etc. However, one of the major sources of uncertainty in rock physics modeling arises due to our lack of knowledge about input parameters. This uncertainty can be reduced by constraining input parameters (for example, compositional maturity and textural maturity) as guided by sequence stratigraphic framework. Future developments of reservoir property prediction from seismic amplitude should benefit from close coupling between sequence stratigraphy and rock physics.

## Development of Concept and Methodology

How can we obtain critical sediment parameters (and their spatial variation) from sequence stratigraphic interpretation and link them to seismic signatures? In the following section we outline the three main steps in our conceptual methodology. The next section applied these steps to a dataset from the Campos Basin. A workflow with the key steps is shown in Figure B-1.

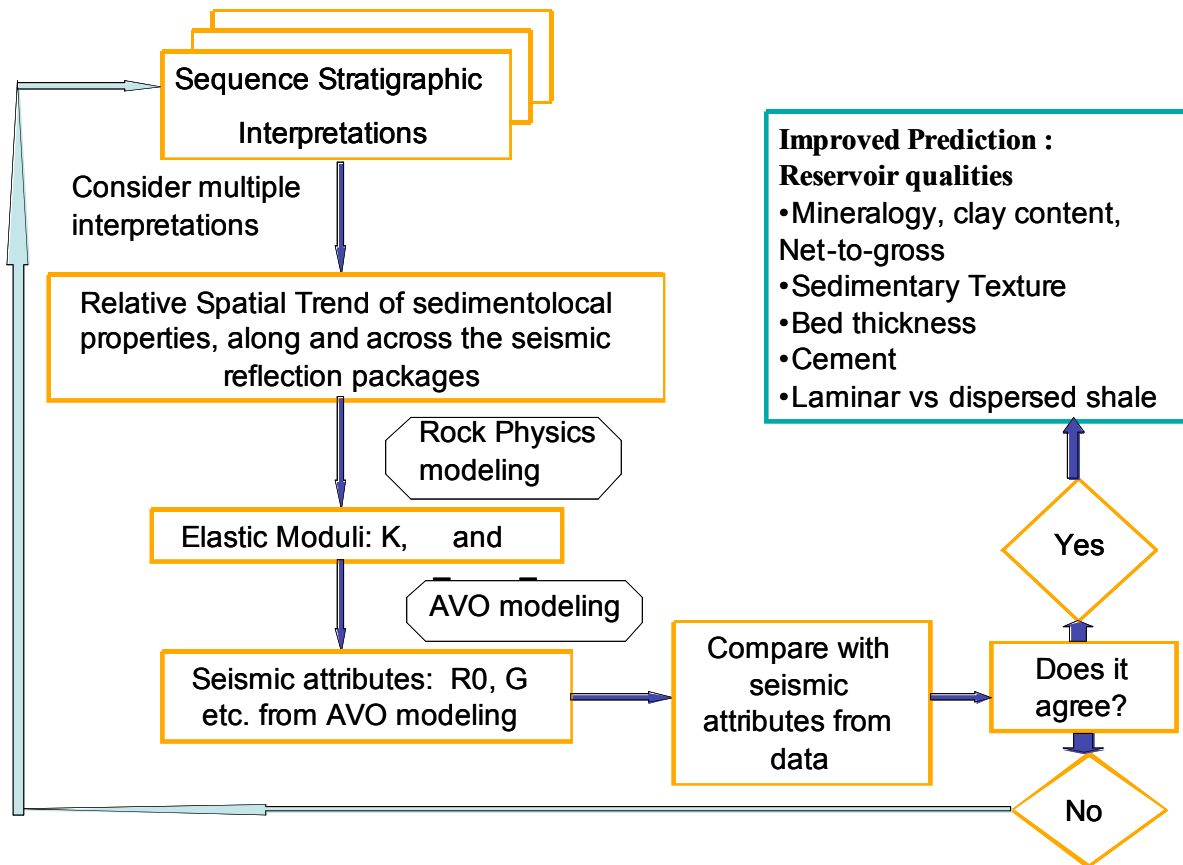


Figure B-1. Workflow for integrating sequence stratigraphy and seismic, using rock physics models.

### **Step-1A: Understanding the systematic change of sedimentological properties with depositional cycles in a predictable fashion**

Wagoner et al. (1990) showed that the following sedimentological properties change predictably during transgression and regression:

- Sand-shale ratio
- Bed Thickness
- Grain-size
- Sorting
- Bio-turbation

Interestingly the changes in these sediment properties have opposite trends for transgression (shore line is approaching towards land) vs. regression (shore line is retreating towards basin). However there is uncertainty in these trends. During regression depositional energy tend to increase upward resulting in increase in bed-thickness, higher net-to-gross, better sorting and decrease in bio-turbation. On the other hand, marine transgression signifies decrease in depositional energy and exhibits an opposite trend of the above sediment parameters. These sediment parameters can be grouped as, compositional maturity and textural maturity parameters. They constitute important sediment properties that affect the elastic properties of the rocks and in turn affect seismic amplitudes.

### **Step-1B: Understanding spatial gradients of sedimentological properties**

Gradients of sediment parameters are not same across the seismic reflector vs. along the reflector. Most seismic reflectors and their amplitudes correspond to chronostratigraphic surfaces with a few exceptions. Chronostratigraphic surfaces represent depositional hiatus. Changes in sedimentological properties are abrupt across the hiatus and gradual along the hiatus (Emery and Myers, 1996).

The spatial gradients can be calibrated from well data. Estimating the lateral trends requires multiple wells or horizontal wells. In the absence of such data one might assume that sediment parameters change linearly along the seismic reflector and in discrete steps across the reflector. Thus, using sequence stratigraphy, we obtain relative trends of variation in sediment properties within a depositional sequence. These trends then constrain the input parameters in rock physics modeling.

## **Step-2: Rock physics analysis**

Rock physics establishes the relation between sedimentological properties and elastic moduli. After we determine the spatial trends of sediment parameters in a stratigraphic package, appropriate rock physics models are selected. The input parameters are guided by our results from step 1. The rock models are calibrated to well log data. As output we obtain effective bulk modulus, shear modulus and density, as well as  $V_p$  and  $V_s$  as a function of porosity.

## **Step-3: AVO modeling and interpreting seismic amplitude**

AVO forward modeling (Shuey's approximation) is used to obtain intercept and gradient at key stratigraphic interfaces using effective moduli predicted from rock physics analysis in step 2. Trends in compositional and textural maturity are carried through from sequence stratigraphy, to the AVO plane, via rock physics. Finally, the modeling results can be used to interpret observed amplitudes in terms of sedimentological properties and reservoir quality.

## **Example from Campos Basin, Offshore Brazil**

We have applied this concept in a deep-water turbidite system from Campos Basin, offshore Brazil. Sequence stratigraphic principles are less well-understood in deep water depositional system (Emery and Myers, 1996). Rock physics modeling can be useful tool to aid stratigraphic interpretations in deep-water systems. The facies package was deposited during low stand system tract (LST). Our interpretation was based on (a) basin history (Peres, 1990) (b) geometry and truncation patterns of reflectors (Figure B-2) and (c) stacking patterns of well logs (Figure B-3). The most likely depositional environment is submarine fan system.

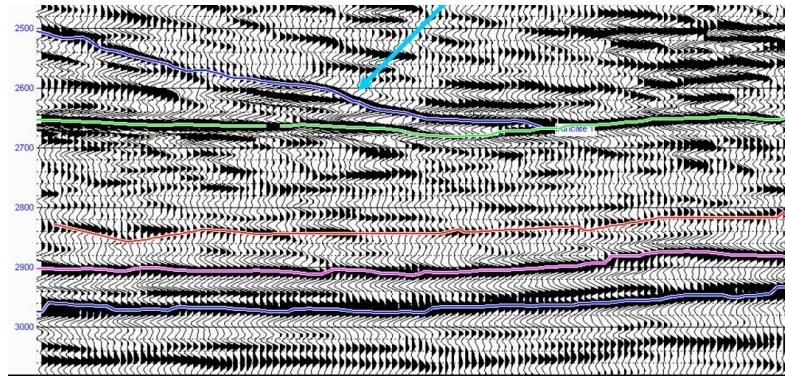


Figure B-2: The blue arrow indicates sub-marine fan system.

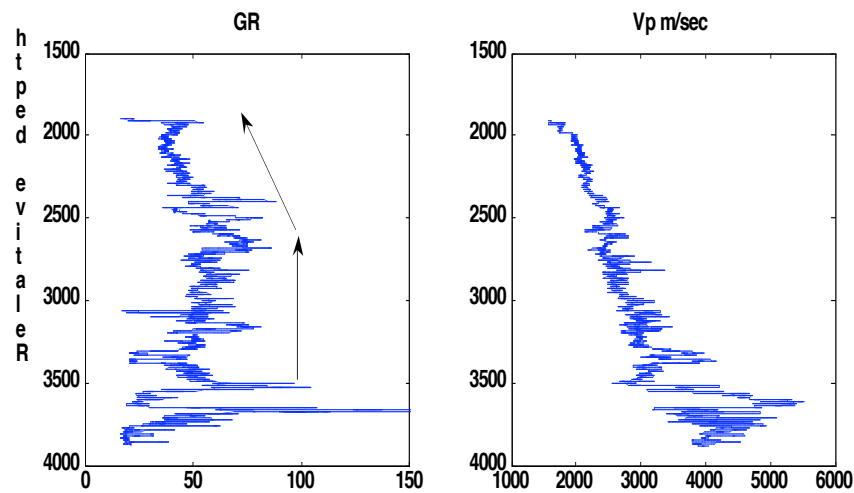


Figure B-3: In well log blocky motif corresponds to aggradational / channel deposits and coarsening-up motif corresponds to progradational depositional lobes.

We considered three para-sequences (PS) within the prograding depositional lobes (Figure B-4) and used sequence stratigraphic principles to obtain relative trend of sorting, an important parameter that controls porosity, elastic moduli, and hence seismic velocities. We create sorting trends as follows:

1. Sequence stratigraphic model from deep water prograding depositional lobes indicate that sorting increases vertically upward. Therefore we select lower PS to be poorly sorted, middle PS moderately sorted and the upper one is well sorted.
2. Laterally sorting improves linearly basin-ward within each para-sequence (Figure 4). Thin-section or core data available at any para-sequence could have verified or modified these sorting trends.

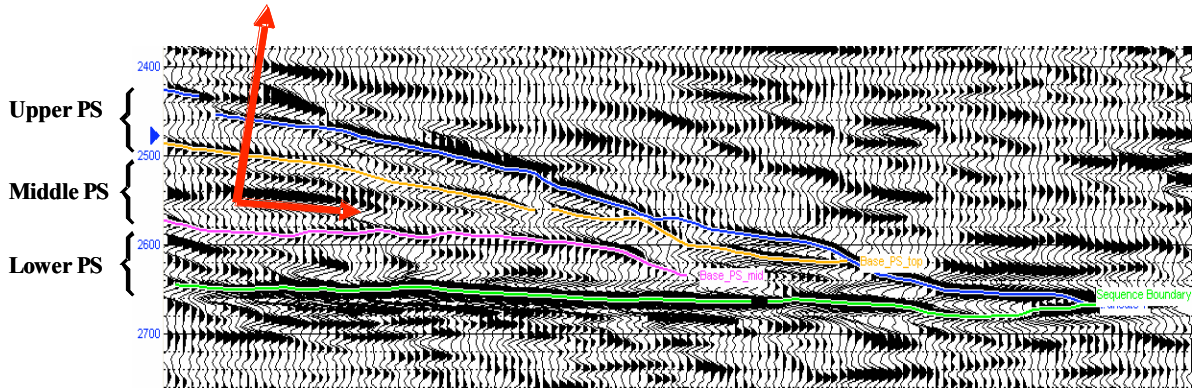


Figure B-4: Three parasequences (PS) interpreted within progradational depositional lobes. Changes in sorting is abrupt across the para-sequence boundaries and gradual along the boundaries.

We used experimental sorting-porosity relationship for artificially mixed sand (Beard and Weyl, 1973; Jordan and Campbell, 1984). Figure B-5 shows range of porosities for different sorting and various sandstone grain-sizes. Sorting is expressed in terms of the standard deviation of the distribution of the logarithm of the grain size. A plausible porosity section is shown in Figure B-6.

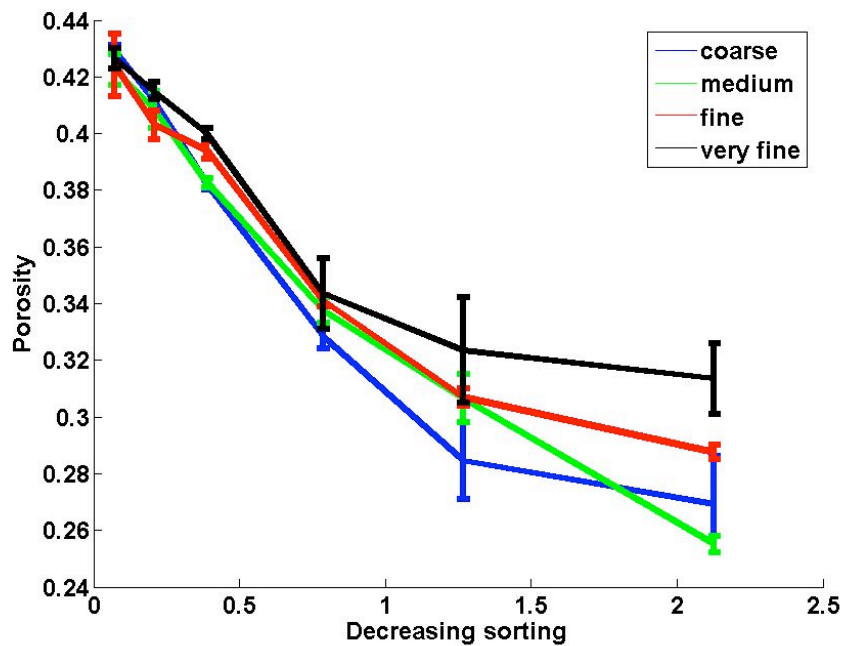


Figure B-5: Porosity decreases with deteriorating sorting. Different curves represent different grain sizes in sandstone (Beard and Weyl, 1973; Jordan and Campbell, 1984).

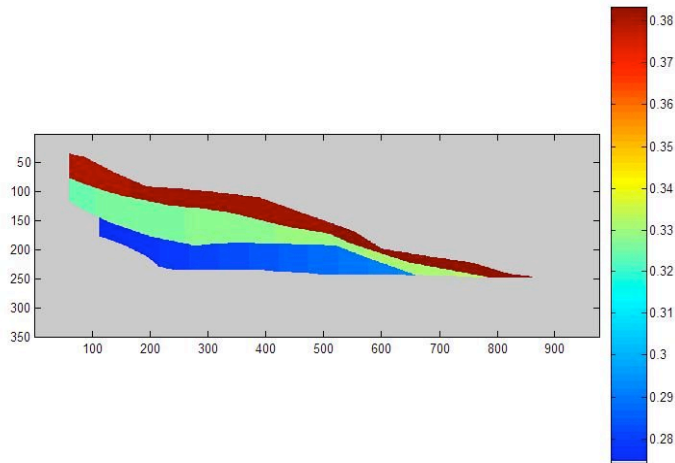


Figure B-6: Porosity section obtained using sorting-porosity relationship for artificially mixed sand.

The sandstones in submarine fans are compositionally immature. Therefore we used the unconsolidated sand model (Dvorkin and Nur, 1996; Mavko et al., 1998) with 80% quartz, 20 % feldspar and 10 % clay. A relatively lower quartz/ feldspar ratio indicates compositional immaturity. The unconsolidated sand model is used to compute elastic moduli of both well sorted and poorly sorted sands. Sorting deteriorates from the well sorted end member as additional smaller grains fill the pore space. This increases the number of grain contacts and contact stiffness. The effective moduli at the well sorted, high porosity end member (~40%) are computed using Hertz-Mindlin (Mindlin, 1949) theory assuming coordination number (average number of grain contacts) of 6. Moduli of poorly sorted sand with porosities between 0 to critical porosity (~40%) are interpolated between mineral point and well-sorted end member using the lower Hashin-Shtrikman bound.

Figure B-7 shows porosities and velocities obtained from a neighboring well log and the predicted velocities using the unconsolidated sand model as described above. The  $V_p$  from well log is in good agreement with the model prediction. However the prediction for  $V_s$  is not good. To model spatial variation of effective moduli the porosity section from sequence stratigraphic interpretation is used as input to the calibrated rock model.

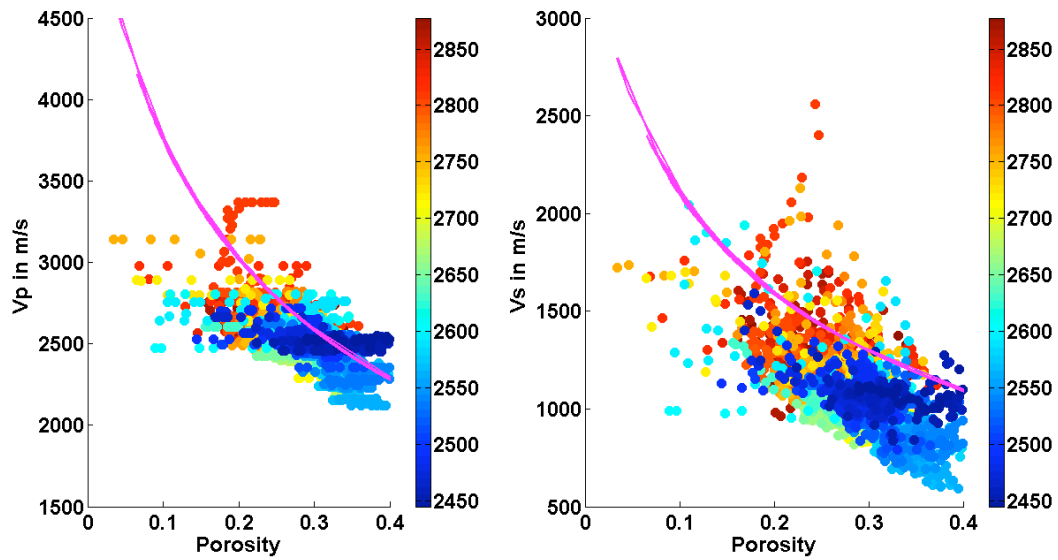


Figure B-7: The scatter points show measurements of porosities and velocities from well log in prograding lobes. The magenta line is obtained using rock physics modeling for unconsolidated sand.

The effective  $V_p$ ,  $V_s$ , and density are used to compute intercept ( $R_0$ ) and gradient ( $G$ ) at the interfaces of the three para-sequences. They indicate distinct trends in  $R_0$ - $G$  plane (Figure B-8). These trends can be used as a template to guide the interpretation of observed intercept and gradient from real seismic data. Since these trends incorporate the information from sequence stratigraphy, they can be used to predict the spatial variation in reservoir properties. But more than the qualitative trends, we can now make quantitative interpretations about porosity and sorting based on the calibrated rock model.

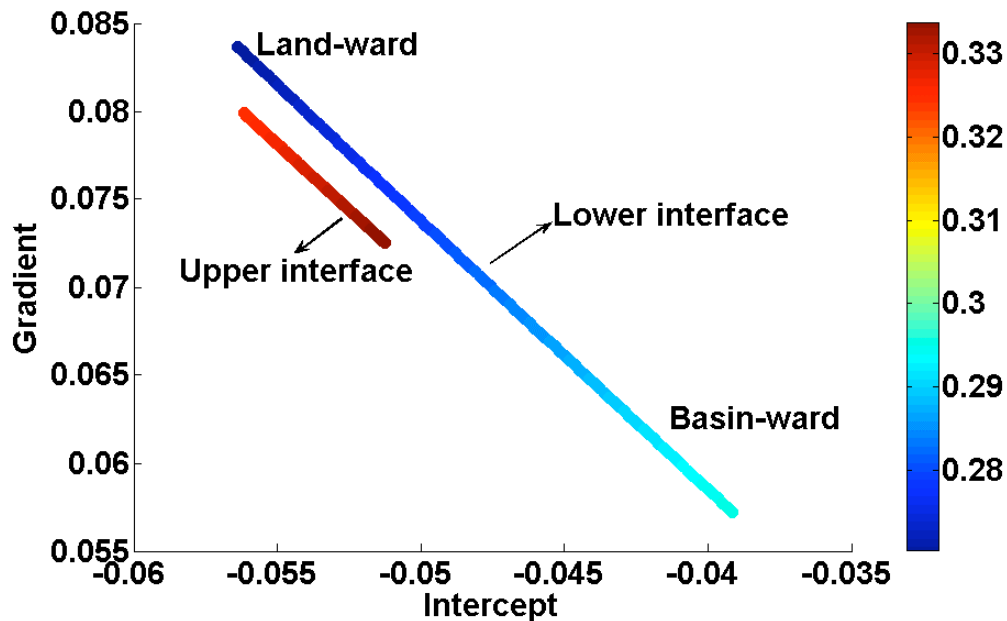


Figure B-8: AVO modeling results: Intercept and Gradient crossplot color-coded by porosity. They indicate distinct trend of variation in reservoir properties from landward to basin-ward.

In summary, we have developed a method to obtain spatial trends of sedimentological parameters from sequence stratigraphic interpretations. These trends are relative in a stratigraphic sequence. We have determined trends of grain-sorting in prograding lobes of submarine fan in Campos basin, Brazil using this method. However there is uncertainty in our interpretations since sequence stratigraphic principles are not very robust in deep water turbidite system. A further development to this workflow will be to consider multiple interpretations.

Rock physics modeling was constrained using trends of grain sorting as guided by sequence stratigraphic interpretations. In addition, the sands in submarine fan are compositionally less matured. Therefore the mineralogy was constrained by higher feldspar content.

The effective moduli computed from rock physics modeling were used to generate AVO attributes at two para-sequence boundaries. In R0-G plane we get linear trend of variation in sediment properties from landward to basin-ward. The trend indicates the mean of probability distribution of sedimentological properties and the variability will add scatter around this trend. Textural maturity progressively increases along this trend basin-ward. Furthermore since these trends are calibrated with the rock physics model it is possible to make quantitative interpretations about porosity and sorting. For example porosity progressively changes from ~31% to ~33% and ~27% to ~30% along upper and

lower interfaces respectively. The direct advantage of integrating sequence stratigraphy and rock physics is that seismic attributes (eg. intercept, gradient etc.) can be interpreted in terms of underlying sedimentological properties.

## References

- Avseth, P., Mukerji, T., and Mavko, G., 2005, Quantitative Seismic Interpretation: Applying Rock Physics Tools to Reduce Interpretation Risk: Cambridge University Press.
- Beard, D. C., and Weyl, P. K., 1973, Influence of texture on porosity and permeability of unconsolidated sand: American Association of Petroleum Geologists Bulletin, 57, 349-369.
- Dvorkin, J., and Nur, A., 1996, Elasticity of high-porosity sandstones: Theory for two North Sea datasets: Geophysics, 61, 1363-1370.
- Emery, D., and Myers, K., 1996, Sequence stratigraphy: Blackwell scientific publications, Inc.
- Jorden, J. R., and Campbell, F. L., 1984, Well Logging I - rock properties, borehole environment, mud and temperature logging: Society of Petroleum Engineers (SPE) of American Institute of Mining, Metallurgical and Petroleum Engineers (AIME).
- Mavko, G., Mukerji, T., and Dvorkin, J., 1998, The Rock Physics Handbook, tools for seismic analysis in porous media: Cambridge University press.
- Mindlin, RD, 1949, Compliance of elastic bodies in contact: ASME Journal of Applied Mechanics, 71, A-259 -268.
- Mulholland, J.W., 1998, Sequence stratigraphy: basic elements, concepts and terminology: The Leading Edge, 17, 37-40.
- Peres, W.E., 1990, Seismic-stratigraphic study of the Oligocene-Miocene shelf-fed turbidite systems of the Campos Basin, Brazil: Ph.D. thesis, The University of Texas at Austin.
- Stovas, A., Landrø, M., and Avseth, P., 2004, Estimation of net-to-gross and fluid saturation in a fine-layered sand-shale sequence – tested on offshore Brazil data: Society of Exploration Geophysicists International Exposition and 74th Annual Meeting, Expanded Abstracts, 228-231.
- Wagoner, J.C.Van., Mitchum, R.M., Campion, K.M., and Rahmanian, V.D., 1990, Siliciclastic sequence stratigraphy in well logs, cores and outcrops: The American Association of Petroleum Geologists, Methods in Exploration Series, no. 7.

## ATTACHMENT C

### Sorting and Packing Effects on the Elastic Properties of Sands

#### Abstract

This section analyzes the effects of grain-size distribution (sorting) and packing on the porosity and elastic properties of granular materials, and how their effects differ. The effective medium contact theory for random packings of granular aggregates is used to approximate the effect of grain-size distributions. Based on that theory, an idealized model for tight (rhombohedral) packing of quinary mixtures is used to calculate the effective elastic properties of the aggregate, by performing stochastic simulations. The main source of uncertainty in these simulations comes from the coordination number. In spite of the approximations, the uncertainty in coordination number, and the limitations of using an idealized packing model, the results demonstrate that the sorting effect in the velocity-porosity plane follows a flatter trend than the modified Hashin-Shtrikman lower bound (MHSLB). In fact, the theoretical analysis demonstrates that the MHSLB should constitute an upper bound for the effect of sorting. On the contrary, the effect of packing can generate a trend with a steeper slope than the one predicted from the MHSLB. This steeper trend has been observed in laboratory studies and can be explained as the result of increasing grain-contact areas and incremental grain stabilization. Consequently, whereas the MHSLB is an approximate upper bound for the sorting effect, it should be considered a lower bound for the effect of packing. These conclusions are in agreement with results obtained from laboratory data in previous studies, and with subsurface core and well-log data.

#### The Rock-Physics Depositional Trend: Sorting or Packing?

Sandstones at similar depths or confining pressures present a relatively flat trend in the velocity-porosity plane (C-1). This flat trend results from significant changes in porosity associated with very small changes in elastic stiffness. The main porosity-reduction mechanisms related to this flat-trend are matrix (clay) content, sorting, and mechanical compaction, as shown by Marion *et al.* (1992), Avseth *et al.* (2000), Dvorkin and Gutierrez (2001), Zimmer *et al.* (2002), and Zimmer (2003). For uncemented sandstones at the same pressure conditions, sorting and clay are considered to be the dominant mechanisms affecting this velocity-porosity trend. The trend can be reproduced using the modified Hashin-Strickman lower mound (MHSLB), and has been called the

uncemented sandstone model (Mavko *et al.*, 1998), or the rock physics depositional trend (Avseth, 2000).

Grain-size distribution, or sorting, significantly affects not only the porosity (e.g. Beard and Weyl, 1973) but also the elastic properties of granular materials, as demonstrated by Estes *et al.* (1994), Avseth *et al.* (2000), Gutierrez and Dvorkin (2001), Gutierrez (2001), and Zimmer (2003). In spite of this importance, there are few experimental and theoretical studies about the effect of sorting. Dvorkin and Gutierrez (2001) present a model for binary mixtures that combines Hertz-Mindlin theory with modified Hashin-Shtrikman lower bounds to predict the elastic properties of the mixture. According to these authors, the sorting effect can be approximated using the MHSLB.

In the case of clean sand aggregates at similar pressure conditions, the uncemented trend is considered to be solely the effect of sorting (Avseth, 2000; Gutierrez, 2001). However, mathematical models of identical spheres demonstrate that a similar effect can be obtained by changing the packing of the aggregate, without increasing the confining pressure. Therefore, packing and sorting seem to have a similar effect on the velocity-porosity trend. The assumption that the uncemented trend is controlled by depositional factors (Avseth, 2000) disregards the effect of packing, which is often post-depositional. So far, there is not a physical explanation for the use of the MHSLB to model the effect of sorting. In addition to this, current rock physics models do not explain how we can distinguish between the sorting and packing effects on porosity and the elastic properties of granular aggregates.

Characterizing the effect of sorting on the elastic properties of granular materials can improve the methods to estimate and determine lithofacies and reservoir quality using sonic logs. The sorting effect can also be used to predict the variation in seismic response away from well control. Therefore, understanding the effect of sorting on the elastic properties of sands can help to assess the uncertainties associated with these predictions.

This section presents an analysis of the effects of grain-size distribution and packing on the elastic properties of granular materials, based on effective medium models. The next section discusses the measures of sorting or grain-size distribution, explains the relationships between porosity, sorting and packing, and their link to the depositional environments. After that, the following section reviews the aspects of the effective medium theories that are relevant to sorting and packing effects, and postulates some approximations to account for the presence of different grain sizes in the contact models. The succeeding section introduces an old, idealized model for quinary mixtures. This model is used in the stochastic simulation of the effect of sorting on the elastic properties,

explained in the section afterwards. The final sections show the comparison to real data, discuss the results and present the conclusions.

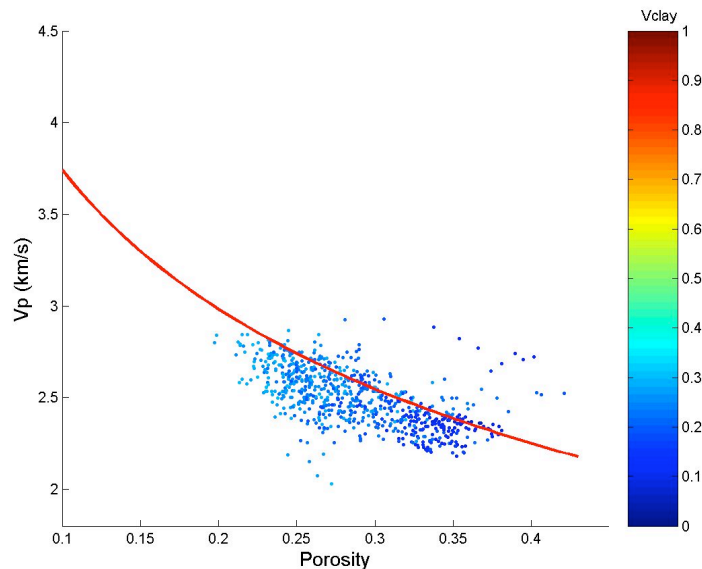


Figure C-1: The depositional trend of sands in the velocity-porosity plane. The data corresponds to uncemented sands from fluvial deposits (well Apiay-1). Data colored by clay fractio (Vclay).

### Sorting, Packing, Porosity and Depositional Lithofacies

Sorting and packing are textural properties of the sediment, initially associated with the depositional processes. Sorting, or grain-size distribution, refers to the spread of the grain-size population. The grain size by itself is a measure of the center of that population. Packing refers to the grain concentration and is closely linked to porosity. Indeed, sorting, packing and porosity are closely related. The main textural components of sandstones are: grains, pores, matrix (clay), and cement (e.g. Selley, 1988). If we incorporate the matrix within the grain-size population, sorting and packing become the two dominant factors controlling porosity, and to some extent permeability, in uncemented sands. Permeability is linked to sorting and packing because of the effect of porosity, however permeability also depends on grain size and clay content.

### Measures of Grain Size and Sorting

Grain size and sorting describe, respectively, the measures of the center and the spread of a grain population. In general, the grain size can be any measure of the population's center, either the mean, the median, or the mode, whereas sorting should be the respective measure of the population's spread, such as the standard deviation, the

interquartile range, or the maximum absolute deviation. Although the application of these definitions to unconsolidated sands should be straightforward, there is no general agreement on which statistical parameters are the most appropriate measures, as explained below.

The grain size depends on the choice of the measure of the center. The logarithmic PHI scale was proposed by Krumbein (1936), as the most convenient scale to perform statistical analysis of grain-size distributions in sediments. As shown in Equation B.1, PHI is the negative, base-2 logarithm of the grain size in millimeters ( $D$ ). The classes are defined according to Wentworth's arithmetic scale (Wentworth, 1922). This usage conforms to the fact that most of the natural grain-size populations follow a log-normal distribution function. This fact introduces the first problem regarding the actual measure of the grain size: what is the right measure of the center, the mean or the median? For example, Pettijohn (1975) pointed out that sedimentologists commonly use the mode as the measure of grain size. Given that many populations show a lognormal distribution function, the median is probably the best measure of the center.

$$PHI = -\log_2(D). \quad (B.1)$$

There is no unified measure of the spread of the grain-size distribution. Inter-percentile ranges in the PHI scale have been proposed as the most rigorous measures of sorting (Krumbein, 1938; Inman, 1956). However, the coefficient of variation (Equation B.2) is also a consistent measure of sorting. Authors proposing inter-percentile ranges have differed in the bounding percentiles: Krumbein (1936; 1938) proposed the interquartile range, which is equivalent to the sorting coefficient defined by Trask (1932); while Inman (1956), and Otto (1939), proposed the difference between the  $P_{84}$  and  $P_{16}$  percentiles. Some authors have found it convenient to normalize the inter-percentile ranges by the median (i.e. Rogers and Head, 1961). Sohn and Moreland (1968) used the coefficient of variation, defined as the standard deviation ( $\sigma$ ) normalized by the mean ( $\mu$ ) of the grain-size distribution. Both methods of normalization provide consistent measures of sorting and are approximately equivalent. However, the coefficient of variation is preferable, since the normalized inter-percentile range presents the inconvenience of a singularity around grain sizes of 1 mm. Throughout this section we use the coefficient of variation as the Sorting Index (SI):

$$SI = \frac{\sigma}{\mu}. \quad (B.2)$$

## Grain-size Distribution, Porosity and Permeability

Given a similar stage of packing, porosity of granular materials decreases as the standard deviation of the grain-size distribution increases. In other words, porosity decreases as sorting deteriorates (Figure C-2). This relationship has been demonstrated by various authors (Walton and White, 1937; Sohn and Moreland, 1968; Beard and Weyl 1973; and Zimmer, 2003). Other authors have observed a similar effect in binary mixtures (Fraser, 1935; Cumberland and Crawford, 1987), though they could not identify similar trends in multi-component mixtures. A linear trend between porosity and the sorting index can be derived from the published data (Figure C-3), which in general can be expressed as follows:

$$\phi = \phi_0 - \beta \frac{\sigma}{\mu}, \quad (\text{B.3})$$

where  $\phi_0$  is the critical porosity of the aggregate, and the slope ( $\beta$ ) has been found to vary between 0.11 and 0.19. The critical porosity, as defined by Nur *et al.* (1995), can be considered the well-sorted end member. Since porosity determines both the reservoir's final storage capacity and its permeability, grain-size distribution is therefore affecting both reservoir volumes and fluid flow in uncemented sand reservoirs. As can be observed in Figure C-4, the other property controlling permeability is the dominant grain size.

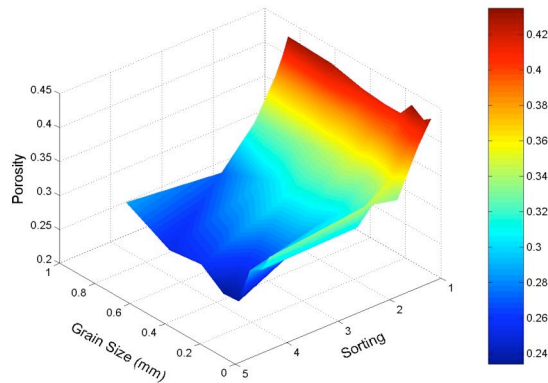
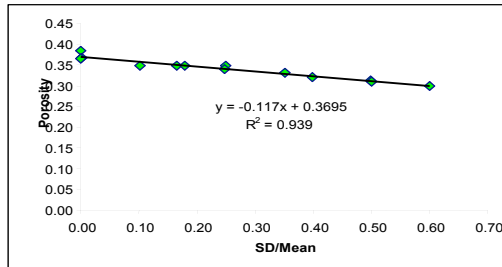
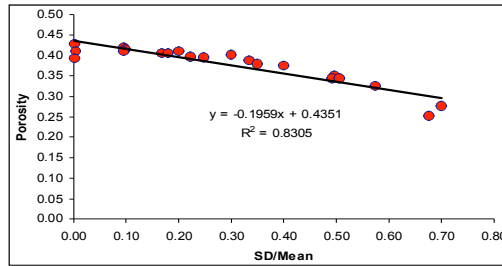


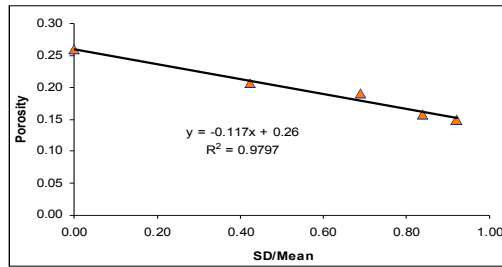
Figure C-2: Porosity of artificial sand mixtures as a function of grain size and sorting. Sorting is expressed as standard deviation. Based on data by Beard and Weyl (1973).



(a)



(b)



(c)

Figure C-3: Linear relationship between porosity and the sorting index  $\sigma/\mu$ ; (a) and (b) correspond to laboratory results published by Sohn and Moreland (1968); (c) corresponds to an idealized quinary mixture modeled by White and Walton (1937).

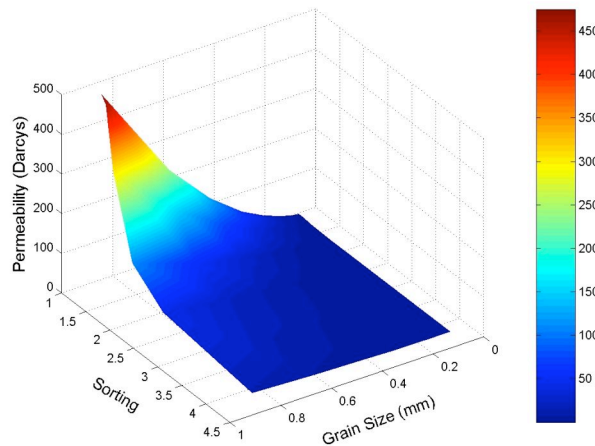


Figure C-4: Permeability of artificial sand mixtures as a function of grain size and sorting. Sorting is expressed as standard deviation. Based on data by Beard and Weyl (1973).

## Sorting and Depositional Environments

Grain-size distributions reflect provenance, sediment-transport conditions, and the depositional process (Visher, 1999). According to Visher (1969), a grain-size distribution is composed of multiple log-normal populations. These populations are combined by multiple processes of sediment transport associated with traction, saltation and suspension, the three mechanisms of sediment transport in fluidized flows (e.g. Selley, 1988).

Visher (1969) divided the cumulative distribution function (CDF) of grain size, in the PHI scale, into three main components, each one corresponding to the main transporting mechanisms: traction, saltation and suspension (Figure C-5). The major truncation points occur about the transitional grain size values, which are those affected by two transporting mechanisms. These truncation points are defined as the 2-phi and the 3-phi break points. The former marks the transition between traction and saltation, and decreases in response to decreasing shear stress. The latter indicates the transition from saltation to suspension and decreases according to decreasing turbulence (Visher, 1999).

Although the relationship between sorting and depositional environments is not unique, grain-size distributions are always linked to the physics of the sedimentary processes. The non-uniqueness of sorting as an indicator of specific depositional settings derives from the fact that there are other variables involved, like provenance and sediment transport. Grain-size distribution depends not only on the specificities of the depositional setting, but also on the ability of the transporting current to separate different grain-size populations. Beach sediments, for example, are constantly reworked and sorted, therefore beach deposits tend to be well to very well sorted. However, if non-sorted sediments, like debris flows, are constantly discharged to the beach, then the most likely final result will be poorly to moderately sorted sediments. In spite of this non-uniqueness, the variations of sorting within a specific stratigraphic unit are always governed by the mechanics of sedimentation, as demonstrated by Inman (1949) and Visher (1969).

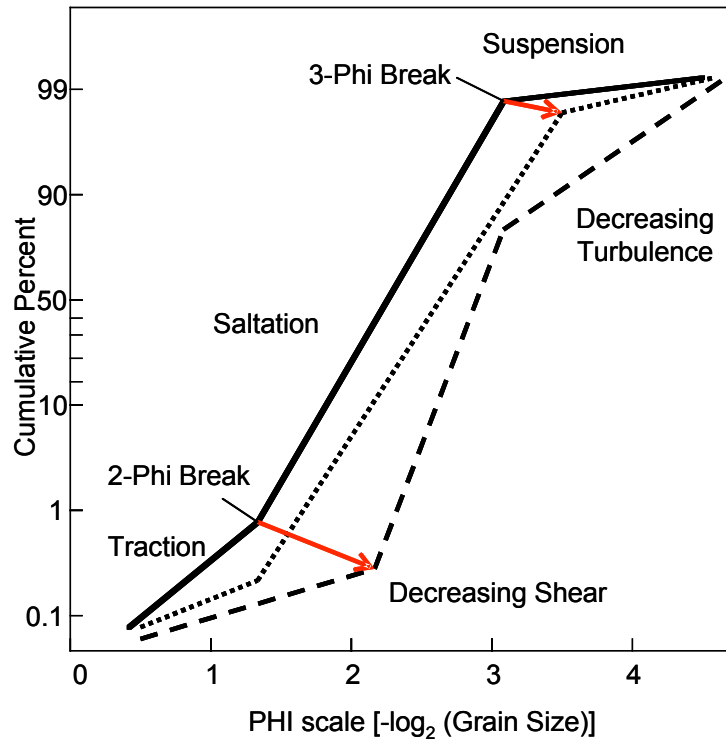


Figure C-5: Schematic cumulative frequency plots of grain-size distribution, illustrating the concept of the 2-phi and 3-phi breaks, and their general relationship with the mechanics of sedimentation according to Visher (1999).

### Measures of Packing

Among several measures of packing the most common are the grain concentration, the coordination number (Allen, 2001), and the intergranular contact (Fuchtbauer, 1974). The grain concentration, or fractional volume concentration of particles ( $X$ ), is directly related to porosity ( $\phi$ ):

$$\phi = 1 - X \quad (\text{B.4}).$$

The coordination number ( $C$ ), the average number of grains in contact with each individual grain, affects the stiffness of the aggregate. The intergranular contact describes the type of grain contact –punctual, tangential, concave-convex, or sutured–, and is usually a measure of the degree of mechanical compaction and pressure-solution, two processes related to diagenesis rather than to the depositional environment. According to Murphy (1982), and Zimmer (2003), porosity and coordination number can be related by the following expression:

$$C = 24e^{-2.547\phi} - 0.3731 \quad (\text{B.5}).$$

However, there are other factors affecting porosity, like sorting (Beard and Weyl, 1973; Allen, 2001), grain shape (Allen, 2001), and grain angularity. Therefore the relationship between coordination number and porosity is not unique (Allen, 2001).

Table B.1: Main packing types for identical sphere packs (after Mavko *et al.*, 1998; Bourbie, 1987).

Packing Type	Porosity	Coordination Number	Comments
Cubic	0.476	6	Unlikely
Hexagonal	0.395	8	Lose
Rhombohedral	0.259	12	Tight
Random	~0.36	~9	Most Likely

Like sorting, packing has a strong effect on porosity and therefore on permeability. The relationship between packing, coordination number and porosity has been analyzed by several authors (Graton and Fraser, 1935; Bourbie *et al.*, 1987; Murphy, 1982; Cumberland and Crawford, 1987). The effect of packing on both porosity and permeability was extensively analyzed by Graton and Fraser (1935). Murphy (1982) and Cumberland and Crawford (1987), identified the concomitant variation in both porosity and coordination number associated with changes in packing. For idealized packs of identical spheres these relationships are shown in Table B.1.

### Packing and Depositional Environments

According to Allen (2001), laboratory experiments demonstrate that the conditions of deposition have a strong effect on the concentration of natural sediments. The results from different studies (Steinour, 1944; Kolbuszewski, 1948; Walker and Whitaker, 1967; and Macrae and Gray, 1961) indicate that the grain concentration varies from a constant value of about 0.65, comparable with that of dense haphazard packing, at small rate of deposition, to a lower constant value of about 0.55, comparable with that of loose haphazard packing, at higher rate of deposition.

A systematic relationship between depositional environments and packing has not been established. There are some general observations: e.g. clean turbiditic sands tend to preserve high porosities at significant burial depths in spite of having moderate sorting; beach deposits tend to have a tighter packing than fluvial point bars and therefore similar initial porosities, in spite of their better sorting. However, a systematic analysis does not exist. One reason might be that porosity variations associated with differences in packing

linked to the depositional environment are, in many cases, overprinted by mechanical compaction during the early stages of burial.

## **Incorporating Sorting into Effective-Medium Models**

In order to take into account the effect of grain-size distributions on the effective elastic properties of granular material, our approach is to take the existing effective-medium models for uniform sphere packs, and modify them to incorporate the appropriate grain-size average. In other words, by finding the relevant averages of the variables involved in the computation, we can find approximate solutions to the effective elastic modulus. The following paragraphs will demonstrate that the appropriate averaging method varies, depending on the assumptions made during the derivation of each particular expression. For example, the harmonic average is the exact solution for the radius of curvature at the grain contact, whereas the average surface area requires a different averaging expression.

### **2.4.1. Contact Models**

The starting point of effective-medium models based on contact mechanics is the solution of the normal and shear stiffness for two grains in contact. The following paragraphs outline this solution and explain the average required in the case of grains with different grain radii.

#### **2.4.1.1 Radius of Grain-Contact Area**

Timoshenko and Goodier (1956, p. 412) present the general solution for the pressure distribution within the contact area of two grains with identical elastic properties but different grain radii ( $R_1$  and  $R_2$ ). The radius of the surface of contact ( $a$ ) is given by

$$a = \left( \frac{3}{4} \frac{F(1-\nu)}{G} \frac{R_1 R_2}{(R_1 + R_2)} \right)^{1/3}, \quad (\text{B.6})$$

where  $F$  is the force applied at the grain contact,  $\nu$  is the Poisson's ratio of the mineral, and  $G$  is the shear modulus. This expression is equivalent to the following equation

$$a = \left( \frac{3}{8} \frac{F(1-\nu)}{G} R_c \right)^{1/3}, \quad (\text{B.7})$$

where

$$R_c = 2 \left( \frac{R_1 + R_2}{R_1 R_2} \right)^{-1}. \quad (\text{B.8})$$

Equation B.7 is general for isotropic, linear elastic grains and can be extended to the case of a small sphere in contact with a hypothetical sphere with infinite radius.

#### 2.4.1.2 Normal and Shear Stiffness at the Grain Contact

Solutions for the normal stiffness of two grains in contact are presented by Mindlin (1949), Digby (1981), Walton (1987), and Johnson (1992), among others. Both normal and shear stiffness depend on the radius of the area of grain contact. The magnitude of this dependence varies with the loading sequence or the friction coefficient assigned to the grain surfaces. In general the normal stiffness is given by (Mindlin, 1949):

$$S_n = \frac{4aG}{1-\nu}. \quad (\text{B.9})$$

The variation of the shear stiffness is more sensitive to the sequence of loading, the area of contact, and the friction coefficient. Different solutions to the shear stiffness have been given; in general they agree in proposing that the shear stiffness at the grain contact may vary from 0 to a maximum value given by

$$S_t = \frac{8aG}{2-\nu}. \quad (\text{B.10})$$

Different mechanisms have been proposed to explain the variations in the shear stiffness at the grain contact. For example, Mindlin (1949) proposed that the controlling factor is the coefficient of friction, according to the expression:

$$S_t = \frac{8aG}{2-\nu} \left( 1 - \frac{F_x}{\xi F_z} \right)^{1/3}, \quad (\text{B.11})$$

where  $F_x$  and  $F_z$  stand for the shear and normal tractions at the grain contact, and  $\gamma$  is the coefficient of friction. From this equation it follows that if  $F_x$  equals the product  $\xi F_z$ , then the shear stiffness is null. A similar model was proposed by Walton (1987). Digby (1981) related the shear stiffness to the pre-existing radius of the area of grain contact ( $b$ ), as follows:

$$S_t = \frac{8bG}{2-\nu}. \quad (\text{B.12})$$

From this expression follows that if the pre-existing radius of the grain-contact area is close to zero, the initial shear stiffness is negligible. Null shear stiffness at the grain

contacts does not necessarily imply lack of rigidity of the aggregate. Bachrach (1998) associated variations in the rigidity of shallow unconsolidated sands with the proportion of null-shear-stiffness contacts.

#### **2.4.1.3 Normal Force at the Grain Contact**

Approximate solutions for the normal force at the grain contact are presented by Digby (1981) and Walton (1987). Digby (1981) demonstrates that the normal force is given by

$$F = \frac{4\pi R^2 P}{(1-\phi)C}, \quad (\text{B.13})$$

where  $P$  is the applied hydrostatic pressure and  $\phi$  is porosity.  $R$  and  $C$  stand for the sphere radius and the coordination number, respectively. According to Digby (1981), this result agrees exactly with the solution for different grain sizes obtained by Brandt (1955). This expression is also equivalent to the equations presented by Walton (1987). The expression  $4\pi R^2$  represents the surface area of each identical sphere. For varying grain sizes, the normal force at the grain contact becomes a function of the average grain surface area ( $S_{avg}$ ) and the grain coordination number ( $C_g$ ).

#### **2.4.1.4 The Coordination Number of a Binary Mixture**

The average coordination number of a mixture ( $C_{avg}$ ) increases as sorting deteriorates; however the variation of  $C_{avg}$  in binary mixtures is not linear and reach an upper limit as the number of small spheres, with low coordination number, increases. This is because the average coordination number depends not only on the number of grains per volume, but also on the volumetric average of grain sizes. The maximum number of small spheres ( $C_{big}$ ), of radius  $R_{small}$ , surrounding a bigger sphere, of radius  $R_{big}$ , depends on the ratio between the total surface area around the big sphere, and the area of a circle of radius  $R_{small}$ . This maximum coordination number can be approximated by the following expression:

$$C_{big} \approx \frac{3}{4} \left[ 4 \left( \frac{R_{big}^2}{R_{small}^2} + 2 \frac{R_{big}}{R_{small}} + 1 \right) \right]. \quad (\text{B.14})$$

The fraction (3/4) has been introduced to fit the maximum coordination number of identical spheres to 12, instead of 16. Assuming  $C_{small}$  as the average coordination number for the small spheres, where  $C_{small} \leq C_{big}$ , the average coordination number of the whole aggregate is:

$$C_{avg} = \frac{\#Contacts}{\#Spheres} = \frac{AC_{big} + AC_{big}C_{small} + ABC_{big}C_{small}}{A + AC_{big} + ABC_{big}}, \quad (B.15)$$

where  $A$  is the total number of spheres, and  $B$  is the proportion of small spheres that are not in contact with the big spheres. Figure C-6 illustrates the results obtained from Equations B.14 and B.15, taking  $A = 8$ , and different values for  $C_{small}$  and  $B$ . It clearly shows that the ratio between  $C_{avg}$  and  $C_{big}$  rapidly decreases to almost zero, as the ratio of  $R_{big}$  to  $R_{small}$  increases. Meanwhile the ratio of  $C_{avg}$  to  $C_{small}$  increases and exponentially reaches an upper limit, where  $C_{avg}$  is slightly larger than  $C_{small}$ .

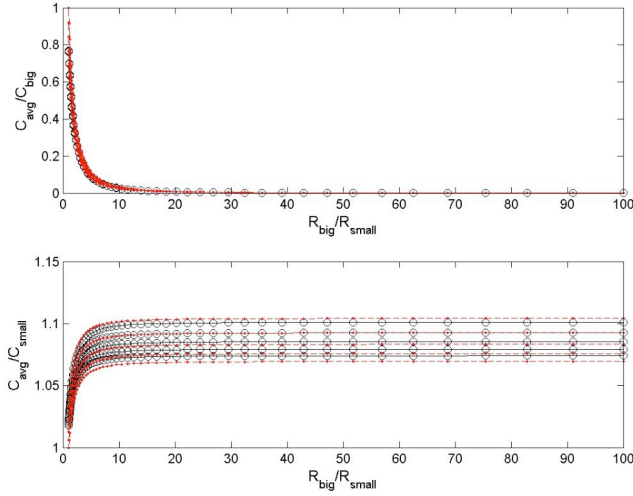


Figure C-6: Variation of  $C_{avg}$  as the ratio between  $R_{big}$  and  $R_{small}$  increases (sorting deteriorates). For large values of  $R_{big}/R_{small}$ ,  $C_{big}$  is much larger than both  $C_{small}$  and  $C_{avg}$ .  $C_{avg}$  increases as sorting deteriorates; however it rapidly reaches an upper limit slightly larger than  $C_{small}$ .

#### 2.4.1.5 The Softening Effect of Variable Grain Size

Putting small spheres in between larger spheres has a softening effect on the elastic modulus of sphere packs. This can be mathematically demonstrated throughout the analysis of uniaxial deformation of three grains in contact, based on the sketch shown in Figure C-7. The elastic modulus ( $M_1$  and  $M_2$ ) for the uniaxial deformation of the two configurations shown in Figure C-7 are given by

$$M_1 = \frac{\partial P}{\varepsilon_1} = \frac{L_1}{\partial \delta_0 + \partial \delta_1} \partial P, \quad (B.16)$$

$$M_2 = \frac{\partial P}{\varepsilon_2} = \frac{L_2}{\partial \delta_0 + \partial \delta_2} \partial P. \quad (B.17)$$

where  $\varepsilon_1$  and  $\varepsilon_2$  are the respective uniaxial strains. To demonstrate that  $M_1$  is also larger than  $M_2$  we need to prove that  $\Delta\delta_1$  is smaller than  $\Delta\delta_2$ , since  $L_1$  is larger than  $L_2$ . For any grain contact  $\Delta\delta$  is given by (i.e. Mavko *et al.*, 1998)

$$\partial\delta = \frac{\partial F}{Sn}. \quad (\text{B.18})$$

Considering that the force at the grain contacts is the same, and recalling equations B.6 and B.9, it follows that  $Sn_1$  is larger than  $Sn_2$  and consequently:

$$\partial\delta_1 = \frac{\partial F}{Sn_1} < \frac{\partial F}{Sn_2} = \partial\delta_2. \quad (\text{B.19})$$

Therefore  $M_1$  is larger than  $M_2$ .

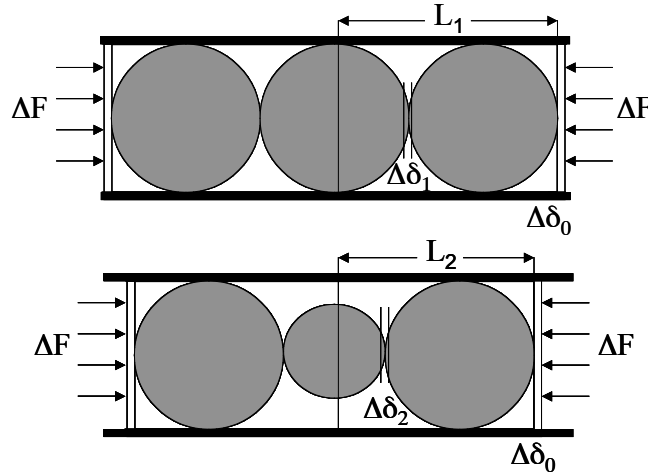


Figure C-7: Sketch for the analysis of uniaxial deformation of three grains in contact.

#### 2.4.1.6 Effective Elastic Modulus of Sphere Packs with Variable Grain Size

Winkler (1983) demonstrated that the general solutions for the effective elastic properties of random packs of identical spheres, derived by Digby (1981), are not specific to Digby's model and can be generalized to different contact models. From Digby's derivation, the effective elastic properties of a random packing of spheres is given by (Winkler, 1983):

$$K_{eff} \approx \frac{C(1-\phi)}{12\pi R} Sn, \quad (\text{B.20})$$

$$G_{eff} \approx \frac{C(1-\phi)}{20\pi R} \left( Sn + \frac{3}{2} St \right). \quad (\text{B.21})$$

To incorporate the effect of grain-size distribution into these models, grain radius ( $R$ ), coordination number ( $C$ ), normal stiffness ( $Sn$ ), and shear stiffness ( $St$ ) are replaced in the expressions above for their equivalent averages. Then we can rewrite the previous equations:

$$K_{eff_{sort}} \approx \frac{C_{avg}(1-\phi)}{12\pi R_{avg}} Sn_{avg} \quad , \quad (B.22)$$

$$G_{eff_{sort}} \approx \frac{C_{avg}(1-\phi)}{20\pi R_{avg}} \left( Sn_{avg} + \frac{3}{2} St_{avg} \right). \quad (B.23)$$

These equations can be used as a first approximation to model the effect of sorting on the effective elastic properties. The question is then, which are the appropriate averages to use?

#### ***2.4.1.7 What are the Appropriate Averages?***

The averages required refer to either the local average for two grains in contact, or the global average of the aggregate. Whereas the different averages for sphere radii have an exact solution, the averages for coordination number and the average ratio  $a/R$  are inferred. For example, the harmonic average for the radius of curvature for two grains in contact is exact (Timoshenko and Goodier, 1956). For a sphere configuration like that shown in Figure C-8, the different averages are indicated in Table B.2.

It becomes clear, by looking at Table b.2, that variable sphere sizes in contact require the evaluation of different average radii for each expression. The best example is the difference between the local average radius of curvature ( $Rc$ ) and the average grain radius required for the average surface area ( $R_{avg}$ ). The former requires the harmonic average of the sphere radii in contact, whereas the later average is given by the following expression:

$$R_{avg} = \left( \sum_k f_k R_k^2 \right)^{1/2} \quad (B.24)$$

These two are exact results. Another difference seems to exist between the local radius of curvature and the global average sphere radius ( $Rg$ ). Either the arithmetic average or the geometric average is proposed for  $Rg$ . The arithmetic average provides the best results during stochastic simulation, since enhances the softening effect of variable grain sizes. However a rigorous justification of its use is lacking. It is important to point out that coordination numbers vary within a small range; therefore the different choices of

averages for local and global coordination numbers do not have a dominant effect in the final result. Notice also that all these expressions reduce to the Hertz-Mindlin model when we consider identical spheres. They will also reduce to Hertz-Mindlin expressions if we use the harmonic average for local radius of curvature, average sphere radius, and average surface area.

The expressions presented in Table B.2 imply that introducing small spheres between the contacts of larger spheres may actually decrease the aggregate stiffness. Although this effect might not be intuitively obvious, it agrees with the fact that the area of grain contact is controlled by the radius of the small sphere, whereas the average sphere radius is dominated by the large sphere. This softening effect of small spheres is comparable to the effect of grain angularity analyzed by Bachrach *et al.* (2000).

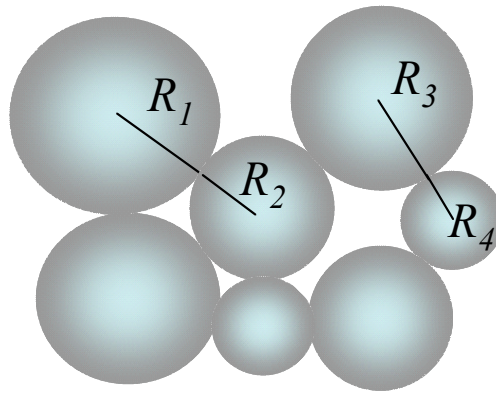


Figure C-8: An aggregate of spheres with variable radii.

Table C-2: Summary of equations and variables used to incorporate variable sphere radii into effective-medium contact models.

Variable	Expression	Reference or Assumption
Local grain-contact area between $R_i$ and $R_j$	$a_{ij} = \left( \frac{3}{8} \frac{F_{ij}(1-\nu)}{G} Rc_{ij} \right)^{1/3}$	Timoshenko and Goodier (1956)
Local radius of curvature of $R_i$ and $R_j$	$Rc_{ij} = 2 \left( \frac{R_i + R_j}{R_i R_j} \right)^{-1}$	Timoshenko and Goodier (1956)
Local coordination number	$C_{ij} = 2 \left( \frac{1}{C_i} + \frac{1}{C_j} \right)^{-1}$	C controlled by the weakest contact

Volumetric average radius	$R_e = \left( \sum_k f_k R_k^3 \right)^{1/3}$	Exact solution for the average volumetric radius.
Global average surface area	$S_{avg} = 4\pi \sum_k f_k R_k^2$	Exact solution for the average surface area.
Intergranular force between $R_i$ and $R_j$	$F_{ij} = \frac{S_{avg} P}{C_{ij} (1 - \phi)}$	Digby (1981)
Global average ratio $\alpha = \frac{a}{Rg}$	$\alpha_{avg} = \sum_k f_k \alpha_k ; \text{ where:}$ $\alpha_k = \frac{a_{ij}}{Rg_{ij}}$	$Rg$ differs from the radius of curvature and corresponds to the global volumetric average radius
Global average coordination number	$C_{avg} = \sum_k f_k C_k$	$C_k$ varies between 6 and 12
Effective Bulk Modulus	$K_{eff_{sort}} = \frac{C_{avg} G(1 - \phi)}{3\pi(1 - \nu)} \alpha_{avg}$	Generalized Hertz-Mindlin for average $C$ and $\alpha$

#### 2.4.2. The Modified Hashin-Shtrikman Lower Bound (MHSLB) and Sorting

The MHSLB can be considered an upper bound for the sorting effect on the elastic properties of granular materials. Dvorkin and Gutierrez (2001) used the MHSLB to model the effect of sorting in unconsolidated sandstones, based on the theoretical analysis and experimental results for binary mixtures. Although a good approximation, the use of binary mixtures and the MHSLB to estimate the effect of variable grain size does not take into account the softening effect of introducing small spheres between large spheres. As a result of the variable grain size, the normal and shear stiffness at these contacts decrease, resulting in an effective elastic modulus lower than that predicted from the MHSLB. Recent laboratory studies by Zimmer (2003) show that the effect of sorting follows a flatter trend than the one predicted by the MHSLB (Figure C-9). Consequently, the MHSLB provides a stiffer estimate of the actual impact of varying grain size, and constitutes an empirical upper bound for the concomitant effect of sorting on the elastic properties and porosity of granular materials.

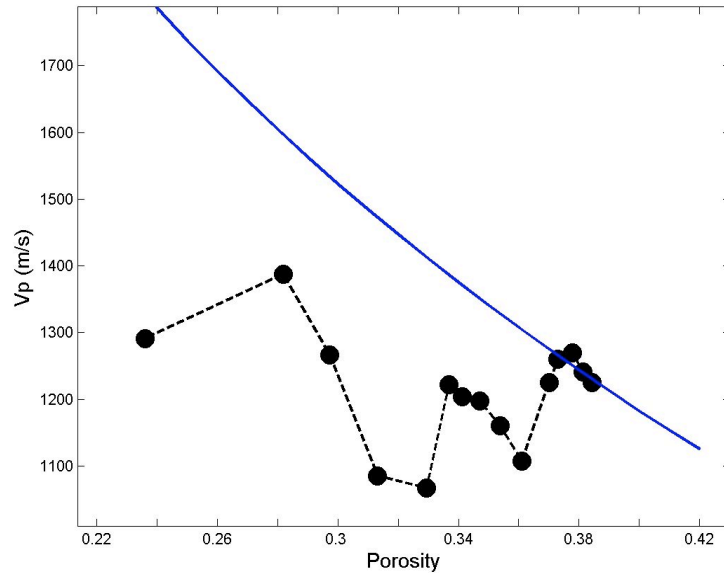


Figure C-9: Sorting trend for six different sand aggregates, with variable sorting, at 5 MPa confining pressure (after Zimmer, 2003). The large variations in porosity are related to the changes in sorting. The blue line corresponds to the Hashin-Strickman lower bound, after fitting the first data value. Notice the flat and irregular trend associated with the variations in sorting.

## Modeling the Effect of Packing

In the case of idealized spheres, the main effects of grain rearrangement are reducing porosity and incrementing coordination number, as shown in Table B.1. Other possible additional effects involve grain stabilization and change in the grain-contact area. The packing effect can be modeled using either Hertz-Mindlin contact theory or the MHSLB. In both cases, the modeling results underestimate the increase in elastic stiffness associated with packing, as observed in laboratory analysis (Zimmer, 2003). Hertz-Mindlin and MHSLB models provide similar results, both neglecting the impact of grain stabilization and local increase in grain-contact area. From this analysis it follows that the MHSLB constitutes a lower bound for the packing trend in the velocity-porosity plane. Consequently, it also constitutes an empirical lower bound for the overall effect of mechanical compaction on the elastic properties of granular materials.

### 2.5.1. Modeling the Packing Effect with Hertz-Mindlin Theory

The pure packing effect obtained from the Hertz-Mindlin model underestimates the slope observed in laboratory data, as shown in Figure C-10. Hertz-Mindlin theory for the elastic properties of granular materials is summarized in Equations B.6 to B.13, and

Equations B.20 to B.21. As documented by Mavko et al. (1998), for identical spheres the model becomes independent of the sphere radius. Besides the elastic properties of the minerals ( $G$  and  $\nu$ ) and the confining pressure ( $P$ ), the dominant parameters become the grain-contact area ( $a$ ), porosity ( $\phi$ ) and coordination number ( $C$ ). For the case of ideal spheres, the change in grain-contact area is exclusively associated with confining pressure, because the grains do not have rectilinear faces. Therefore, the only variables controlling the change in elastic properties associated with grain accommodation are porosity and coordination number. To use Hertz-Mindlin theory to model the packing effect, the mutual change of porosity and coordination number can be estimated from Murphy's relationship (Equation B.5). Figure C-10 compares the trend obtained from Hertz-Mindlin model, with the trend observed from laboratory results (Zimmer, 2003). An assumption of no shear stiffness at the grain contacts was necessary to match the laboratory data. The slope of the data is slightly larger than the slope obtained from the Hertz-Mindlin model.

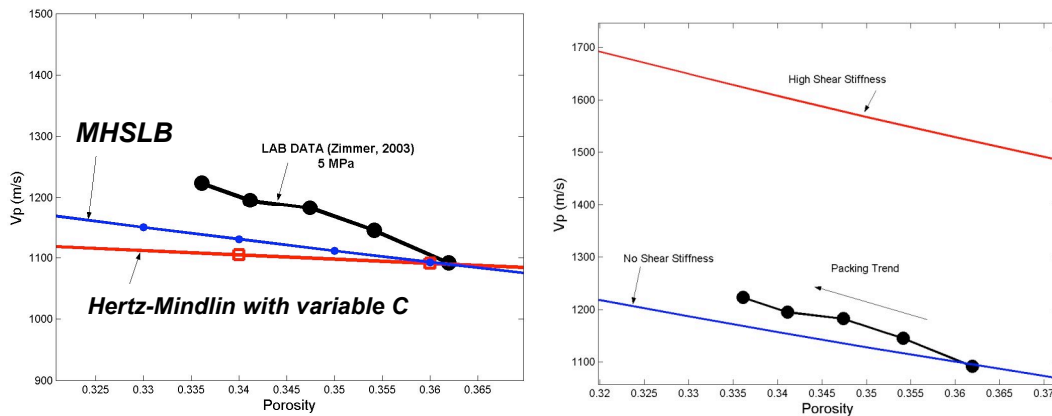


Figure C-10: Comparison between laboratory results showing the effect of packing (Zimmer, 2003), and the modeled effect of packing using the modified Hashin-Shtrikman lower bound (MHSLB), and Hertz-Mindlin (HM) theory combined with Murphy's relationship for  $C$  and  $\phi$  (Eq. B.5). Figure on the left shows the results for the Unconsolidated Sandstone Model (Mavko, et al., 1998), which combines both the HM theory (for the anchor point) and the MHSLB. The red line shows that HM theory overestimates the velocity for unconsolidated sands. To fit the data, a correction factor for shear stiffness is necessary. The slope of the packing trend is slightly but systematically steeper than the MHSLB.

Another effect associated with mechanical compaction is grain stabilization (i.e. Zimmer, 2003). Laboratory and field studies of unconsolidated sandstones at low confining pressure demonstrate that to fit the data, low or no shear stiffness at the grain contacts has to be assumed (Bachrach, 1998; Zimmer, 2003). This discrepancy has been explained as the result of grain angularity (Bachrach, 1998) and grain sliding or rolling

(Zimmer, 2003). On the other hand, Avseth (2000) and Gutiérrez (2001) have successfully used Hertz-Mindlin to model velocities of friable (uncemented) sandstones at depth. This discrepancy suggests that there is a compaction stage at which grain sliding or rolling is no longer feasible because of tight packing, and therefore the assumptions of the Hertz-Mindlin theory become valid. Figure C-10 illustrates the difference between the assumptions of no shear stiffness and high shear stiffness at the grain contacts.

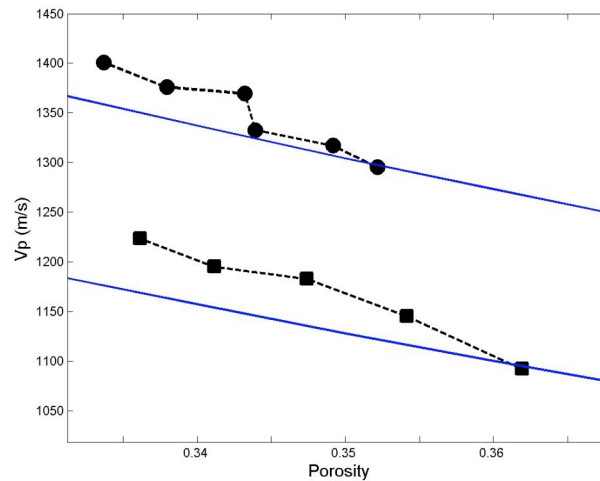


Figure C-11: Compaction trend for a sand aggregate at 5 and 10 MPa confining pressures, after different loading cycles (Zimmer, 2003). The blue curves are the Hashin-Strickman lower bounds, after fitting the first data point. Notice the steeper slope of the compaction trend.

### 2.5.2. The Modified Hashin-Shtrikman Lower Bound and Packing

The comparison of the packing trend obtained from the MHSLB and laboratory results (Figure C-11), shows that the MHSLB underestimates the effect of packing. The packing trend obtained from the MHSLB is about the same as that obtained from the Hertz-Mindlin model (Equations B.7, B.9, B.10, B.13, B.20, and B.21). The trends obtained from Hertz-Mindlin theory and MHSLB do not account for the effect of grain stabilization. In addition to this, the Hertz-Mindlin theory assumes idealized spheres that do not increase the grain-contact area after grain rearrangement. These two factors will increase the aggregate's elastic modulus, as the steeper slope of the laboratory data indicates. Consequently, both the Hertz-Mindlin model and the MHSLB constitute lower bounds for the effect of grain accommodation on both porosity and the elastic properties of granular materials. In particular, the MHSLB can be considered a lower bound for the effect of mechanical compaction.

## An Idealized Quinary Mixture

In order to mathematically evaluate the effect of sorting, we use a model for gradual infilling of a tight rhombohedral packing of spheres developed by White and Walton (1937). These authors calculated the size and the number of gradually smaller spheres required to fill the spaces between larger spheres. Starting from the tight packing of identical spheres, they made the analysis for five different sphere sizes forming a quinary mixture (Table B.3). They also calculated the porosity reduction and the increment in surface area, as the mixture changed to binary, ternary, quaternary and quinary. The sorting index for each mixture has been derived from their results. Table summarizes their results, and includes the sorting index of these mixtures. In spite of its idealized rhombohedral packing, White and Walton's study gives us the basic information to calculate the effect of sorting using the equations in Table .

Table B.3: Parameters for the groups of infilling spheres for a rhombohedral packing (after White and Walton, 1937). The first column corresponds to the rhombohedral packing of identical spheres. The following columns indicate the size and volumes of the infilling spheres, and the final volume, porosity, surface area and sorting index of the resulting mixture.

	1st	2nd	3rd	4th	5th	Filler
<b>Radius</b>	r	0.414r	0.225r	0.177r	0.116r	Very small
<b>Relative # of spheres</b>	1	1	2	8	8	
<b>Volume</b>	$4.189r^3$	$0.298r^3$	$0.0476r^3$	$0.0225r^3$	$0.0066r^3$	
<b>Added volume</b>	$4.189r^3$	$0.298r^3$	$0.0952r^3$	$0.180r^3$	$0.0526r^3$	$0.622r^3$
<b>Total volume of spheres</b>	$4.189r^3$	$4.487r^3$	$4.582r^3$	$4.762r^3$	$4.815r^3$	$5.437r^3$
<b>Porosity</b>	0.2595	0.207	.19	0.158	0.149	0.039
<b>Surface area</b>	$12.566r^2$	$14.732r^2$	$16.004r^2$	$19.080r^2$	$20.456r^2$	
<b>Sorting Index (SD/mean)</b>	0.0	0.42	0.69	0.84	0.92	

## Stochastic Simulation of Effective Elastic Properties

In order to evaluate the effect of grain-size distribution we use the quinary-mixture model from White and Walton (1937), and perform stochastic simulations using the equations in Table B.2. The input parameters for this algorithm are the grain-size distributions, the porosity, the coordination numbers for each grain size, and the elastic properties of the solid. The grain-size distributions vary as we add smaller fractions to the aggregate, starting from identical spheres (1<sup>st</sup> column in Table B.3), and then adding

smaller spheres: 2<sup>nd</sup> column for a binary mixture, 3<sup>rd</sup> column for a ternary mixture, and so on. For each case we modeled a mixture with 2400 grains. The coordination numbers for the larger spheres increase as we add smaller spheres, reaching a top value of 19, under the assumption that all the added spheres are in contact with the largest spheres. However the coordination number of the added smaller spheres is always low (6-9). The harmonic average for the local  $C_{ij}$  was used in order to give more weight to the small sphere's  $C$ .

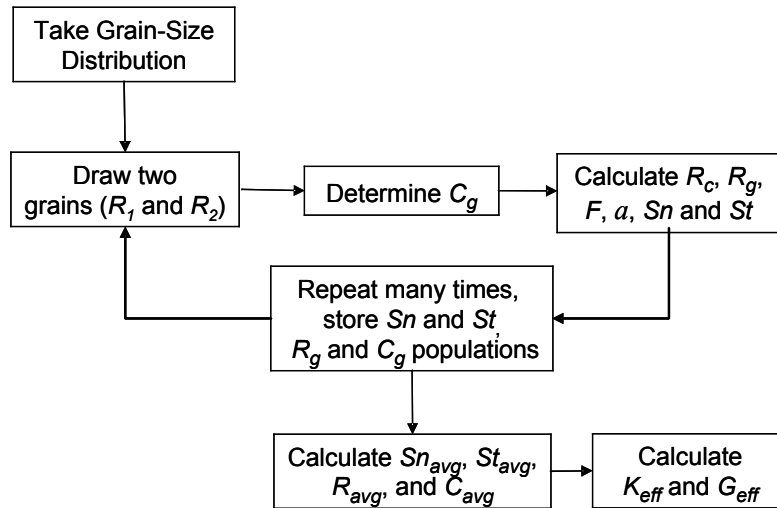


Figure C-12: Algorithm to evaluate the effect of grain-size distribution on elastic properties, using stochastic simulation.  $C_g$ ,  $R_c$ , and  $R_g$  are the averages of coordination number, radius of curvature and grain radius at each grain contact;  $F$ ,  $a$ ,  $Sn$  and  $St$  are force, radius of grain contact area, normal and shear stiffness at each grain contact.  $Sn_{avg}$ ,  $St_{avg}$ ,  $R_{avg}$ , and  $C_{avg}$  are the global averages of normal and shear stiffness, grain radius, and coordination number.

The algorithm steps are schematically shown in Figure C-12, and the green lines in Figure C-13 outline the results obtained from this algorithm. For every grain-size distribution, each grain size has a specific coordination number; therefore the coordination number at each grain contact ( $C_{ij}$ ) is determined from the drawn grain radii  $R_i$  and  $R_j$ . The global averages of grain radius and coordination number are calculated from the populations  $R_{gij}$  and  $C_{ij}$ . To evaluate the uncertainty associated with the which local and global coordination numbers are appropriate, additional simulations were performed using different options for the global ( $C_{avg}$ ) and local ( $C_{ij}$ ) coordination numbers. The results, also shown in Figure C-13, indicate a variation from 10% to 16% for a given grain-size distribution, specified by porosity and sorting. As expected, the assumption of constant  $C_{avg}$  and  $C_{ij}$  generates the lowest variability. Remarkably, the algorithm outlined in Figure C-12 produces an irregular trend similar to the one observed in the laboratory data.

The range of variability obtained from the stochastic models is small, and outlines a velocity-porosity trend flatter than the one predicted from the MHSLB. Fluid substitution puts the results within the framework of the well-established rock physics depositional and diagenetic trends. The final results are shown in Figure C-14. Within this framework, it is clear that the scatter introduced by the uncertainty of the coordination number is relatively small, and all the different results follow a relatively flat trend. Using the highest-porosity value as the anchor point, it is clear that the results from the stochastic simulations follow a flatter trend than the MHSLB.

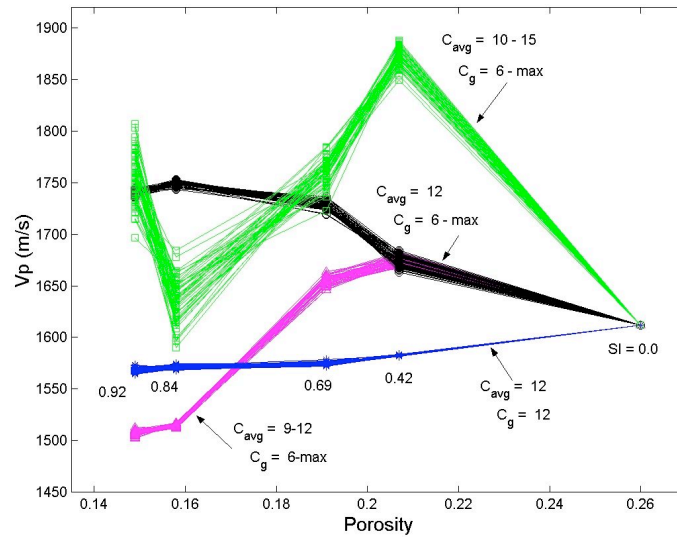


Figure C-13: Results from the stochastic simulation. The green line corresponds to the algorithm outlined in Figure C-16. SI corresponds to the sorting index for each grain-size distribution (Equation 2). The other lines show results from different simulations, assuming  $C_{avg}$  either is 12 or varies from 9 to 12, and  $C_g$  either is 12 or varies from 6 to the maximum possible for each mixture.

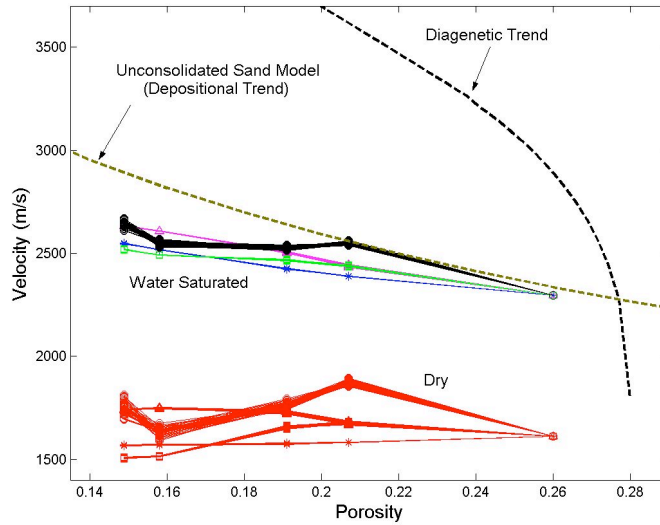


Figure C-14: Comparison of the results from the stochastic simulation with the rock-physics diagenetic trend and the unconsolidated sandstone model. The slope of the results, after fluid substitution, show a flatter trend than the one predicted from the unconsolidated sandstone model (modified Hashin-Strickman lower bound).

## Comparison with Real Data

In essence, the theoretical modeling and the results from the stochastic simulations predict that the sorting effect has a flatter trend in the velocity-porosity plane than the packing effect. Whereas the MHSLB constitutes an upper bound to the sorting effect, it can be considered a lower bound for the packing effect. As shown below, both laboratory and subsurface data corroborate that the sorting effect follows a flatter trend than the MHSLB.

### 2.8.1. Comparison with Laboratory Data

There is good agreement between the sorting effect in both velocity and porosity observed in laboratory experiments (Zimmer, 2003), and the one predicted from the stochastic simulation (Figure C-15). The shown laboratory data correspond to measurements of sand and glass-bead aggregates with different sorting, at the same confining pressure (5 MPa). The samples were prepared under similar protocols; therefore, the porosity variation between samples is assumed to be exclusively caused by sorting (Zimmer, 2003). The lower porosity for the theoretical textural models is the consequence of the idealized rhombohedral packing, a very unlikely configuration for unconsolidated sands. The comparison, however, is based on the departure of each trend from its respective MHSLB. As can be observed in Figure C-15, the overall trend is

flatter than the MHSLB, especially because of the break in the trend as the sorting deteriorates. In the theoretical models, this break is driven by the introduction of the smaller spheres. A similar break is observed in the laboratory data, suggesting that indeed small spheres have a softening effect on the aggregate.

A better understanding of this comparison can be obtained by looking at the slope of the velocity change, rather than the actual velocity values (Figure C-16). In this comparison you can clearly see that the laboratory data show abrupt changes in the slope of the velocity-porosity trend. The MHSLB predicts a constantly increasing slope, which cannot reproduce the actual variability in the data. On the contrary, the results from the stochastic simulations reproduce the variable slopes, which overall create a flatter trend for the sorting effect.

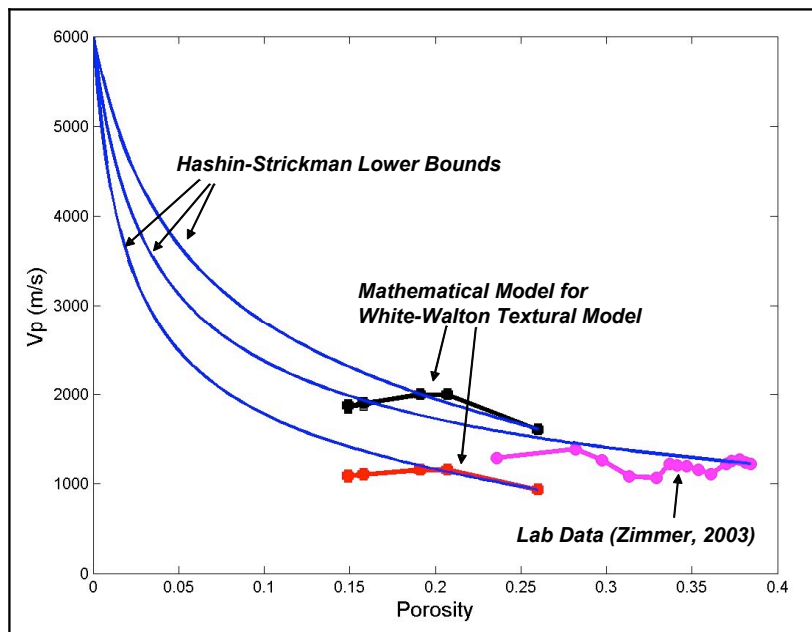


Figure C-15: Comparison of the theoretical results from stochastic simulation for water saturated (black) and dry (red) aggregates, and fluid-substituted laboratory measurements (magenta) performed by Zimmer (2003). Whereas the MHSLB predicts a gradually increasing velocity, both the results from the stochastic simulation and the laboratory data show a highly variable slope, which overall translates into a flatter trend for the sorting effect.

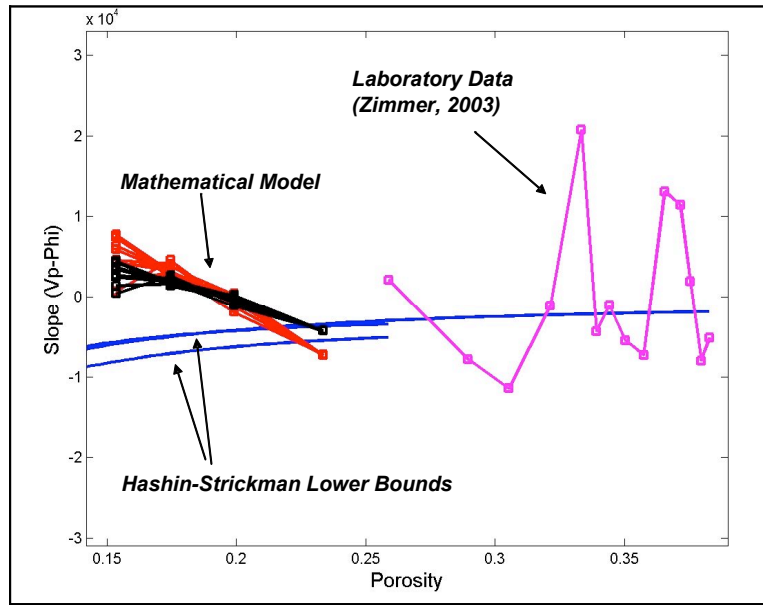


Figure C-16: Comparison of the velocity-positivity slopes predicted from MHSLB, the stochastic simulation, and the actual slopes observed in laboratory data. Contrary to MHSLB, the stochastic simulation based on the theoretical formulation presented here can generate variable slopes such as those observed in the data.

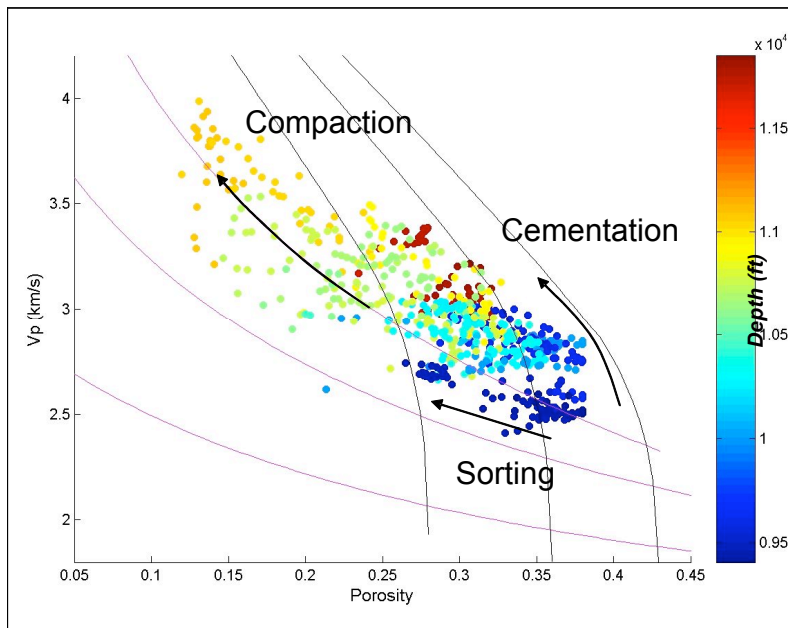


Figure C-17: Well-log data of sandstones from one single stratigraphic sequence within an oil field. The graph shows the three main trends for sandstones: the flat trend associated with the sorting effect, the compaction trend, and the steep diagenetic trend. As predicted from the theoretical model, the MHSLB constitutes an upper bound for the sorting trend.

### 2.8.2. Comparison with Subsurface Data

The velocity-porosity trend observed in uncemented sandstones in the subsurface agrees with the flat trend predicted from our theoretical analysis (Figure C-17). The flat trend is depicted by the shallower sands (blue dots in Figure C-17), and follows a gentler slope than the one predicted from the MHSLB (magenta lines in Figure C-17). The velocity and porosity data shown correspond to well-log measurements obtained along an interval where core porosity and sorting data were also available (Figure C-18 and Figure C-19). A least-squares regression was obtained for the correspondence between sorting and porosity from the core data (Figure C-19). The least-squares regression also indicates a small negative correlation between porosity and the grain size, which indicates a minor influence of packing, probably associated with grain angularity (fine grains tend to be more angular than coarser sands). However, the effect of sorting on porosity, in these sands, is stronger than the effect of packing. The high-porosity have better sorting than the low-porosity clean sands. These two different types of sands create the flat trend observed in the velocity-porosity plane.

The grain-size distribution was obtained from laser particle size analysis (LPSA). Similar data were available from other cores (Figure C-20), but the depth shifts required to compare with well-log data was not available. In both cases, the least-squares regressions show that although sorting has a strong effect on porosity, there is a small component associated with grain size itself (Figure C-21). This grain-size component is probably the effect of grain angularity, since finer grain sizes tend to be more angular. It is important to emphasize that the coefficient of variation (Sorting Index) of these log-normal distributions is the best parameter to model the relationship between sorting and porosity. Similarly, the median is a better measure of the average grain size than the mean. The combination of the two core data sets provide a linear regression that approximates the regressions obtained from previous laboratory data, and from the modeled quinary mixture (Figure C-5).

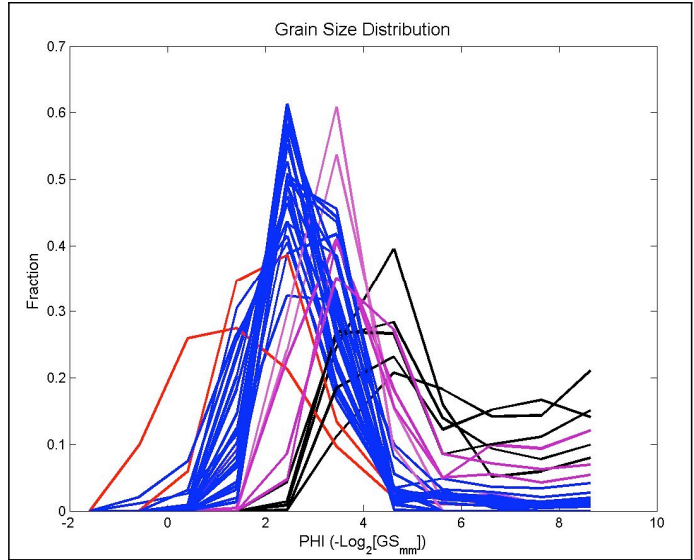


Figure C-18: LPSA grain-size distribution from core samples. The sampled interval corresponds to the same well-log data shown in Figure C-21.

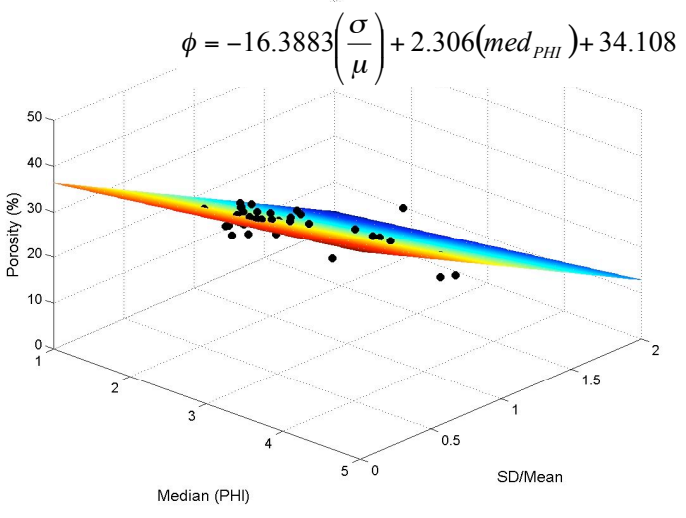


Figure C-19: Visualization of the least-squares regression between porosity ( $\phi$ ), the coefficient of variation ( $\sigma/\mu$ ), and the median grain size in PHI scale ( $med_{PHI}$ ), from core samples. Porosity is given in percentage or porosity units. The samples are sandstones and correspond to the grain-size distributions shown in Figure C-18 and the well-log data shown in Figure C-19.

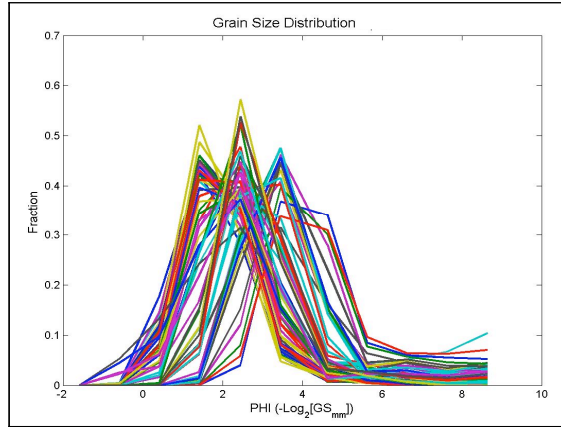


Figure C-20: LPSA grain-size distribution obtained from a different well and stratigraphic interval than the one shown in Figure C-18.

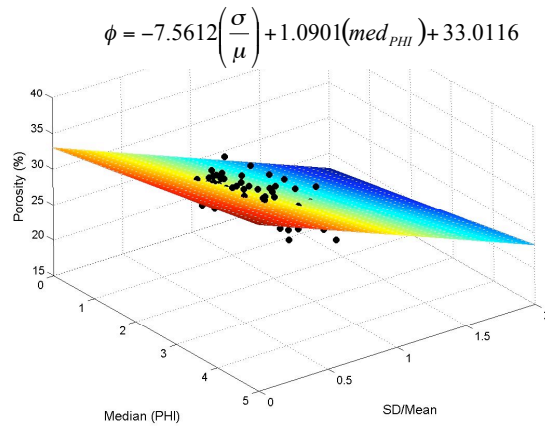


Figure C-21: Visualization of the least-squares regression between porosity, median grain size (PHI scale) and coefficient of variation, corresponding to the data shown in Figure C-20.

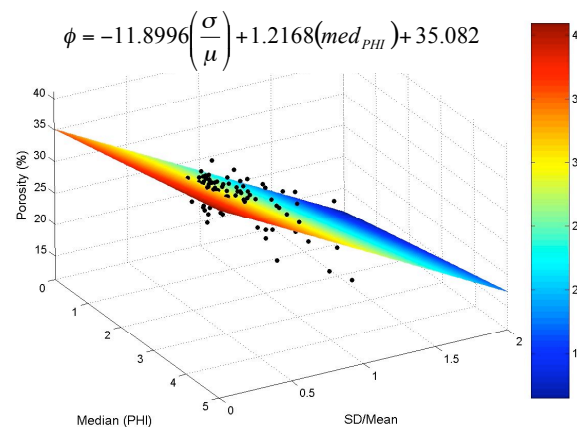


Figure C-22: Visualization of the least-squares regression between porosity, median grain size (PHI scale), and coefficient of variation, corresponding to the combination of the data shown in Figure C-18 and Figure C-20.

## Discussion

Local and global average parameters and stochastic simulation have been necessary to introduce variable grain sizes into effective-medium contact models. A rigorous analytical solution of the elastic modulus of aggregates with variable grain size has not been the purpose of this work. Such a solution would vary depending on the spatial distribution of grain sizes. The stochastic approach followed in this work accounts for this variability, assuming is random, and allows us to evaluate the uncertainties associated with the local coordination number and the averaging methods. The results obtained by this approach suggest that statistical mechanics rather than deterministic solutions might be the right direction for further improvements in the effective-medium theory for granular aggregates.

The theoretical analysis, laboratory measurements, and subsurface data, all indicate that effect of sorting on the elastic properties of granular materials generates a flatter trend in the  $V_p$ - $\phi$  plane than the one predicted by the MHSLB. This flatter trend seems to be the consequence of a softening effect caused by introducing small spheres between large spheres. This softening effect of the small spheres is comparable to the effect of grain angularity analyzed by Bachrach *et al.* (2000). The effect has been theoretically modeled and observed in laboratory, and becomes evident in samples with large contrasts in grain size. For all practical purposes, the MHSLB should be considered an upper bound for the concomitant effect of sorting on the elastic properties and porosity of granular materials.

In contrast to the case of sorting, the MHSLB constitutes an approximate lower bound for the packing effect. The comparison of Hertz-Mindlin models, MHSLB and laboratory data shows that the trend associated with packing follows a steeper slope than the one predicted by any of these models. Grain stabilization and increasing grain-contact area by grain accommodation can both increase the aggregate stiffness. Zimmer (2003) obtained a similar conclusion. Bachrach (1998) modeled the variation in Poisson's ratio and shear stiffness based on the proportional increment of non-zero shear stiffness contacts. Since the slope predicted from both Hertz-Mindlin and the MHSLB models are similar, we can conclude that the MHSLB underestimates the actual packing trend.

Overall, the MHSLB constitutes a good approximation for the depositional trend in high-porosity sands (Avseth, 2000; Gutierrez and Dvorkin, 2001). The success of the MHSLB in reproducing the depositional trend might be the result of a combined effect of sorting and packing. Extension of the depositional trend to low-porosity sands should be cautiously done. The difference in surface area associated with changes in sorting may

influence the distribution of quartz cementation. Other factors like grain dissolution of feldspars may also have an effect. Although the trend observed in the velocity-porosity plane can be used to infer the variations in sorting of clean sands, it is always convenient to verify by looking at cuttings descriptions, thin sections and cores.

The effect of sorting on the elastic properties of high-porosity sands and sandstones differs from those of clay content and mechanical compaction. Although poor sorting is commonly associated with clay content, imposing an additional mineralogic effect on the elastic properties, the effect discussed here refers to grains with similar composition. For example, small amounts of clay can actually increase the elastic stiffness of an aggregate by acting as weak cementing material at the grain contacts (e.g. Dvorkin *et al.*, 1994). The sorting effect discussed here is independent and additional to the effect of clay content. On the other hand, mechanical compaction induces grain rearrangement, stabilization, and elastic deformation. Elastic deformation by itself does not induce a significant porosity reduction (e.g. Zimmer, 2003), and is induced by increasing confining stress. In contrast, grain rearrangement is an inelastic process that induces significant porosity reduction concomitant with the increment of the elastic stiffness. Grain rearrangement and stabilization tend to increase with depth, whereas sorting does not change with depth. Consequently, the gradual and concomitant variation of porosity and velocity with depth can be an additional criteria to distinguish between the sorting and packing effects.

## **Conclusions**

The theoretical analysis presented in this paper indicates that the effect of sorting on both porosity and the elastic properties of granular materials differs from the effect of packing. This conclusion is also corroborated by the laboratory measurements and subsurface data. According to these results, variations in sorting generate a flatter trend in the velocity-porosity plane, with a slope gentler than the modified Hashin-Shtrikman lower bound (MHSLB). In contrast, variations in packing tend to generate a steeper slope than that predicted using the MHSLB. In general, whereas the MHSLB is a reasonable upper bound for the sorting effect, it constitutes a lower bound for the packing effect.

## **References**

Allen, J. R. L., 2001, Principles of Physical Sedimentology, George Allen & Unwin (Publishers), London, 272 p.

- Avseth, P., J. Dvorkin, G. Mavko, and J. Rykkje, 2000, Rock physics diagnostic of North Sea sands: Link between microstructure and seismic properties. *Geophysical Research Letters*, **27**, 2671-2764.
- Avseth, P., 2000, Combining Rock Physics and Sedimentology for Seismic Reservoir Characterization in North Sea Turbidite Systems. Ph.D. thesis, Stanford University.
- Bachrach, R., 1998, High-resolution shallow seismic subsurface characterization. Ph. D. thesis, Stanford University.
- Bachrach, R., J. Dvorkin, and A. Nur, 2000, Seismic velocities and Poisson's ratio of shallow unconsolidated sands, *Geophysics*, **65**, 559-564.
- Beard, D. C., and P. K. Weyl, 1973, Influence of texture on porosity and permeability of unconsolidated sand. *American Association of Petroleum Geologists Bulletin*, **15**, 2, 349-369.
- Bourbie, T., O. Coussy, and B. Zinsner, 1987, *Acoustics of Porous Media*, Gulf Publishing Co., Houston, 334 pp.
- Brandt, H., 1955, A study of the speed of sound in porous granular media, *Journal of Applied Mechanics*, **22**, 479-486.
- Cumberland, D. J. and R. J. Crawford, 1987, *The Packing of Particles*, Elsevier Science Publishers, Amsterdam.
- Digby, P. J., 1981, The effective elastic moduli of porous granular rocks, *Journal of Applied Mechanics*, **48**, 803-808.
- Dvorkin, J., A. Nur, and H. Yin, 1994, Effective properties of cemented granular materials, *Mechanics of Materials*, **18**, 351-366.
- Dvorkin, J., and M. A. Gutierrez, 2001, Textural sorting effect on elastic velocities, part II: elasticity of a bimodal grain mixture, *Society of Exploration Geophysicist Annual Meeting*, Expanded Abstracts.
- Estes, C.A., G. Mavko, H. H. Yin, and T. Cadoret, 1994, Measurements of velocity, porosity and permeability on unconsolidated granular materials, *Stanford Rock Physics and Borehole Geophysics Project*, annual report, **55**, G1-G9.
- Fraser, H. J., 1935, Experimental study of the porosity and permeability of clastic sediments: *Journal of Geology*, **43**, 910-1010.
- Fuchtbauer, H., 1974, *Sediments and Sedimentary Rocks 1*, in *Sedimentary Petrology* by W. v. Engelhardt, H. Fuchtbauer and G. Muller, Part II. John Wiley and Sons, New York, 464 pp.
- Graton, L. C., and H. J. Fraser, 1935, Systematic packing of spheres –with particular relation to porosity and permeability: *Journal of Geology*, **43**, 785-909.

- Gutierrez, M., 2001, Rock physics and 3D Seismic Characterization of Reservoir Heterogeneities to Improve Recovery Efficiency, Ph. D. dissertation, Stanford University.
- Gutierrez, M., J. Dvorkin, and A. Nur, 2001, Textural sorting effect on elastic velocities, part I; laboratory observations, rocks physics models, and applications to field data, Society of Exploration Geophysicist Annual Meeting, Expanded Abstracts.
- Inman, D. L., 1949, Sorting of sediments in the light of fluid mechanics, *Journal of Sedimentary Petrology*, **19**, 51-70.
- Inman, D. L., 1956, Measures for describing the size distribution of sediments, *Journal of Sedimentary Petrology*, **22**, 125-145.
- Johnson, K. L., 1985, *Contact Mechanics*, Cambridge University Press, 452 pp.
- Kolbuszewski, J., 1948, An experimental study of the maximum and minimum porosities of sands, *Proc. 2<sup>nd</sup> Int. Congress of Soil Mechanics*, **7**, 47-49.
- Krumblein, W. C., 1936, The use of quartile measures in describing and comparing sediments, *American Journal of Science*, **32**, 98-111.
- Krumblein, W. C., 1938, Size frequency distributions of sediments and the normal phi curve, *Journal of Sedimentary Petrology*, **8**, 84-90.
- Macrae, J. C. and W. A. Gray, 1961, Significance of the properties of materials in the packing of real spherical particles, *Br. J. Appl. Phys.*, **12**, 162-172.
- Marion, D., A. Nur, H. Yin, and D. Han, 1992, Compressional velocity and porosity in sand-clay mixtures, *Geophysics*, **57**, 4, 554-563.
- Mavko, G., J. Dvorkin, and T. Mukerji, 1998, *The Rock Physics Handbook, tools for seismic analysis in porous media*, Cambridge University press, New York, pp 329.
- Mindlin, R. D., 1949, Compliance of elastic bodies in contact, *Journal of Applied Mechanics*, **16**, 259-268.
- Murphy, D. W., III, 1982, *Effect of Microstructure and Pore Fluids on The Acoustic Properties of Granular Sedimentary Materials*, Ph. D. dissertation, Stanford University.
- Nur, A., G. Mavko, J. Dvorkin, and D. Gal, 1995, Critical porosity: The key to relating physical properties to porosity I rocks, in *Proc., 65<sup>th</sup> Annual International Meeting, Society of Exploration Geophysicists*, 878.
- Otto, G. H., 1939, A modified logarithmic probability graph for the interpretation of mechanical analyses of sediments, *Journal of Sedimentary Petrology*, **9**, 62-76.
- Pettijohn, F. J., 1975, *Sedimentary Rocks*, 3<sup>rd</sup> edition, Harper and Row publishers, New York, 628 pp.

- Rogers, J. J. and W. B. Head, 1961, Relationship between porosity, median size, and sorting coefficients of a synthetic sand, *Journal of Sedimentary Petrology*, **31**, 467-470.
- Selley, R., 1988, *Applied Sedimentology*, Academic Press, San Diego, 523 pp.
- Sohn, H. Y. and C. Moreland, 1968, The effect of particle size distribution on packing density, *Canadian Journal of Chemical Engineering*, **46**, 162-167.
- Steinour, H. H., 1944, Rates of Sedimentation, *Ind. Engng. Chem.*, **46**, 162-167.
- Timoshenko, S. P., and J. N. Goodier, 1956, *Theory of Elasticity*, 2<sup>nd</sup> edition, McGraw-Hill, New York, 567 pp.
- Trask, P. D., 1932, *Origin and environments of source sediments of petroleum*, Gulf Pub. Co., Houston, 323 pp.
- Visher, G. S., 1969, Grain size distributions and depositional processes, *Journal of Sedimentary Petrology*, **39**, 1074-1106.
- Visher, G. S., 1999, *Stratigraphic Systems: Origin and Application*, Academic Press, New York, 700 pp.
- Walker, B. P., and T. Whitaker, 1967, An apparatus for forming uniform beds of sand for model foundations tests, *Geotechnique*, **17**, 161-167.
- Walton, K., 1987, The effective elastic moduli of a random packing of spheres, *Journ. Mech. Phys. Solids*, **35**, 213-226.
- Wentworth, C. K., 1922, A scale of grade and class terms for clastic sediments, *Journal of Geology*, **30**, 377-392.
- White, H. E., and S. F. Walton, 1937, Particle packing and particle shape, *Journal of the American Ceramists Society*, **20**, 155-166.
- Winkler, K. W., 1983, Contact stiffness in granular porous materials: comparison between theory and experiment, *Geophysical Research Letters*, **10**, 1073-1076.
- Zimmer, M., M. Prasad, and G. Mavko, 2002, Empirical velocity-pressure and porosity-pressure trends in unconsolidated sands, *SEG Annual Meeting, Expanded Technical Program Abstracts*, **72**, 1866-1869.
- Zimmer, M., 2003, *Controls on the Seismic Velocities of Unconsolidated Sands: Measurements of Pressure, Porosity and Compaction Effects*, Ph. D. dissertation, Stanford University.

## ATTACHMENT D

### SEISMIC RESPONSE OF CARBONATE-CEMENTED SANDSTONES

#### **Abstract**

This paper focuses on how carbonate cementation precipitated at key sequence stratigraphic surfaces impact the seismic impedance. Our goals are two-fold: (1) to identify the sedimentological variations within carbonate-cemented sandstones and (2) to quantify their effects on P-impedance. To accomplish this goal, we identify the relationship between carbonate cementation and key stratigraphic surfaces, such as incision surfaces and the flooding surfaces. Next, we use effective medium models to quantify the impact of sediment parameters on P-impedance. We find that the carbonate-cemented sandstones are extremely heterogeneous in nature, even within a depth interval of ~60 meter in our study area offshore Equatorial Guinea, West Africa. Their grain-size, sorting, mineralogy, clay-content, amount of cement and degree of leaching vary considerably. We identify two distinct clusters of data in the P-impedance vs. porosity plane. The carbonate-cemented sandstones from the base of incisions are usually associated with lower shaliness, lower porosity, and higher P-impedance. On the contrary, data from the top of flooding surfaces exhibit higher shaliness, higher porosity and lower P-impedance. The contact cement model fails to predict the trend shown by the later cluster of data. The predictions using the constant-cement model with 1% constant carbonate cement, and the modified stiff-sand model with ~15% critical porosity agree reasonably well with the data. Furthermore, we find that the modified differential effective media model with 40% percolation porosity, and Berryman's self consistent model with 20% percolation porosity fit P-impedance vs. porosity trend of the carbonated cemented sandstones. In conclusion, the carbonate cements are different than the siliciclastic cements in terms of sedimentological parameters, and the commonly used rock physics model for quartz cemented sandstones are not always suitable to predict P-impedance vs. porosity trends for the carbonate-cemented sandstones. We recommend

testing the predictions of rock physics models against data, classified by key stratigraphic surfaces.

## **Introduction**

This paper focuses on how carbonate cementation precipitated at key sequence stratigraphic surfaces, such as flooding surface and incision surfaces, impact seismic impedance. We find that the carbonate-cemented sandstones from the base of incisions usually exhibit lower shaliness, lower porosity, and higher P-impedance. On the contrary, those from the top of flooding surfaces exhibit higher shaliness, higher porosity and lower P-impedance.

Carbonate diagenetic processes, cementation and dissolution, can destroy or enhance the reservoir quality of rock. Precipitation of extensive calcite cement during burial diagenesis can strongly modify the depositional porosity and permeability of a sandstone reservoir. Carbonate cement may make flow paths more tortuous and decrease permeability (Kantorowicz et al., 1987; Saigal and Bjørlykke, 1987; Bjørkum and Walderhaug, 1990; McBride et al., 1995; Morad, 1998) because it is commonly concentrated in layers or concretions rather than being uniformly distributed. As noted by Kantorowicz et al. (1987), these cemented zones may segment a reservoir into relatively isolated compartments, as well as create barriers to lateral or vertical flow of hydrocarbons and formation waters. Generally, cementation is considered in a negative light because it implies a decrease in pore volume, pore size and pore-throat size. However, cementing agents may increase rigidity allowing the sediments to better withstand compaction from overburden stress (Pittman and Larese, 1991). Leaching and subsequent dissolution of carbonate cement can generate the secondary porosity and enhance the permeability.

Although carbonate cements can have a major impact on reservoir quality in siliciclastic reservoirs, no existing rock physics model specifically demonstrates how carbonate cementation affects the seismic impedance. The existing granular media models, such as the contact-cement model and stiff-sand model (Dvorkin et al., 1996; Mavko et al., 1998), and the constant-cement model (Avseth et al., 2005) have been shown to be useful for quartz-cemented sandstones. However, these models have not been tested rigorously for carbonate-cemented sandstones.

We hypothesize that since carbonate cements are different than siliciclastic cements in terms of cement morphology, and they are much more sedimentologically heterogeneous than silica cement, the existing rock model for quartz cement may not be

appropriate to explain these carbonate-cemented sandstones. To our surprise, we find that the constant cement model (Avseth et al., 2005) explains the P-impedance vs. porosity trend in carbonate-cemented sandstones in a field data set. On the other hand, the contact-cement model (Dvorkin et al., 1996; Mavko et al., 1998) fails to explain the data as we expected, specifically when the carbonate-cemented sandstones belong to the top of flooding surfaces/parasequence boundaries. The stiff-sand model (Gal, 1998) overpredicts P-impedance significantly. In addition, the modified differential effective medium model (Mukerji et al., 1995) and the self-consistent model (Berryman, 1995) explain the P-impedance vs. porosity trends for carbonate cementation at the incision surfaces as well as the flooding surfaces. However, it is difficult to interpret sedimentary texture from the modified differential effective medium and the self-consistent models.

We have organized the paper in three different sections. First we review the morphology of the carbonate cement and show how it is different than the silica cement, then; we review the relationship between the carbonate cementation and sequence stratigraphic principles. Next we use the data from a carbonate-cemented sandstone interval at Equatorial Guinea, West Africa to identify what are the key sedimentological parameters varying within carbonate-cemented sandstones followed by sequence stratigraphic interpretations. Finally, we test the effective medium models (granular media models as well as inclusion based models), with the aim to quantify the impact of sediment parameters and key stratigraphic surfaces on seismic impedance.

### **morphology of carbonate cements**

Cements can be placed in two major categories based on their spatial relationship to framework grains: rim cements and occluding cements (Figure D-1). Rim cements, such as quartz overgrowths, exhibit a regular relationship to framework grain boundaries. Occluding cements, such as carbonate cements, fill pores with no preferred relationship to grain surfaces. These differences suggest that rock physics models for quartz-overgrowth might not be appropriate for carbonate-cemented sandstones.

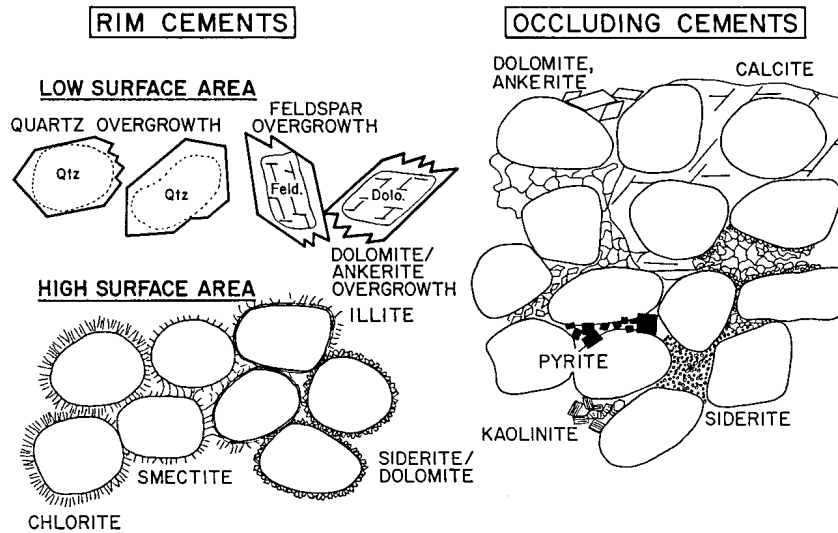


Figure D-1: There are two major categories of cement based on their spatial relationship to framework grains: rim cements (left) and occluding cements (right). The morphology of carbonate cement is distinctive than siliciclastic cement. Carbonate cements occlude in the pore network, and siliciclastic cements form coatings or rims around framework grains.

### Relationship between carbonate cement and sequence stratigraphy

In this section, we review one geological theory that explains role of sequence stratigraphy in precipitation of carbonate cements in siliciclastic sequences. However, there are at least two other geological theories that explain the origin of carbonate cements.

Sequence stratigraphic concepts have direct impact on diagenesis (Giles, 1997). The direct impact occurs during the formation of Type I sequence boundaries (i.e. an unconformity and its correlative conformity) and during the formation of maximum flooding surfaces (maximum landward extent of marine facies within any sequence) (Figure D-2). A type I sequence boundary is created by a drop in relative sea-level, and this gives rise to an additional hydraulic head. An increase in hydraulic head drives pore waters of meteoric origin into the sedimentary basin. As a consequence, sediments in the vicinity of unconformity are subjected to alteration by meteoric fluids. Mixing zones are driven basinward by drop in relative sea-level. During the subsequent rise in relative sea-level, mixing zones are driven landward. The decrease in the hydraulic head accompanying the relative sea-level rise reduces the potential for meteoric water to penetrate into the basin. Such mixing zones have a major impact on the carbonate minerals present in the sediments. Meteoric waters are more likely to be supersaturated with silica and undersaturated with respect to calcium carbonate (Walderhaug and Bjorkum, 1992).

Maximum flooding surfaces are formed at times of maximum rise of relative sea-level in a depositional sequence (Wagoner et al., 1988) and consequently result in hiatus or relative starvation of siliciclastic sediments in a basin. Such hiatus often manifest themselves as marine hardgrounds (Loutit et al., 1988). Marine hardgrounds are characterized by carbonate cements formed due to prolonged residence time of the sediments close to the sediment-water interface (Taylor et al., 2000), and carbonate bioclastic lags (Kertzer et al., 2002). Reservoir quality of sandstones below sequence boundaries can be improved owing to percolation of meteoric water and dissolution of unstable framework grains and cements (Kertzer et al., 2003).

There is no unanimous agreement about role of sequence stratigraphy in carbonate cementation in siliciclastic sediments among the geologists. Two other theories that explain the origin of carbonate cementation in sandstones are briefly mentioned below.

**1. Compaction and de-watering:** This hypothesis suggests that the fluid necessary for carbonate cementation is obtained from compaction and dewatering of neighboring shale layers. But, one pore volume of calcite cement requires at least 100,000 to 300,000 pore volumes of water. Thus compactive influx is inadequate as a source for such large volumes of fluid (Berner, 1980; Bjorkum and Walderhaug, 1990).

**2. Local diffusion process:** This hypothesis considers that the calcium from carbonate fossils migrates to the nucleation site by means of local diffusion (Bjorkum and Walderhaug, 1990). Sometimes carbonate cementations are observed in greater depth of basins, which is beyond the reach of meteoric water. The advantage of the local diffusion process is that it explains carbonate cementation at greater depth beyond the percolation limit of meteoric water.

In the present study area, there is abundance of fossil debris in carbonate-cemented sandstones, as evident from core observations. We think that the fossil debris act as precursor of carbonate cementation at marine flooding surfaces (para-sequence boundaries). The goal in this paper is to identify the seismic response of these carbonate cements associated with the key stratigraphic surfaces.

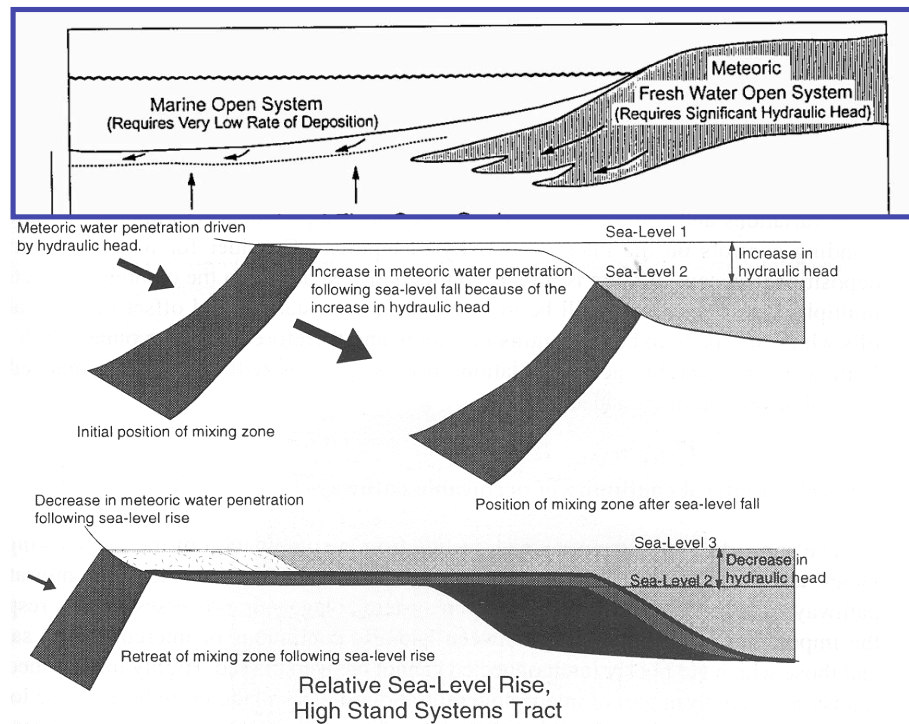


Figure D-2: Relationship between sequence stratigraphy and mixing zone. During relative sea-level fall (low stand system tract), mixing zone penetrate basin-ward. On the contrary, there is a retreat of mixing zone during relative sea-level rise (high stand system tract). Mixing zones are characterized by solution supersaturated with quartz and undersaturated with respect to calcium carbonate. (This figure is taken from Giles, 1997)

## High Resolution Sequence Stratigraphic Interpretation

We perform high-resolution sequence stratigraphic interpretation followed by rock physics analysis of carbonate-cemented sandstones. Our study integrates data from different scales, such as, 3D post-stack seismic, well logs, cores, thin-section, XRD and grain-size data. The data used in present paper are from turbidite slope channels offshore Equatorial Guinea, West Africa.

The reflection seismic data shows the geometry of a min-basin formed by erosion of channel during fall in relative sea level (Figure D-3). The seismic reflections, calibrated with well logs and core observations, demonstrate that cemented sandstones below uncemented sandstones generate significant impedance contrast. Figure D-3 shows that reflections from overlying mudstones to underlying uncemented sandstones are characterized by a decrease in acoustic impedance. On the contrary, reflections from overlying uncemented sandstones to underlying cemented sandstones are characterized

by an increase in acoustic impedance. We find that the cemented sandstones are a seismically mappable unit over a lateral distance of about 100s of meter. Figure D-4 shows the geobody we mapped from AVO intercept and gradient volumes using the well control. The geobody shows average amplitude over a window of 6 ms above and below the reflection event from uncemented sandstone to cemented sandstone.

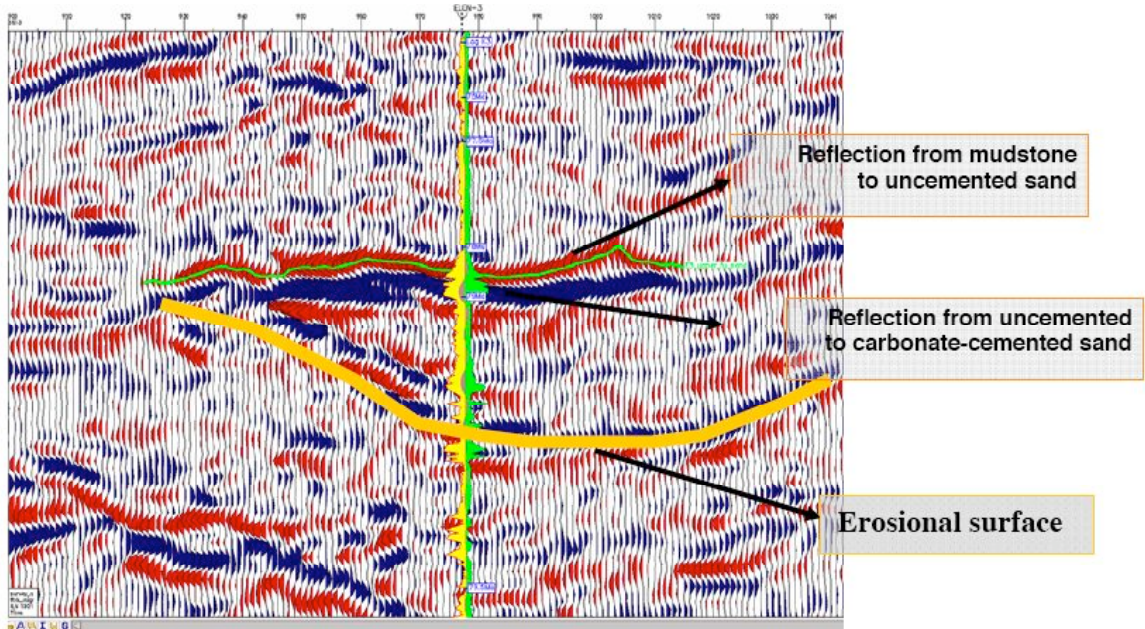


Figure D-3: Post-stack, time-migrated seismic section showing sediments deposited in the mini-basin developed on continental slope at Equatorial Guinea. The orange curve represents an erosional surface. The well-logs (yellow: gamma-ray and green: resistivity) can be used to identify the vertical stacking of sands. The synthetics (pink curve) displayed at the well is of reverse polarity. Cemented sands are acoustically harder (blue event) than uncemented sands (red event)

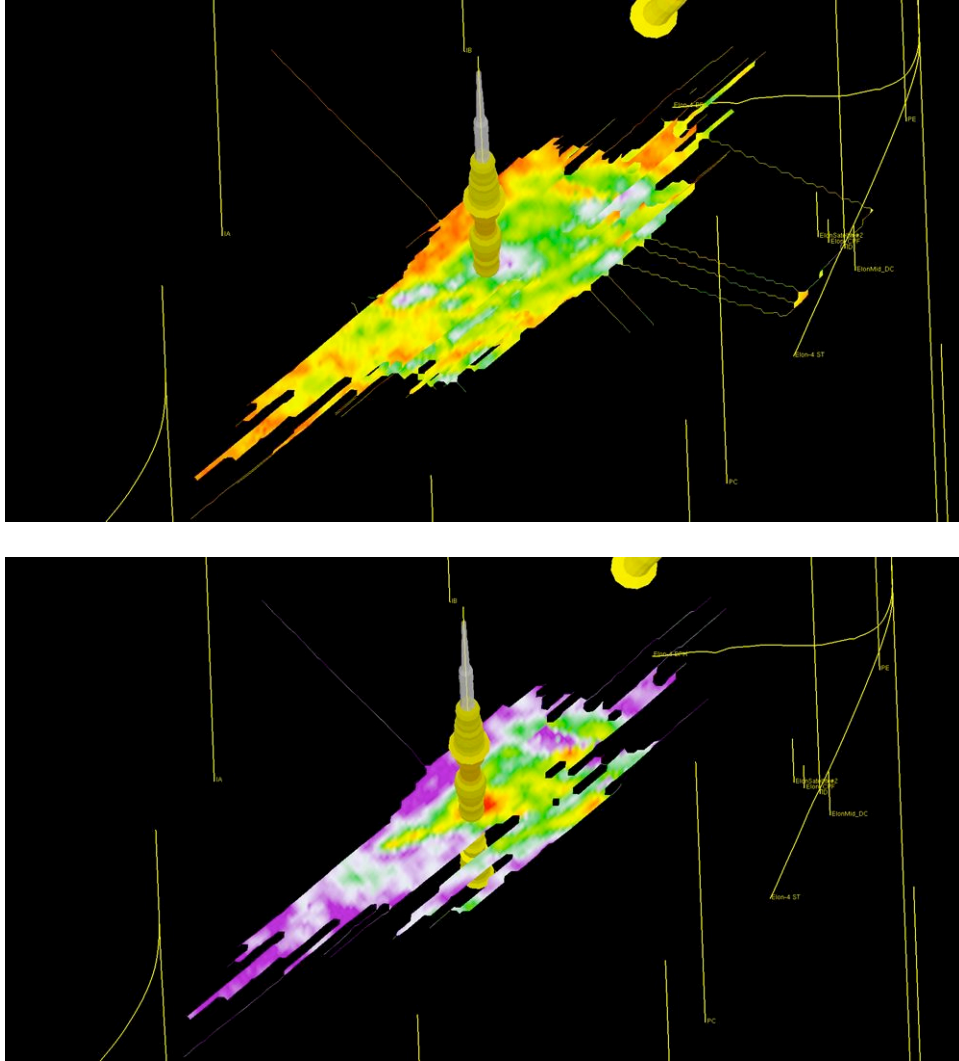


Figure D-4: The geobody mapped from seismic data characterizing cemented sand interval. The maps show average amplitude over a window of 6 ms above and below the reflection event. Top: geo-body mapped from AVO intercept volume; Bottom: geo-body mapped from AVO gradient volume.

The well logs calibrated with core observations reveal that carbonate-cemented sandstones have lower porosity than the coarser uncemented lithofacies. This could be due to cementation occluding the pore network. In addition, we observe very high velocities ( $\sim 4500$  m/sec) at the well logs are associated with carbonate cement. Figure D-5 shows the P-impedance vs. total porosity of six different lithofacies: thick sand, thick-thin sand, thin sand, carbonate-cemented sand, conglomerate and mudstone. The different lithofacies were identified by Lowe (2004) based on grain-size, bed-thickness and sand:shale ratio from core observations of our study area. These facies are usually common in a turbidite fining-upward sequence. We observe that the carbonate-cemented sandstones exhibit higher P-impedance than other lithofacies at the well (Figure D-5).

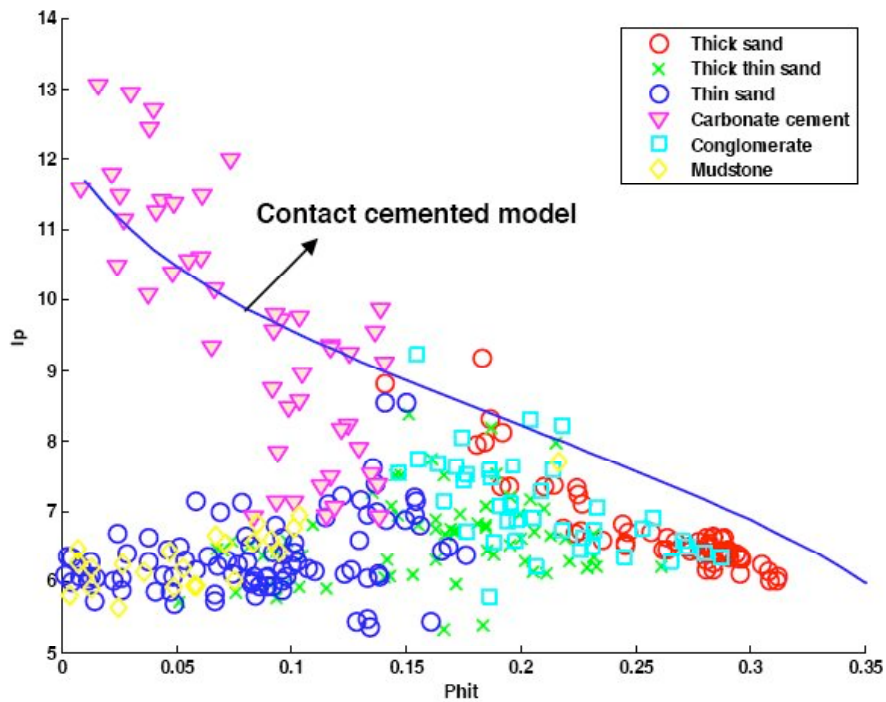
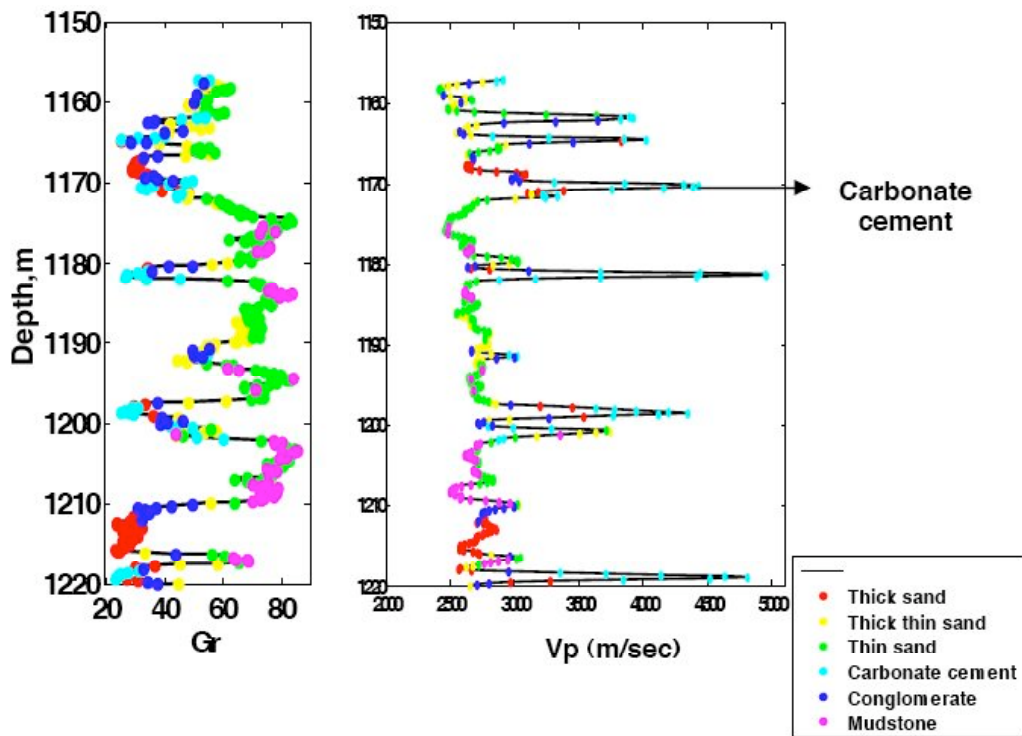


Figure D-5: Top: well log response containing cemented sand intervals; Bottom: P-impedance ( $I_p$ ) vs total porosity ( $Phit$ ) colorcoded by different facies. Note that the cemented sandstones (purple triangles) have higher P-impedance than other lithofacies. The contact cement model (Dvorkin et al., 1996) does not fit the cemented sandstones with relatively lower  $I_p$ .

In the present section, we observe that the carbonate cementation in siliciclastic sediments has distinct signatures on post-stack seismic data and well logs. The carbonate-cemented sandstones beneath uncemented sandstones can generate significant impedance contrast, and can be persistent over 100s meter of lateral distance. On the well log, carbonate-cemented sandstones exhibit higher velocities and P-impedance than other lithofacies. We also observe that the most commonly used cemented sandstone model (contact cement model formulated by Dvorkin et al., 1996) do not always fit the P-impedance vs. porosity trend of carbonate-cemented sandstones. This model fails when carbonate-cements have relatively lower P-impedance. In the next section, we identify the variations in key sedimentological parameters within the carbonate-cemented sand interval.

### **Key Sedimentological Parameters Within Carbonate-cemented Sandstones and their Impact on P-impedance**

In this section, we identify the key sediment parameters that vary within carbonate-cemented sandstone interval and demonstrate how they affect seismic velocities measured at the well. In the next section, we will test different rock models with the well data with the goal to relate the sediment parameters with elastic properties.

We identify the following variations in sedimentological parameters within carbonate-cemented sandstone interval.

1. Mineralogy of cement ( calcite and ankerite)
2. Amount of cement
3. Clay content
4. Position of cements at different stratigraphic surfaces (incision surface and flooding surface)
5. Grain size and sorting variations

The impact of each of these sediment parameters on seismic velocities and porosities are described below.

#### **1. Mineralogy of cement**

The XRD analysis of 11 samples from the carbonate-cemented sandstone interval show that carbonate cement mineralogy varies from Calcite (Ca-rich) to Ankerite (Mg-rich) (Figure D-6A). Ankerite is an intermediate product between calcite (the calcium-

rich end member) and dolomite (the magnesium-rich end member). The samples below 1190 meter depth are mostly rich in ankerite. The other dominant phases in cemented-sand include quartz, K-feldspar and plagioclase. There are trace amount of pyrite, illite, smectite, kaolinite and chlorite.

Figure D-6B shows the  $V_p/V_s$  of carbonate-cemented sandstones from well logs. The  $V_p/V_s$  predicted by Greenberg and Castagna (1992) for different lithologies, such as, sandstone, shale, limestone and dolomite are also plotted in the same figure. The  $V_p/V_s$  of calcite-cemented sandstones have slightly higher  $V_p/V_s$  trend predicted by the model for limestone. The  $V_p/V_s$  of ankerite-cemented sandstones show a large scatter. The scatter in  $V_p/V_s$  for same mineralogy could be due to variation in other sediment parameters.

Figure D-6C shows P-impedance ( $I_p$ ) vs. total porosity ( $\phi_{it}$ ) from the same well logs, color-coded by cement mineralogy. The samples below 1192 meter depth in the well are mostly rich in ankerite cement. We observe that calcite-cemented sands and ankerite-cemented sands have different trends in P-impedance vs. porosity plane. The sandstones rich in ankerite cement display higher intercept than the sandstones rich in calcite cement.

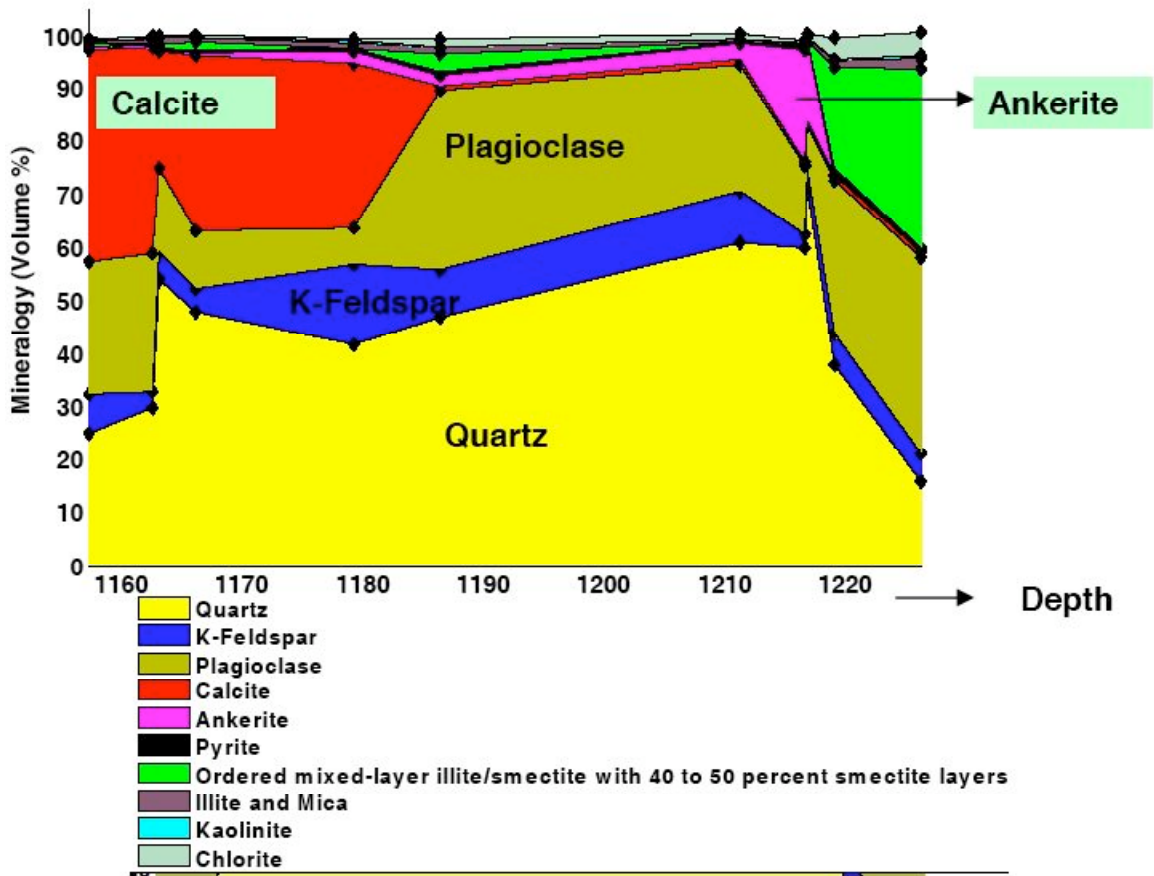


Figure D-6A: XRD analysis of 11 samples from the carbonate-cemented sandstone interval show two different mineralogy of carbonate cement: Calcite and ankerite.

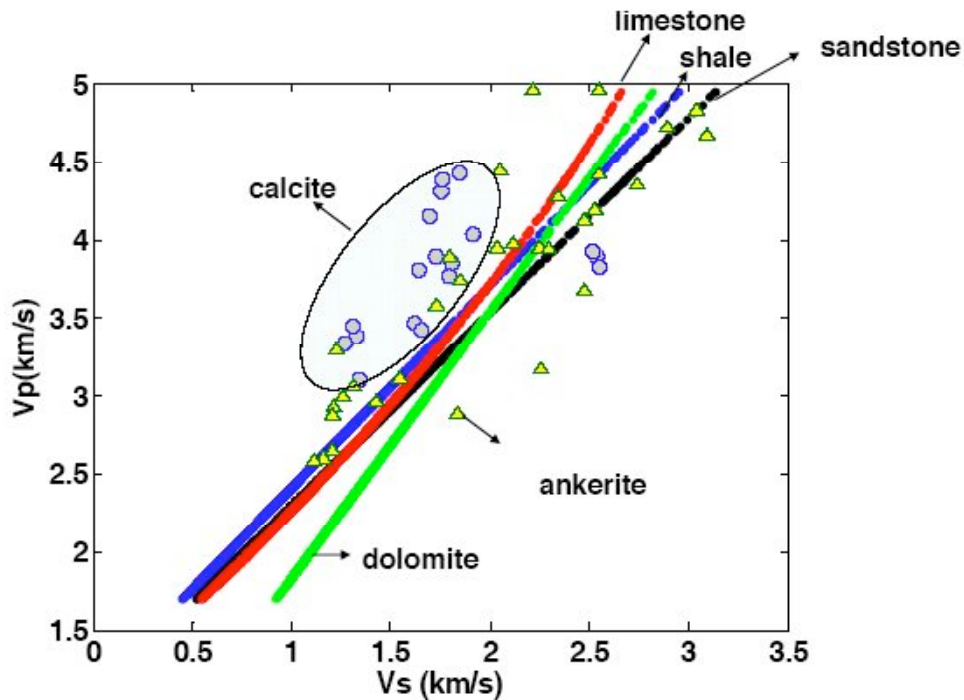


Figure D-6B: Comparisons of the  $V_p/V_s$  of carbonate-cemented sandstone from well logs with the  $V_p/V_s$  given by Greenberg and Castagna (1992). The blue circles are from the calcite-interval and yellow-triangles from the ankerite interval. The data show wide range of scatters.

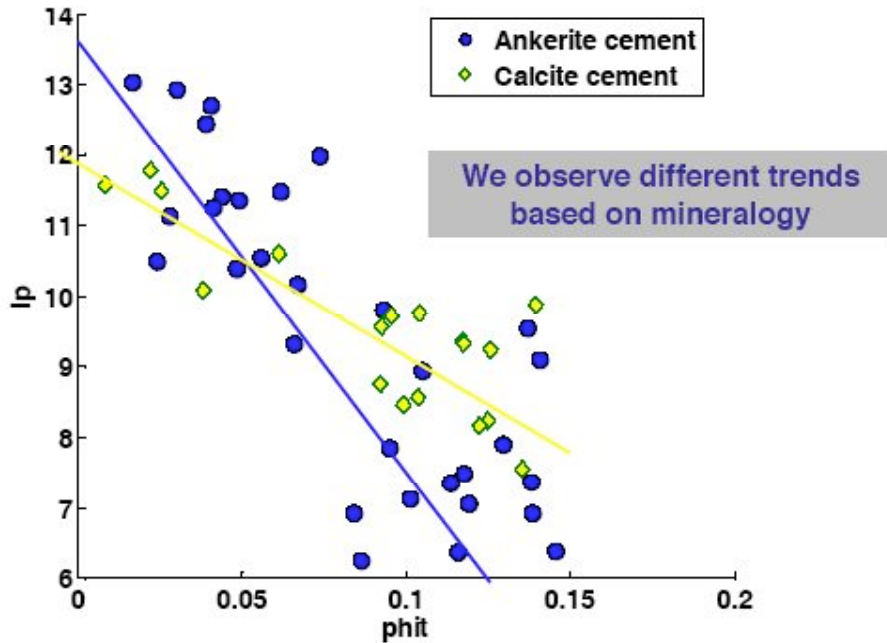


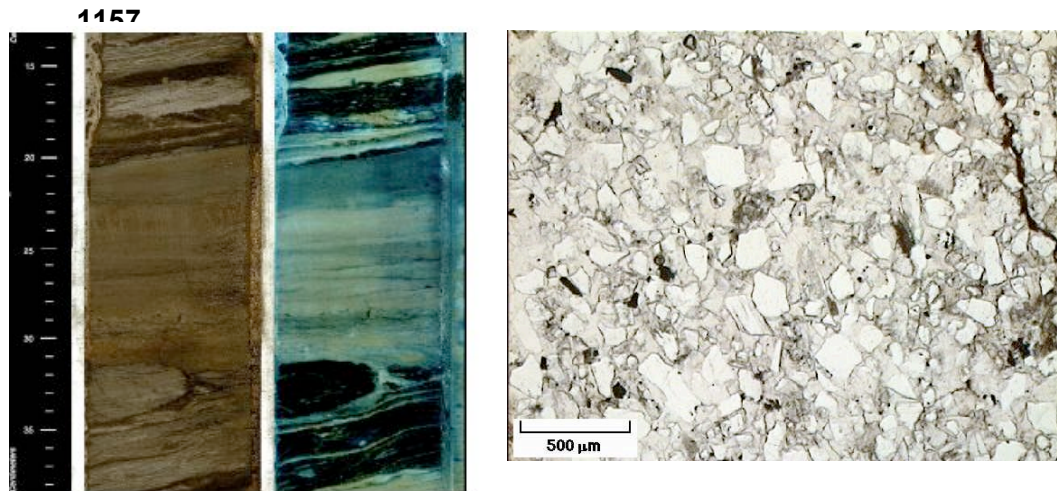
Figure D-6C: P-impedance ( $I_p$ ) vs total porosity ( $phit$ ) from well logs color-coded by cement mineralogy. The blue circles are from the calcite cemented interval and the yellow-triangles from the ankerite cemented interval. The data from different cement mineralogy indicate different intercepts.

## 2. Amount of cement

The XRD analysis indicates that amount of cement is highly variable. It can occupy 2% to 40% of solid volume of rock (Figure D-6A). Figures D-7A, D-7B and D-7C show thin sections at different depths with varying amount of carbonate cements and porosities. Carbonate cements, when present is higher amount (~40 % of rock volume), can occlude all the interparticle porosity (Figure D-7A). Thin-sections show that ankerite is more prone to leaching (dissolution) than calcite. Leaching reduces cement volume and can create secondary porosity. Figure D-7B shows incipient leaching of ankerite cement creating a small secondary porosity. Extensive leaching of ankerite cement leads to significant secondary porosity (Figure D-7C). In general, higher the cement volume, lower is the porosity. The secondary porosity increases with an increase in degree of leaching.

Figure D-7D shows how the amount of cement controls P-impedance. The amount of cement is obtained from XRD analysis at different depths. P-impedances are obtained from the well logs at the same depths as XRD samples. We assume that all the carbonates

occur as cements, which may not be always true. We observe that the P-impedances from 2 Mrayls to 13 Mrayls with carbonate-cement volume increasing from 2% to 40%.



The calcite cement (40 percent of solid volume) occludes all interparticle pore space.

Figure D-7A: Left: core photo in plain light and ultra-violet light showing laminations. Right: Thin-section at depth 1157.25 m. Calcite cement occludes all porosity in the sandstone.

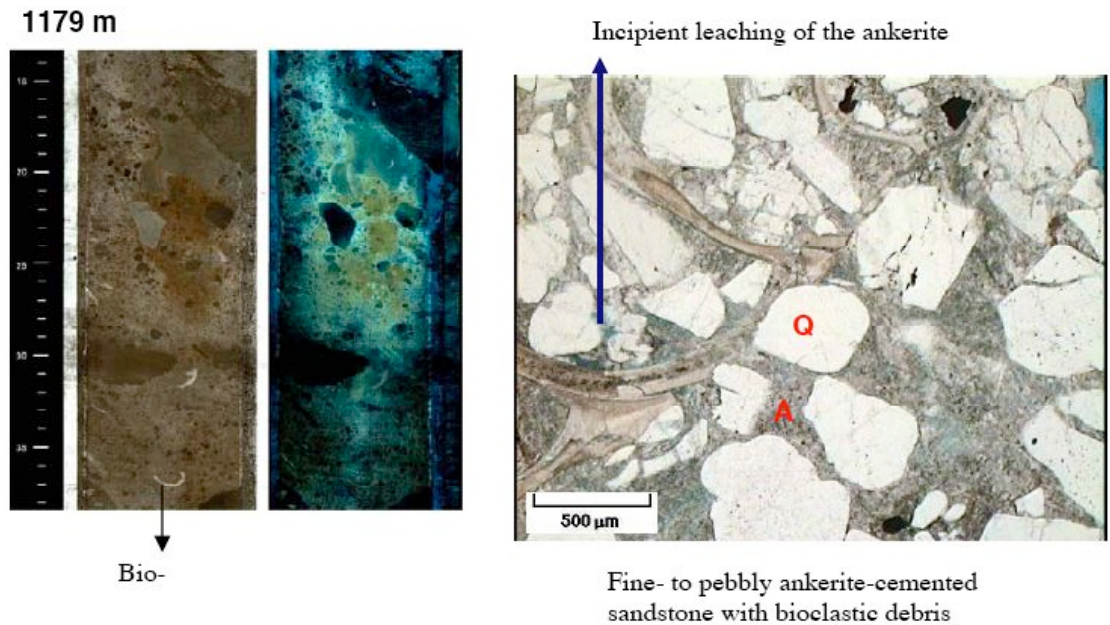


Figure D-7B: Left: core photo in plain light and ultra-violet light. Right: Thin-section at depth 1179.25 m. Blue indicates porosity. Incipient leaching of ankerite cements creating secondary porosity.

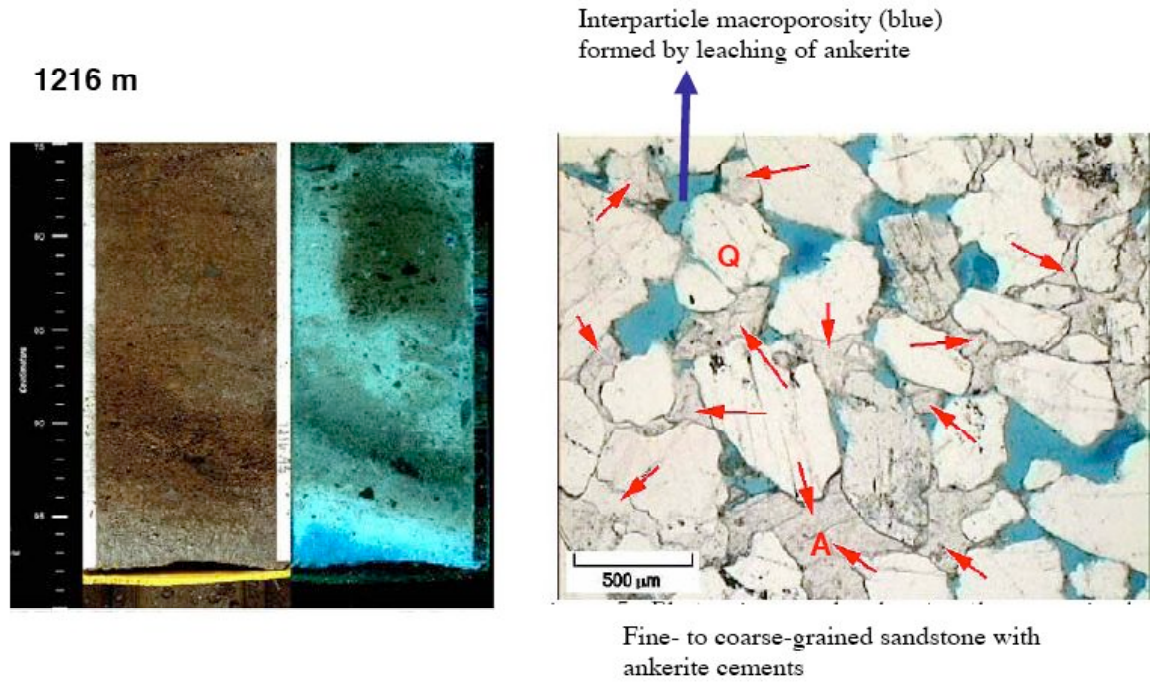


Figure D-7C: Left: core photo in plain light and ultra-violet light. Right: Thin-section at depth 1216.85 m. Blue indicates porosity. Leaching of ankerite cements creates significant secondary porosity. The red arrow indicates ankerite cement and porosity created by dissolution at the grain contacts.

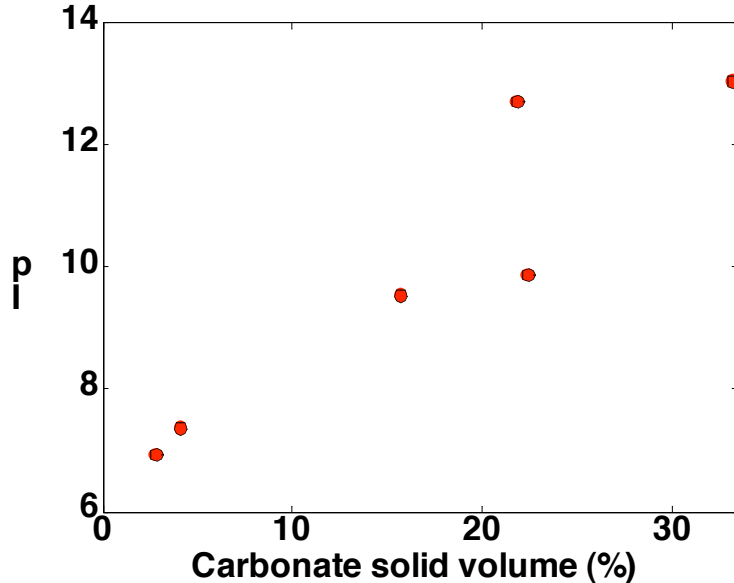


Figure D-7D: Carbonate solid volume (%) vs. P-impedance ( $I_p$ ). The carbonate solid volume (%) is obtained from XRD analysis and  $I_p$  is obtained from corresponding depth at the well. We observe that  $I_p$  increases from 6 Mrayls to 13 Mrayls with carbonate volume increasing from 2 to 35 %.

### 3. Clay content

In order to understand the effect of clay-content on P-impedance, we crossplot P-impedance vs. porosity measured from well logs color-coded by gamma-ray index. We assume that gamma-ray index is an indicator of clay-content in the present data. We observe that cemented sands with higher clay content are associated with higher porosity which contradicts the usual relationship between clay content and porosity (Figure D-8). Usually increasing shaliness adds clay in the pore-network and decreases porosity (Avseth et al., 2005). In this case, we think that sandstones with lower shale content are more prone to cementation; hence, exhibit reduced porosities with cements occluding the pore space. The samples with higher total porosity show lower P-impedance (Figure D-8).

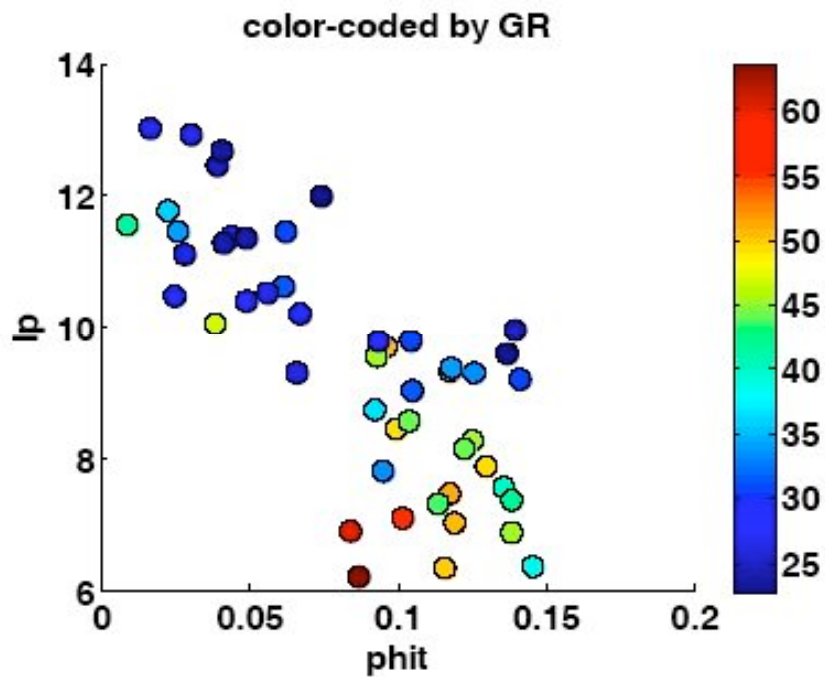


Figure D-8: P-impedance ( $I_p$ ) vs total porosity ( $phit$ ) from well logs color-coded by gamma ray index. We think that the sandstones with lower shale content are more prone to cementation, hence, exhibit reduced porosities.

### 4. Position of cements with respect to stratigraphic surfaces

We find that reservoir quality depends on position of cements with respect to flooding surfaces. A flooding surface is defined as a surface created in response to an increase in water depth and typically bounds parasequences (Posamentier & Allen, 1999). A flooding surface is also termed as parasequence boundary. We identify the flooding

surfaces based on the patterns in gamma-ray logs (Figure D-9). Usually, each para-sequence is characterized by a fining-upward pattern on gamma-ray log and a flooding surface is identified when gamma-ray index reaches its maximum value. On the contrary, an incision surface is characterized by minimum value of gamma-ray index. Figure D-9 also shows P-impedance ( $I_p$ ) vs total porosity ( $\text{phit}$ ) from well logs along with Hashin-Shtrikman upper and lower bounds (Mavko et al., 1988) computed for a mixture of calcite and water. The data shown in this figure are taken from a carbonate-cemented sand interval. We observe two distinct clouds of data in the P-impedance vs. porosity plane. The data with purple stars occur at the base of incision surface and have lower porosity and higher  $I_p$ . The data with red squares occur at the top of flooding surface and have higher porosity and lower  $I_p$ . The porosity is selectively enhanced in the carbonate-cemented sandstones when they occur at top of the flooding surfaces. We think that leaching (dissolution of cement) is facilitated by its proximity to the flooding surface, thereby, creating secondary porosity.

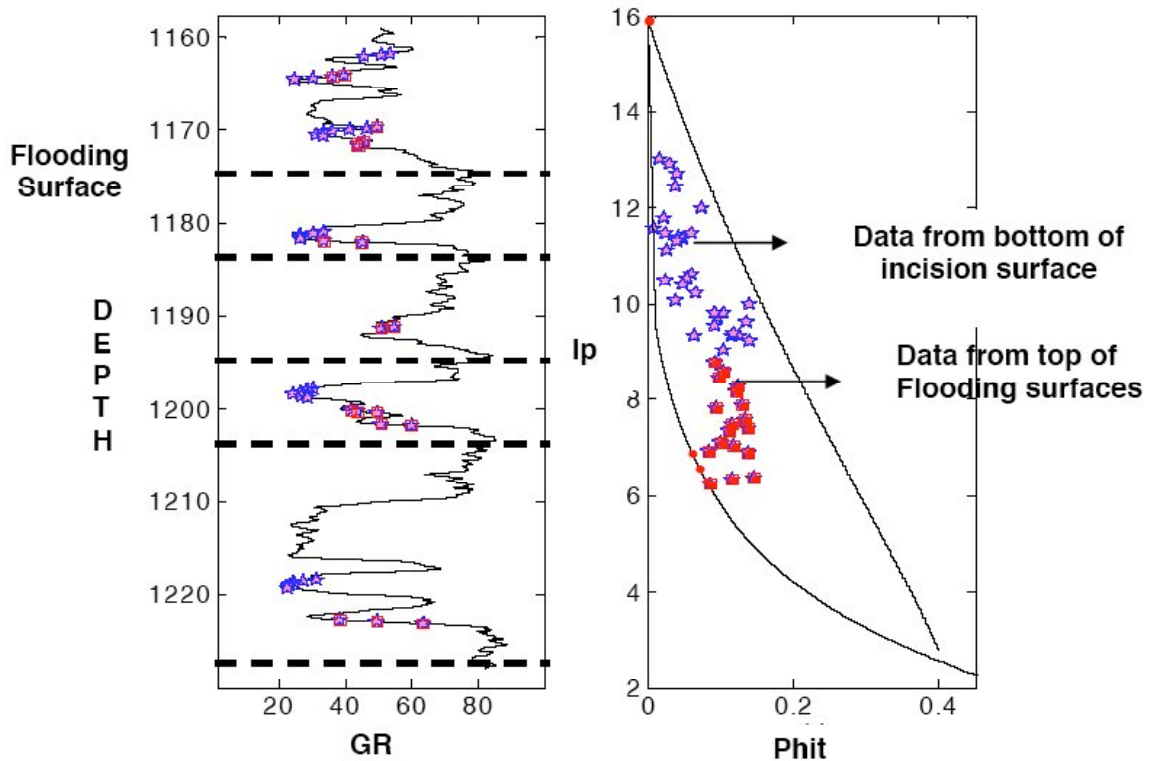


Figure D-9: Left: Gamma ray log with para-sequences bounded by flooding surfaces. Right: P-impedance ( $I_p$ ) vs total porosity ( $\text{phit}$ ) from well logs with Hashin-Shtrikman upper and lower bounds computed for a composite of quartz and water. The data belong to cemented sand interval. The data with purple stars occur at the

base of incision and have lower porosity and higher  $I_p$ . The data with red squares occur at the top of flooding surface and have higher porosity and lower  $I_p$ .

**5. Grain size and sorting variations**

Grain size and variations in grain-size (sorting) are important constituents of sedimentary texture. In present study, we obtain these parameters from laser particle size analysis (LPSA). Figure D-10A shows gamma-ray and P-impedance in the well along with median grain size and sorting obtained from LPSA of core samples. The grain-size is expressed in phi-scale (negative  $\log_2$  of grain-size measured in millimeter). There are different quantitative definition of sorting in the sedimentology literature (eg., Otto, 1939; Inman, 1957, Folk and Ward, 1957 and McCammon, 1962). We use Folk and Ward (1957) method to compute sorting coefficient as described below.

$$\text{Sorting coefficient} = (p_{84} - p_{16})/4 + (p_{95} - p_5)/6.6 \tag{1}$$

where, p represents percentile of grain size expressed in the phi-scale. A higher value of sorting coefficient represents poor sorting and a lower value of sorting coefficient represents better sorting.

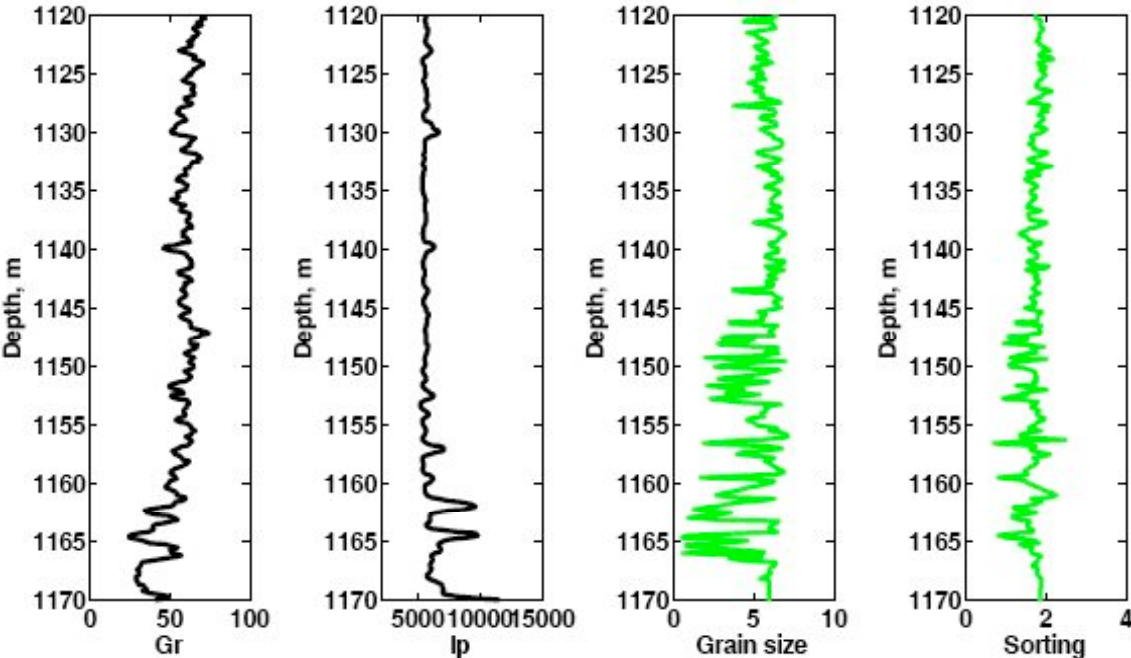


Figure D-10A: Gamma-ray (Gr) and P-impedance (Ip) in the well along with median grain size and sorting coefficient.

Figure D-10B shows the effect of grain-size and sorting on porosity and P-impedance on the carbonate-cemented sandstone. We observe that grain-size have practically no influence on porosity and P-impedance with present data. However, better-sorted cemented sandstones are usually associated with higher porosity. Figure D-10C shows sorting coefficient vs. grain size color-coded by P-impedance. In this figure, the grey points indicate data from all the lithofacies within a sequence, while the colored points indicate data only from the carbonate-cemented sandstones. We observe an inverted ‘V’ pattern in the grain size vs. sorting domain. Furthermore, we observe that sorting is better for coarse and fine end-members of grain-size. The fine end-members have better sorting than coarse end members. The lowest sorting coefficient, 0.75, is observed when the grain-size is very fine. On the contrary, the coarsest end member has sorting value 1.25, higher than the finest grain-size. The sorting becomes poorer by mixing different grain-sizes. Sorting coefficient decreases from 0.75 to 2.75 as coarse fractions are added to the fine fractions. This coefficient increases from 1.25 to 2.75 as fine fractions are added to the coarse grains.

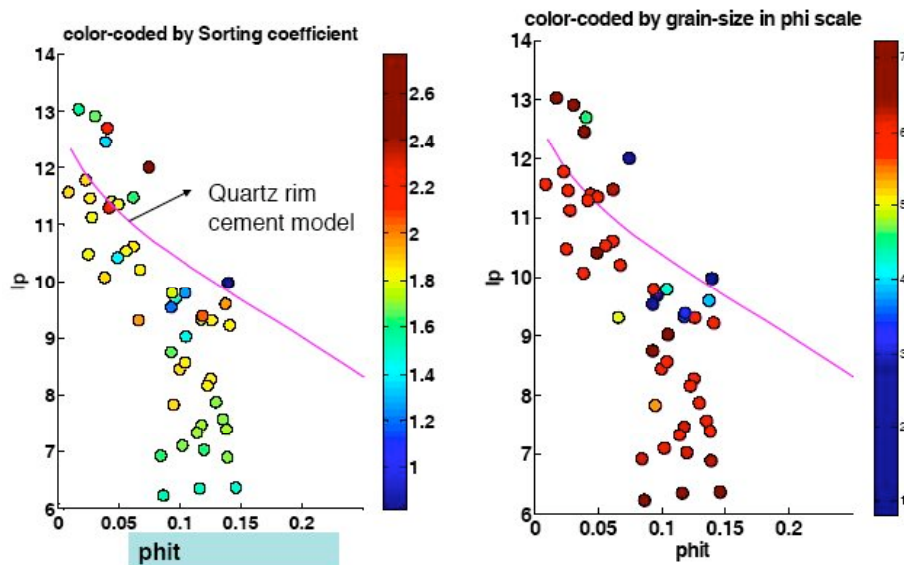


Figure D-10B: Left: P-impedance ( $I_p$ ) vs. total porosity (phit) color-coded by sorting coefficient. The sandstones with higher porosity are usually better sorted. Right: P-impedance ( $I_p$ ) vs. total porosity (phit) color-coded by median grain-size.  $I_p$  is not affected by grain-size.

sorting vs. grain-size colorcoded by P-impedance (IP)

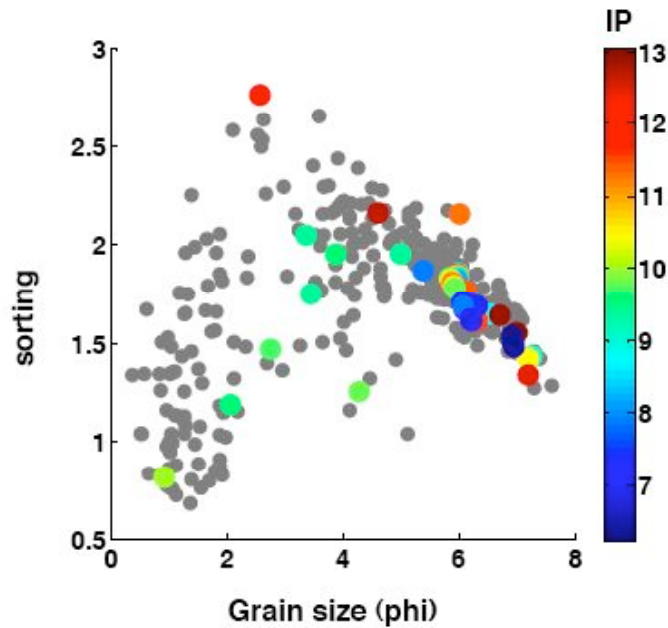


Figure D-10C: sorting coefficient vs. grain size (phi) color-coded by P-impedance (IP). The grey points indicate data from all the lithofacies within a sequence, whereas, the colored points indicate data from carbonate-cemented sandstones. The data show an inverted 'V' in the grain size- sorting domain.

In this section, we have shown how different sedimentological parameters, such as, mineralogy, cement volume, shaliness, sorting, and position of cement in stratigraphic surfaces affect porosity and P-impedance of carbonate-cemented sandstones. One interesting observations from the data mining is that there are two distinct clusters in the P-impedance vs. porosity plane. The data near the top of flooding surface usually exhibit higher porosity, higher shaliness and lower P-impedance. They form separate cluster from the data at the incision surface, which are characterized by lower porosity, lower shaliness and higher P-impedance. The following section aims to identify appropriate rock physics models that will explain the variation in these sediment parameters.

### **Rock Physics modeling of carbonate-cemented sandstones**

In the above section, we have shown that carbonate-cemented sands are highly heterogeneous. The cement mineralogy, cement volume, clay-content and sorting is highly variable. It is challenging to incorporate all these sedimentological variations in a single rock physics model. In this section, we test how different granular media models for cemented sandstones as wells as inclusion models explain the P-impedance vs. porosity trend in the carbonate-cemented sandstones.

## **(A) Testing granular media models**

We test three different granular media models: the contact cement model (Dvorkin et al., 1996), the stiff-sand model (Gal et al., 1998), and the constant-cement model (Avseth et al., 2000) in order to evaluate how the  $I_p$ -porosity trends predicted by these models correspond to the data from carbonate-cemented sandstones. These models have been shown useful for quartz cemented sandstones (Avseth et al., 2005).

Figure D-11 shows  $I_p$  and porosity measured at the well in carbonate-cemented sandstones, along with the modified upper and lower Hashin-Shtrikman bounds computed for a mixture of calcite and water. The  $I_p$  vs. porosity trends predicted by the contact cement, constant cement, and stiff-sand models are also shown in Figure D-11. We observe that the contact cement model (Dvorkin et al., 1996) does not fit the data at all porosity range. The identification of incision-surface and flooding surface reveal that the Dvorkin's cemented sand model explains the  $I_p$ -porosity trend of carbonate-cemented sands deposited at the incision-surface. However, this model fails to explain the  $I_p$ -porosity trend of data deposited at the top of flooding surfaces.

The reasons the contact cement model fail to fit this data could be as follows:

1. Cement geometry: Dvorkin's cement model is derived for cement at grain contact or coating (rim) around grain. Carbonate cement in our study area are mostly occluding as observed from thin sections, thereby, violating the assumption of ideal geometry.
2. Cement volume: Dvorkin's cement model is only applicable for very low amount of cement. Present dataset have cement volume varying from 2 to 40 %.
3. Porosity range: Granular media models, such as, Dvorkin's contact cement model is valid for medium to high porosity sands (20 to 40 % porosity). Present dataset shows much lower porosity range (0 to 15 %) due to extensive cementation.

The stiff-sand model (Gal et al., 1998) also fails to explain the  $I_p$ -porosity trend of the carbonate-cemented sand (Figure D-11). This model over-predicts P-impedance. Although the stiff-sand model does not fit the  $I_p$ -porosity trend in our data, we can obtain a reasonable fit by changing critical porosity from 40 % to 15 % in this model (Figure D-12). We call this modified stiff-sand model in this paper. The heuristic argument for changing critical porosity is that the onset of carbonate cementation starts at much lower

porosity (about 15 %). The modified stiff-sand model provides a better fit to the data than original stiff-sand model (Figure D-12).

The constant-cement model (Avseth et al., 2000) with 1% constant cement explains the  $I_p$ -porosity trend in these data reasonably well (Figure D-11). The advantage of constant cement model is that it considers sorting variation, and, from our previous section on data mining we know that sorting coefficient is variable from 0.75 to 2.75 within the carbonate-cemented sandstones. However, the disadvantages of using constant cement model are as follows:

1. Constant cement volume: The constant cement model of Avseth et al (2000) is valid for constant amount of cement which contradicts present data. The present data has highly variable (2-40%) cement volume.
2. Low cement volume: The constant cement model (Avseth et al., 2000) is applicable only for weakly cemented rock (1-5% cement volume).
3. Porosity range: The granular media models, such as, constant cement model is valid for medium to high porosity sands (20 to 40% porosity). Present dataset have lower porosity range (0 to 15%) due to extensive cementation.

The above reasons suggest that although the constant cement model explains the  $I_p$ -porosity trend in the data, this model might fit the present data for wrong reasons. Nevertheless, the constant cement model can be a useful tool to explain the  $I_p$ -porosity trend of carbonate-cemented sandstones in present study area.

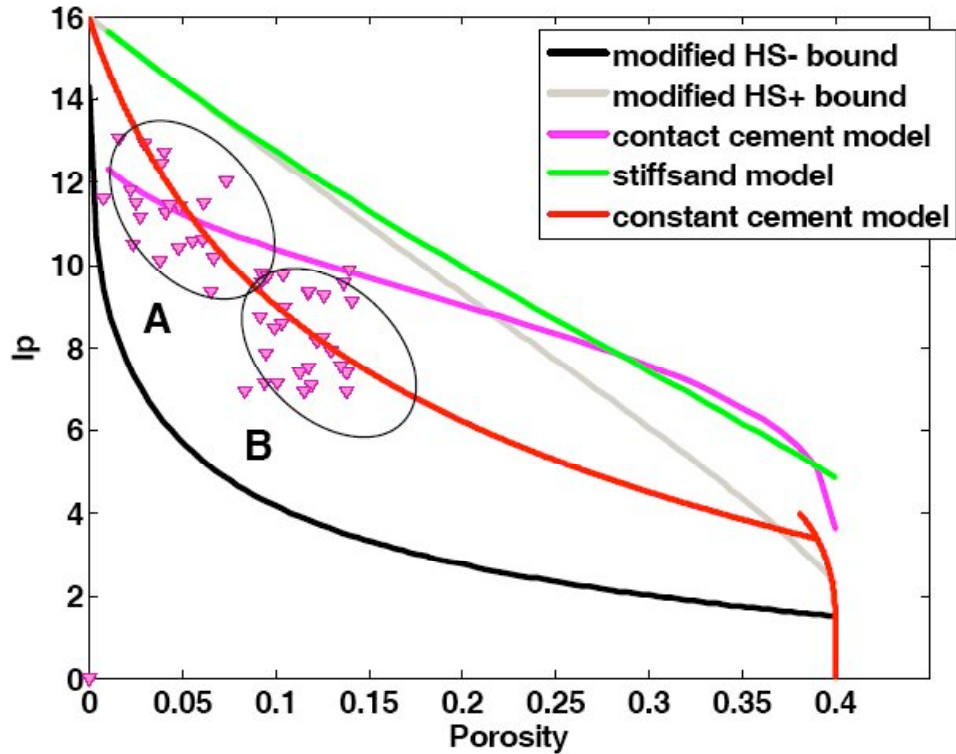


Figure D-11: Comparisons of  $I_p$  and porosity of carbonate-cemented sandstone with those predicted by existing rock physics models. The clusters A and B represent data from the incision-surfaces and top of the flooding-surfaces respectively. The contact cement model (magenta line) does not fit the data from cluster B. The stiff-sand model (green line) overpredicts  $I_p$ . The constant cement model with 1% constant cement (red line) fits both clusters A and B.

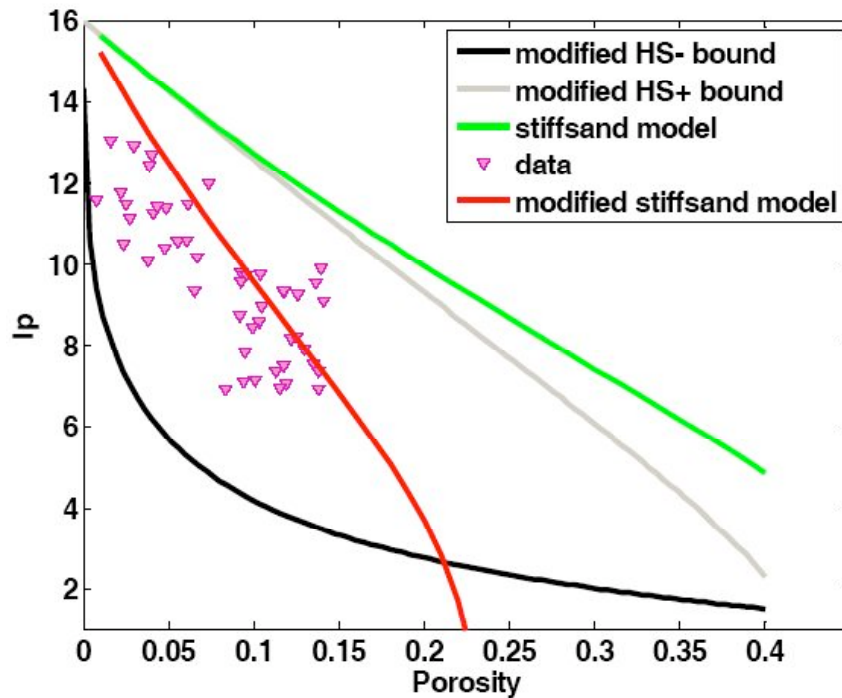


Figure D-12: Comparisons of  $I_p$  and porosity of carbonate-cemented sandstone with those predicted by the stiff-sand model (green) and the modified stiff-sand model (red). The modified stiff-sand model is obtained by changing critical porosity from

40 % to 15%. The modified stiff-sand model provides a better fit to the data than original stiff-sand model.

### (B) Differential effective media models and self-consistent models

Granular media models are mostly applicable for medium-high porosity sands. Therefore, they might not be suitable for the data in lower porosity regime (porosity < 15 %). We test how the differential effective media (DEM) models and the self-consistent models (SCM) explain the P-impedance vs. porosity trend in carbonate-cemented sandstones.

Figure D-13 shows the data along with predictions of  $I_p$  at different porosities using conventional DEM and modified DEM (Mukerji et al., 1995). The conventional DEM overpredicts  $I_p$  significantly. The modified DEM with 40 % percolation porosity, background matrix consisting quartz and calcite, and inclusions with aspect ratio 0.5 provides a reasonable fit to these data.

Figure D-14 shows how the predictions using SCM (Berryman, 1995) compares with data from carbonate-cemented sandstones. We use the background consisting quartz, calcite and clay, and aspect ratio 0.5 for all the phases to compute the effective elastic moduli. The original SCM has percolation behavior at porosity ~50 % and overpredicts  $I_p$  significantly. We obtain modified SCM by lowering the percolation porosity ~ 20 %. The modified SCM provides a reasonable fit to these data.

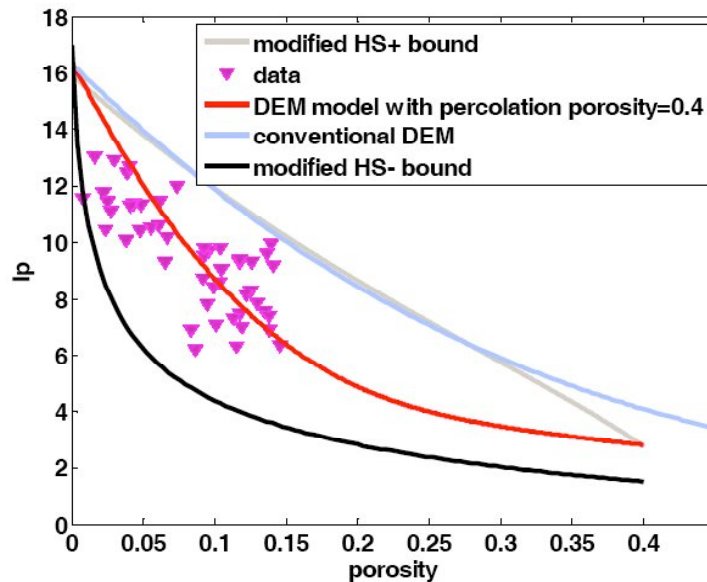


Figure D-13: Comparisons of  $I_p$  and porosity of carbonate-cemented sandstone with those predicted by the conventional DEM (blue) and the modified DEM (red). The parameters in modified DEM model are: 40 % percolation porosity, background matrix consisting quartz, calcite and clay, and inclusions with aspect ratio 0.5. The modified DEM provides a better fit to the data than the conventional model.

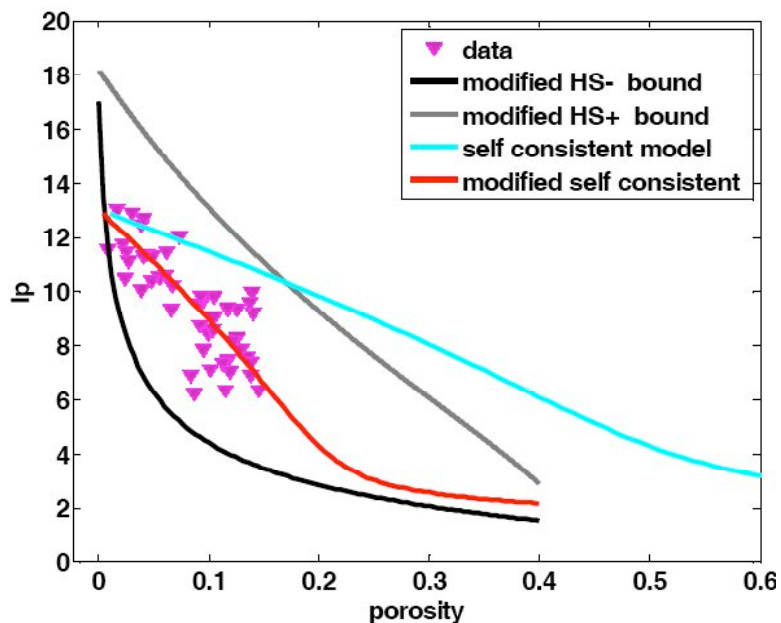


Figure D-14: Comparisons of  $I_p$  and porosity of carbonate-cemented sandstone with those predicted by the conventional SCM (blue) and the modified SCM (red). The parameters in SCM involve background matrix consisting quartz, calcite and clay, and inclusions with aspect ratio 0.5. The modified SCM is obtained by decreasing the percolation porosity from 50% to 20%. This modified SCM provides a better fit to the data than the original SCM.

## Discussions

This paper focuses on how carbonate cementation precipitated at key sequence stratigraphic surfaces, such as, the flooding surface and the incision surface, impact the seismic impedance. Our goals are two-fold: (1) to identify the sedimentological variations within carbonate-cemented sandstones; and (2) to quantify the effect of these variations on P-impedance through rock physics modeling.

We study the carbonate-cemented sandstones deposited in a mini-basin setting at Equatorial Guinea, West Africa. We find that the cemented sandstones are extremely heterogeneous in nature within the reservoir interval. Their grain-size, sorting, mineralogy, clay-content, amount of cement and degree of leaching vary considerably. These variations in sedimentological properties affect the seismic response. Key observations are:

1. Different cement mineralogy (calcite and ankerite) have different trends in P-impedance vs. porosity plane.
2. Cemented sands with higher shale content are associated with higher porosity. This observation contradicts the usual relationship between shaliness and

porosity. In this case, we think that sandstones with lower shale content are more prone to cementation; hence, they exhibit reduced porosities with cements occluding the pore space. The samples with higher total porosity have higher P-impedance.

3. Reservoir quality depends on position of cemented sandstones in a stratigraphic sequence. We observe that porosity is selectively enhanced in the carbonate-cemented sands when they occur at top of the flooding surfaces. We think that dissolution of cement is facilitated by the proximity to the flooding surface, thereby, creating secondary porosity.
4. Grain-size has practically no influence on porosity and P-impedance of these carbonate-cemented sandstones. High-porosity sands are usually better sorted. We observe an inverted 'V' pattern in grain size-sorting domain. Sorting is best for coarse and fine end-members of grain-size. Sorting decreases from 0.75 to 2.75 as coarse fractions are added to fine grains.

It is challenging to incorporate all of these sedimentological variations into a single rock physics model. We use different granular media models (the contact cement model, the constant cement model and the stiff-sand model) and different inclusion models (the modified differential effective media model and Berryman's self consistent model) to test how they fit to carbonate-cemented sandstone. The key observations are summarized below.

1. The contact cement model (Dvorkin et al., 1996) fails to explain the P-impedance ( $I_p$ ) vs. porosity trend for carbonate-cemented sands deposited at top of the flooding surfaces. Dvorkin's cement model is derived for cement at grain contacts or coatings (rim) around grain, and is only applicable for very low amount of cement and medium to high porosity sands. The present data violate these model assumptions.

2. The constant cement model (Avseth et al., 2000) with 1% constant carbonate cement explains the  $I_p$ -porosity trend in data. The advantage of the constant cement model is that it considers sorting variation. However, this model is only valid for constant amount of cement and weakly cemented rock.

3. The stiff-sand model (Gal et al., 1996) does not fit these data. However, we can obtain a reasonable fit by changing critical porosity from 40% to 15%. The heuristic argument is that the onset of carbonate cementation starts at much lower porosity (about 15 %).

4. The modified differential effective media model (Mukerji et al., 1995) with aspect ratio .5 and 40% percolation porosity, and the self consistent model (Berryman, 1995)

with 20% percolation porosity explain Ip-porosity trend in the data. However, it is difficult to interpret sedimentary texture from the inclusion models.

## **Conclusions**

We conclude that the carbonate cements are different than siliciclastic cements in terms of sedimentological parameters, and the common rock physics model for quartz cemented sandstones are not always suitable to predict P-impedance vs. porosity trends for the carbonate-cemented sandstones. The carbonate-cemented sandstones are found to be extremely heterogeneous in nature, even within a depth interval of ~60 meter in our study area offshore Equatorial Guinea, West Africa. Their grain-size, sorting, mineralogy, clay-content, amount of cement and degree of leaching vary considerably. There are two distinct clusters of data in the P-impedance vs. porosity plane. The carbonate-cemented sandstones from the base of incision surfaces exhibit lower shaliness, lower porosity and higher P-impedance. On the contrary, data from the top of flooding surfaces exhibit higher shaliness, higher porosity and lower P-impedance. The contact cement model fails to predict the trend shown by the later cluster of data. The predictions of constant cement model and the modified stiff-sand model agree with both clusters of data reasonably well. Furthermore, the modified differential effective media model and the modified self-consistent model provide reasonable fits to these carbonate-cemented sandstones. We recommend testing the predictions of rock physics models against data, classified by key stratigraphic surfaces.

## **REFERENCES**

- Avseth, P., 2000, Combining rock physics and sedimentology for seismic reservoir characterization in North Sea turbidite systems: Ph.D. thesis, Stanford University.
- Avseth, P., Mukerji, T., and Mavko, G., 2005, Quantitative Seismic Interpretation: Applying Rock Physics Tools to Reduce Interpretation Risk: Cambridge University Press.
- Berner, R.A., 1980, Early Diagenesis: A Theoretical Approach: Princeton University Press.
- Berryman, J.G., 1995, Mixture Theories for Rock Properties: A handbook of physical constants, T.J. Athrens,ed. American Geophysical Union, Washington, D.C., 205-228.
- Bjørkum, P. A., and O. Walderhaug, 1990, Geometrical arrangement of calcite cementation within shallow marine sandstones: Earth-Science Reviews, **29**, 145–161.
- Dvorkin, J. and Nur, A., 1996, Elasticity of high-porosity sandstones: Theory for two North Sea datasets: Geophysics, **61**, 1363-1370.
- Folk, R., 1964, A review of grain-size parameters: Sedimentology, **6**, 73-93.

- Folk, R.L., and Ward, W.C., 1957, Brazos river bar, a study in the significance on grain-size parameters: *Journal of sedimentary petrology*, **27**, 3-27.
- Gal, D., Dvorkin, J., and Nur, A., 1998, A Physical Model for Porosity Reduction in Sandstones: *Geophysics*, **63**, 454-459.
- Giles, M. R., 1997, *Diagenesis: a quantitative perspective*: Boston, Kluwer Academic Publishers.
- Greenberg, M.L., and Castagna, J.P., 1992, Shear-wave velocity estimation in porous rocks: Theoretical formulation, preliminary verification and application: *Geophysical Prospecting*, **40**, 195-209.
- Inman, D.L., 1952, Measures of describing the size distribution of sediments: *Journal of sedimentary petrology*, **22**, 125-145.
- Kantorowicz, J. D., Bryant, I. D., and Dawans, J. M., 1987, Controls on the permeability and distribution of carbonate cements in Jurassic sandstones: Bridport Sands, southern England, and Viking Group, Troll field, Norway, in J. D. Marshall, ed., *Diagenesis of sedimentary sequences*: Oxford, Blackwell, 103–118.
- Ketzer, J.M., Morad, S., Evans, R., and Al-Aasm, I.S., 2002. Distribution of diagenetic alterations in fluvial, deltaic, and shallow marine sandstones within a sequence stratigraphic framework: Evidence from the Mullaghmore Formation (Carboniferous), NW Ireland: *Journal of Sedimentary Research*, **72**, 760-774.
- Ketzer, J.M. and Morad, S. 2006. Predictive distribution of shallow marine, low-porosity (pseudomatrix-rich) sandstones in a sequence stratigraphic framework--example from the Ferron sandstone, Upper Cretaceous, USA: *Marine and Petroleum Geology*, **23**, 29-36.
- Loutit, T.S., Hardenbol, J., Vail, P.R., Baum, G.R., 1988. Condensed sections: the key to age determination and correlation of continental margin sequences. In: Wilgus, C.K., Hastings, B.S., Kendall, C.G.St.C., Posamentier, H.W., Ross, C.A., Van Wagoner, J.C. (Eds.), *Sea-Level Changes: An Integrated Approach*. Soc. Econ. Paleontol. Mineral., Spec. Publ. **42**, 183–213.
- Mavko, G., T. Mukerji and J. Dvorkin, 1998, *The Rock Physics Handbook, tools for seismic analysis in porous media*: Cambridge University press, New York, 329.
- McBride, E. F., Milliken, K. L., Cavazza, W., Cibir, U., Fontana, D., Picard, M.D., and Zuffa, G.G., 1995, Heterogeneous distribution of calcite cement at the outcrop scale in Tertiary sandstones, northern Apennines, Italy: *AAPG Bulletin*, **79**, 1044–1063.
- McCammon, R.B., 1962, Efficiencies of percentile measures for describing the mean size and sorting of sedimentary particles: *J. Geol.*, **70**, 453-465.
- Morad, S., 1998, Carbonate cementation in sandstones: distribution patterns and geochemical evolution, in S. Morad, ed., *Carbonate cementation in sandstones*: International Association of Sedimentologists Special Publication, **26**, 1–26.
- Mukerji T., Berryman J.G., Mavko G. and Berge P.A, 1995, Differential effective medium modeling of rock elastic moduli with critical porosity constraints: *Geophysical Research Letters*, **22**, 555–558.
- Otto, G.H., 1939, A modified logarithmic probability graph for the interpretation of mechanical analyses of sediments: *Journal of sedimentary petrology*, **9**, 62-76.
- Posamentier, H.W., and Allen, G.P., 1999, *Siliciclastic sequence stratigraphy: concepts and applications*: SEPM Concepts in Sedimentology and Paleontology, **7**, 210 p.

- Pittman, E. D., and Larese, R. E., 1991, Compaction of Lithic Sands: Experimental Results and Applications: AAPG Bulletin, **75**, 1279- 1299.
- Saigal, G. C., and K. Bjørlykke, 1987, Carbonate cements in clastic reservoir rocks from offshore Norway—relationships between isotopic composition, textural development and burial depth, in J. D. Marshall, ed., Diagenesis of sedimentary sequences: Oxford, Blackwell, 313–324.
- Taylor, K.G., Gawthorpe, R.L., and Vanwagoner, J.C., 1995, Stratigraphic Control on Laterally Persistent Cementation, Book-Cliffs, Utah: Journal of the Geological Society, **152**, 225-228.
- Taylor, K.G., Gawthorpe, R.L., Curtis, C.D., Marshall, J.D., and Awwiller, D.N., 2000, Carbonate Cementation in a Sequence-Stratigraphic Framework: Upper Cretaceous Sandstones, Book Cliffs, Utah-Colorado: Journal of sedimentary research, **70**, 360-372.
- Wagoner, J.C.Van., Mitchum, R.M., Campion, K.M., and Rahmanian, V.D., 1990, Siliciclastic sequence stratigraphy in well logs, cores and outcrops: AAPG methods in exploration series, **7**, 63 p.
- Walderhaug, O., and Bjorkum, P.A., 1992, Effect of Meteoric Water-Flow on Calcite Cementation in the Middle Jurassic Oseberg Formation, Well 30/3-2, Veslefrikk Field, Norwegian North-Sea: Marine and Petroleum Geology, **9**, 308-318.

## ATTACHMENT E

### QUANTIFYING SPATIAL TRENDS OF SEDIMENTOLOGICAL PARAMETERS

#### Abstract

Our overall goal is to identify links between conventional stratigraphic interpretation and quantitative seismic amplitudes and impedances. In this paper, we demonstrate how rock physics models for P-impedance can be reconciled with log data as a means to reveal spatial trends of quartz:clay ratio and sorting. The quartz:clay ratio and sorting are important sediment parameters that affect seismic impedance and porosity. First, we identify probable spatial trends of quartz:clay ratio and sorting as predicted from conventional stratigraphic interpretations. Next, these trends are evaluated using well data, and the same well data are used to calibrate the rock models that provide links between P-impedance and quartz:clay ratio, and sorting. We test this methodology using the well log data from a shaly-sand turbidite sequence deposited within mini-basin settings at the continental slope of Equatorial Guinea, West Africa.

We observe a systematic variation of quartz:clay ratio from proximal to distal locations even within a single facies. Furthermore, we quantify that the quartz:clay ratio changes from [0.5:0.5] to [1:0] along the direction of flow, based on the trends of P-impedance vs. porosity as predicted by the rock model for uncemented sands. The downdip trend of quartz:clay ratio as revealed from the data, contradicts the grain-size predictions from common sequence-stratigraphic models. However, the results are in agreement with spill-and-fill sequence stratigraphic model in mini-basin setting. In addition, porosity at the distal location (~25 % to 35%) is higher than the porosity at the proximal location (~20 % to 23%). This trend is explained by a sequence stratigraphic model which predicts progressive increase in sorting by turbidity current along the flow, as well as, quantified by a rock model that heuristically accounts for sorting. Our results can be applied to improve quantitative predication of sediment parameters from seismic impedance, away from well locations.

## Introduction

This paper focuses on quantifying variation of sediment properties from proximal to distal location based on geophysical measurements. We have quantified the spatial trends of quartz:clay ratio and sorting based on calibrated rock models at the well locations. The wells are spatially located from proximal to distal location of the channelized, turbidite sequence.

Sequence stratigraphy is a geological interpretation tool for process/response events (Mulholland, 1998). It can predict the likely occurrence of reservoir facies, source rocks and seals. Conventional stratigraphic interpretation from seismic data has been predominantly qualitative based on visual inspection of geometric patterns in post-stack seismic reflection data (Playton, 1977; Neal and Vail, 1993; Brown, 1996; Zeng et al., 1996). However, quantitative interpretation of seismic attributes is possible if we can extract information about compositional maturity (quartz:clay ratio) and textural maturity (sorting, grain angularity, sphericity and roundedness) using principles of sedimentology.

Rock physics provides the fundamental basis for quantitative interpretation of seismic amplitudes in terms of sediment parameters, like porosity, quartz:clay ratio, sorting, and diagenetic cements (Castagna, 2001; Braaskma et al., 2002; Gutiérrez et al., 2002; Latimer et al., 2000; Avseth et al., 2005; Florez, 2005). In quantitative seismic interpretation, model parameters are calibrated at the well locations. However one of the major sources of uncertainty in rock physics modeling arises due to our lack of knowledge about trends of input parameters away from the wells.

Rock physics modeling away from the wells should benefit from the trends of sediment parameters predicted by sequence stratigraphy. Various authors have shown that sequence stratigraphy can provide predictive trends of spatial variations of sedimentological parameters within a sequence away from the wells (Wagoner et al., 1990; Posamentier and Allen, 1993). However, it is essential to validate and calibrate such trends predicted by sequence stratigraphy with those predicted by rock physics model at the well locations..

We have organized this paper in three different sections. First, we present the spatial trends of sand:shale (quartz:clay) ratio and sorting as predicted from sequence stratigraphic models of deep-water channelized deposits. Next we interpret sequences using seismic and well data from similar depositional environment. Finally, we link spatial trends of sediment parameters with P-impedance based on P-impedance vs.

porosity patterns obtained from rock physics modeling at wells, spatially located from proximal to distal part of a channel.

### **Spatial Trend of Sediment Properties in Deep-water Settings**

In this section, we discuss trends of sand:shale ratio and grain-size variation (sorting) in deep-water settings where channelized turbidite sands are deposited in mini-basins. The relative trends of sediment parameters in stratigraphic sequence can be obtained in three different ways: outcrop observations, numerical simulations, and laboratory experiments. These trends can then be applied to similar depositional environments after calibrating P-impedance vs. porosity patterns predicted by rock models at the wells.

Detailed outcrop studies of the internal facies architecture of turbidite systems provide key predictive insights into analogous intervals in the subsurface (e.g., Browne and Slatt 2002). Outcrop studies on submarine-canyon fills exposed at Wagon caves, California, show that median grain size and standard deviation of grain-size (sorting) improves vertically upward (Anderson et al., 2006). The spatial variations in sediment characteristics within a parasequence can be attributed to both source area effects and local hydrodynamic factors. Spatially sand:shale ratio decreases in the downdip direction (Kirk, 1980) due to decrease in flow energy within channel. Sorting also improves from proximal to distal location due to segregation of clay from silt particles (Piper, 1978).

Numerical simulation of turbidity currents usually agree with outcrop observations. Simulation results with mini-basin settings show that progressively finer-grained materials are deposited at the distal location, along with better sorting at the distal location than updip proximal location (Lerch et al., 2005).

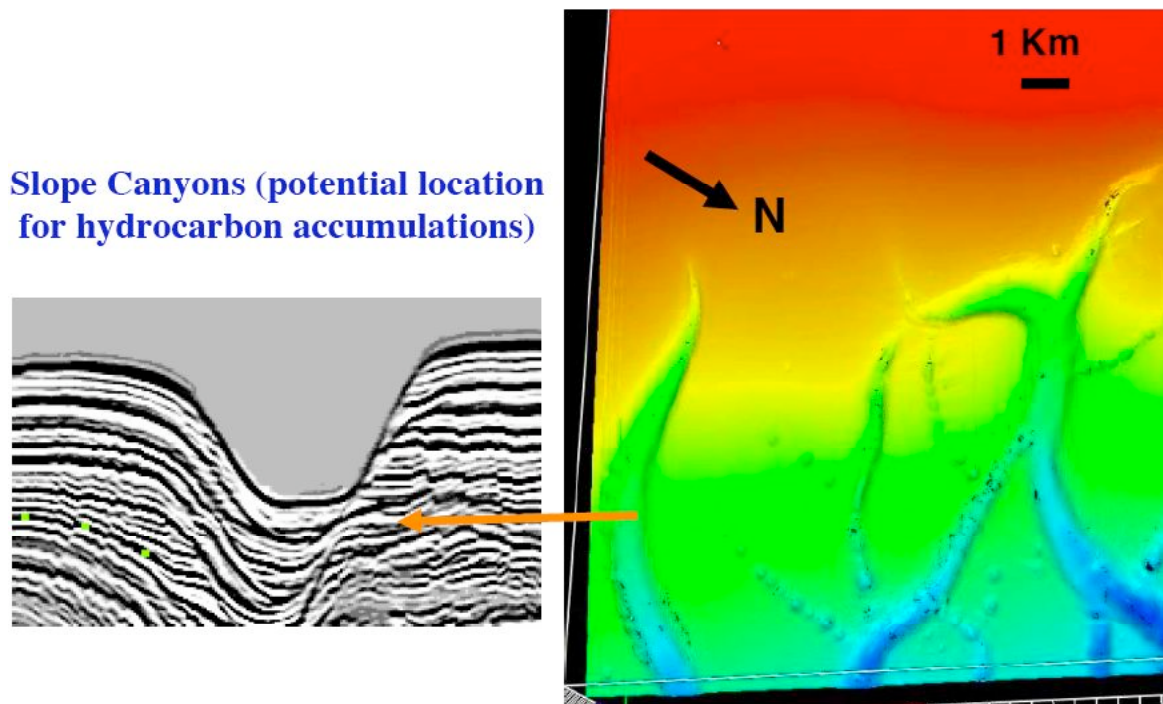
Laboratory simulations of turbidity currents in mini-basin settings (Brunt et al., 2004) contradict the grain size prediction from outcrop by Kirk (1980), predicting a downdip increase in sand:shale. Brunt et al. (2004) show that progressively greater proportions of coarser grained material can be spilled downstream as the degree of confinement is reduced in mini-basin settings (spill-and-fill model). Therefore, downdip increase in quartz:clay ratio as observed from the subsurface data of similar depositional environment can be interpreted in terms of downdip decrease in confinement of flow in the mini-basin.

### **Sequence Stratigraphic Setting of the Study Area**

We select channelized turbidite sandstones deposited offshore Equatorial Guinea, West Africa. We select these data to test the predictions of sand:shale ratio and sorting

from sequence stratigraphic model of similar environment, and link these sediment parameters with seismic impedance at the well.

We find that the much of the sandstones in the study are likely to be deposited within the confines of submarine canyons. Figure E-1 shows our interpretation of present-day seabed mapped from 3D post-stack, time-migrated seismic data. The map shows incisions or erosions by the submarine channels (Figure E-1). This incision can create ~200 m of depression. These depressions created by the submarine canyon give rise to mini-basin settings. The geometry of the mini-basin and successive fills can be observed from the vertical seismic section (Figure E-1). The sandstones deposited within mini-basin constitute the primary exploration target in deep water (Dailly et al., 2002). Submarine canyons are important conduits for the transport of coarse-grained sediment into the deep sea on most continental margins (Shepard and Dill 1966; Normark and Carlson 2003). Stacked successions of coarse-grained, high-density turbidity current deposits and related architectural elements of submarine canyon fills usually constitute significant petroleum reservoirs (Anderson et al., 2006).



**Slope Canyons (potential location for hydrocarbon accumulations)**

Figure E-1: Seismic stratigraphic interpretation. Right: Present-day sea-floor map interpreted from 3D post-stack, time-migrated seismic data. We observe incisions created by submarine canyons on the continental slope. Right: Geometry of mini-basin on vertical seismic section. The mini-basins are formed by incision of submarine canyons. The incised-fill sandstones may be potential reservoir.

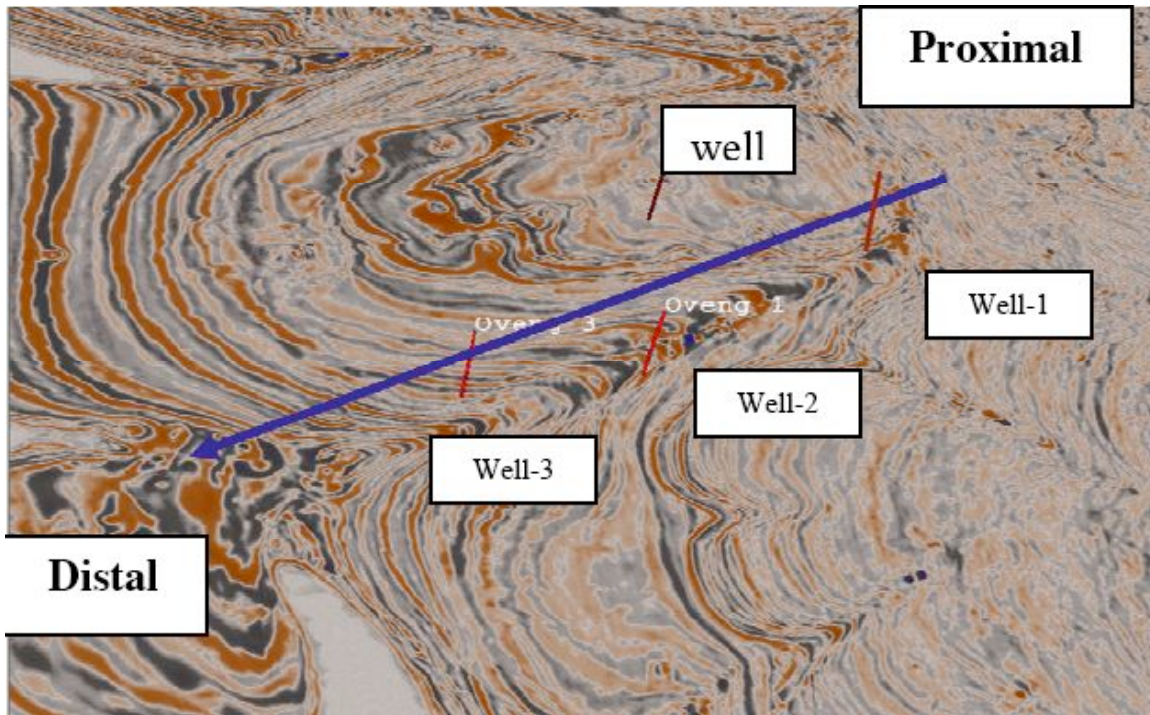


Figure E-2: Time section showing wells in channelized turbidite deposits from proximal to distal location.

We select three wells from proximal to distal locations of the channelized turbidite sequence. Figure E-2 shows the spatial location of these wells within a channel. Well-1 is the proximal well, well-2 is the middle well, and well-3 is the distal well. The well logs show fining-up motif, which is typical for channelized sequences and indicate decrease in depositional energy vertically upward. Figure E-3 shows an example of a fining-up sequence from well-3. We observe a blocky motif on the well logs just beneath the fining-up sequence. The core descriptions report that the fining-up sequence is usually uncemented, and the blocky sequence is usually associated with carbonate-cemented sandstones. In this paper, we focus on spatial variations of sand:shale ratio and sorting of the fining-up, uncemented sandstones. For this, we select similar fining-up sequences in three different well from similar depth interval. The seismic response of carbonate-cemented sandstones is discussed in paper-B5 of this SRB annual volume.

The well-log motif alone cannot confirm the depositional environment. Fining-upward patterns on well logs suggest different possible environments. For example, tidal channels, fluvial point bars, and turbidite channels all show characteristic fining-upward patterns. In the present study area, the well logs along with geometry from seismic data suggest that the channels were deposited in a deep-water environment. Core descriptions from the same study area (Lowe, 2004) confirm that the shaly-sand, fining-up sequence were deposited by high-density turbidity current in submarine canyon.

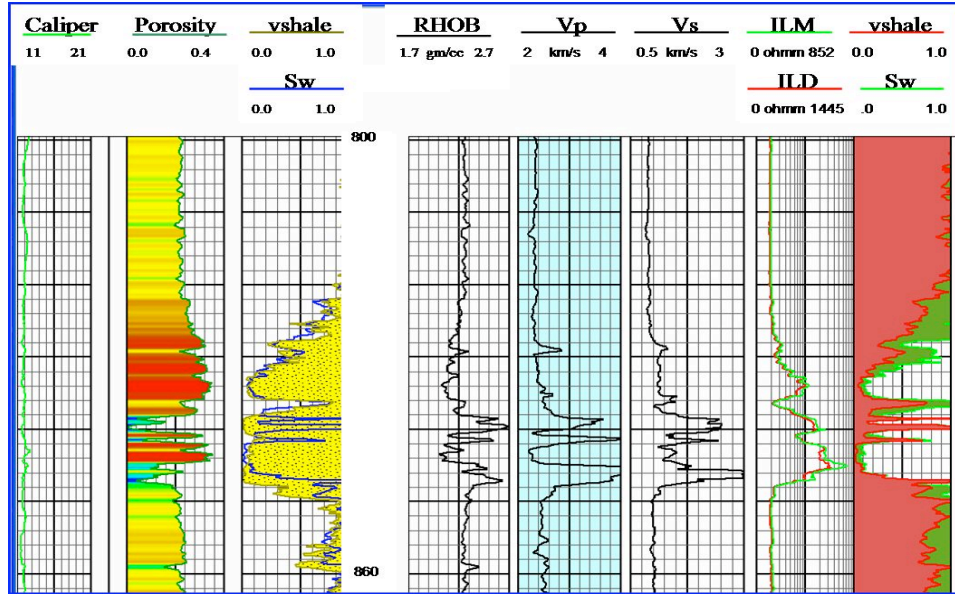


Figure E-3: Well-logs from well-3 showing an example of fining-upward shaly-sand sequence. We select similar fining-upward sequence at similar depth-interval in three different wells to identify the link between sediment parameters and P-impedance.

We expect that quartz:clay should decrease from well-1 to well-3 for a channelized sequence. The depositional energy decreases along the flow direction, thereby, resulting in higher fractions of finer particles at the distal location. In addition, we expect that sorting should improve at the distal location with deflocculation process. Deflocculation segregates clay from silt particles by the turbidity current, and improves sorting. The next section illustrates how these expected spatial trends of quartz:clay ratio and sorting correspond to the well data and calibrated rock models at the wells.

### Calibration of Rock Models at the Wells

We test two different rock models, the cemented-sand model and the uncemented-sand model (Dvorkin and Nur, 1996; Mavko et al., 1998). In both models, the effective moduli at the well-sorted, high-porosity end member (~40% for sandstones) are computed using Hertz-Mindlin (Mindlin, 1949) theory. Hertz-Mindlin contact theory provides the following expressions for the bulk ( $K_{HM}$ ) and shear ( $G_{HM}$ ) moduli of a dense random pack of identical spherical grains subject to an effective pressure  $P$  (Mavko et al., 1998):

$$K_{HM} = \left[ \frac{C^2(1-\phi_0)^2 G^2}{18\pi^2(1-\nu)^2} P \right]^{1/3} \quad (1)$$

$$G_{HM} = \frac{5 - 4\nu}{5(2 - \nu)} \left[ \frac{3C^2(1 - \phi_0)^2 G^2}{2\pi^2(1 - \nu)^2} P \right]^{1/3} \quad (2)$$

where  $\phi_0$  is the critical porosity (~40 % in sandstones), C is the coordination number/ average number of grain contacts; G and  $\nu$  are the mineral shear modulus and Poisson's ratio. The elastic moduli at the zero-porosity end member are given by mineral moduli.

In the uncemented sand model or friable-sand model (Dvorkin and Nur, 1996; Mavko et al., 1998), the effective elastic moduli of sand with porosities between 0 to critical porosity (~40%) are interpolated using the lower Hashin-Shtrikman bound (Mavko et al., 1998). The heuristic argument for this is that adding small grains in the pore space is the elastically softest way to add mineral. The lower bound (an isostress model for suspensions) is always the elastically softest way to mix multiple phases.

In the cemented sand model (Dvorkin and Nur, 1996; Mavko et al., 1998), effective moduli of sand with porosities ranging between 0 to critical porosity (~40%) are interpolated using the upper Hashin-Shtrikman bound (Mavko et al., 1998). The heuristic argument for this is that adding cement in pore-network is the elastically stiffest way to add minerals. The upper bound (an isostrain model) is always the elastically softest way to mix multiple phases.

Figures E-4, E-5 and E-6 compare data from wells ranging from proximal to distal location along with predictions of P-impedance vs. porosity trends from rock physics models. The data are color-coded by  $v_{shale}$ . The solid black lines indicate predictions from the uncemented rock model for different quartz:clay ratios, and, the magenta lines are predictions from the cemented sand model for quartz:clay ratio equal to 1:0. We observe that the uncemented rock model predicts an increase in P-impedance with increase in quartz:clay ratio for a constant porosity (Figures E-4, E-5 and E-6). This suggests that as the composition maturity (quartz:clay ratio) improves and the other parameters remain unchanged, the P-impedance will increase. We obtain different contours of clay content by varying quartz:clay ratio in the uncemented or friable-sand rock model. This model predicts an increase in P-impedance with decrease in porosity along a particular clay contour (Figures E-4, E-5 and E-6). We attribute the increase in P-impedance along a particular clay contour due to different degree of sorting, according to the argument by the friable-sand model.

The cemented-sand model, which is suitable for stiffer sediments, does not fit the trend in the present well data. This observation is in agreement with core observations, which do not show any evidence of cement in the fining-upward sequence. Figures E-4 and E-5 show P-impedance vs. porosity at the proximal well (well-2) and the middle well

(well-3). We observe that the sand-rich and clay-rich facies in these two wells separate into two different clusters. The sand-rich facies (low vshale content) exhibit higher P-impedance than shaly facies (high vshale content). Two distinct clay contours of 0 % and 60 % clay, as predicted from the uncemented rock model, pass through the mean of these clusters. However, the transition from sandy to shaly facies in the distal well (Figure E-6) shows a gradual increase in P-impedance transects the clay contours ranging from 0 to 100 % clay content.

Finally, we summarize the spatial patterns of P-impedance vs. porosity as observed from three well locations in Figure E-7. The black arrow indicates flow direction within the channel. There are two different patterns of P-impedance vs. porosity at the proximal well locations and the distal well location. In the proximal well locations, the sand-rich and shale-rich facies separate into two different clouds. On the contrary, there is a gradual transition from sandy to shaly facies at the distal location. This probably suggests that two distinct depositional energy prevailed at the proximal locations, whereas, depositional energy changed gradually at the distal location. The rock physics models calibrated at the wells can be used to predict sediment parameters from P-impedance.

The next section will quantify the spatial variation of quartz:clay ratio and sorting (porosity) within a single facies based on the well data and the calibrated rock model at the wells.

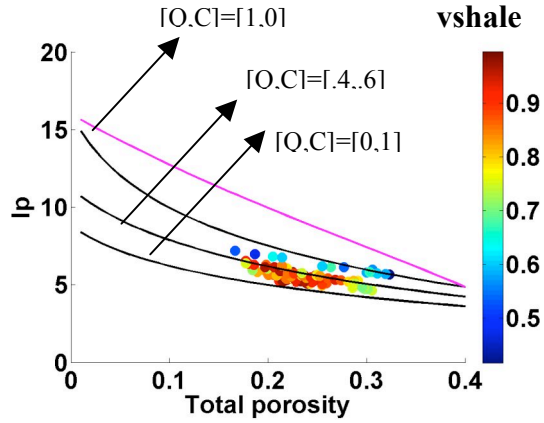


Figure E-4: P-impedance ( $I_p$ ) vs. total porosity at well-1 situated at proximal location. [Q,C] represent quartz and clay content input to uncemented rock model. The black lines represent P-impedance predicted by uncemented rock model for different quartz:clay ratio at different porosities. Magenta line shows  $I_p$ -porosity trend predicted by cemented-sand rock model.

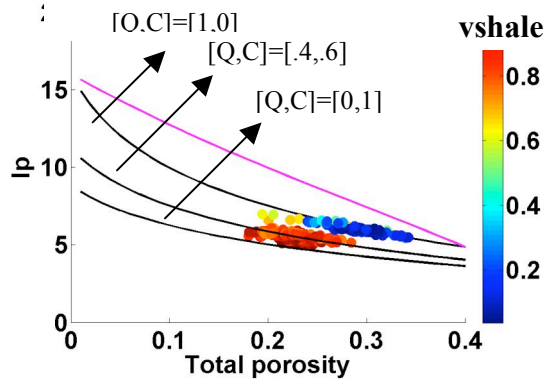


Figure E-5: P-impedance ( $I_p$ ) vs. total porosity at well-2 along with predictions from rock models.

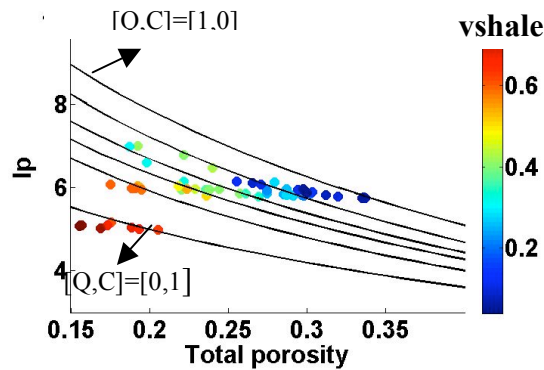


Figure E-6: P-impedance ( $I_p$ ) vs. total porosity at well-3 along with predictions from rock models.

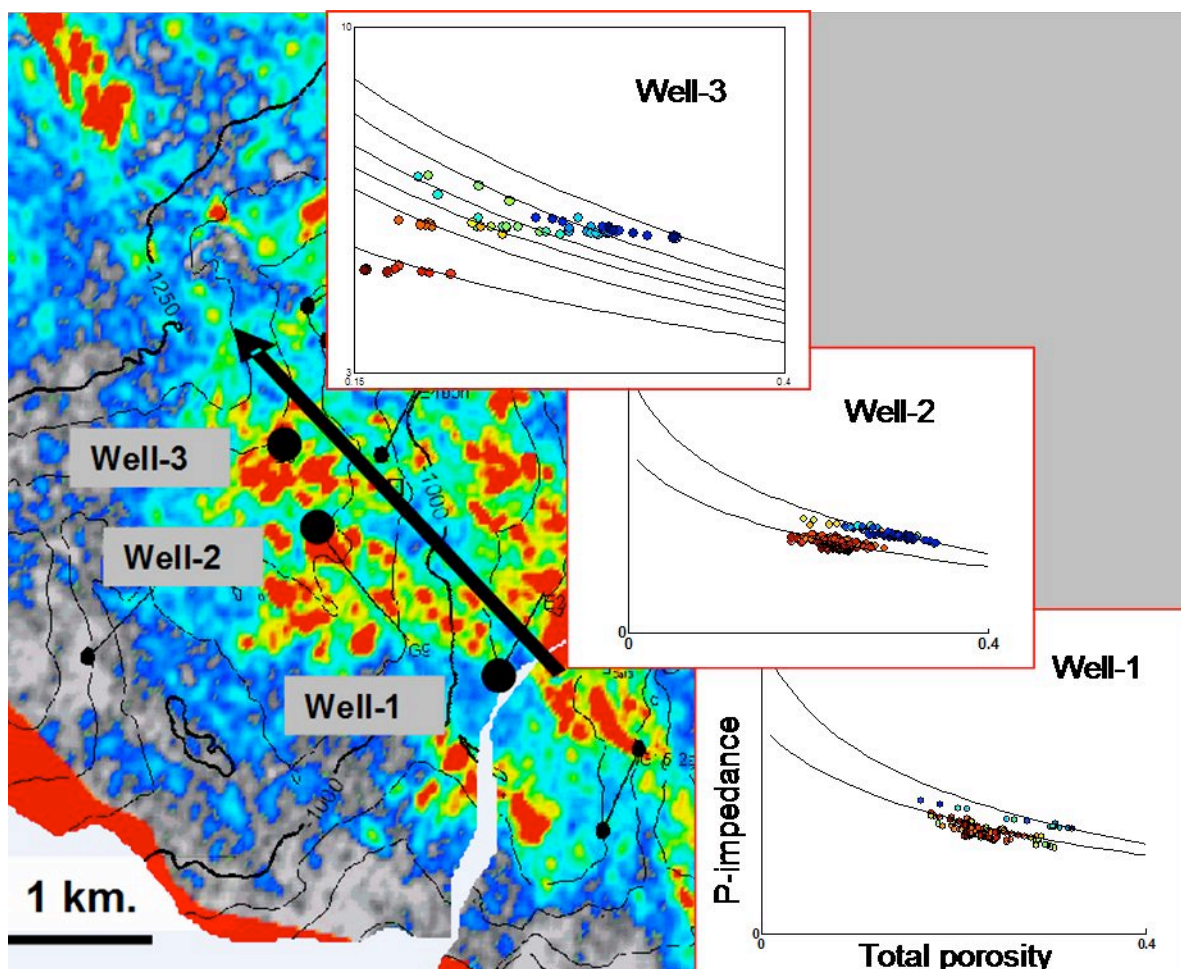


Figure E-7: Seismic amplitude map showing channelized turbidite sequence. Well-1, 2 and 3 are located from proximal to distal locations. The black arrow indicates flow direction within channel. Spatial patterns of P-impedance vs. porosity can be observed from the trends predicted by rock model at the well locations.

### Spatial Trend of Sediment Properties in Sand-rich Facies

We isolate the sand-rich facies deposited near the base of sequences. The goal is to identify spatial variations of sedimentological parameters within a single facies. Core descriptions from the same field reveal that facies deposited near the base of fining-up sequences are mostly massive sandstone to thick-bedded sandstone with higher potential to contain hydrocarbon. Figure E-8 shows the P-impedance and porosity at three wells for this massive sandstone facies, along with P-impedance vs. porosity trends predicted

from the uncemented rock model for different quartz:clay ratio. We observe that the same facies at the distal location has higher porosity and higher P-impedance than the proximal location. The rock model calibrated with data indicates a downdip increase in porosity, quartz:clay ratio and P-impedance(Figure E-8).

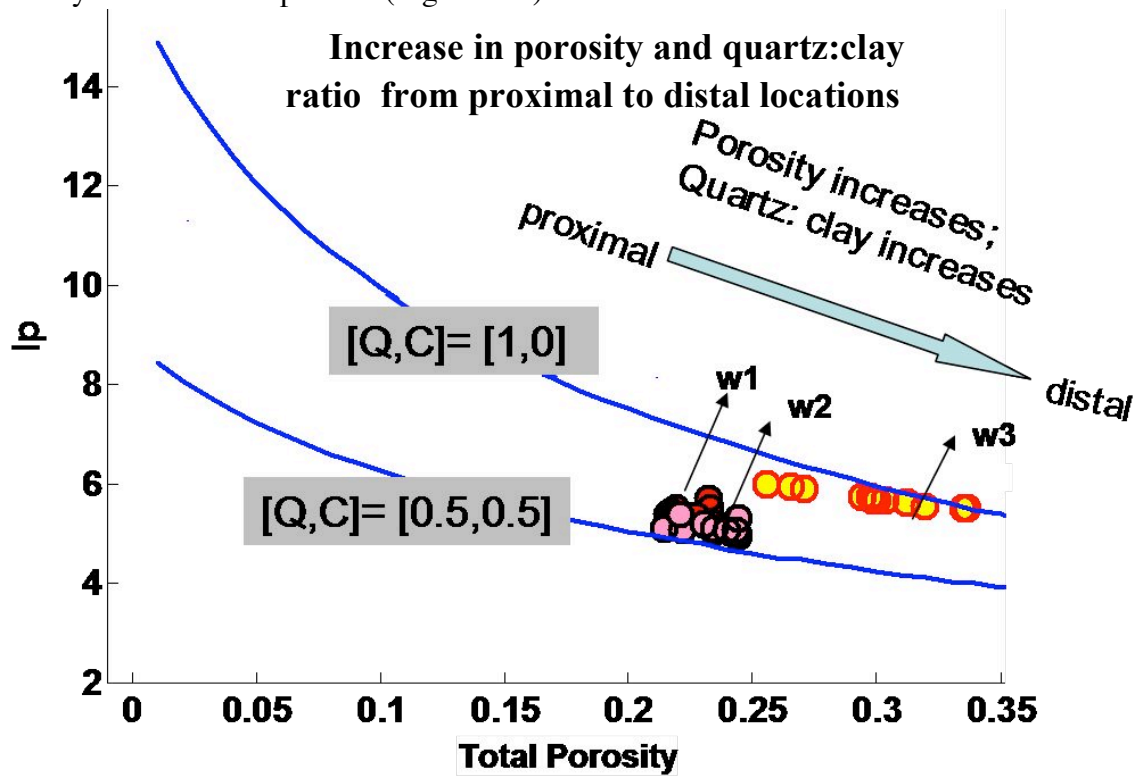


Figure E-8: Spatial trend of sediment properties of thick-bedded sandstone (potential reservoir facies). Porosity and quartz:clay ratio increases from proximal to distal location

The downdip increase in porosity (Figure E-8) can be explained by improved sorting along the direction of transport of sediments by turbidity current. Sequence stratigraphic studies in deep-water (Piper, 1978) indicate that deflocculation (segregation of clay from silt particles) caused by turbidity current increase sorting distally. Numerical simulations of turbidity current in submarine canyon (Lerch et al., 2005) also indicate improved sorting along the direction of transport in submarine canyons.

The rock models are calibrated with well log data, and, they show a decrease in clay content from proximal to distal location (Figure E- 8). This observation contradicts the trend of sand:shale ratio predicted from general sequence stratigraphic models (Kirk, 1980). In general, the sequence stratigraphic models predict an increase in clay content along flow-direction, since depositional energy gradually diminishes with distance.

However, laboratory experiments of turbidity current (Brunt et al., 2004) demonstrate that it is possible to spill coarser sand fractions (higher quartz content) in distal location.

In ponded mini-basin settings (basins that are linked streamwise), as an upstream mini-basin is filled with sediment, progressively more overspill is directed into the next mini-basin downstream. Progressively greater proportions of coarser-grained material are spilled downstream as the degree of confinement is reduced (Brunt et al., 2004). Therefore downdip increase in quartz:clay ratio as observed from calibrated rock model can be interpreted in terms of downdip decrease in confinement of flow in mini-basins.

## **Conclusions and Discussions**

We have quantified the trends of spatial variations of sedimentological parameters in a rock-physics plane (P-impedance vs. porosity plane). The spatial trends of quartz:clay ratio and sorting are obtained for channelized turbidite facies deposited in mini-basin settings at Equatorial Guinea, West Africa. The sand-rich and clay-rich facies separate in two distinct clusters in P-impedance vs. porosity plane at the proximal and the middle well. The sand-rich facies (low vshale content) exhibit higher P-impedance than shaly facies (low vshale content). Two distinct clay contours of 0 % and 60 % clay as obtained from uncemented rock model pass through the mean of these clusters. However in the distal well, P-impedance from sand to shale increases gradually and transects different clay contours ranging from 0 to 100 % clay content. This probably suggests distinct depositional energy prevailed at the proximal locations, whereas, depositional energy changed gradually at the distal location.

We have selected thick-bedded to massive sandstone facies deposited at the base of fining-up sequences (potential reservoir facies) to identify spatial patterns of reservoir qualities and link them with seismic impedances. Rock physics modeling shows that the same facies is characterized by higher P-impedance at the distal well location, which corresponds to a higher quartz:clay ratio. The quartz:clay ratio changes from [0.5:0.5] to [1:0] along the direction of flow. In addition, porosities at the distal location (~25% to 35%) are higher than porosities at the proximal location (~20% to 23%).

In general, we expect a downdip decrease of coarser fractions (quartz) with depositional energy diminishing along the flow direction. However, in present study, we observe an increase in quartz:clay ratio from proximal to distal locations (Figure E-8). This can be explained by spill-and-fill model in mini-basin settings. Brunt et al. (2004) show that progressively greater proportions of coarser grained material are transported downstream as the degree of confinement is reduced in mini-basins. Therefore, downdip

increase in quartz:clay ratio can be interpreted in terms of downdip decrease in confinement of flow. The higher porosity at the distal well location observed in P-impedance vs. porosity plane are in agreement with sequence stratigraphy, which predicts progressive increase in sorting by turbidity currents along flow direction.

We have developed a methodology to quantify spatial trends of sediment parameters using stratigraphic interpretations and rock models calibrated at the wells. The method is applied on a turbidite, channelized sequence to quantify spatial trends of quartz:clay ratio and sorting. Our method can be applied to interpret sediment parameters from P-impedance prediction of sediment parameters from seismic impedance, away from well locations.

## References

- Anderson, K., Graham, S., and Hubbard, S., 2006, Facies, architecture, and origin of a reservoir-scale sand-rich succession within submarine canyon fill: insights from Wagon caves rock (Paleocene), Santa Lucia Range, California, U.S.A: *Journal of Sedimentary Research*, **76**, 819-838.
- Avseth, P., Mukerji, T. and Mavko, G., 2005, *Quantitative Seismic Interpretation: Applying Rock Physics Tools to Reduce Interpretation Risk*: Cambridge University Press.
- Bachrach, R., Dvorkin, J. and Nur, A., 2000, Seismic velocities and Poisson's ratio of shallow unconsolidated sands: *Geophysics*, **65**, 559-564.
- Braaksma, H., Kenter, J.A.M., Proust, J.N., Dijkmans, V., Hoek, T.V. and Drijkoningen, G.G., 2002, Controls on acoustic properties of upper siliciclastic rocks (Boulonnais, northern France): *Geophysics*, **68**, 58-69.
- Brown, A., Wright, R.M., Burkart, K.D., Abriel, W.L., Interactive seismic mapping of net producible gas sand in the Gulf of Mexico: *Geophysics*, **49**, 6, 686-714.
- Browne, G.H., and Slatt, R.M., 2002, Outcrop and behind-outcrop characterization of a late Miocene slope fan system, Mt. Messenger Formation, New Zealand: *American Association of Petroleum Geologists, Bulletin*, **86**, 841-862.
- Brunt, R., McCaffery, W., and Kneller, B., 2004, Experimental modeling of the spatial distribution of grain size developed in a fill-and-spill mini-basin setting: *Journal of Sedimentary Research*, **74**, 438-446.
- Castagna, J. P., 2001, Recent advances in seismic lithologic analysis: *Geophysics*, **66**, 42-46.
- Dailly, P., Lowry, P., Goh, K., and Monson, G., 2002, Exploration and development of Ceiba Field, Rio Muni Basin, Southern Equatorial Guinea: *The Leading Edge*, **21**, 1140-1146.
- Dvorkin, J. and Nur, A., 1996, Elasticity of high-porosity sandstones: Theory for two North Sea datasets: *Geophysics*, **61**, 1363-1370.
- Florez, J.M., 2005, *Integrating geology, rock physics, and seismology for reservoir-quality prediction*: Ph.D. Thesis, Stanford University.

- Gassmann, F., 1951, Über die Elastizität poroser Medien, Vierteljahrsschrift der Naturforschenden Gesellschaft in Zürich, **96**, 1-23
- Gutiérrez, M., Dvorkin, J., and Nur, A., 2002, Stratigraphy-guided rock physics: The Leading Edge, **21**, 98-103.
- Kirk, R.M., 1980, Mixed sand and gravel beaches: morphology, processes and sediments: Progress in Physical Geography, **4**, 189–210.
- Latimer, R., Davidson, R., 2000, An interpreter's guide to understanding and working with seismic-derived acoustic impedance data: The Leading Edge, **19**, 242-256.
- Lerch, C., Strauss, M., Meibur, E., Kneller, B., Glinsky, M., Kuzmin, S., Hall, B., 2006, Numerical Simulation of Turbidity Currents: A Progress Report on Development and Applications: AAPG Annual Convention, Search and Discovery Article #40209.
- Lowe, D.R., 2004, Report on core logging, lithofacies, and basic sedimentology of Equatorial Guinea: Hess internal report.
- Mavko, G., T. Mukerji and J. Dvorkin, 1998, The Rock Physics Handbook, tools for seismic analysis in porous media: Cambridge University press, New York, 329.
- Mindlin, R.D., 1949, Compliance of elastic bodies in contact: ASME Journal of Applied Mechanics, **71**, A-259 -268.
- Mulholland, J.W., 1998, Sequence stratigraphy: basic elements, concepts and terminology: The Leading Edge, 37-40.
- Neal, J., Risch, D. and Vail, P., 1993, Sequence stratigraphy- a local theory with global success: Oilfield review, 51-62.
- Normak, W.R., and Carlson, P.R., 2003, Giant submarine canyons; is size any clue to their importance in the rock record?, in Chan, M.A., and Archer, A.W., eds., Extreme Depositional Environments; Mega End Members in Geological Time: Geological Society of America, Special Paper 370, p. 175–190.
- Piper, D.J.W., 1978, Sedimentation in Submarine Canyons, Fans and Trenches: Turbidite muds and silts on deepsea fans and abyssal plains.
- Playton, C.E., 1977, Seismic stratigraphy- applications to hydrocarbon explorations: AAPG Memoir, **26**, The American association of petroleum geologists, 516.
- Posamentier, H.W., and Allen, G.P., 1993, Sequence stratigraphy and facies model of an incised valley fill: the Gironde estuary, France: Journal of Sedimentary Research, **63**, 378-391.
- Shepard, F.P., and Dill, R.F., 1966, Submarine Canyons and Other Sea Valleys: Chicago, Rand McNally, 381 p.
- Wagoner, J.C.Van., Mitchum, R.M., Campion, K.M. and Rahmanian, V.D., 1990, Siliciclastic sequence stratigraphy in well logs, cores and outcrops: AAPG methods in exploration series, **7**.
- Zeng, H., Beckus, M.M., Barrow, K.T and Tyler, N., 1996, Facies mapping from three dimensional seismic data: potential and guidelines from a tertiary sandstone-shale sequence model, Powderhorn field, Calhoun Country, Texas: AAPG Bulletin, **90**, 16-46.
- Wagoner, J.C.Van., Mitchum, R.M., Campion, K.M., and Rahmanian, V.D., 1990, Siliciclastic sequence stratigraphy in well logs, cores and outcrops: The American Association of Petroleum Geologists, Methods in Exploration Series, no. 7.

## **National Energy Technology Laboratory**

626 Cochrans Mill Road  
P.O. Box 10940  
Pittsburgh, PA 15236-0940

3610 Collins Ferry Road  
P.O. Box 880  
Morgantown, WV 26507-0880

One West Third Street, Suite 1400  
Tulsa, OK 74103-3519

1450 Queen Avenue SW  
Albany, OR 97321-2198

539 Duckering Bldg./UAF Campus  
P.O. Box 750172  
Fairbanks, AK 99775-0172

Visit the NETL website at:  
[www.netl.doe.gov](http://www.netl.doe.gov)

Customer Service:  
1-800-553-7681

